UNIVERSITY OF LONDON THESIS

Degree PhD Year 2008 Name of Author EHLERS, FLEMMING, JOACHIM, HEINRICH

MODELLING OF THE INTERACTIONS OF Cu AND RARE EARTH METAL WITH Si(001)

F. J. H. EHLERS, UNIVERSITY COLLEGE LONDON, D.PHIL THESIS

22nd February 2008

ProQuest LLC
789 East Eisenhower Parkway
P.O. Box 1346
Ann Arbor, MI 48106-1346

I, Flemming Joachim Heinrich Ehlers, confirm that the work presented in this thesis is my own. Where information has been derived from other sources, I confirm that this has been indicated in the thesis.

Abstract

Cu is one of the most detrimental impurities to the Si devices. A theoretical investigation into diffusing interstitial Cu (Cu_i) in Si and the interactions of Cu_i with other impurities and defects of the host lattice is strongly desired in order to understand and control the reaction paths of this impurity. We have performed *ab initio* modelling of the interactions of isolated Cu_i with bulk Si and the Si(001) surface, presenting explanations to a previously unsolved phenomena for the interactions of Cu with Si: according to our studies, Cu is a shallow donor with a closed $3d$ shell, strongly affected by inherent distortions of the Si environment. The attraction of Cu to Si(001) is explained by surface reconstruction induced distortions of the Si environment with Cu-Si bond formation (leading to trapping of the impurity) only occuring within three layers of the surface. Our results provide promising results for gettering of Cu and Cu nanowire formation on the Si(001) surface.

Rare earth (RE) disilicide nanowires on the Si(001) surface have been intensely studied by experiment as a candidate for next generation interconnects in devices. Our investigations of these systems represent the first theoretical studies of the interacting wire and substrate. We have focussed on the importance of treating the wire growth as a 1D phenomenon, presenting a new candidate structure for the epitaxially grown wire on the basis of these considerations. Our studies, involving Y (not a RE metal but displaying the same behaviour with regards to wire growth) for simplicity, have verified the stability of the wire relative to the RE metal and Si atom reservoirs on the substrate. Finally, initial studies of atomic strings observed in very recent experiments upon deposition of Y on Si(001) have been carried out.

Contents

List of Figures

List of Tables

Acknowledgements

- With the kind of things that you're working on, if it weren't for the fact that you were interested in the topic, you would be hating it, no?
C. B. L. Ehlers, 2007

Without the fruitful interactions with my two supervisors, David Bowler and Andrew Horsfield, the thesis would never have ended up looking anything like this. I can only produce decent work if interacting with people with whom I get along. At times when I have needed it, the feedback from both Dave and Andrew has been exactly what was required: I very much appreciate the opportunity that fate provided for me to collaborate with these people. It has been a pleasure, even though writing the thesis has sometimes been absolute hell, due to the severe time limitations ultimately imposed on this part of the project. I have been extremely inspired by the work I have been involved with and I hope this shines through in the presentation (otherwise it is going to be 300 long pages..). This work was funded by the Interdisciplinary Research Collaboration (IRC) on Nanotechnology. I furthermore acknowledge funding and computer resources made available by the National Institute for Materials Science (NIMS) in Japan for my visit at NIMS where some of the calculations of this work were performed.

My three and a half years in the UK have changed me completely. I know that this might be a phrase used too often, but in this case the change is so large that I can no longer truly recognize the person who left Denmark in April 2004. I have had so many amazing and challenging experiences while being in London that I think, having the slightest idea of what was in stock for me at the point of my arrival back then, I would probably have found an excuse to stay at home. Living, with all that has involved, has sometimes been considerably more challenging than studying, but also immensely rewarding. I have no intention of including a full list of all the people who have had an important influence on my life here, only I hope that I have made every one of them aware, either through my words or my actions (or, preferably, both) how much they have mattered, and will continue to matter, to me.

Finally, I want to thank my absolutely extraordinary family in Denmark for being there all along, whenever I needed their support, and for being exactly the way they are.

Chapter 1

THEORETICAL TECHNIQUES

1.1 INTRODUCTION

This chapter will contain a brief introduction to the theory used for the calculations described in Ch. 5 and Ch. 6. In Sec. 1.2 we will present the basic problem of interest, to determine the minimum energies for the system under investigation (with the main task being to describe accurately the results of the interactions between the electrons in the system, the N-electron problem), and discuss the fundamental approximations needed in order to be able to attack this problem at all. The section will include a presentation of density functional theory (DFT), which forms the basis upon which all calculations in this work has been performed. DFT itself has various levels of accuracies as this approach to solving the N-electron problem involves leaving one energy term (the exchange-correlation energy E_{xc}) unknown: practical use of DFT involves a well-defined approximation to this term. In Sec. 1.3 we will describe various approximations suggested for describing E_{xc}.

Following the discussions of basic theory in Sec. 1.2 and Sec. 1.3, the next two sections of this chapter will deal with practical ways of applying DFT. A key issue here (but by no means the only issue of importance) is how to reduce the amount of time needed to do calculations on a particular system without leaving out any of the important physics of the problem. In Sec. 1.4 we will describe the idea of pseudopotentials (PPs), which serves as a nice example of an attempt to keep things right only where they need to be. All the calculations presented in this work has been based on the PP approach, but two methods, the plane wave code VASP and the atomic type orbital code PLATO, have been employed: In Sec. 1.5, we will present these two methods and discuss reasons for choosing one over the other.

1.2 THE *N*-ELECTRON PROBLEM AND DENSITY FUNCTIONAL THEORY

1.2.1 FUNDAMENTAL APPROXIMATIONS: *N*-ELECTRON PROBLEM DEFINED

The studies performed in this work basically involve structural optimization: given a collection at ions and electrons, we want to know which arrangement(s) will be the energetically most favourable according to theory. Quantum mechanics tells us that the answer to this question is obtained by minimizing the expectation value for the Hamiltonian operator $\hat{H}$ (which contains all the operators for the interactions between the constituents) with respect to the wavefunction Φ (the norm square of which equals the particle probability distribution) for the set of electrons and nuclei, with the restriction that this wavefunction be normalized. This amounts to solving (using conventional bra-ket notation)

$$\delta\{< \Phi|\hat{H}|\Phi > -\mu < \Phi|\Phi >\} = 0 \tag{1.1}$$

where the lagrange multiplier μ, by construction, will describe the set of local minimum energies for the system.

As the electrons are much lighter than the nuclei, they move much faster: the *Born-Oppenheimer approximation* takes this fact into account by assuming that, for a given set of positions for the nuclei, the electrons will be in their ground state (GS). This means that the problem described with Eq. 1.1 is now separated into *(i)* minimizing the expectation value for the Hamiltonian operator $\hat{H}_{el}$ for a system of *fixed* nuclei with respect to the N-electron wavefunction Ψ (which depends on the choice of positions for the nuclei)

$$\delta\{< \Psi|\hat{H}_{el}|\Psi > -\lambda < \Psi|\Psi >\} = 0 \tag{1.2}$$

and *(ii)* minimizing the energy of the ions moving (as specified by the presence of the kinetic energy operator $\hat{T}_{nucl}$) in the field E generated by the electrons [1] with respect to the ion wavefunction Λ (i.e., $\Phi = \Lambda\Psi$)

$$\delta\{< \Lambda|\hat{T}_{nucl} + E|\Lambda > -\xi < \Lambda|\Lambda >\} = 0. \tag{1.3}$$

The Born-Oppenheimer approximation basically is always made. An additional frequently used fundamental simplification of Eq. 1.1 consists in ignoring thermal excitations of the electrons, i.e., performing the calculations at T = 0 K. At RT, the electron occupancies will differ from their zero temperature values in a range no larger than $\sim k_B T$ (0.025 eV), which makes it evident that the approximation is quite justifiable at this temperature.

1.2.2 SOLVING THE *N*-ELECTRON PROBLEM

Eq. 1.2, called the *N-electron problem* below, is basically impossible to solve exactly due to the complexity of the correlations between the electrons. The simplest approximation of practical use, the *Hartree-Fock (HF) approximation*, neglects correlations

[1] I.e., in Ref. 1.3, E describes the value obtained for λ upon solving Eq. 1.2

entirely: it is assumed that Ψ is an antisymmetrized product (Pauli exclusion principle satisfied) of N one electron wavefunctions ψ_i. Solving the N-electron problem with the requirement that every ψ_i be normalized (i.e., introducing a set of N Lagrange multipliers in Eq. 1.2) leads to a set of N HF equations (see e.g. [1], Ch. 17). In this approximation, each electron experiences the mean field generated by all the other electrons, but in addition, as a result of the antisymmetrization, an exclusion zone for electrons of the same spin is established around each electron: this is the exchange hole, as first discussed by Slater [2].

The HF approximation represents the first step towards what is, in principle, a method to solve the N-electron problem to any desired accuracy: as the N-electron wavefunction Ψ can always be written as a sum of sets of N antisymmetrized one electron wavefunctions (Slater determinants), the multi-configurational HF (MCHF) method, where more than one Slater determinant is included for the description of Ψ, presents one way to further progress. Truly efficient MCHF is very time consuming, though, and there are other, more efficient ways of dealing with the introduction of correlations (for a recent review, see Ref. [3]). These methods, however, are only now finding their way into condensed matter studies [4]. As the studies of the present work have been performed within a different theoretical framework (to be described) below, we shall not to go into further detail with this issue.

At the time of writing, the majority of the studies of condensed matter systems (including the calculations to be presented in this work) are performed on the basis of *density functional theory (DFT)*. The fundamental strength of DFT lies in the reduction of the problem of N interacting electrons to that of N independent pseudoelectrons moving in an effective potential which, in principle, includes correctly the effect of the interactions between the electrons. The starting point of DFT is the *Hohenberg-Kohn (HK) theorem* [5] which was later generalized by Levy [6]. We will follow the Levy approach here.

Consider the energy functional $E[n]$, defined as

$$E[n] = min_{|\Psi|^2 \hookrightarrow n} < \Psi|\hat{H}_{el}|\Psi > \tag{1.4}$$

where Ψ represents all wavefunctions associated with the fixed density n, including those that are not eigenfunctions of $\hat{H}_{el}$. The HK theorem now states that if the external potential $\hat{V}$ in $\hat{H}_{el}$ is a local one-body operator $v(\vec{r})$, the following two statements hold true:

$$E[n] \geq E_{GS}, \tag{1.5}$$

$$E[n_{GS}] = E_{GS}, \tag{1.6}$$

where E_{GS}, n_{GS} are the GS energy and density of the system, respectively. Eq. 1.5 is clear from the minimal property of E_{GS}. For Eq. 1.6, another minimal property applies: with the requirement on $\hat{V}$, the expectation value of this operator is *fixed* for a given density. The minimization procedure for $E[n]$ in Eq. 1.4 therefore applies in practice to the remaining terms only. These terms are 'universal' (not containing any

system dependence, apart from the requirement on the number of electrons), leading to the equality in Eq. 1.6.

The HK theorem states that the properties of the system described with Eq. 1.2 are completely determined by the GS electron density n_{GS}. This is a change to the well known statement that the system properties are completely defined by the external potential $\hat{V}$. The power of the HK theorem becomes evident if one considers the following: define a system of non interacting pseudoelectrons influenced by some effective potential $\hat{V}_{eff}$ such that the GS density n_{GS} of this system by construction in general will equal the true n_{GS}. In this case, one can simply solve the set of one electron equations for the noninteracting pseudoelectrons in order to solve Eq. 1.2.

The above idea describes the approach to decoupling the N-electron problem suggested by Kohn and Sham [7]. By *(i)* separating the electrostatic interaction (fixed for a given n) between the electrons from the full set of interaction effects, with the rest included in the exchange-correlation energy functional $E_{xc}[n]$, and *(ii)* including in this term the differences [2] between the expectation value for the kinetic energy of the electrons for the interacting and noninteracting system, one finds, from minimizing the expectation value for the two respective Hamiltonian operators with the usual constraint (see Sec. 1.2.1), that $\hat{V}_{eff}$ must satisfy

$$\hat{V}_{eff} = \int d\vec{r_i}\{2n(\vec{r_i})/|\vec{r_i} - \vec{r}|\} + v(\vec{r}) + (\delta E_{xc}[n]/\delta n)|_{\vec{r_i}=\vec{r}}. \qquad (1.7)$$

[2] Due to the differences between the electron wavefunctions in the two approaches.

1.3 EXHANGE-CORRELATION FUNCTIONALS

Practical DFT requires an approximation for the unknown exchange-correlation functional $E_{xc}[n]$ in Eq. 1.7. Various such approximations are widely used, each performing well in their own area (see e.g. Ref. [8]), and it is beyond the scope of this presentation to discuss this highly developed topic in detail: rather, we will include here only a few comments on the approximations to $E_{xc}[n]$ used in our work.

The *local density approximation* (LDA) suggested by Kohn and Sham [7], calculates $E_{xc}[n]$ by assuming that, at a given position $\vec{r}$ in the system, with density $n(\vec{r})$, the exchange-correlation energy will be equal to the value obtained for the homogeneous electron gas with the same density. Thus:

$$E_{xc}[n] = \int d\vec{r}\,\varepsilon_{xc}(n[\vec{r}])n(\vec{r}). \tag{1.8}$$

This approach has the appeal that it only requires knowledge of the exchange correlation density ε_{xc} for the homogeneous electron gas at realistic densities $n(\vec{r})$. Such knowledge was obtained at the time when LDA was presented by interpolation between results for systems with higher and lower electron densities, but more recently, Ceperly and Alder, [9] using a Monte Carlo method, have calculated ε_{xc} for all densities. In all modern calculations with LDA (including those performed in our work), the exchange-correlation energy is obtained from fitting to the Ceperley-Alder data (for references, see Ref. [8]).

It was highly surprising in the early days of DFT based studies that LDA, which amounts to a gradient expansion of $E_{xc}[n]$ to first order in n, outperforms second order gradient expansion approximations (GEAs). Perdew [10] explained this by showing that the exchange part of the LDA (this part being the key problem with the second order GEA under consideration) satisfies three fundamental rules required from the general definition of exchange (an occupation averaged exchange hole suggested by Slater [2] for optimal decoupling of the N HF equations): *(i)* exact removal of all electrons with the same spin as the electron under consideration at the center of the exchange hole (Pauli exclusion principle), *(ii)* exchange hole electron density (i.e., the amount of electrons removed from the system) integrating to 1 (for cancellation with the self interaction in the electrostatic interaction term in the HF equation *and* DFT), and *(iii)* nonpositivity of the exchange hole (electrons with same spin never attracted to each other). The second order GEA exchange hole, by comparison, did not satisfy the last two of these rules. The first generalized gradient approximation (GGA) to $E_{xc}[n]$ was defined [11] as a relatively crude correction scheme to ensure that all three properties were satisfied. Substantial improvement of the GEA results were obtained already with this approximation. [11] Following the introduction of the GGA approach, more sofisticated GGAs, the Perdew-Wang 1991 (PW91) approximation [12] and the Perdew-Burke-Ernzerhof approximation, [13] have been developed. For most purposes, these GGAs lead to only slightly different results, but as noted by Mattsson *et al.* [8], the PBE GGA is less prone to numerical instabilities. Most of our calculations have used the PW91 GGA. We have not described the (straightforward) generalization to a spin polarized system in the above, but refer to e.g. Ref. [14], Ch. 8 for details.

1.4 HOW TO DESCRIBE THE ELECTRON WAVEFUNCTION: PSEUDOPOTENTIALS AND PAW POTENTIALS

Given the periodic translation symmetry of the Hamiltonian $\hat{H}_{el}$ (see Sec. 1.2) in the condensed matter problems of interest in this work, the electron wavefunction ψ can always be expanded in terms of plane waves (PWs). However, as the wavefunction varies very rapidly near the nucleus (reflecting the large kinetic energy of the electron in this region) the maximum value of the wavevector k_{max} needed for a sufficiently accurate description of ψ will be extremely high: the large number of PWs consequently required in this approach to the problem will be prohibitive.

It is fairly clear how, very generally speaking, this problem should be solved: there is really no need to describe ψ very precisely close to the nucleus as this is not the region of overlap between electron wavefunctions on different atoms and thus of little importance to the questions of bond formation in condensed matter. For this reason, essentially all approaches to constructing a practical set of basis functions for the description of ψ involve a separation of the system into *(i)* spherical regions around the nuclei and *(ii)* the 'bonding region' outside these spheres. While there is no single requirement that determines when a useful basis set has been created, the main aim is to obtain an accurate description of ψ in the bonding region using as few basis functions as possible for the given choice of starting point (type of basis set). There is also the crucial (and highly challenging) general question of *transferability*: that the particular approach, if truly useful, should be applicable to a description of most systems involving the particular element in question.

The *pseudopotential* (PP) concept involves *(i)* leaving the core electrons out of the problem entirely (assuming that these states differ negligibly from the states of the free atom) and *(ii)* changing the potential inside of the above mentioned spherical regions such as to ensure that the behaviour of the valence electron wavefunctions in the bonding region are changed as little as possible by the first step in the approach. The key potential advantages in this idea is that *(i)* there are less electrons to deal with and *(ii)* the rapid variation of the original wavefunction in the spherical region can now be avoided. [3] There is no unique answer to the question of how to model the potential inside the spherical region (see e.g. Ref. [15]) but the following set of desirable properties serve as good guidelines: *(i)* at the boundary between the two regions, the potential should be smooth for all practical purposes. *(ii)* As the states of the atoms broaden into bands when dealing with condensed matter, the PP in practice must describe sufficiently precisely the electron wavefunctions in a region around the energy of the original state. *(iii)* An integration of the part of the electron wavefunction included in the spherical region should give the same result before and after the introduction of the PP for the part of the wavefunction in the bonding region to remain unscaled. It has been shown by Hamann *et al.* [16] that fulfillment of the last requirement above is obtained if the electron wavefunction logarithmic derivative and the energy derivative

[3] One of the key elements here is that with the removal of the core electrons, the lowest valence wavefunctions of a given character can now be nodeless.

of this quantity for a given PP equal their counterparts for the original wavefunction. This property, which is referred to as 'norm conservation' is an acceptable fulfillment of the two last requirements mentioned above and norm conserving PPs for this reason have proved successful in many situations. There are, however, important examples where the norm conservation requirement is found to be restrictive (see e.g. Ref. [17]): while it is beyond the scope of this presentation to discuss more recent developments of the PP in detail, we emphasize that there are PPs widely used these days which have relaxed the norm conservation condition.

The present discussion has not been complete and for more information on the PPs (especially recent developments in this field) we refer to Ref. [14], Ch. 11. A series of references adding more detail to the comments of PPs made here have been included below: the first steps towards the PP approach were made by Philips and Kleinman [18] and Antoncik [19], with a very general form for a proper construction of the PP derived by Austin *et al.* in Ref. [15]. Norm-conserving PPs were introduced by Hamann *et al.* in Ref. [16]. These PPs have formed the basis of many more recent PPs, for instance the PPs by Goedecker, Teter and Hutter [20] used in the present calculations with PLATO (see Sec. 1.5). The PPs used in the VASP calculations (see Sec. 1.5) of the present work are the Vanderbilt ultrasoft (US) PPs [17] which, among other things, involve relaxing the requirement of norm conservation.

The PP approach has fairly recently been superseded by the projector augmented wave (PAW) method [21]. The PAW method has been implemented in VASP [22].

1.5 METHODS FOR ELECTRONIC STRUCTURE CALCULATIONS: VASP AND PLATO

A PW expansion of the electron wavefunction as obtained with DFT was abandoned at the beginning of Sec. 1.4 but the development of PPs allow for a reintroduction: most of the calculations described in this work were performed using Vienna *ab initio* simulation package (VASP) [23, 24] which employs Vanderbilt ultrasoft PPs [17] and uses a PW basis set. The appeal of this basis set is its simplicity: tuning the precision in calculations only involves changing a single parameter, the maximum value k_{max} for the wavevector in the PW expansion (i.e., increasing the number of basis functions) or, equivalently, the maximum energy cutoff $E_{cut} = (\hbar^2 k_{max}^2)/(2m)$. The recommended setting for E_{cut} for certain desired 'levels' of precision in calculations on a given element is supplied in the corresponding PP file. In calculations on compounds, with the level of desired precision defined, VASP chooses the highest value from the set of E_{cut} for the various elements involved. VASP has been widely used for the electronic structure calculations in condensed matter physics in recent years (at the point of Christmas 2006, the original VASP paper, Ref. [23], has been cited 1,811 times). As mentioned in Sec. 1.4, VASP also supports PAW potentials. [22].

A different approach to describing the electron wavefunctions involves using a much smaller basis set of *pseudo atomic orbitals*. Sanchez-Portal *et al.* [25] have suggested a method for evaluating (by projection of one basis set onto the other) how well the electron wavefunctions obtained in a PW based calculation can be reproduced by a basis set of pesudo atomic orbitals (PAOs). This method offers a simple way to evaluate the number and range of basis functions needed to match the result of a PW calculation. The method presented in Ref. [25] has been used for the construction of the PAOs for the spanish initiative for the electronic structure with thousands of atoms (SIESTA) [26, 27] and the package for linear combination of atomic type orbitals (Plato) [28]. The use of PAO based codes for examination of condensed matter physics problems has increased in recent years, with good reason: while PAOs are arguably more difficult to deal with than PWs (see below), there are clear advantages (the question of transferability, see Sec. 1.4, probably being the potentially most important) in using a localized basis set for *(i)* the studies of large systems in general (computational cost increasing less rapidly with respect to the number of atoms in the system) and *(ii)* for studies of surface properties in particular (where large regions of vacuum will be present for the cell describing the system). In addition to the remarks made in Ref. [25], the discussions in Ref. [28] have made it clear that there is little (if any) reason to dismiss PAOs on the basis of their 'lack of accuracy'.

The PAO basis set in general only consists of a very small number of basis functions (as opposed to a PW basis set): a typically sufficient basis set used in Plato (see Ref. [28]) includes *(i)* orbitals for the valence electron levels obtained for the neutral atom (confined by an infinite square well potential to ensure well defined range) and *(ii)* orbitals for the valence electron levels and the level for the first higher value of the orbital angular momentum, obtained for the doubly positively charged ion. A cutoff radius of ~ 3.7 Å for the orbitals was recommended in Ref. [28].

One huge advantage in performing calculations with known comparable accuracy

using a PW and an PAO based code is that population analysis, with all its potential pitfalls (see Sec. 5.2.4.2 for brief comment), is readily performed for the atom centered basis functions in the PAO based code [4]: indeed, this is part of our reason for using Plato in the present work. For potentially important information on how to get accurate results with Plato, the reader is referred to our recently published paper, Ref. [29]. This paper also shows, through a particular example, the importance of using a 'proper' basis set in the calculations with an PAO based code and thus emphasizes the presence of dangerous pitfalls in this approach to solving the N-electron problem.

One of the ways in which PAOs appear superior to PWs is their scaling properties for large systems. VASP is estimated to work without serious N^3 scaling problems [5] for systems containing up to a few thousand atoms but new 'order N' ($O(N)$) codes that can handle much larger systems are either under development these years (Conquest being one example, see e.g. Ref. [30]) or already available (such as SIESTA [26, 27]). For a fairly recent review of $O(N)$ codes, see Ref. [30].

[4] For the PW code, projection of the electron wavefunctions onto spherical harmonics within spheres surrounding each ion does produce some information about the characters of the given wavefunction, but very often this information is not particularly clear.

[5] N^3 scaling here means that the time needed to do a particular calculation scales as the number of atoms cubed.

Chapter 2

TECHNICAL ISSUES

2.1 INTRODUCTION

While Ch. 1 discussed the basics of the theory upon which the calculations of this work have been based, the present chapter deals, generally speaking, with issues related to 'how to get things right', given the starting point for the calculations defined by the choice of method. In Sec. 2.2.1 we will discuss 'general issues', i.e., those related to the choice of parameters in the code, given a particular system under investigation. This section will contain remarks on how to increase the efficiency of Brillouin Zone (BZ) sampling. In Sec. 2.2.2 we will discuss modelling related issues, i.e., how to describe the actual system of interest properly in the first place. This section will focus on supercells which have been used in all calculations of this work. Both discussions will be rather general/basic, with the considerations related to the actual studies performed being postponed until later chapters.

2.2 CONVERGENCE WITH RESPECT TO THE PARAMETERS IN THE CODE

2.2.1 THE CHOICE OF *K* MESH

In order to evaluate the sum of the electron energies (or any other property of the system where the evaluation involves integration over the BZ) accurately with a small set of k points, one makes use of the symmetries of the system under investigation. Chadi and Cohen [31] presented a systematic way of obtaining to arbitrary accuracy the value of a smoothly varying function with the periodicity of the reciprocal lattice integrated over the BZ and divided by the volume of the reciprocal unit cell: they replaced the original function by a completely symmetrized (with respect to lattice symmetries) function and ordered the terms in a Fourier expansion of this function according to symmetry related lattice vectors of the same length. The lowest term in this expression would equal the desired quantity.

As the expansion coefficients in this expression should rapidly decay towards zero for a well behaved function, it was argued that this lowest term could be estimated to arbitrary accuracy as a linear combination of the symmetrized function evaluated at a set of k points such that cancellation of all terms but the first one in the expansion would occur up to a certain length of the lattice vectors in the expression. Sets of k points, with accuracy balanced against the number of points in the set, were suggested in Ref. [31] for the most common lattices. This interpolation scheme was later improved by Monkhorst and Pack [32], their chosen k mesh involving equidistantly spaced k points for any crystal under investigation. The Monkhorst-Pack (MP) k mesh is the most widely used choice of mesh in calculations. Practically all the studies in this work have employed this type of mesh.

Special care must be taken when evaluating the sum of the electron energies for metals: the presence of partially filled bands with only little dispersion at the Fermi energy ε_F means that a slightly inaccurate description of the band structure at energies in this region can lead to a clearly incorrect value for the energy of the system. An alternative to the above described method, particularly suitable for metals, is the tetrahedron method with Bloechl corrections [33]. It is beyond the scope of this presentation to describe this method.

2.2.2 SMEARING OF THE FERMI-DIRAC FUNCTION

Although all calculations of this work are meant to describe systems at zero temperature, a rigorous T = 0 K calculation, where the electrons occupy the N lowest levels of the system with probability 1 and all levels above the highest of these are unoccupied, is not recommended. This very abrupt change in the Fermi-Dirac (FD) probability distribution function can be a serious obstacle to convergence in optimization: if it is likely that a given electron level is fully occupied for a given set of ionic positions but unoccupied after a small change of these positions, the resulting change in the forces on the ions will be likely to keep preventing these from falling below the desired tolerance. The system will be almost, but never well optimized. This situation is particularly likely to happen for metals.

Rather than increasing the number of k points in the MP mesh to obtain convergence, the choice is to abandon the abrupt change in the FD function, i.e., to use partial occupancies (a 'finite temperature approach', where the relation of the 'temperature' to real temperature in general is not clear), with some reliable way of getting back to the result that would be obtained in the limit T = 0 K. This approach was suggested by Gillan [34], with the actual finite temperature smeared FD function as the example. Other suggestions have been made for more efficient finite temperature approaches [35]. In our calculations with VASP, we have typically used Gaussian smearing, where the smoothed FD function is modelled with the error function $erf(\varepsilon/\sigma)$, centered at ε_F. The 'temperature' (related to σ as T = σ/k) is varied by changing the width σ of this function in the code, with the default value for this parameter in VASP being 0.2 eV. Finite temperature approaches are not recommended for the tetrahedron method with Bloechl corrections [33].

2.3 CONVERGENCE WITH RESPECT TO THE DIMENSIONAL PARAMETERS FOR THE CHOSEN SYSTEM: THE SUPERCELL APPROXIMATION

The use of a supercell for the description of e.g. an isolated impurity in a bulk crystal (such as the study of interstitial Cu in bulk Si described in Sec. 5.2) or a group of adatoms at a surface (an example being the study of Y atom strings on the Si(001) surface in Sec. 6.3) has the basic advantage to a description of the impurity in an atomic cluster that surface effects are eliminated: the basic idea for the above mentioned situation (with the concept, however, easily generalized to studies of isolated impurities at surfaces, see Sec. 8.1 for a very brief introduction) is to insert the impurity in a 'fairly large' cell which is then the new unit cell of the structure. With periodicity assumed along all directions, an unphysical ordered arrangement of impurities is created. This highligths the key potential disadvantage in the supercell approach: for the results obtained in this type of study to be reliable, one has to make sure that cell size convergence has been obtained for the interaction between adjacent impurities. If this is not the case, and increase in the number of atoms for the system is impractical, remaining errors due to these interactions need to be estimated. Various types of errors exist: *(i)* elastic errors (due to relaxations of the surrounding lattice in response to the presence of the defect) *(ii)* electrostatic errors (due to Coulomb interaction between adjacent defects), and *(iii)* defect state wave function overlaps (of importance, for instance, for shallow donors where defect wavefunctions will be very diffuse).

Convergence of formation energies of various defects in InP has been carefully investigated recently by Castleton and Mirbt using VASP. [36, 37] The results of these studies are a strong support for finite size scaling the results as situations were encountered where even a 512 atom cell appeared to be insufficient to produce a well converged formation energy. For the systems under investigation (simple cubic cells with volume $V_i = L_i^3$) the set of formation energies $E(L_i)$ were fitted with the expression

$$E(L_i) = E(\infty) + \alpha_1/L_i + \alpha_3/V_i \tag{2.1}$$

where the term varying as L^{-1} was clearly needed while the term varying as L^{-3} was selected from least squares fitting comparison with other (L^{-1}, L^{-n})-combinations. In Eq. 2.1, $E(\infty)$ is the formation energy obtained for a truly isolated defect.

The same conclusion for the terms required in Eq. 2.1 has actually been obtained previously by Makov and Payne, [38] in a more rigorous approach to this problem. However, recent studies by Castleton *et al.* [39] on charged defects in semiconductors suggest that the Makov-Payne proportionality constants are incorrect.

Chapter 3

EXPERIMENTAL TECHNIQUES

3.1 INTRODUCTION

A proper introduction to experimental techniques, while potentially highly useful for the discussions of the interpretation of the experimental results for RE disilicide nanowires on the Si(001) surface (see Sec. 6.2.2) has not been included in the present work: we shall provide below only a brief introduction to the method of scanning tunneling microscopy (STM) which has proved an extremely useful tool for experimental studies of nanostructures on semiconductor surfaces and therefore, probably more than any other experimental equipment referred to in this work, deserves a fair elaboration. In Sec. 3.2, we will give a brief introduction to the principles of STM and also discuss how to model STM images in order to compare theoretical and experimental results, an issue to be discussed further, for practical studies, in Sec. 5.4.2.3.

3.2 STM, INTRODUCTION AND MODELLING

Scanning tunneling microscopy (STM) is based on the quantum mechanical phenomenon of tunneling (the fact that a particle with a given energy E has a finite probability of penetrating a barrier constituting a repulsive potential V where $V > E$). In STM, a metal tip is brought so close (a few Å) to the sample that, with a voltage difference between tip and sample, the probability of an electron tunneling through the vacuum barrier to the region of lower energy becomes appreciable. The fundamental strength of the STM is not the magnitude of the current but the fact that the tunneling probability increases primarily exponentially with decreasing barrier width (with the exact exponential variation obtained in the simplified situation where the two systems are unaffected by the change in the tip-sample distance). This gives atomic resolution in the direction normal to the sample. If the tip is sharp in the sense that it has a single atom closer to the surface than any other atom, atomic resolution is obtained in the di-

rections parallel to the surface as well. In summary, therefore, one can obtain an image of the surface electronic structure by scanning the tip across the surface.

In practical STM, the tip is attached to piezoelectric materials (which expand or contract when subjected to a voltage) controlling the required Å-scale movements along all directions. A current feedback loop is used to control the distance between tip and sample: typically, the tip is run in 'constant current mode' where the tip-sample distance is varied to keep I fixed. The changes in the distance obtained through this procedure gives the STM image of the surface. For unwanted processes on the surface to be reduced to a minimum, experiments are performed in ultra high vacuum (UHV) conditions.

STM is an invaluable tool for the study of nanostructures on a substrate: as an actual image of the surface is produced, one obtains very direct information of what is happening here upon deposition of submonolayers of adatoms on the surface. This is an unparalleled strength when comparing to other techniques for examining the surface properties. The apparent 'clarity' of the images can often be misleading, though, if too strong links are established between surface electronic structure and ionic positions: many examples exist where a change of bias voltage changes structures on the surface from 'apparent protrusions' to 'apparent trenches'. It is beyond the scope of this brief review to go into further details with how to obtain reliable information about the ionic positions from the STM images.

As most studies of nanostructure formation on a substrate involve STM imaging these days, an optimal comparison of theory and experiment naturally involves STM modelling on the theoretical side. Only little is known about the tip structure and composition, this part of the system consequently forming the key obstacle to highly developed modelling (see e.g. Ref. [40]). The simplest approximation forming the basis for theoretical STM image construction is the Tersoff-Hamann approximation, [41, 42] where the tip structure is ignored entirely (point probe) and the tip-sample current is calculated from the Bardeen formalism [43]: in this approach to the tunneling problem, the two systems are treated as separate entities, and with the further simplification of the ignored tip structure, the current will be proportional to the integrated density of states over an interval defined by the bias voltage: with a voltage difference V between tip and sample, electrons in the energy range between $\varepsilon_F - eV$ and ε_F will be allowed to tunnel from sample to tip, producing a 'filled state image' (with an 'empty stage image' obtained for a bias voltage of the opposite sign). For investigations of nanostructures on semiconductor substrates often quite large bias voltages (up to a few V) are used. For these 'standard situations', qualitatively correct predictions are expected with the Tersoff-Hamann approximation (see e.g. Ref.[44]). In our studies of Cu at the Si(001) surface discussed in Sec. 5.4.2.3, we will use the program bSKAN, developed by Hofer, [45, 44] and the Tersoff-Hamann approximation for the theoretical STM image construction.

Chapter 4

REASONS FOR THE STUDIES OF THE PRESENT WORK

4.1 INTERACTIONS OF Cu WITH THE Si LATTICE

4.1.1 INTRODUCTION: REASONS FOR FOCUSSING ON THE INTERACTIONS OF ISOLATED INTERSTITIAL Cu WITH BULK Si AND THE CLEAN Si(001) SURFACE

The theoretical studies of Cu-Si interactions performed in the present work have focussed on isolated interstitial Cu (Cu_i) in bulk Si at the Si surface, but the general interest in Cu/Si systems goes far beyond this point, as will be briefly discussed in the following. Cu based interconnects were successfully introduced for application in ultralarge scale integrated devices by IBM almost a decade ago [46] and Cu metallization has now acquired a mature role in semiconductor technology. Compared to Al, the previous choice of material for interconnects, Cu has a series of evident advantages, frequently mentioned in the literature: key examples are the lower resistivity of Cu and the fact that Cu wires produced with lithography are both more narrow and less prone to electromigration than the Al wires.

Cu, when mentioned in conjunction with Si, also has a very dark side, which is more closely connected with the studies of the present work: while Cu has very desirable properties for interconnects, diffusing Cu in Si is one of the most detrimental impurities to devices, primarily due to its tendency to form precipitates: these charged Cu silicides (Cu_3Si, structure unknown) introduce deep levels in the band gap [47] and have been mentioned as *(i)* the cause of significant increases in the leakage current of the *p-n* junction, *(ii)* degradation of the gate oxide and resulting leakage current of MOS capacitors, and *(iii)* efficient minority carrier recombination sites, with Ref. [48] providing a fairly recent review on the experimental studies into these issues.

The use of Cu in production schemes has greatly enhanced the risk of contaminating the Si devices with Cu (although also chemical processing of Si is known to be an important issue in this respect [49]). This risk is further emphasized [48] by the fact that Cu is an extremely fast diffuser in Si [50]: when depositing Cu for the use as interconnects, a highly efficient barrier material between Cu and Si is required in order to prevent Cu from diffusing into the device, where it can travel significant distances even at RT [48]. These extremely demanding criteria for the barrier quality present the key reason why successful integration of Cu into device processing was only fairly recently obtained.

As noted by Weber in Ref. [51], the ultimate goals when dealing with a given defect in the Si wafer are *(i)* control of its formation and *(ii)* a well established picture of its influence on device performance. On the basis of the above remarks on the detrimental effects of Cu to Si devices, understanding the behaviour of this impurity evidently has a very high priority, and a considerable amount of knowledge [48] has been gained on this issue, with some of these conclusions to be included in the following parts of this section.

Despite the immense amount of theoretical and, primarily, experimental work performed on Cu in Si, however, there are still, at the time of writing, outstanding fundamental questions regarding the behaviour of isolated Cu_i in bulk Si (the typical state of dissolved Cu for moderately doped Si, see e.g. Ref. [52]) and the interactions of this impurity with other defects in the Si lattice. In making the choice to focus, in our initial studies of Cu-Si interactions, on the extremely simple system of bulk Si Cu_i, clarifying the details of the electronic state for Cu in this state, we are, on the one hand, setting ourselves a fairly modest goal, considering the wealth of interactions of Cu with the impurities and defects in the Si lattice reported in the literature. On the other hand, it is evident that in order to model more complex systems reliably, theory must be able to provide a thorough understanding of this system. As will be discussed in Sec. 4.1.2 (and in more detail in Sec. 5.2.1), this statement seems to have been largely ignored in the literature, in the sense that various clear discrepancies between the theoretical and experimental understanding of bulk Si Cu_i have not been rigorously studied by theory, a fact which is only partly explained by the challenges to comparing theoretical and experimental results for this impurity (see Sec. 5.2.1.1): in other words, there is, in our opinion, very good reason to devote a high level of attention initially to the theoretical investigation of isolated Cu_i in bulk Si, clarifying the various outstanding issues for this system before moving on to modelling systems of real interest to the influence of Cu on devices. We shall discuss in Sec. 5.5 (and to some extent below) how this choice of approach to understanding the interactions of Cu with the Si lattice provides us with sufficient information to make educated guesses for explanations of a series of puzzling phenomena involving interactions of Cu with defects in the Si lattice.

In addition to the studies of bulk Si Cu_i we shall devote attention also to the properties of Cu_i near the Si(001) surface. As described in Sec. 4.1.3 (and in more detail in Sec. 5.3.1.1), experiment has reported almost complete Cu outdiffusion to this surface for moderately doped Si and comparatively low Cu contamination levels. With the present understanding of the behaviour of Cu in Si, as noted by Istratov and Weber [48], this observation is a consequence of *(i)* the absence of other highly stable

sinks for the diffusing impurity and *(ii)* the extremely low barrier [50] to Cu diffusion in Si, i.e., there is effectively, for certain Cu contamination levels, nothing that prevents Cu from moving to the surface of the sample which is always a stable sink for impurities (we shall discuss this issue further in Sec. 4.1.3). The detailed mechanism for Cu outdiffusion, on the other hand, is yet to be clarified at the time of writing. We shall consider the very early stages of Cu outdiffusion to clean Si(001), studying Cu within a few layers of this surface as well as on it, and suggest clear similarities, on the basis of these studies and the conclusions obtained for bulk Si Cu_i, between the explanation for the outdiffusion and the behaviour of Cu near defects in bulk Si. As will be discussed further in Sec. 5.5, this result has prospects for the much desired control of Cu in Si: we shall present preliminary studies into the issue of Cu nanowire formation on the Si(001) surface in Sec. 5.4.3.

As a consequence of the above described rather narrow focus of the studies of interactions of Cu with Si in this work, the literature review to be presented below in this section leaves out discussions of the larger part of the experimental and theoretical work performed on this issue, providing only brief introductions to issues highly relevant to the present work: [1] Sec. 4.1.2 will discuss the experimental and theoretical understanding of the electronic state of bulk Si Cu_i, clarifying the reasons for performing further theoretical studies into this issue. Sec. 4.1.3 will give a brief introduction into the most important reaction paths for Cu_i in moderately doped Si, emphasizing the reasons for performing theoretical investigations into Cu outdiffusion to the Si(001) surface (we shall postpone a discussion of the experimental work performed on systems with Cu on the Si(001) surface until Sec. 5.4.1.1). Finally, in Sec. 4.1.4, we shall provide an introduction to the reported experimental conclusions for Cu nanowire formation on Si substrates.

4.1.2 ELECTRONIC STATE OF INTERSTITIAL Cu IN BULK Si: DISAGREEMENT BETWEEN EXPERIMENT AND THEORY

It is well established [52, 53] that Cu *(i)* almost exclusively diffuses as an interstitial defect in moderately doped Si and *(ii)* is a shallow donor Cu_i^+. Disputes remain, however, about the electronic state of this impurity. The electron configuration for Cu in vacuum is $[Ar]3d^{10}4s^1$. For Cu_i^+ in vacuum, the $4s$ electron has been removed and the ion thus has the stable $3d$ closed shell configuration with a very small radius of ~ 0.7 - 0.8 Å. If the same thing occured for Cu_i^+ in Si, as noted by Istratov and Weber [54], this would result in a very weak interaction of this impurity with the surrounding lattice, offering an explanation for its high diffusivity. [50] This explanation for the electronic state of bulk Si Cu_i is the one generally accepted by the experimental community. [54]

The theoretical community has challenged this view, making reference to both calculations and the experimentally observed behaviour of Cu interacting with various

[1] In all cases, we shall provide further information on these topics as an introduction to the actual theoretical investigations performed, see the text below for cross references.

defects in the Si lattice. The most prominent criticism of the above experimental conclusion has been provided by Estreicher, [55], who, in the first theoretical study of Cu_i^+ including distortions of the surrounding lattice, reported weak but covalent Cu-Si bond formation, with *(i)* appreciable promotion of electrons from the 3*d* to the 4*sp* shells for Cu and *(ii)* electrons borrowed from the surroundings (a Mulliken population analysis revealed occupation numbers of $\sim$ 0.9 electrons per 4*sp* orbital). These early studies were performed using H terminated Si clusters and simplified HF theory (described in further detail in e.g. Ref. [56]). More recently, very similar results were obtained by Estreicher (briefly described in Ref. [56]) in supercell calculations using the atomic type orbital code SIESTA, the main difference being a smaller number of promoted electrons ($\sim$ 1) for the Cu atom obtained in these studies.

It remains to be clarified whether the above theoretical description of bulk Si Cu_i is to be associated with a very small barrier to diffusion of the impurity, similar to the experimental value [50] of 0.18$\pm$0.01 eV. Woon *et al.* [57] reported a barrier of 0.24 eV to Cu diffusion in Si on the basis of studies of Cu_i^+ in rigid H terminated Si clusters of various sizes (see Sec. 5.2.1.1 for details). While this value was not rigorously converged with respect to the size of the cluster, no values obtained in these investigations were higher than 0.30 eV. These calculations were performed within the same theoretical framework as the studies of Ref. [55], but the authors of Ref. [57] found that the Cu 3*d* shell was closed for the energetically most favourable configuration, suggesting, on comparing with the remarks in Ref. [55], that the basis sets used in these two studies were different (the amount of computational details provided being insufficient to clarify this issue). No studies of the barrier to Cu diffusion in Si were performed in Ref. [55]. Other theoretical studies of bulk Si Cu_i have been performed as well [58, 59, 60], yielding, in some cases, values for the activation energy to Cu diffusion in Si. These studies, however, have not focussed on the electronic state of the Cu atom, and it is therefore not clear to what extent they support the picture of bulk Si Cu_i presented in Ref. [56].

In addition to the theoretical conclusions of Ref. [55, 56], Estreicher argued [56] that various experimental observations appear to disagree with the picture of Cu_i^+ as unable to interact covalently with impurities and defects in the Si lattice: *(i)* the experimentally reported [61] dissociation energy of 1.02$\pm$0.07 eV for a Cu_s- Cu_i pair is significantly higher than expected for a purely Coulombic interaction. *(ii)* The same conclusion is reached for Cu-acceptor binding energies obtained for various acceptors in Si [62, 63, 64] while in addition, these energies are found to be acceptor dependent. Finally, *(iii)* Cu_i has been reported [65] to form strong bonds at cavities in Si, covering the surface of this extended defect.

Theoretical investigations have been performed into the binding of Cu at various acceptors [66, 67, 68, 69], the comparability of these studies with experimental conclusions suffering, however, from the fact that even the supercells used in more recent studies must be considered too small for the interactions between adjacent Cu-acceptor pairs to be reduced to a negligible level. Furthermore, generally, relatively little information on the properties of the bonding of Cu with the acceptor as obtained from calculations has been provided in these references. While the theoretical studies to be presented in this work do not involve Cu-acceptor interactions, we shall make further

comments on this issue in Sec. 5.5, when summarizing the results of our studies of Cu interactions with Si.

4.1.3 REACTION PATHS FOR DIFFUSING Cu IN Si

In order to clarify how to control most efficiently the behaviour of diffusing Cu in Si, in particular keeping this impurity out of the active regions of the device to the maximum possible extent, knowledge on the reaction paths for interstitial Cu in Si is highly valuable. Measurements of the solubility of Cu in weakly doped ($\sim 10^{16}$ cm^{-3}) Si by Weber [70] suggested that this parameter reaches $\sim 10^{18}$ cm^{-3} at $\sim$ 1325 K but drops orders of magnitude to $\sim 10^{14}$ cm^{-3} at $\sim$ 775 K. Assuming that extrapolation of the linear (on a logarithmic scale) behaviour of the solubility curve to lower temperatures is justifiable (none of the other transition metals investigated in Ref. [70] display a behaviour that suggests otherwise), one obtains a vanishing Cu solubility in Si (less than $\sim$ 1 cm^{-3}) at room temperature. This means that interstitially diffusing Cu in Si dissolved at typical annealing temperatures will not remain in this state upon a change to ambient conditions: some defect reaction will occur.

Extensive studies of the possible reaction paths (see Ref. [48] for a recent review) have shown that, for moderately doped Si with a low level of extended defects, Cu primarily will either *(i)* form precipitates (Cu silicides) in the bulk or *(ii)* diffuse to the surface of the Si wafer, with the details of the chosen reaction path showing a strong dependence on *(i)* the sample being n-Si or p-Si and *(ii)* the Cu contamination relative to the dopant concentration [71, 72]. These reaction paths are clearly distinguished: for high Cu contamination levels ($\sim 10^{17}$ cm^{-3}), Cu has been reported, on the basis of numerous experimental studies (see Ref. [48] for references), to form Cu silicides near the surface. The Cu outdiffusion reaction path mentioned in the above, however, involves not only comparatively lower Cu concentrations (see Sec. 5.3.1.1 for details), it is also an agglomeration phenomenon involving comparatively much longer time scales [73]. Finally, Shabani *et al.* [71], the first group to report the existence of this reaction path, noted that Cu recovered at the surface of the wafer during this process could be easily removed with a dilute HF:H_2O_2 cleaning solution, suggesting that Cu did not form strong bonds with Si (e.g. Cu silicide) at the surface. We shall discuss both of these reaction paths in more detail in Sec. 5.3.1.1 as an introduction of our theoretical studies of Cu outdiffusion to the clean Si(001) surface.

As noted by Istratov and Weber in Ref. [48], the conclusion from experiment that only very stable sinks (including extended defects in the crystal in this discussion) can efficiently trap diffusing Cu_i in Si (the amounts of Cu relative to the Cu contamination level trapped by point defects being reported [73] to be $\sim$ 0.1%) is explained essentially by the extremely low diffusion barrier of 0.18$\pm$0.01 eV for this impurity [50]: Cu, as a consequence, is only temporarily trapped by e.g. acceptors, with a corresponding reduction of the effective diffusion coefficient depending on the dopant concentration, [2]

[2] In particular, these conclusions have explained [48] why the previously accepted experimental data for the Cu diffusivity obtained by Hall and Racette [52], suggesting an activation energy of 0.43 eV, are so clearly

but experiment strongly suggests that the binding energy for Cu at these impurities is too weak to keep Cu from ultimately moving away in the search of more stable sinks.

The experiments by Shabani *et al.* [71] on Cu outdiffusion to the Si(001) surface (to be discussed in more detail in Sec. 5.3.1.1) serve as an illuminating example of the behaviour of Cu in the absence of stable sinks in the bulk of the Si sample. In these experiments, a Cu contaminated Si sample was annealed initally, leading to a homogeneous distribution of Cu_i in the wafer, and cooled subsequently in air, a choice of quenching rate too slow for a supersaturated population of Cu_i to be maintained, according to the studies of Flink *et al.* in Ref. [72]. The experiments of Ref. [71] revealed, however, that outdiffusion of the entire amount of Cu to the Si surface could be triggered after the cooling process had ended by removing the surface oxide grown during cooling, with the authors also reporting that no agglomeration of Cu at the Si/oxide interface was observed, regardless of the time elapsed since the cooling process, if the surface was not modified as described above. In other words, regardless of the actual trapping mechanism for Cu in bulk Si in these experiments (see Ref. [73] for suggestions), Cu was found to diffuse to the Si surface as soon as the conditions were changed appropriately for a stable sink to be created in this region. This experimental result emphasizes the very large influence of stable sinks on the properties of diffusing Cu_i in Si.

4.1.4 Cu NANOWIRES ON A Si SUBSTRATE

The reports on formation of Cu nanowires on Si substrates have typically involved experimental techniques that, when used for the present purpose, are still at an early stage of development [74, 75, 76, 77, 78]: the width of the Cu nanostructures are too large for these structures to qualify as nanowires, and no consideration has yet been paid in these experiments to the crucial issue of preventing Cu from diffusing into the substrate (see Sec. 4.1.1). Actual Cu nanowires have been observed, though: Tokuda *et al.* [79, 80, 81] have reported selective Cu adsorption with Cu nanowire formation along the step edges of a H terminated Si(111) surface, as observed with atomic force microscopy (AFM), by deliberate Cu contamination (10 ppm) of the ultralow-dissolved-oxygen water used (initially, without the Cu) for reducing the sample roughness. Wires were reported to grow upon immersion of the Si sample in this solution for $\sim$ 10 s at RT. The wire formation is believed to be due to the presence of OH-terminated sites at the step edges: experiments [79] reveal growth of Cu dots rather than wires upon a reduction of the number of such sites due to changes in the cleaning process, and theoretical studies [82] have supported this suggestion as well. Examination of the amount of adsorbed Cu as a function of step density [81] has further supported the conclusion of preferential Cu adsorption along the step edges and suggested that the nanowires are only a single atom wide. More recent studies by the same group [83] have involved attempts to control the step edge formation on Si(111). The

different from the more recent results of Ref. [50]: these experiments did not describe the intrinsic diffusion of Cu but rather a situation where the diffusing impurity was slowed down due to temporary trapping by the large concentration of B ($\sim 10^{20}$ cm^{-3}) in the samples used in these experiments. For the samples used in the studies of Ref. [50], the B doping level was very low ($\sim 10^{14}$ cm^{-3}), leading to the diffusion coefficient increasing by orders of magnitude.

structure of the substrate below the Cu NW is unknown at present. In continuation of the discussion at the beginning of this subsection, it is of crucial importance to resolve this issue in order to clarify the stability of these wires.

4.2 RARE EARTH METAL DISILICIDE GROWTH ON A Si(001) SUBSTRATE

4.2.1 INTRODUCTION: ON THE INTEREST IN NEXT GENERATION INTERCONNECTS

In Sec. 4.1.1, we discussed briefly how Cu metallization has added tremendous complexities (in addition to the clear benefits of using Cu as the material for interconnects in devices) to device processing. The focus in these opening remarks was primarily on the potentially disastrous consequences of having an inefficient barrier separating Cu from Si. On a more general level, as a consequence of the continuing demands for smaller feature sizes in ultralarge scale integrated devices, the upper limit to the allowed Cu contamination level in the device region decreases consistently, and thus, the requirements for the efficiency of Cu gettering (removal of the impurity from the device region) continue to get more and more demanding. For the same reason, and of central interest to the present discussion, increasingly extreme requirements to the performance of the interconnects apply. An issue that has long been of key concern in this respect concerns the lithography based methods by which these interconnects are produced: recent work (see Ref. [84] for references) has suggested that if wires that are both *(i)* as narrow as a few tens of Å and *(ii)* having reliable properties, i.e., a sufficiently high crystalline quality, are desired, an alternative production scheme is required.

It is fairly evident, given the above general remarks, why growth of highly elongated nanostructures with a naturally low level of defects on a Si substrate has received a lot of attention in recent years: while, on the one hand, with some of these systems being 1D to an extraordinary good approximation (see below), they display a wealth of interesting properties not observed for 2D or 3D systems (see e.g. Ref. [84] for comments and references), they also represent, depending on the level of ease of and control on their growth, potential candidates for producing interconnects with widths well below current day interconnects. [3] The low level of defects for these structures should be associated with both more reliable properties and, depending on the material used, the system being comparatively less prone to failures in actual application. We shall clarify in Sec. 4.2.2, when discussing methods for producing these structures, why this comparatively higher structural quality is often attained.

The amount of published papers making reference to nanostructures as possible 'next generation interconnects' is enormous, for several reasons: *(i)* experiment involving atom adsorption on the Si(001) surface keeps revealing nanostructures with large aspect ratios. [4] *(ii)* It is not a necessary condition for the nanostructures to receive attention in the above context that they are conducting as they might still provide a tem-

[3] On a general level, the systems investigated are not Cu nanowires, for reasons clarified at the beginning of this discussion. Some experiments have reported Cu nanowire formation on a Si substrate, however, with this issue discussed in Sec. 4.1.4.

[4] As a fitting example, we shall discuss in the present work (see Sec. 6.3) theoretical modelling of Y atomic strings on Si(001) observed in experiment by Owen (yet to be published), with experimental results on this system not previously reported in the literature.

plate for a nanowire obtained by adsorbing metal subsequently onto the structure (an example for such a system being the Bi nanolines on Si(001) [85], to be discussed below). *(iii)* And, finally, while the Si(001) surface is the technologically relevant surface where present day devices are being grown, the studies of next generation interconnects are not limited to this surface or even to the choice of Si as a substrate, the possibility of Si/Ge or Ge-based next generation devices also being frequently explored in the literature (as an example of some interest to the present work, see Ref. [86]).

An additional and less interesting reason for the wealth of nanowires and nanolines reported in the literature over the recent years is related to the fact, as noted by Bowler [84], that the definition of these systems is somewhat vague. Within the restriction that the nanostructures should be actual candidates for interconnects in future devices, a basic requirement must be that they should be more narrow than existing interconnects (i.e., preferably only a few tens of Å) while on the other hand, lengths starting from several hundred Å are still needed for practical application purposes. As the objective of the present discussion is not to give a general introduction to the state of the field of nanowires and nanolines on a semiconductor substrate, but rather to introduce a few such systems of particular interest to the present work (to be described below), we emphasize these dimensional requirements primarily to make the reader aware that a lot of the 'nanowires' reported in the literature are actually to be regarded as nanostructures that might grow as wires if the experimental parameters are tuned appropriately in future studies. More importantly, whenever these systems are referred to as nanowires in cases where actual nanowires have also been grown for the system in question, this can be the cause of unnecessary confusion, as the relation between these two sets of systems can be questionable in important respects. [5]

The discussion below will involve, firstly (in Sec. 4.2.2), an introduction to two systems, *(i)* dangling bond wires and *(ii)* Bi nanolines on Si(001), representing examples of two essentially different ways of creating potential next generation interconnects on this surface. This approach is chosen to give a very preliminary introduction to the field, with much more information to be obtained from e.g. the recent review of nanowires and nanolines on the Si(001) surface in Ref. [84]. [6] Secondly, we shall discuss in Sec. 4.2.3 the primarily experimental studies of rare earth disilicide nanowires on the Si(001) surface, the topic of our theoretical investigations to be presented in Ch. 6. For a recent review on these systems, we refer to Ref. [87].

[5] We shall discuss an example of this issue for epitaxially grown RE disilicide nanostructures on the Si(001) structure in Sec. 4.2.3.

[6] Furthermore, an introduction to the Bi nanolines will prove useful for the discussions of Y atomic strings on the Si(001) surface in Sec. 6.3

4.2.2 DANGLING BOND WIRES AND Bi NANOLINES ON THE Si(001) SURFACE: EXAMPLES OF TWO CONCEPTUALLY DIFFERENT WAYS OF PRODUCING NEXT GENERATION INTERCONNECTS

The suggestions for next generation interconnects in device technology divide into two basic groups [84]: one approach *(i)* involves creation of a nanopattern of preferential adsorption sites on the substrate where metal atoms are subsequently deposited. The appeal of this method is the high level of control in the creation process while the disadvantage is the fact that only a single wire template site is created at a time. Furthermore, while the wire template in this approach can be quite well defined this does not necessarily guarantee a high quality of the wire subsequently grown. We shall discuss the example of dangling bond (DB) wires on the Si(001) surface briefly below.

Another intriguing path *(ii)* is self-assembled nanowires and nanolines on the surface (often formed simply by annealing at 'the right' temperature, initiating a given reaction, with the suitable amount of adatoms of interest deposited on the substrate initially). As will be described below, with reference to Bi nanolines on Si(001) (and, in Sec. 4.2.3, rare earth disilicide nanowires on this surface), this process can yield nanostructures with a low level of defects, the main challenge for this group of systems being the control of the process (location, growth direction, and suppression of unwanted growth side effects).

DB wires on the Si(001) surface belong to the first of the above mentioned groups (although they also have very interesting properties on their own, see Ref. [84]). They are created by the selective removal of H atoms on an otherwise H terminated Si(001) surface ((2×1) surface reconstruction) with STM as first reported by Lyding *et al.* [88]. Hitosugi *et al.* [89] have reported wires only a single atom wide obtained with this method. A high level of control can be achieved in this process, with wires running both parallel and perpendicular to the Si dimer row directions. Studies of adsorption of atoms onto the DB wires have been performed for a series of elements (see Ref. [84] for a recent list): the H atoms on the surrounding terrace typically act as an efficient mask such that preferential adsorption to the wire template is obtained. Well defined wire structures are yet to be obtained with this method, though. Doping of DB wires has also been considered, albeit only in theoretical studies: it has been predicted [90] that a metallic wire can be obtained this way for a wire two atoms wide.

A highly interesting example of self-assembled nanolines (NLs) on Si(001) (of relevance to our studies, see Sec. 6.3) is obtained [91] when depositing $\sim$ 1 ML of Bi on this surface and annealing at 845 - 875 K (where most of the Bi desorbs). A pair of perfectly straight lines are formed, each with atomic width and a fixed total width of 15 Å, and attaining lengths of up to several thousands of Å. Each pair of lines grow on a single terrace, perpendicular to the Si dimer row direction, and with the terrace conforming to the lines to a considerable degree [91]. The impressive quality of these nanostructures (defects hardly ever being observed in experiment [85]) makes them highly interesting templates for nanowires (the Bi NLs themselves are semiconducting

Figure 4.1: STM image of an isolated pair of Bi NLs (moving through the square in the figure) on the Si(001) surface and (inset, Si atoms dark grey, Bi atoms black) the Haiku reconstruction explaining the structure of these lines. See text for details. *Image courtesy of J. H. G. Owen, K. Miki, and D. R. Bowler.*

with a band gap wider than the band gap for the surrounding Si [92], the lines therefore being of interest in the present context as a wire template). We shall discuss below the studies performed into this issue.

The structure of the Bi NLs has been explained [85] by a very large local reconstruction of the substrate, typically referred to as the Haiku structure, for reasons to be clarified below. The substrate reconstruction bears some resemblance to the A type (or 5-7-5) structure which has been suggested as the explanation for the straight lines of protrusions and trenches observed for various group-V terminated Si and Ge surfaces (see, e.g., Ref. [93]) as a method of strain relief for these systems. The A type structure itself involves a large amount of local (tensile) strain. Two closely spaced Bi NLs on A type reconstructions therefore repel each other. In order to eliminate this effect, four Si atoms per Bi dimer pair are removed in the region between the lines: while the A type reconstruction conserves the local number of atoms in the substrate, the reconstruction explaining the Bi NLs does not. The resulting Haiku structure (the name offers a simple introduction to the appearance of the reconstuction: when viewed along the NLs, the typical hexagons for the Si lattice have been replaced by pentagons and heptagons in a V-shaped 5-7-5-7-5 pattern, see Fig. 4.1) explains the reason for the straightness of the lines: the calculated kink energy is over 2 eV. [84]

A series of theoretical and experimental studies of adsorption of various metals on Bi NLs on an otherwise passivated Si(001) surface have been performed recently (see Ref. [87]). Equally intriguing is the suggestion of the A Type and Haiku structures as explanation for the appearance of long straight Y atomic strings on Si(001) in recent experiments by Owen (yet to be published), see Sec. 6.3.

4.2.3 RARE EARTH METAL DISILICIDE NANOWIRES AND 3D ISLANDS ON THE Si(001) SURFACE: A BRIEF INTRODUCTION

RE disilicide nanowires on the Si(001) surface, like the Bi nanolines, represent nanostructures forming by self-assembly. Since their discovery about a decade ago by Preinesberger *et al.* [94] about a decade ago, especially the Stanley Williams group at Hewlett-Packard labs have devoted a great deal of attention to this system as a candidate for next generation interconnects in device structures. We shall give only a very brief introduction to these systems in the following, as e.g. Sec. 6.2.2 will discuss the experimental knowledge on these systems relevant for our discussions in a high level of detail, with also detailed information on the RE/Si(001) wetting layers, often mentioned in conjunction with the wires (for reasons to be clarified below) included later in the text (see Sec. 6.2.3.4).

Thin films of epitaxially grown RE metal disilicide on Si(111) have long been of interest because of the low Schottky-barrier heights (0.3 - 0.4 eV) on *n*-type Si [95, 96]. The RE disilicides grown on the Si(111) surface crystallize in the hexagonal AlB_2 structure (see Fig. 6.1), with the *c* axis perpendicular to the surface. The lattice mismatch between substrate and overlayer is typically quite small, meaning that high quality films can be created (in UHV conditions) by annealing at around 775 K. RE disilicide films with the AlB_2 structure have also been observed in experiments involving RE metal deposition on the Si(001) surface (in this case with the *c* axis in the substrate plane), but in this case, the overlayer/substrate lattice mismatch is highly anisotropic and the structure is only metastable: in addition to the AlB_2 structure, also the $ThSi_2$ and $GdSi_2$ structures, which have a larger unit cell, conceptually similar to the cell shown in the left part of Fig. 6.2, but with twice the cell dimension along the [1-100] direction and with every second pair of RE metal planes displaced by half the value of the other basis vectors. For these structures, the overlayer/substrate lattice mismatch values are also typically large, but with significantly less anisotropy. Apart from the clear structural differences, the stoichiometry of RE disilicide in the AlB_2 structure is also different from what is obtained for the $ThSi_2$ and $GdSi_2$ structures, with recent experiments by Ji *et al.* [97] confirming the presence of a significant amount of Si vacancies for bulk RE disilicides with the AlB_2 structure (the general rule of thumb being that one out of every sixth Si atom is missing).

The above mentioned lattice mismatch anisotropy for RE disilicides with the AlB_2 structure growing on the Si(001) surface suggest high energy penalties due to rapidly increasing strain for growth of the overlayer along one direction, but significantly less prohibited growth along the perpendicular direction, i.e., growth of highly elongated nanostructures, or nanowires, on the surface. These wires are observed upon deposition of submonolayers of RE metal (1 monolayer (ML) of atoms = 6.78×10^{14} cm^{-2}) on Si(001), as first observed by Preinesberger *et al.* [94] for Dy on Si(001). Nogami *et al.* [98] were the first ones to confirm that the term wires was justifiable by showing that these structures are metallic.

The typical widths (heights) of the RE disilicides nanowires are $\sim$ 10 - 100 Å (a few Å) while lengths of several microns have been reported. For the lowest RE metal

Figure 4.2: Experimental STM image of Er nanowires on a Si(001) substrate. See text for (general) details. *Image courtesy of Y. Chen, D. A. A. Ohlberg, G. Medeiros-Ribeiro, Y. A. Chang, and R. S. Williams.*

coverages required for NW formation, the variation in the wire width is explained by the choice of the RE metal while for somewhat larger (still submonolayer) RE metal coverages, both width and height start changing (the latter increasing) as wires start growing in bundles. The length of the wires does not appear to restricted by the lattice mismatch at all, but growth of the wires along the length direction is still effectively limited by the substrate: as the wires grow perpendicular to the Si dimer row direction on the surrounding terrace and never cross steps, a pattern of perpendicular wires on different terrace levels is generally observed (see Fig. 4.2) with the length of the wires ultimately limited by the growth on wires on the adjacent terraces. For low RE metal coverages it becomes evident that the terraces conform to the wires to a high degree: a growing RE disilicide nanowire will typically drag the terrace along with it out over the step edge in the vicinity, and thus the average length of the NWs will typically be longer than the average terrace widths before the RE metal deposition. On vicinal Si(001), where primarily terraces with Si dimer rows running along one direction (perpendicular to the step edge) are found, very long nanowires have been grown (see e.g. Ref. [99]). While these systems are commonly referred to as RE disilicide nanowires, Sc and Y, which are not RE metals, display similar behaviour when deposited in submonolayer amounts on Si(001).

Chapter 5

INTERACTIONS OF ISOLATED Cu WITH Si

- Most [scientific] papers should never have been published.
A. S. Torralba, 2006

5.1 INTRODUCTION

This chapter presents the results of the theoretical studies of Cu-Si interactions performed in the present work. Our key motivation for focussing our investigations on the topics discussed in the following, in particular the reason for devoting a high level of attention initially to isolated Cu_i in bulk Si, has been described in Sec. 4.1.1. Furthermore, a relatively detailed introduction to the work performed on this issue has been postponed until the introductions to Sec. 5.2 (studies of bulk Si Cu_i), Sec. 5.3 (studies of Cu outdiffusion to the clean Si(001) surface), and Sec. 5.4 (studies of *(i)* Cu on the clean Si(001) surface and *(ii)* Cu_i at the Haiku structure (described in some detail in Sec. 4.2.2)). Fairly important considerations considered so lengthy and technical that they would interrupt the general flow of the text (an example being the convergence with respect to cell dimension for the energies of isolated Cu near the Si(001) surface) have been postponed until Sec. 8.2. For a summary and outlook for these studies, we refer to Sec. 5.5. Most of the studies of bulk Si Cu_i described in Sec. 5.2 have been published in Ref. [29], with papers planned for both *(i)* the studies of Cu outdiffusion to the Si(001) surface and *(ii)* Cu on the Si(001) surface.

5.2 ELECTRONIC STATE OF INTERSTITIAL Cu IN BULK Si

5.2.1 INTRODUCTION

5.2.1.1 A SURVEY OF PREVIOUS WORK ON ISOLATED INTERSTITIAL Cu IN BULK Si OF INTEREST TO THE CURRENT STUDIES

As discussed in Sec. 4.1.2, relatively few theoretical investigations, performed essentially by only one group, have addressed the issue of the electronic state of Cu_i in bulk Si: results of several structural optimizations of this configuration have been reported in the literature [55, 58, 56, 59, 60], but in most cases, little attention has been paid to the question of Cu-Si covalent bond formation raised initially by Estreicher in Ref. [55]: Kamon *et al.* [58] studied the barrier to diffusion of 3*d* transition metals in Si using the FLAPW method and the LDA to E_{xc}. A Γ point calculation involving partial relaxation of the Si lattice in response to the presence of the impurity yielded the conclusion for Cu (and other late 3*d* transition metals) that the hexagonal face of the surrounding Si cage was a energetically clearly more favourable site, with an energy difference of 0.35 eV, compared to the T site.

This result, which was explained by promotion of electrons from the Cu 3*d* to the 4*s* level for Cu moving towards the hexagonal face and a comparatively higher coordination number for the impurity at this site, was in clear contrast with previous theoretical results by Woon *et al.* [57], where studies of the Cu diffusion path in a rigid H terminated Si cluster $Si_{30}H_{40}$ produced a barrier of similar height, 0.24 eV, but with the T site as the energetically favourable site for Cu in Ref. [57]. [1] Thus, even though both of these studies opposed the experimental conclusion that the 3*d* shell remain closed for Cu_i in bulk Si (the calculations of Ref. [57] being performed within the same theoretical framework as studies of Ref. [55]), the conclusions by Kamon *et al.* [58] evidently can not be regarded, without further investigation, as being in clear agreement with the conclusions by Estreicher [55] with respect to the electronic state of bulk Si Cu_i. Unfortunately, this issue was not addressed in Ref. [58], where no reference was made to the studies by Woon *et al.* [57]. Furthermore, essentially no details on the system used for the theoretical modelling in Ref. [58] was provided in this paper, making it very difficult to draw conclusions regarding the reliability of the two diffusion barrier studies in question.

More recently, the barrier to Cu diffusion in bulk Si has been investigated by Shirai *et al.* [59] using MD simulations with Troullier-Martins PPs [101] as implemented in the Osaka 2002 code and the parametrization to LDA by Perdew and Zunger [102]. Zero temperature calculations performed initially for Cu_i in a Si 64 atom supercell produced an energy difference of 0.32 eV between the configurations with Cu at the T site and at the hexagonal face, with the T site configuration being the energetically favourable site, i.e., supporting the conclusion by Woon *et al.* in Ref. [57]. The focus of Ref. [59], however, was on the Cu diffusivity as obtained in the MD simulations (performed using a smaller cell), the electronic state of bulk Si Cu_i being discussed

[1] It was not specifically stated in Ref. [57] that the T site is the most favourable location for Cu, this information being included, however, in Ref. [100].

only to the extent that on the one hand, *(i)* the energy contours for Cu near the T site were found to be very weakly varying on the basis of the MD simulations while on the other hand, *(ii)* the electronic charge density suggested charge accumulation between Cu and the nearest neighbour Si atoms for the surrounding cage, in contrast, according to the authors, with the picture of bulk Si Cu_i as a 'tiny charged ball' with a closed $3d$ shell.

Finally, Latham *et al.* [60] recently reported results of structural optimization of bulk Si Cu_i as described with a 64 Si atom supercell using PPs constructed on the basis of the Hartwigsen-Goedecker-Hutter scheme [103] as implemented in the LSDA based Gaussian code AIMPRO [104, 105]. The bulk of the results presented in Ref. [60] did not involve isolated Cu_i in Si, and it was briefly mentioned that *(i)* Cu was located at the T site with *(ii)* a donor level at E_c - 0.03 eV, i.e., the shallow donor nature of this impurity was reproduced by theory. [2]

Relatively little experimental information is available on bulk Si Cu_i. The essential parameter providing information on the behaviour of this impurity is the diffusion barrier, determined only within the last decade by Istratov *et al.* [50]: this does explain, to some extent, why determining the Cu diffusivity in Si in theory has been preferred to focussing on the electronic state of Cu_i in bulk Si. The shallow donor behaviour of bulk Si Cu_i is well established by experiment, with a recent experimental value [106] of E_c - 0.15 eV for the donor level. As discussed in Sec. 2.3, however, theoretical studies of semiconductors generally underestimate the band gap, with complex effects on the defect levels, an issue which is still under investigation. In the present discussion, we shall only note that caution is advised when comparing results for the location and properties of a defect level as obtained by theory with experimental results. We shall comment further on this issue for bulk Si Cu_i in Sec. 5.2.5.

As discussed above, the bulk of the information from theory on the electronic state of bulk Si Cu_i has been provided by Estreicher and co-workers (see Refs. [55, 56]). We shall discuss in detail the more recent of these results, on which we have focussed our attention in our theoretical studies of this system, to be described briefly in Sec. 5.2.2, at the end of this discussion. Initially, however, we shall focus our attention on a highly confusing fact regarding the information on the structural parameters reported for the optimized configuration in these papers. Fig. 1 of Ref. [55] shows a Cu atom which has moved so far away from the T site, towards one of the nearest neighbour atoms, that the set of next nearest neighbours has changed from to the Si atoms forming bonds with the Si atom closest to Cu. Assuming a practically rigid Si lattice, a choice justified by the information in Ref. [55], [3] we find that the required Cu movement for this change in the set of next nearest neighbours to occur is at least 0.4 Å, but the movement suggested in

[2] We shall discuss below why one should be cautious about concluding too much from the second of these statements.

[3] Neither Fig. 1 of Ref. [55] or the somewhat more illuminating Fig. 2 of Ref. [56], reproduced as Fig. below in the text (Fig. 5.1), showing the same configuration according to the figure caption, show a highly distorted Si cage in response to the Cu off-center movement. Furthermore, as noted in the text below, Estreicher, in Ref. [55], specifically states that the relaxations of the Si host in response to the presence of Cu is very small.

Figure 5.1: Optimized configuration with Cu_i^+ in a H terminated Si cluster (H atoms not shown in figure) as obtained in the calculations of Ref. [55]. The Cu atom is described by the red sphere in the figure. See text for details. *Image courtesy of S. K. Estreicher.*

Fig. 1 of Ref. [55] clearly appears to be larger (see Fig. 5.1).

There is, however, no mention of this off-center movement at all in either Ref. [55] or Ref. [56] (where these results are also discussed), and further, the information in the text seems to fundamentally disagree with the information from the above mentioned figure: Cu_i is reported to be very near the T site upon optimization with four *nearest* neighbour Si atoms, i.e., a movement suggesting a Cu displacement of *clearly less* than 0.4 Å. The Si atoms have been reported in Ref. [55] to move away from Cu by less than 0.05 Å, in further support of calculations producing a configuration where Cu essentially stays at the T site. Finally, no difference between the structural parameters obtained in the studies of bulk Si Cu_i in Ref. [55] and the more recent studies of Ref. [56] has been reported.

We made no attempt to clarify the above described clear discrepancy at the onset of our theoretical studies of bulk Si Cu_i, to be described briefly in Sec. 5.2.2: in other words, we have made no attempt to clarify whether Cu is actually located very close to the T site or significantly displaced from this position according to the studies of Ref. [56] (which have received the most of our attention in the discussions below in this section). With this unsolved issue at the back of our mind, we have made the choice to regard the information on the optimized configuration provided by Fig. 5.1 as reliable, describing bulk Si Cu_i as clearly off-center in these calculations, whenever referring to the optimized structural parameters for this configuration below in our discussions. We emphasize, however, that this choice is made for simplicity in the discussion, i.e., the fully optimized bulk Si Cu_i configuration obtained in Ref. [56] might

actually have Cu located very close to the T site. We shall postpone further discussions of this issue until Sec. 5.2.4.3 when discussing the differences between the structural parameters for bulk Si Cu_i and the conclusions of previous theoretical studies.

For the structural optimization of bulk Si Cu_i^+ by Estreicher in Ref. [56], a single Cu ion in a Si 64 atom supercell was considered. Calculations were performed using Kleinman-Bylander NC PPs [107] as implemented in the pseudo atomic orbital code SIESTA [108, 27], using the parametrization to the LDA to E_{xc} by Perdew and Zunger [102]. A double zeta (DZ) basis set, i.e., two *s* and two sets of *p* orbitals per atom, was chosen for all Si atoms but those comprising the cage surrounding Cu. For these atoms, an additional set of *d* orbitals were added to the basis set, i.e. the basis employed for this situation was double zeta with polarization (DZP). [4] For Cu, two *s*, two sets of *p*, and one set of *d* orbitals were included in the basis set. [5] An orbital cut-off radius of $5a_0$ (2.6 Å) was chosen for all orbitals. The most dense *k*-point grid employed in these studies was a (2, 2, 2) MP *k*-mesh. Estreicher made few direct comments on the results obtained in these studies in Ref. [56] but noted that the essential difference when comparing with the results obtained in Ref. [55] was the amount of electrons promoted from the Cu 3*d* to the 4*sp* shells, leading to weak but covalent bond formation with the nearest neighbours in the surrounding cage, with a promotion of $\sim$ 1 electron predicted on the basis of the SIESTA studies. [6]

5.2.2 INTRODUCTION TO OUR WORK

The present section describes the results of our theoretical investigations bulk Si Cu_i, with Sec. 8.2 containing the bulk of the discussions of computational details. While previous theoretical studies have primarily focussed on the energy barrier to diffusion of this impurity in Si (see Sec. 5.2.1.1) we have aimed at clarifying, in our studies, the electronic state of this impurity, in the attempt to provide a satisfactory answer to the clear discrepancies between the current theoretical and experimental understanding of this system. Sec. 5.2.3 will present the results of the structural optimization of bulk Si Cu_i described by depositing either a single Cu atom or a Cu ion, Cu_i^0 and Cu_i^+, respectively, in a Si 64 atom supercell. We shall show that the results obtained for the structural parameters and electronic charge density depend only weakly on the charge state of Cu (a conclusion to be explained in Sec. 5.2.4.2) and the selected approximation to the exchange-correlation energy E_{xc} (GGA and LDA based studies were performed).

The detailed analysis of the electronic state of bulk Si Cu_i is presented in Sec. 5.2.4. Calculations have been performed using both the plane wave based code VASP (used for the structural optimization studies described in Sec. 5.2.3) and the pseudo atomic orbital code Plato (see Sec. 1.5 for brief comments on these methods and their con-

[4] It is not entirely clear to us whether this statement provides a correct understanding of the information in Ref. [56] or whether the larger basis set was used only for the nearest neighbour Si atoms to Cu. We shall discuss these two possible theoretical descriptions of the system further in Sec. 5.2.4.3.

[5] The reader should note that this basis set is not of the conventional DZP form, where only one set of *p* orbitals, but two sets of *d* orbitals would be used for the description of Cu.

[6] For a discussion of the structural parameters for bulk Si Cu_i obtained in the studies of Ref. [56] we refer to the discussion regarding the interpretation of Fig. 5.1 above in the text.

ceptual differences): this choice was made partly in order to extract more complete information about the system compared to what could be obtained with e.g. a study involving VASP based calculations only. The pseudo atomic orbital based studies had an additional purpose: as will be clarified in Sec. 5.2.4.2, we arrived at the conclusion that bulk Si Cu_i is a shallow donor with a loosely bound 4*s* state and a closed 3*d* shell, in agreement with the experimental picture presented in Sec. 4.1.2 but in marked contrast with the theoretical conclusions reported by Estreicher [56], obtained using the pseudo atomic orbital based code SIESTA. The Plato based studies therefore were also aimed at clarifying the reasons for the discrepancies between our results and those obtained in Ref. [56]. Sec. 5.2.4.3, discussing this latter issue, will show that the results obtained in Ref. [56] involved using an incomplete basis set for the Si atoms away from Cu, leading to artificial confinement of electrons (as opposed to formation of weak covalent Cu-Si bonds, as concluded in Ref. [56]) in the region around the impurity.

Finally, Sec. 5.2.5 discusses the cell dimension convergence of the bulk Si Cu_i energy: we shall clarify at this point that the diffuse Cu 4*s* state is almost entirely contained for Cu in a Si 216 atom supercell, i.e., the overlap of adjacent 4*s* wave function, the expected main cause of remaining errors in the bulk Si Cu_i energy at the 64 atom cell level, is almost negligible when using this larger cell.

5.2.3 OPTIMIZED STRUCTURAL PARAMETERS FOR INTERSTITIAL Cu IN BULK Si

In order to clarify the preferred site for Cu_i in bulk Si, we have structurally optimized both systems with *(i)* an interstitial Cu atom, Cu_i^0, and *(ii)* an interstitial Cu ion, Cu_i^+, in Si supercells of various sizes: the studies described in the present subsection focus on calculations with a single Cu atom/ion in a Si 64 atom cell, performed using VASP (for further comments on computational details, see below). As discussed in Sec. 4.1.2, Cu is a shallow donor and therefore always ionized in Si. For theoretical studies employing a supercell approximation, a charged impurity is considerably more difficult to handle, however, than a neutral impurity: the increased level of interaction between impurities in adjacent cells requires comparatively much larger cells for an acceptable level of convergence in the formation energy of the defect and, possibly, the structural parameters for the configuration to be obtained. This demand can not be met in present day simulations, and in practice, corrections for these errors therefore will have to be applied for the smaller cells used in actual theoretical studies. As discussed in Sec. 2.3, a complete understanding of the necessary corrections for a reliable description of this type of system is yet to be obtained. For this reason, we have made the choice to focus in the present work on bulk Si Cu_i^0, including studies of Cu_i^+primarily for the sake of comparison with the previous theoretical studies by Estreicher [56], where only the charged impurity was studied. [7] For simplicity, in the discussion below, we shall omit

[7] We shall discuss in Sec. 5.2.4.2 how, in addition, the calculations on bulk Si Cu_i^+ serve the purpose of supporting the conclusions obtained for the electronic structure of this impurity in the Cu_i^0 studies. The conclusion of a high comparability of the results obtained for neutral and charged Cu_i in Si, discussed in that part of the thesis, is of crucial importance to the present studies: as discussed in Sec. 4.1.2 bulk Si Cu_i is a shallow donor according to experiment and therefore essentially always positively charged.

the superscript specifying the charge of the impurity considered in calculations: unless otherwise noted, the discussion will involve the interstitial Cu atom in Si.

As discussed in Sec. 5.2.1.1, the optimized bulk Si Cu_i configurations reported in various theoretical studies differ markedly. The configuration obtained for Cu_i in a Si 64 atom supercell in the studies performed by Estreicher [56] appears to have Cu quite far from the T site, towards one of the nearest neighbour Si atoms for the surrounding cage, with other theoretical results [59, 60] for Cu in this cell supporting the T site as the energetically favourable site for Cu_i in Su. Yet another theoretical study [58] of this system reported a Cu movement to the hexagonal face of the Si cage: in this case, however, the Si supercell was smaller, containing only 16 atoms.

In our approach to identifying the energetically most favourable position for Cu_i in bulk Si, we have focussed on some, but not all, previous theoretical results: Our own initial studies did not indicate the presence of a structural instability with Cu at the T site but on the other hand involved no attempts to move Cu significantly away from this site at the onset of optimization. In our structural optimization of bulk Si Cu_i we therefore carefully (see Sec. 8.2.2) searched for a structural instability similar to the one described in Fig. 2 of Ref. [56]. We shall discuss the results of these studies below. We made no attempt to move Cu away from the T site towards other regions of the cage, i.e., we did not investigate the suggestion by Kamon *et al.* [58] that the hexagonal face for this cage is an energetically clearly more favourable site for Cu compared to the T site. We shall, however, comment further on this result in Sec. 5.2.4.3.

In addition to the Si 64 atom supercell, the VASP studies also employed a Si 216 atom cell in order to address the convergence of the formation energy of bulk Si Cu_i with respect to cell dimension. We shall comment on the optimized values for the structural parameters and formation energy obtained in these studies below, postponing a full discussion of the convergence issue until Sec. 5.2.5.

The VASP based calculations on bulk Si Cu_i employed Vanderbilt US PPs [17], using either *(i)* the LDA or *(ii)* the PW91 GGA to E_{xc}. For the Si host, the experimental lattice parameter of 5.43 Å for Si at ambient conditions was chosen. In both sets of calculations, a converged energy and structural parameters for the system with Cu in a Si 64 atom supercell were obtained using a plane wave energy cutoff value of 248.3 eV, a width of 0.1 eV for the chosen Gaussian smearing scheme, and a (4, 4, 4) MP k mesh. For this choice of parameters, the pressure on the clean Si cell was found to be quite small, suggesting changes in the lattice parameter within a few hundredths of an Å for the fully optimized system. For further comments on computational details, we refer to Sec. 8.2.2.

There were various reasons for performing structural optimizations using two approximations to E_{xc}. On a general level, testing the reliability of the results of theoretical DFT based studies by using more than e.g. the PW91 GGA to E_{xc} is strongly recommended [8] (we shall discuss this issue further in Sec. 5.4.2 in particular, when presenting the results obtained in LDA and GGA based calculations for Cu on the Si(001) surface). Furthermore, for the present situation, LDA based studies are strictly needed, both *(i)* for comparison with the previous theoretical results by Estreicher [56] and *(ii)* as a test of the relibiality of the population analysis for the system performed on the basis of calculations with the pseudo atomic orbital based code Plato, within the

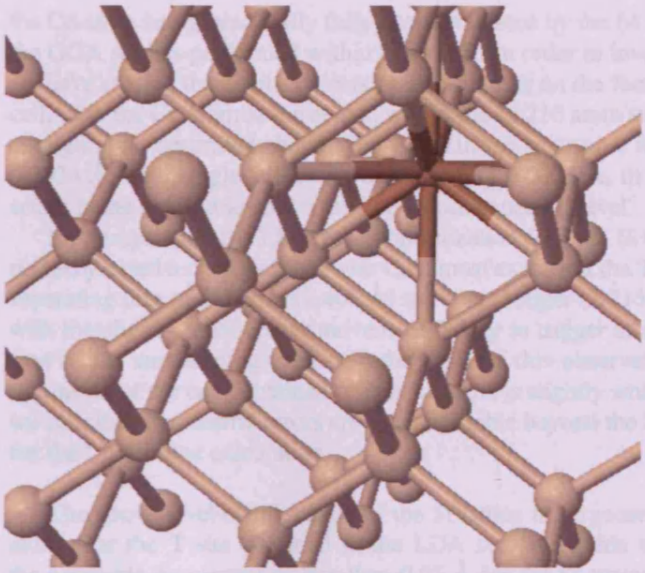

Figure 5.2: Optimized fully converged configuration with Cu_i in a Si 64 atom supercell as obtained in GGA based studies using VASP (see text for details). The Cu atom is the smaller, dark brown sphere in the figure. On optimization, Cu is located exactly at the T site with the nearest neighbour Si atoms moving away from the impurity by 0.07 Å. Optimization within the LDA leads to an almost equivalent configuration (described in further detail in the text).

LDA (see Sec. 5.2.4). On the other hand, GGA based results are generally regarded as more reliable than results obtained within the LDA for bulk properties [8]. In summary, therefore, there were very good reasons for performing studies of bulk Si Cu_i in the present work using both the LDA and the PW91 GGA to E_{xc}.

Fig. 5.2 shows the optimized configuration for Cu_i in the Si 64 atom supercell as obtained in the GGA based calculations within the above described theoretical framework and specified precision. The Cu atom is located essentially at the T site, with the Cu-Si distances increasing from the value of 2.351 Å for a rigid cell with Cu exactly at this location to 2.425 Å (three shorter distances) and 2.432 Å (one longer distance). The slight Cu off-center movement does not introduce any asymmetry in the expansion of the cage, the rms value for the Si-Si distances involving the Si atoms comprising the cage being 2.387 Å with a scatter of less than 0.001 Å for the individual bond lengths.

In the calculations performed with Cu in the 216 Si atom cell, the structural parameters appear to be basically unaffected by increase in the precision beyond the initial choice described in Sec. 8.2.2 (for further details, see Sec. 5.2.5): for this situation, Cu is located exactly at the T site with an outwards movement of the nearest neighbour Si atoms by 0.076 Å and the same rms value for the cage Si-Si distances as obtained with Cu_i in the Si 64 atom cell. This clearly points towards the structural relaxations around

the Cu atom being practically fully accommodated by the 64 Si atom cell according to the GGA studies performed within this work. In order to investigate this issue further, we have studied the displacements of the Si atoms on the faces of an artificial 64 atom cell, with the Cu atom at the center, within the Si 216 atom supercell for the optimized configuration described above. For this cell, the rms value for the displacements was 0.0026 Å, with single values never exceeding 0.0073 Å, in strong support of elastic errors being negligible above the Si 64 atom supercell level.

By comparison, the LDA based optimization for bulk Si Cu_i in the Si 64 atom supercell yielded a configuration with Cu almost exactly at the T site, the Cu-Si distances separating into one shorter (2.408 Å) and three longer (2.416 Å) distances, once again with the slight Cu off-center movement failing to trigger an asymmetry in the expansion of the surrounding cage. On the basis of this observation and the fact that the expansion of the cage obtained within the LDA is slightly smaller than the GGA result, we conclude that elastic errors are also negligible beyond the Si 64 atom supercell level for the LDA based calculations.

The above level of relaxation of the Si lattice in response to the insertion of a Cu_i atom near the T site obtained in the LDA studies of this work is highly similar to the outwards movement of less than 0.05 Å for the Si atoms in the cage surrounding Cu_i^+ reported in calculations by Estreicher in Ref. [56]. As discussed in detail in Sec. 5.2.1.1, these results, however, appear to suggest a significant movement of Cu away from the T site, a feature not reproduced in our theoretical studies. As an initial attempt to investigate this issue further, [8] we performed VASP based studies resembling the SIESTA based studies of Ref. [56] as closely as possible, i.e., we studied Cu_i^+ in the same Si 64 atom supercell as previously but using k-point grids ranging from k = 0 to a (3, 3, 3) MP k mesh, choosing for all studies a 233.7 eV plane wave energy cutoff and a width of 0.1 eV for the Gaussian smearing scheme. In order to investigate the influence of choosing a charged impurity over a neutral impurity in these studies, structural optimizations of bulk Si Cu_i^0 were performed alongside the Cu_i^+ studies for all situations considered.

These studies (see Sec. 8.2.2 for full details) did not reveal any structural instabilities similar to those described in Fig. 2 of Ref. [56]: in all cases, with the exception of a comparatively large distortion for the optimized bulk Si Cu_i^0 configuration obtained in the Γ point calculation, Cu stayed very close to the T site with the Cu-Si distances being within 0.01 Å of the above mentioned fully converged LDA values, regardless of the detailed choice of impurity. We therefore conclude that *(i)* there is no indication, on the basis of our VASP studies, that differences between optimized structural parameters obtained in various theoretical studies of bulk Si Cu_i can be explained by the impurity being neutral in some studies and charged in others. [9] In addition, *(ii)* we have found no suggestions from the above described calculations that the significant movement of Cu away from the T site in Fig. 2 of Ref. [56] can be reproduced in studies with a plane

[8] We shall discuss this issue in considerably higher detail in Sec. 5.2.4 when attempting to perform calculations similar to the studies of Ref. [56] using the pseudo atomic orbital based code Plato rather than VASP.

[9] We shall discuss the reason for the close similarity of the structural parameters for bulk Si Cu_i^0 and bulk Si Cu_i^+ in Sec. 5.2.4.2.

wave based code.

Finally, the key difference between the LDA and GGA based studies is the energy for bulk Si Cu_i, with the LDA result being lower by more than 1.3 eV compared to the GGA result. For the present studies, this difference is not of considerable interest, as preliminary investigations into the electronic structure of the system have not revealed any truly significant differences between the two results: in other words, as we have found no indications that the electronic state of Cu is described in a highly different manner within the two theoeretical frameworks considered in the above, we are not concerned about focussing, in our investigations of the electronic structure for this system described in Sec. 5.2.4, on calculations performed within the LDA, even though it is generally expected [8] that bulk properties are described better within the GGA. We shall discuss the LDA and GGA predictions for the formation energies of Cu in Si further in both Sec. 5.3.2 and Sec. 5.4.2.2, with the latter of these discussions addressing the above issue in slightly more detail.

5.2.4 ELECTRONIC STATE OF INTERSTITIAL Cu IN BULK Si

5.2.4.1 ON THE COMPARABILITY OF THE PLATO AND VASP LDA STUDIES PERFORMED IN THIS WORK

As discussed in Sec. 5.2.3, the VASP based studies of bulk Si Cu_i performed in this work did not reveal the cause of the apparent discrepancy between various previous theoretical results [56, 60] regarding the structural details for this system: in our calculations, Cu was always found to occupy the T site, in agreement with the conclusions by Latham *et al.* [60] and Shirai *et al.* [59]. While our studies were performed within a theoretical framework with close similarities to the chosen approach by Estreicher in Ref. [56] to describing this system, a key difference, impossible to address in the studies of Sec. 5.2.3, was the choice of a plane wave based code in our calculations as opposed to the pseudo atomic orbital based code (SIESTA) used in the studies of Ref. [56]. As improvements in the accuracy of the description of the system under investigation with these two types of code follows quite distinct paths (see Sec. 1.5), it is not straightforward to point out an error in theoretical studies performed using e,g. a pseudo atomic orbital code on the basis of calculations performed using a plane wave code. For this reason, in order to investigate properly the reason for the discrepancies between our results and those reported in Ref. [56] for the structural details of bulk Si Cu_i, we should investigate this system using a pseudo atomic orbital based code in addition to the studies described in Sec. 5.2.3. Another reason for performing such studies concerns the main focus of the present theoretical study, the electronic state of Cu_i in Si. We deliberately did not address this issue in Sec. 5.2.3: as will be clarified below, the information obtained from population analysis on the basis of comparable results obtained using both a plane wave based and a pseudo atomic orbital based code gives a comparatively much stronger insight into this issue.

The above considerations describe the key reasons for performing studies of bulk Si Cu_i using also a pseudo atomic orbital based code in the present work. We have chosen

Table 5.1: Calculated Cu-Si distances for Cu_i at the T site in a Si 64 atom supercell using VASP and Plato within the LDA: the subscripts in the first column are shorthand notation for the Plato basis sets described in further detail in Table 5.2.The tabulated distances are mean values; the scatter in the actual values was always within 0.01 Å.

Basis	Code	r_c / a_0	|Cu - Si| / Å
$SN_{5.5}$ *(i)*	Plato	5.5	2.405
SN_6 *(ii)*	Plato	6.0	2.454
DN/DNP *(iii)*	Plato	5.5	2.439
DNP *(iv)*	Plato	6.0	2.441
-	VASP	-	2.411

the code Plato [28] for these studies. This code employs the PP and parametrization of the LDA to E_{xc} by Goedecker, Teter, and Hutter [20] and as such, we expect the results obtained for a fully converged basis set to be highly similar to the results obtained in the VASP LDA studies of Sec. 5.2.3. We shall discuss this issue further in the following.

Table 5.1 includes the structural parameters for bulk Si Cu_i, described with a Si 64 atom supercell (the same system, including choice of lattice parameter, as used for the VASP LDA studies of Sec. 5.2.3), as obtained on optimization using the various Plato basis sets considered in the present work. Essential details for these basis sets are provided in Table 5.2, with a full discussion into both this issue and other computational details included in Sec. 8.2.3. All calculations (including the VASP LDA result in Table 5.1) were performed using a (3, 3, 3) MP k mesh and Gaussian smearing with a 0.05 eV width. [10] For the integral grid mesh used in the Plato calculations (see Sec. 8.2.3), a spacing of 0.150 (0.175) Å for the basis sets with cutoff-radius 5.5 (6.0) a_0 was chosen on the basis of investigations with the SN basis sets, described in Sec. 8.2.3.

In all studies but the one performed using the DNP basis set (where Cu was expected, on the basis of the conclusions in Sec. 5.2.3 to be located essentially at the T site), optimization was started with Cu slightly off-center by 0.19 Å in the undistorted cage, moved towards one of the nearest neighbour Si atoms. On optimization, however, Cu was found to be located essentially at the T site, regardless of the basis set used, with only the expansion of the surrounding Si cage varying with the choice of orbitals. [11]

We interpreted the variation in these cage expansions as follows: the relatively large increase obtained when comparing the results of the calculations with the two SN basis

[10] When discussing the convergence in the energy and structural parameters of bulk Si Cu_i for the VASP based calculations within the LDA in Sec. 8.2.2, we concluded that fully converged values for these parameters were obtained using a (4, 4, 4) k mesh, the same studies also showing, however, that the values obtained when using the coarser (3, 3, 3) k mesh are not changed appreciably.

[11] An additional optimization of bulk Si Cu_i was performed using the DN/DNP basis set but with the larger set of Si orbitals used only for the nearest neighbour Si atoms (as opposed to all Si atoms in the cage surrounding Cu as described for the DN/DNP basis set in Table 5.1). The result obtained from this calculation showed only weak differences when compared to the alternative result in Table 5.1, Cu still being located at the T site with the mean value for Cu-Si distances reduced to 2.429 Å.

Table 5.2: Key computational details (choice of orbitals and cutoff radius r_c for the Plato studies, plane wave energy cutoff value for the VASP studies) for the Plato and VASP basis sets used for the studies of bulk Si Cu_i performed in the present work. For further details, see Sec. 8.2.2 and Sec. 8.2.3.

Basis	Code	Basis set details
$SN_{5.5}$ *(i)*	Plato	*sp* (Si), *ds* (Cu)
SN_6 *(ii)*	Plato	*sp* (Si), *ds* (Cu)
DN/DNP *(iii)*	Plato	$sps^*p^*d^*$ (Si I), sps^*p^* (Si II), $dsps^*p^*$ (Cu)
DNP *(iv)*	Plato	$sps^*p^*d^*$ (Si), $dsd^*s^*p^*$ (Cu)
-	VASP	Plane wave energy cutoff 248.3 eV

sets, i.e., upon increasing the cut-off radius of the orbitals but otherwise using conceptually the same basis set, can be explained by this set essentially being too small: the fact that the cage expansion obtained with the $SN_{5.5}$ basis set is quite close to the VASP LDA value must be regarded as coincidental, with the SN_6 basis set evidently providing a more correct description, according to the conclusions in Ref. [28] regarding the cut-off radius convergence (we shall comment further on this issue below). The cage expansion obtained with the SN_6 basis set, on the other hand, is clearly above the VASP LDA value, suggesting that there is an insufficient amount of freedom for the construction of the electronic charge density when using this basis set, leading in turn to an increased repulsion of the atoms in the Si cage by the Cu atom. Upon a further increase in the cut-off radius beyond the value of 6 a_0, i.e., 3.2 Å, used for the SN_6 basis set and towards the fully converged value [28], we would expect the cage to expand even further, taking the structural parameters even farther away from the LDA result.

On the face of it, the cage expansion obtained using the larger DNP basis set appears somewhat troubling in this respect, when considering the completeness of this set. Firstly, the mean value for the Cu-Si distances obtained for this situation are also clearly above the VASP LDA value with the choice 6 a_0 for the orbital cut-off radius. Secondly, when comparing with the results obtained with the SN_6 basis set, it appears that the addition of orbitals has close to no effect. The reported values in Ref. [28] for the optimized bulk Si lattice parameter obtained using the Si part of the SN_6 and DNP basis sets (see Table I in this reference) provides some insight into this issue: with the chosen value of the orbital cut-off radius, the lattice parameter of 5.416 Å obtained with the SN_6 basis set is, once again coincidentally, quite close to the chosen value of 5.43 Å for the supercell used in calculations. By comparison, the lattice parameter of 5.330 Å obtained for the DNP basis set at this cut-off radius is clearly below this value, and the value for the bulk modulus furthermore is $\sim$ 15% higher for this situation. Both of these differences suggest that, in comparison with the SN_6 basis set, the stifness of the Si-Si bonds in the DNP basis set calculation is clearly lower, leading to an incorrectly pronounced expansion of the Si cage containing the Cu impurity. This error would essentially be corrected if calculations were performed using a cut-off radius of 7.0 a_0 for this basis set (see Table I of Ref. [28]). However, as no such studies have been performed in the present work, in the absence of knowledge on the overestimation of the cage expansion for the DNP basis set results in Table 5.1, we can not verify the com-

pleteness of the Plato DNP basis set by comparing the optimized structural parameters for bulk Si Cu_i as obtained in calculations with this basis set with converged parameters obtained using VASP within the LDA. We shall discuss below an alternative approach to clarifying this issue.

On the basis of the above considerations for the DNP basis set, we have made no attempt here to evaluate the completeness of the DN/DNP basis set making reference only to the optimized structural parameters obtained for bulk Si Cu_i for this situation. The cage expansion obtained in calculations with this basis set is found to be highly similar to the DNP basis set result. As will be discussed in Sec. 5.2.4.3 this does not suggest that there is very little difference between the configurations obtained in these two studies: indeed, this apparent similarity of the optimized configurations, like the apparent similarity discussed in the above for the SN_6 and DNP basis set results, is basically to be regarded, rather, as an example that one should be extremely cautious about drawing conclusions about the comparability of results, obtained using clearly distinctive approaches to describing the system theoretically, on the basis of structural parameters alone.

On summarizing the above studies, the question remains: is the Plato DNP basis set complete to an acceptable level, where comparison with results of the VASP LDA studies can safely be performed? A way of obtaining more information on this issue would be to compare the electronic charge densities for bulk Si Cu_i as obtained using the two theoretical descriptions of this system. We have not performed such a study, however, partly as the number of Plato basis sets is so small that the level of convergence in case of differences between the two charge densities is challenging to address. For the time being, therefore, we shall assume that the very general considerations presented in the above discussion provide sufficient justification for using the Plato DNP basis set for the studies of the electronic structure of bulk Si Cu_i to be discussed in Sec. 5.2.4.2. We shall clarify through the considerations presented in the following, why we see no clear warning signs in this choice of approach.

5.2.4.2 ELECTRONIC STRUCTURE OF INTERSTITIAL Cu IN BULK Si: SUPPORT FOR THE *3d* SHELL BEING CLOSED

In order to gain information on the electronic state of bulk Si Cu_i as described using the various Plato basis sets of Table 5.1, we have performed a Mulliken population analysis [109] on the results described in Sec. 5.2.4.1. The net atomic charges for Cu and some of the closest Si atoms for the various optimized configurations have been tabulated in Table 5.3 while the Cu electron occupation numbers have been tabulated in Table 5.4. Before discussing the results of this study, we shall comment briefly on the basic limitations of this type of study: on a very basic level, regardless of the code used for the calculations (but with the choice of code having a clear influence on the details of the actual procedure of the analysis, see Sec. 1.5), the investigation to be described in the following follows the strategy of ascribing certain amounts of the electronic charge density to a particular atom. This approach can be very revealing for situations where electronic states for an atom in a given crystal structure are highly confined and therefore hardly interacting with the crystal environment, but caution is advised whenever

Atoms	Charge$_{(i)}$/ e	Charge$_{(ii)}$/ e	Charge$_{(iii)}$/ e	Charge$_{(iv)}$/ e
Cu	0.217	0.271	-0.170	0.037
NN Si	-0.039	-0.045	0.033	0.040
next NN Si	-0.015	-0.024	-0.068	-0.026
Si 'cage'	-0.031	-0.049	-0.443	0.040
Other Si	< 0.002	< 0.003	< 0.045	< 0.010

Table 5.3: Net charges for selected individual atoms (rows 1 - 3) and groups of atoms (rows 4 - 5) for bulk Si Cu_i as described with various Plato basis sets: the subscripts in the upper row are shorthand notation for the basis sets described in further detail in Table 5.1. The Si 'cage' with the Cu atom included is defined here as comprised by all the atoms of rows 1 - 3 while the data in row 5 (numerical values) involve all the remaining atoms in the cell. The tabulated numbers in rows 2 - 3 are mean values; the scatter in the actual values is $\sim 0.002e$ or less.

interpreting results for situations where this is not the case. As will be discussed below, even for the conceptually relatively simple situation of Cu_i in bulk Si, the potential ambiguties inherent in the population analysis are evident, and we shall therefore emphasize whenever our investigations do not provide an absolutely clear picture of the interactions of the impurity with the host lattice.

The studies of the present work confirm the conclusions of Ref. [28] that adding Si $3d^*$ orbitals to the basis set is of crucial importance for describing the Si host satisfactorily: for the DNP basis set, the occupation number for these orbitals is 0.24, with the numbers obtained for the $3s^*$ and $3p^*$ orbitals being negligible in comparison. For the interstitial Cu atom in bulk Si, the addition of $4p$ orbitals to the basis set is crucial: both the DN/DNP and the DNP basis set results suggest that inclusion of these orbitals allows for a considerable charge redistribution, with the $4p$ occupation number obtained in these studies being 0.5 or more, this number in both cases being much larger than the almost negligible occupation numbers obtained for the other orbitals added when comparing with the SN basis set. On the basis of the Cu occupation numbers in Table 5.4, this charge redistribution can only to some extent be explained as a promotion of electrons from the Cu $3d$ and $4s$ shells to the $4p$ shell, with also an appreciable amount of charge being dragged in from the surroundings. In particular, the $3d$ electron occupation number is found to be only very weakly dependent on the choice of basis set, with the d shell being almost completely filled. Finally, for the SN and DNP basis sets, the net charge for the Si cage containing the Cu atom is found to be almost zero (numerical value less than $0.05e$). We shall comment further on these issues below.

The Mulliken population analysis of the Plato DNP basis set results does not provide us with sufficient information on the electronic charge density distribution to fully clarify the electronic state of Cu_i in bulk Si. Further information on this issue has been gained, however, from plots of the charge density changes upon insertion of Cu_i^0 in the Si lattice as obtained with VASP, with Fig. 5.3 showing results of such studies. In this

Basis	3*d*	4*s*	4*p*
(i)	9.76	1.03	-
(ii)	9.76	0.97	-
(iii)	9.66	0.77	0.72
(iv)	9.66	0.77	0.54

Table 5.4: Orbital occupation numbers for the completely optimized configuration with the Cu atom at the tetrahedral site in a Si 64 atom lattice according to the Plato results. The labels in the first column are shorthand notation for the basis sets described in further detail in Table 5.1.

figure, for clarity, the charge density as obtained in a static calculation for the Si lattice distorted due to the presence of the Cu atom, but without Cu present in this calculation, was subtracted from the charge density of bulk Si Cu_i in the attempt to eliminate the effects of the Si atom movements on the charge density changes. The result of this procedure showed an addition of charge with evident spherical symmetry over the entire cell, suggesting that Cu_i donates is 4*s* electron to the surroundings, with the 4*s* state being very diffuse.

In order to verify the above result, we performed an additional optimization using the DNP basis set but removing an electron from the system. This calculation yielded a configuration which structurally was found to hardly differ from the result obtained for Cu_i^0 with this basis set, the Cu-Si distances being within 0.003 Å of the values obtained previously. More importantly, a population analysis of this result revealed a fairly comparable removal of charge in the region surrounding each ion in the system, with Cu, in particular, 'losing' only 0.033e in comparison with the situation for bulk Si Cu_i^0 and with only the occupation number for the Cu 4*s* orbital showing a nonneglible change. These results strongly support the above conclusions for the electronic state of bulk Si Cu_i while also explaining why the structural parameters as obtained in the VASP LDA studies of bulk Si Cu_i^0 and Cu_i^+ are highly similar: in the calculations for charged Cu, the charge neutrality of the supercell is ensured by adding a homogeneously distributed background charge to the charge density obtained on optimization. With the above described Plato results confirming the diffuseness of the Cu 4*s* state, there is, on a rather general level, relatively small difference between the calculation for the charged and neutral impurity. Finally, as will be discussed in Sec. 5.2.5, the above described conclusion that Cu_i is shallow donor in Si according to our theoretical studies, has been further verified in investigations of the band structure for the system. [12]

While bulk Si Cu_i is found to donate its 4*s* electron to the Si lattice according to our studies, the Plato DNP basis set result suggests, as noted previously, that the Si cage containing the resulting Cu^+ ion is approximately charge neutral. This result is explained by the efficient screening of the charged impurity: Fig 5.3 shows that the

[12]We have made the choice to deliberately postpone an investigation into the band structure as there is still a considerable amount of dispersion of the Cu 4s level for Cu_i in the Si 64 atom cell, the system under investigation in the present discussion: in order for these studies to provide clear support for the above considerations, investigations of Cu_i in a 216 Si atom cell are needed.

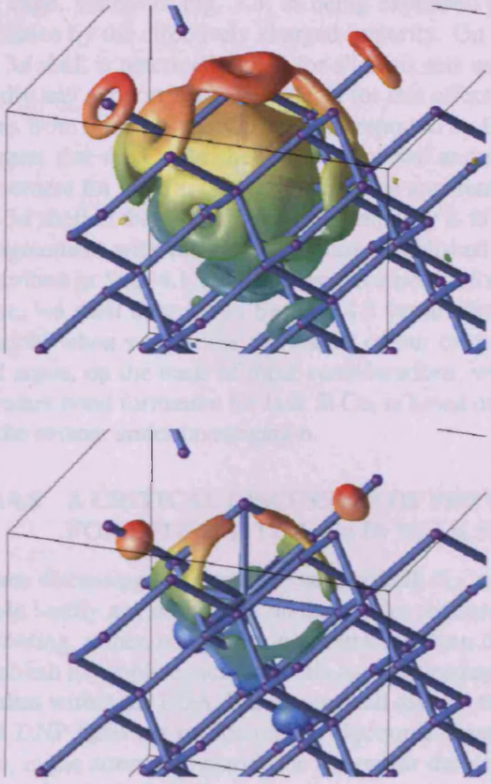

Figure 5.3: Changes in the charge density upon insertion of Cu_i in bulk Si, as obtained with VASP (see text for details). The upper (lower) part of the figure shows specifies regions where charge has been added (removed) when comparing with the original clean Si cell. In both figures, the Cu atom is located at the center of the spherical charge distributions. The approximate numerical values for the charge density contours in these figures are 0.004 e/Å^3(top figure) and 0.01 e/Å^3 (bottom figure).

Si-Si bonds involving the Si atoms with the shortest distances to Cu are significantly weakened, with charge being moved into the cage primarily to the region between Cu and the nearest neighbour Si atoms. Farther away from the impurity, the Si atoms were found to be only weakly affected. We shall discuss the screening further in Sec. 5.5.

The above described conclusions do not unambiguously support the charge accumulation in the region between Cu and the nearest neighbour Si atoms in the surrounding cage, visible in Fig. 5.3, as being explained primarily by the polarization of the Si lattice by the effectively charged impurity. On the other hand, considering that the Cu 3*d* shell is practically filled for all basis sets used in the Plato calculations, there is hardly any support from our studies for this effect being related to promotion of electrons from the 3*d* to the 4*sp* shells as reported by Estreicher in Ref. [56]. We therefore suggest that the Cu 3*d* shell remains closed and only slightly distorted by the Si environment for bulk Si Cu_i (explaining the apparent slight promotion of electrons from the 3*d* shell to the 4*p* shell), i.e., this impurity is to be regarded as a 'tiny charged ball', in agreement with the general picture established by the experimental community as described in Sec. 4.1.2. While we have not performed further direct studies into this issue, we shall describe in Sec. 5.2.4.3 yet another strong support for the above conclusion, when we discuss the results of our calculations with the DN/DNP basis set and argue, on the basis of these considerations, why Estreicher's conclusion of Cu-Si covalent bond formation for bulk Si Cu_i is based on an incorrect theoretical description of the system under investigation.

5.2.4.3 A CRITICAL DISCUSSION OF PREVIOUS THEORETICAL RESULTS FOR INTERSTITIAL Cu IN BULK Si

When discussing the electronic state of bulk Si Cu_i in Sec. 5.2.4.1 and Sec. 5.2.4.2, we made hardly any comments on the results obtained with the Plato DN/DNP basis set, focussing, rather, on conclusions extracted from the DNP basis set studies in order to establish a complete picture of this issue according to the VASP and comparable Plato studies within the LDA. Below, we shall discuss the differences between the DN/DNP and DNP basis set results for the electronic structure of the system under investigation, in the attempt to clarify the reason for the very different conclusions reported by Estreicher in Ref. [56] on the electronic state of bulk Si Cu_i. We shall show in the following that *(i)* the use of the DN/DNP basis set leads to artificial (i.e., unphysical) charge accumulation in the region around the Cu atom and subsequently *(ii)* discuss why the same incorrect description of Cu_i^+ in bulk Si must be expected when using the SIESTA basis set employed in Ref. [56]. Also, we shall include at the end of this discussion brief critical comments on other previous theoretical investigations of bulk Si Cu_i.

In comparison with the conclusions obtained from the population analysis for the DNP basis set, described in Sec. 5.2.4.2, the results obtained with the DN/DNP basis set are markedly different. The Si cage for this basis set is not close to electrically neutral for this situation, but very clearly charged ($\sim$ -0.4*e*), leading to a much more significant charge redistribution farther away from the Cu atom (see Table 5.3). This result is a consequence of the conclusion, as noted in Sec. 5.2.4.2, that the Si $3d^*$ orbitals

Figure 5.4: Variation of cohesive energy for bulk Si with the choice of basis set in calculations with SIESTA. These results suggest that a DZ basis set (second arrow from the top in the figure) is far from being fully converged for this situation. *Image courtesy of J. M. Soler, E. Artacho, J. D. Gale, A. Garcia, J. Junquera, P. Ordejon, and D. Sanchez-Portal.*

are of clear importance to the cohesive properties of clean bulk Si: the smaller of the Si basis sets for the DN/DNP basis set evidently is not fully converged, with the results in Table I of Ref. [28] for the chosen orbital cut-off radius of 6.0 a_0 used in the present work showing a change of almost 0.5 eV/atom in the cohesive energy for this system when the Si $3d^*$ orbitals are added to the basis set. In other words, if a calculation were performed for clean Si employing the two Si basis sets of the DN/DNP basis set but with the larger of these sets used only for a 'special cage' in this lattice, there would be an energy gain associated with moving charge towards this cage, a clearly unphysical situation. This fully clarifies that, for the Plato studies of bulk Si Cu_i, the DN/DNP basis set leads to an essentially incorrect description of the system under investigation, and the conclusions obtained with this basis set can not be regarded as reliable.

The population analysis for the Plato DN/DNP basis set result does not suggest the same amount of electron transfer from the Cu $3d$ to the $4sp$ shells reported by Estreicher in the SIESTA calculations of Ref. [56], the main reason for this presumably being that there are evident conceptual differences between the Plato and SIESTA basis sets which makes such a detailed comparison unjustifiable. It is beyond the scope of the present study to go into detail with these differences. Indeed, we do not need to perform SIESTA calculations in order to show that the problem of artificial electron confinement addressed above for the Plato basis set also applies to the calculations of Ref. [56]: only, we have to verify that the smaller of the Si basis sets used in the SIESTA calculations of this reference suffers from the same incompleteness as described for the DN/DNP basis set above.

Fig. 5.4 shows the variation in the cohesive energy for bulk Si as obtained with various SIESTA basis sets, with the results described in more detail in Ref. [110]. While this figure does not provide information on the cohesive energy of this system obtained with the specific choice of DZ and DZP basis sets used by Estreicher in Ref. [56] (see Sec. 5.2.1.1) it does very clearly show that the smaller basis set is far from being converged. We are not aware of convergence studies into this issue by Estreicher but find it highly unlikely, on the basis of the results in Fig. 5.4, that the DZ basis set should be converged for this situation. We therefore suggest that the Cu-Si bond formation reported in Ref. [56] is actually to be explained as artificial electron confinement as a consequence of the use of an incomplete basis for bulk Si in these calculations.

The large disagreement between various theoretical results with regards to the energetically most favourable location for Cu_i in bulk Si has been described in Sec. 5.2.1.1. Our theoretical studies of this system have not produced sufficient knowledge to rigorously explain these discrepancies: in particular, the Plato based calculations employing the DN/DNP basis set, arguably leading to an incorrect theoretical description of the system under investigation conceptually similar to the theoretical studies of Ref. [56], have not reproduced the apparent (see Fig. 5.1) significant movement of Cu away from the T site obtained in these previous investigations. We do not regard this issue as critical: as discussed in Sec. 5.2.1.1, the optimized bulk Si Cu_i configuration might actually involve Cu located very near the T site, with the level discussion of discussion in Ref. [56] simply being too low to clarify this issue. A considerably more important topic of discussion is the electronic state of Cu_i in bulk Si as obtained in the studies of Ref. [56], an issue which has been discussed thoroughly in the present work.

While we are less concerned about the energetically most favourable position of Cu_i in bulk Si, we note that both our theoretical studies with VASP and Plato have yielded indications that appreciable Cu off-center movements could occur if the precision in calculations is too low. These instabilities have been discussed in detail in Sec. 8.2.2 and Sec. 8.2.3, and we shall return to the conclusions obtained from these studies below. Before that point, however, we shall discuss how, on a more general level, the conclusion obtained in the present work for the electronic state of bulk Si Cu_i, i.e., that Cu *(i)* donates its 4*s* electron to the surroundings with *(ii)* the 3*d* shell remaining closed, gives reason to expect a certain level of scatter in the energetically most favourable location of this impurity as obtained in various theoretical studies, a conclusion which might explain the large structural differences between the optimized bulk Si Cu_i configurations reported up to now in the literature.

On the basis of the results of our studies of bulk Si Cu_i, we would argue that the position of Cu in the Si cage is determined by a competition between *(i)* the Pauli repulsion involving the Cu 3*d* states and the surrounding Si environment (trying to keep Cu at the center of the cage where the wave function overlap is minimal) and *(ii)* the polarization of the Si environment (trying to move Cu away from the T site towards the region where the number of nearest neighbour Si atoms is optimized). In other words, Cu is not kept tightly at the center of the Si cage (or, in other words, the energy contours in the region around the T site should vary only weakly), with a movement of Cu away from its actual preferred position being triggered fairly easily if one of the above effects is described incorrectly.

The above described considerations seem to be supported by the VASP calculations of the present work, both within the GGA and the LDA (see Sec. 8.2.2): if an approximation is used (see Sec. 8.2.1 for details) where a chosen set of the plane wave components from the full set of relevant components for evaluating the total energy contributions are excluded from the studies (with the exclusion starting from the highest magnitude of the reciprocal lattice vector for the complete set, see Sec. 8.2.1 for details), a slight T site instability with a scatter in the Cu-Si distances of 0.03 - 0.04 Å is generated (as opposed to the converged results, where the scatter in these distances is less than 0.01 Å). As we expect the inclusion of the plane wave components ignored in this approach to be associated to a large extent with the description of the Cu 3*d* states, we regard the above results as a suggestion that an accurate description of these states is of significant importance to getting the structural parameters right for bulk Si Cu_i. [13]

In addition to these results, also in the Plato studies, Cu off-center movements, of $\sim$ 0.1 Å, were found to be triggered if the precision in calculations was insufficient. In this case, the movement was related to the real-space grid used in calculations for evaluation of e.g. overlap integrals being too coarse. Once again, we believe that this points towards the description of the Cu 3*d* orbitals being of crucial importance to obtaining the correct position for Cu_i in bulk Si, as these comparatively steeper orbitals should be affected more strongly by the use of a coarse grid in calculations. Finally, we note that, for the Plato studies with the DN/DNP basis set, the variation in the formation energy for Cu around the T site was found to be much weaker than the result obtained with the DNP basis set (see Sec. 8.2.3), a conclusion which might also be valid for the SIESTA studies of Ref. [56], i.e., a Cu off-center movement being comparatively more easily triggered at low precision for this situation.

5.2.5 CONVERGENCE IN THE FORMATION ENERGY OF INTERSTITIAL Cu IN BULK Si WITH RESPECT TO CELL DIMENSION

On the basis of the investigations into the electronic structure of bulk Si Cu_i as obtained in VASP and Plato based studies within the LDA decribed in Sec. 5.2.4 we concluded that *(i)* Cu donates its 4*s* electron to the surroundings and *(ii)* the 4*s* state is quite diffuse, extending over the entire cell. In other words, we must expect from these studies that the formation energy of the impurity is not fully converged at the 64 atom cell level: with reference to the general considerations in Sec. 2.3 for the description of an isolated defect within the supercell approximation, the overlap between the Cu 4*s* wave functions for impurities in adjacent cells evidently is not negligible (see Sec. 5.2.4.2 for details).

In the studies of the cell size convergence to be described below, we have focussed on this Cu 4*s* level dispersion as the main cause of the remaining error in the formation energy of bulk Si Cu_i. We emphasize that rigorous tests of alternative remaining errors

[13] We emphasize that we are not attempting here to understand in detail this erroneous description of bulk Si Cu_i, this issue being seemingly complex with *(i)* the structural parameters for the optimized configuration depending on the location of the T site in the cell for the Si 64 atom supercell studies (see Sec. 8.2.2) and *(ii)* the scatter essentially being removed, without a change of the precision, if a Si 216 atom cell is used (see Sec. 5.2.3). Only, we do not regard any of these additional results as contradicting the above remarks.

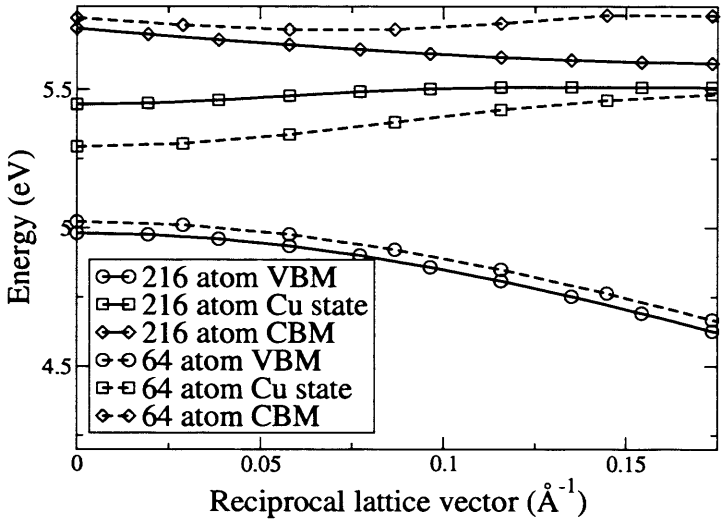

Figure 5.5: Energy bands along [100] for the systems with Cu_i in a Si 64 and 216 atom cell as obtained in the VASP studies. For clarity, only the highest (lowest) Si valence (conduction) band and the Cu 4*s* band have been plotted. The dotted (solid) lines are the results for the 64 (216) atom cells. VBM (CBM) is shorthand notation for valence band maximum (conduction band minimum) while the Cu 4*s* band is labelled 'Cu state'.

have involved only elastic errors, which were found to be almost negligible at the 64 atom cell level in Sec. 5.2.3. As for the disturbance of the Si lattice electronic structure by the Cu impurity, the above suggestion has been based on weaker statements from the discussion in Sec. 5.2.4.2, with, in particular, Fig. 5.3 showing that the screening of the Cu_i^+ ion by the Si lattice is strongly confined to the Si cage atoms and their bonds with the Si atoms from the surrounding lattice. The movement of Cu from a position very near the T site to the exact site upon the increase of the cell size beyond the Si 64 atom cell level, described in Sec. 5.2.3, could very well be a sign of electrostatic errors being nonnegligible for this cell. On the other hand, this movement is quite small (a few hundredths of an Å) and associated with only a very weak energy change as the energy contours around the T site are found to be quite shallow (see Sec. 8.2.2 and Sec. 8.2.3 for related comments). For this reason, we regard the present approach as justifiable.

We have studied the cell size convergence for bulk Si Cu_i through comparison of the formation energies and the band structure along the [100] direction in the supercell (which includes the conduction band minimum [CBM] for clean Si) as obtained in calculations with Cu in *(i)* a Si 64 and *(ii)* a Si 216 atom cell [14] using VASP within the

[14]This approach follows the generally recommended strategy for investigating cell size convergence, where the separation between all adatoms is increased equally.

GGA. For these studies, a plane wave energy cutoff of 233.7 eV and a 0.1 eV width for the Gaussian smearing was chosen, with the calculations on the smaller cell employing a (3, 3, 3) k mesh producing the same k-point density in reciprocal space as obtained with the (2, 2, 2) k mesh used for the larger cell. [15]

The results of these studies are shown in Fig. 5.5. We find that the dispersion of the Cu 4s level is almost eliminated at the 216 atom cell level, strongly suggesting, along with the remarks made previously in this discussion, that an almost fully converged bulk Si Cu_i configuration with regards to the choice of cell dimension has been obtained for this choice of cell. According to the 216 Si atom cell result, the Si band gap is ~ 0.7 eV (clearly lower than the experimental value of 1.1 eV), slightly increased with the insertion of the Cu atom in the cell, with the Cu 4s level located in the range 0.1 - 0.2 eV below the conduction band minimum. We shall comment further on these issues in Sec. 5.5.

[15] With this choice of precision, the structural parameters for Cu in the Si 64 atom cell were slightly different from what has been described in Sec. 5.2.3, but essentially the same conclusion about the structural differences for this system and Cu in the Si 216 atom cell still applies. The studies involved Cu_i^0 only, justified by the conclusions in Sec. 5.2.3 and Sec. 5.2.4.2 for the comparability of the results obtained for bulk Si Cu_i^+ and bulk Si Cu_i^0 at the Si 64 atom cell level.

5.3 Cu OUTDIFFUSION TO THE CLEAN Si(001) SURFACE

5.3.1 INTRODUCTION

5.3.1.1 A SURVEY OF PREVIOUS WORK ON Cu OUTDIFFUSION OF INTEREST TO THE CURRENT STUDIES

Shabani *et al.* [71] were the first group to report complete Cu outdiffusion to the Si(001) surface. In these experiments, various known levels of Cu contamination were introduced in *p*-Si (B-doping) and *n*-Si (P-doping) samples by spin coating, with the samples subsequently heated at 1175 K for 2 h in a furnace under N ambient and cooled partly in the furnace and partly in air. Careful investigations of the Cu distribution throughout the whole sample were performed using total X-ray fluorescence (TXRF, for surface analysis) and graphite furnace atomic absorption spectroscopy (GF-AAS, for bulk analysis). [16] These studies revealed a very homogeneous distribution of Cu in Si for both samples, in accordance with the high diffusivity of this impurity, but for the *n*-Si samples, only 40% of the Cu was recovered in the analysis. The authors suggested that the rest of the Cu was trapped as some Cu_m-P_n compound. More recently, Istratov and Weber discussed [73, 48] enhanced Cu precipitation in *n*-Si as an explanation to this observation. We shall provide the general details of this suggestion below.

Cu RT outdiffusion to the Si(001) surface was triggered for the *p*-Si samples by the removal of the oxide layer grown during cooling: TXRF measurements of the Cu surface concentration immediately after oxide layer removal revealed no detectable amounts of Cu at the surface, regardless of the amount of time elapsed since the cooling process. When the oxide layer was no longer present, however, Cu was found to diffuse gradually to the surface over the order of days, until, after 10 days, close to the entire amount of Cu introduced initially in the sample was detected at the front and back surface of the wafer. If the *p*-Si samples were heated upon removal of the oxide layer, the outdiffusion process was increased dramatically, with more than 90% of the Cu recovered at the wafer surfaces within 1 h for heating at 675 K. In this experiment, a temperature gradient was present over the sample and the authors argued that this might explain the observation that almost 80% of the outdiffused Cu was recovered at the cooler side of the wafer. Finally, additional experiments on air cooled samples revealed that annealing at 675 K could drive Cu towards the surface even if the oxide layer was still present.

In comparison with the *p*-Si samples, *n*-Si showed a very different behaviour: Cu did not diffuse to the surface at RT when the oxide layer was removed and detectable Cu outdiffusion required heating of the sample to at least 475 - 575 K. These observations supported the suggestion made previously by the authors of Ref. [71] that some trapping mechanism was present for this sample.

[16] TXRF measurements also produced some information on the Cu concentration in the sample before the deliberate contamination, with the concentration on the back surface being $\sim 10^9$ cm^{-2} for all samples, more than two orders of magnitude below the lowest level of Cu surface concentration at the front of the sample at the onset of the experiments.

Flink *et al.* [72] investigated the dependence of Cu outdiffusion and precipitation on Cu concentration for *p*-Si (B-doping) by trapping Cu in the interstitial state, as measured using the transient ion drift (TID) technique, through quenching. A correlation of the choice of reaction path with acceptor concentration was reported: the guideline established was that the critical Cu contamination for Cu silicide formation, measured by X-ray fluoresence (XRF), was equal to the acceptor concentration plus $\sim 10^{16}$ cm^{-3}. The authors explained this observation on the basis of the electrically amphoteric nature of the Cu silicides in *p*-Si: these extented defects have been reported [111, 112, 47] to introduce bandlike states in the upper half of the Si band gap. Consequently, they will change their charge state from positive to negative if the Cu contamination level is sufficiently high relative to the dopant concentration to raise the Fermi level ϵ_F above the Cu_3Si band energies. As Cu_i is a shallow donor in Si, the positively charged Cu silicide will repel diffusing Cu ions, the onset of Cu precipitation in *p*-Si therefore evidently requiring Cu contamination levels above the dopant concentration. The authors of Ref. [72] went beyond these general arguments, verifying, in strong support of the above conclusion for the influence on Cu disilicides on the chosen Cu reaction path in *p*-Si, that the observed critical Cu contamination for Cu silicide formation correlated very well with ϵ_F being increased beyond the Cu silicide band energies of $\sim \epsilon_C$-0.2 eV (ϵ_C being the Si conduction band minimum) reported in previous experimental studies [111].

The results of Ref. [72] appear to clarify the essential details of the Cu reaction paths in *p*-Si. [17] Furthermore, when combined with the results of the experiments of Ref. [71] they strongly support the Si(001) surface as the most prominent trapping mechanism for Cu in Si, for Cu contamination levels well below the dopant concentration where the results of Ref. [71] apply: while a supersaturated population of Cu_i can not be created during cooling in air according to the results of Ref. [72], the results of Ref. [71] show that the trapping of Cu that consequently must occur for this situation is only temporary, with the entire amount of Cu still diffusing to the Si(001) surface upon removal of the surface oxide. As discussed in Sec. 4.1.1, this result is expected to be a consequence of the high diffusivity of Cu in Si and the barrier to Cu silicide formation for sufficiently low Cu contamination levels.

The above arguments, on the other hand, do not provide information on the detailed mechanism of the Cu outdiffusion, this issue still being debated in the literature (see Ref. [48] for a list of references). While it is beyond the scope of this study to discuss these investigations on a general level, we shall comment in the following on recent experimental studies of the behaviour of Cu at the SiO_2/Si interface, as these investigations have direct connection with the above mentioned studies by Shabani *et al.* [71]. The influence on the growing oxide on the Cu outdiffusion in the experiments of Ref. [71] was not investigated by the authors of this paper, but it was regarded as more likely that Cu was trapped at the SiO_2/Si interface than moving into the oxide. Experimental studies into this issue by Hozawa *et al.* [113, 114] have suggested, how-

[17] For *n*-Si, there is no repulsion between growing Cu silicide and diffusing Cu. Consequently, as noted by Istratov and Weber in Ref. [48], Cu should be much more likely to precipitate in *n*-Si, this fact offering a possible explanation to e.g. the differences in the behaviour of Cu in *n*-Si and *p*-Si reported by Shabani *et al.* in Ref. [71].

ever, that this statement holds true only for SiO_2 films beyond a certain thickness: for film widths of 30 Å or less, including the typical width of a thermally grown oxide when cooling a Si sample in air upon annealing in UHV conditions, Cu would diffuse through the oxide to the surface of the wafer, while for films of higher thickness, annealing the sample would repel Cu from the SiO_2/Si interface region. We shall briefly return to this issue when discussing the results of our theoretical studies of Cu outdiffusion to the clean Si(001) surface in Sec. 5.3.2.3.

5.3.1.2 INTRODUCTION TO OUR WORK

In our theoretical studies of Cu outdiffusion to the Si(001) surface we have focussed our attention on the conceptually most simple situation where the surface is clean Si(001), primarily as modelling of a thermally grown oxide on this surface is both very demanding with respect to the structural parameters for this system and the size of the unit cell which has to be used for a realistic system to be described. On a general level, the clean Si(001) surface is also expected to be a stable sink for diffusing impurities in clean defect-free Si, but the influence of the oxide on the Cu outdiffusion behaviour clearly should not be entirely neglected, especially considering the larger amount of experimental information present for this situation (see Sec. 5.3.1.1). We shall therefore briefly discuss our results in this context in Sec. 5.3.2.3.

The present section is organized as follows: in Sec. 5.3.2.1, we shall present the results of our total energy calculations on the Cu_i near surface configurations, showing, through comparison with the formation energy obtained for bulk Si Cu_i in Sec. 5.2.3 within the same theoretical framework, that Cu shows a strong preference to move towards the clean Si(001) surface. On the basis of investigations into *(i)* the structural parameters for the Si environment for Cu near the surface and *(ii)* the electronic state of the impurity for these configurations, we shall argue in Sec. 5.3.2.2 that the main reason for the attraction of Cu to the Si(001) surface is asymmetries for the Si cages introduced by the oscillating strain due to the surface reconstruction. The trapping of Cu at the surface is explained by Cu-Si bond formation involving the Cu 4*s* electron and the Si surface dangling bonds. This in turn suggests that the clean Si(001) surface is an extremely efficient sink for diffusing Cu, the impurity being trapped essentially within a few Si layers from the surface. In Sec. 5.3.2.3 we shall discuss the results of our studies in a broader context, considering convergence issues, more subtle simplifications in the theoretical modelling, and (at a very preliminary stage) the application to the more complex situation where the surface is not clean but covered by a thermally grown oxide film. In particular, we shall clarifying through theoretical studies that the results described in Sec. 5.3.2.1 and Sec. 5.3.2.2 apply to truly isolated Cu at the clean Si(001) surface.

5.3.2 THEORETICAL SUPPORT FOR COMPLETE Cu OUTDIFFUSION TO THE CLEAN Si(001) SURFACE

5.3.2.1 VARIATION IN THE FORMATION ENERGY OF CONFIGURATIONS WITH INTERSTITIAL Cu NEAR THE CLEAN Si(001) SURFACE

We have investigated theoretically the mechanism of Cu outdiffusion to clean Si(001) by calculating the formation energies for a series of Cu_i configurations with the impurity within a few layers of the surface using VASP and a surface slab geometry described in Sec. 8.1 for the modelling of the system. [18] A brief description of the computational details in our studies, in particular the chosen values for the parameters in the code, has been provided below. For a full discussion of this issue as well as an introduction to nomenclature used in the following discussion, we refer to Sec. 8.2 and Sec. 8.2.4. The focus of our studies has been entirely on Cu_i as Cu has been reported [52, 53] to almost exclusively diffuse interstitially in moderately doped Si. [19] Furthermore, we have aimed at describing only the behaviour of isolated Cu near the Si(001) surface, comparing the energies for the configurations described below with the formation energy of isolated Cu_i in bulk Si as calculated in Sec. 5.2.3 in order to investigate the stability of the Si(001) surface as a sink for diffusing Cu. In the initial stages of this discussion, we shall not be concerned with the investigation of the convergence of the formation energies with respect to cell dimension which follows naturally from the specified aim of the present study. Only, we state from the outset that the general conclusions described below also apply to the situation of truly isolated Cu, with Sec. 5.3.2.3 clarifying on this issue.

The formation energies relative to the bulk Si Cu_i energy for the complete set of configurations investigated, obtained using a Si 10 layer SC slab (see Sec. 8.1.2), have been included in Table 5.5 while the energies are shown in Fig. 5.6. Calculations were performed using Vanderbilt US PPs [17] as implemented in VASP [23, 24], with both the LDA and the PW91 GGA [12] to E_{xc}. For both studies, a plane wave energy cutoff of 233.7 eV, Gaussian smearing with a width of 0.1 eV, and a (6, 6, 1) Monkhorst-Pack k mesh was chosen. We shall discuss in Sec. 5.3.2.3 the importance of this choice of precision in calculations on the results obtained. For the bulk Si Cu_i energy we used a result obtained for Cu in a 64 Si atom cell, obtained with the same of choice of values for the variable parameters in the code and a (3, 3, 3) k mesh. [20]

[18] We note, at the outset of the discussion, that the present study includes only subsurface configurations, whereas a truly complete study of the behaviour of Cu at clean Si(001) would involve also investigations into the energies for configurations with Cu *on* this surface. We shall deal with the study of the complete set of relevant configurations for outdiffused Cu at Si(001) in Sec. 5.4.

[19] In addition, we have studied only the interstitial Cu atom, Cu_i^0, rather than both Cu_i^+ and Cu_i^0 as in Sec. 5.2. We shall discuss the importance of this simplification when evaluating the results of our studies in Sec. 5.3.2.3.

[20] Considering the expected lack of convergence of the formation energies of Table 5.5 with respect to cell dimension (to be confirmed in Sec. 8.2.4), we found it misleading to use the more well converged energy obtained for Cu in a 216 atom cell for bulk Si Cu_i for the evaluation of the energy changes for Cu moving towards the Si(001) surface. On the other hand, the choice of both cell and k mesh for bulk Si Cu_i is not to be interpreted as ensuring comparability between the bulk and near surface energies in Table 5.5. In particular, the (3, 3, 3) k mesh was chosen 'for simplicity', in order to consider only the effects of changes in the cell

Table 5.5: Formation energies for configurations with Cu_i near the Si(001) surface, relative to the energy of bulk Si Cu_i, as obtained in calculations on a Si 10 layer SC slab using VASP. The names of the configurations have been explained in Sec. 8.2.4. For clarity, approximate values for the Cu depth in the slab are specified through reference to the Si layer which is approximately at level with the Cu atom in question. For the HF(Dimer) configuration, as shown in Fig. 8.8, Cu moves to a position approximately at the center of the hexagonal face between adjacent faces, i..e, approximately between two Si layers, explaining the half integral number in the table below. The Cu_i near surface energies are shown in Fig. 5.6.

Configuration	Cu depth / Si layer - 1	E_{GGA}/ eV/atom	E_{LDA}/ eV/atom
DT	1	-0.99	-0.95
HF(Dimer)	1.5	-0.92	-0.90
T_1(D)	2	-0.71	-0.67
T_2	3	-0.42	-0.40
T_3(Dimer)	4	-0.35	-0.36
T_3(Trench)	4	-0.29	-0.25
T_4(Dimer)	5	-0.28	-0.26
T_4(Trench)	5	-0.22	-0.22
T_5(D)	6	-0.11	-0.10
T_5(U)	6	-0.10	-0.11
Bulk Si Cu_i	∞	0	0

The key reason for performing both LDA and GGA based calculations for the studies of outdiffusing Cu is related to the fact that the topic under investigation concerns the state of Cu in bulk Si as well as (practically) at the surface of the crystal, with the conclusions about the properties of the Si(001) surface as a sink for diffusing Cu obtained on the basis of a comparison of the energies in these two regions. In other words, this investigation spans a region of clearly different crystal environments for Cu, where a single approximation to E_{xc} might fail to produce reliable results throughout the entire range. As the LDA results in Table 5.5 display a variation only very slightly different from the GGA results, we regard this study as a confirmation that the above described problem is of no relevance to the present discussion. Furthermore, for the same reason, we have performed no detailed investigations into the LDA results but focus entirely on the structural parameters and electronic structure of the Cu_i near surface configurations as obtained using the GGA in remaining discussions, unless otherwise noted. [21]

The formation energies of the configurations with isolated Cu_i near the Si(001) surface show a rapid monotonic increase with Cu depth in the slab: the energy of

dimension on the bulk Si Cu_iin the convergence discussions described in Sec. 8.2.4. For a brief presentation of more well converged relative energies, we refer to Sec. 5.3.2.3.

[21] In particular, we have performed no calculations at higher precision for the Cu_i near surface configurations within the LDA, assuming, on the basis of the results in Table 5.5 that changes in the energies very similar to those obtained for the GGA studies, as described in Sec. 5.3.2.3, would occur.

configuration T_2, only three layers from the Si surface dimers, is more than halfway towards the energy of the bulk Si Cu_i configurations, compared to the DT (outermost Cu_i near surface) configuration, strongly suggesting (along with the magnitude of the energy differences obtained) that Cu prefers to reside within a few layers of the Si(001) surface. Fig. 5.6 provides a perhaps more illuminating view of the results obtained, showing very clearly a separation of the formation energies for Cu_i near the Si(001) surface into two regions: when Cu is three layers or more from the Si surface dimers, the energy variation is still relatively weak, showing a gradual decay towards the value for bulk Si Cu_i. [22] We define this region as the 'attraction region' as it has the effect of moving diffusing Cu towards the surface. The actual trapping of Cu only occurs when the impurity is within two layers of the Si surface dimers, the formation energy showing a sudden strong decay as Cu moves from the last configuration in the trapping region, the T_2 configuration, to the adjacent Si 'cage' one level closer to the surface (T_1(D) configuration). We shall refer to this region as the 'trapping region' in the discussions below. We shall discuss the significance of these two regions in Sec. 5.3.2.2 when investigating the electronic state of Cu for the various Cu_i near surface configurations.

5.3.2.2 STUDIES OF THE IONIC AND ELECTRONIC STRUCTURE FOR CONFIGURATIONS WITH INTERSTITIAL Cu NEAR THE CLEAN Si(001) SURFACE

In order to clarify the reasons for Cu outdiffusion to the Si(001) surface we have investigated *(i)* the structural parameters for the Si cages surrounding the various subsurface Cu T sites in the study before and after insertion of the Cu atom and *(ii)* the electronic state of the Cu atom for the different configurations. Below we argue that the outdiffusion involves two steps: firstly, the asymmetric Si cages near the clean Si(001) surface act as a shallow sink for diffusing Cu. Secondly, the actual trapping of Cu at the surface is explained by Cu-Si surface dimer bond formation.

The behaviour of interstitial Cu in bulk Si was investigated in detail in Sec. 5.2. We found that Cu stays at the T site upon optimization with the surrounding cage expanding slightly, the distance between any given pair of adjacent Si atoms in this structure increasing from 2.351 Å to 2.387 Å for the almost truly isolated Cu atom in a 216 Si atom cell. This behaviour is consistent with Cu being a shallow donor: the 4*s* electron is donated to the Si lattice and the resulting closed 3*d* shell Cu_i^+ ion is a tiny charged ball with a radius of $\sim$ 0.7 - 0.8 Å which interacts with its surroundings through Pauli repulsion and polarization of the Si environment.

Compared to the situation for bulk Si, the cages near the Si(001) surface are slightly distorted due to oscillating strain introduced by the surface reconstruction: a scatter in the distances between adjacent Si atoms comprising the cage is introduced. For the cages of interest in this study, distances in the range 2.335 - 2.388 Å are obtained. As these cages are smaller than the bulk Si cage upon insertion of the Cu atom, we conclude that Cu insertion in a near surface cage will still cause expansion of this cage.

[22] We shall consider the decay in more detail in Sec. 5.3.2.3 when discussing the convergence with respect to cell dimension of the formation energies for Cu_i near the Si(001) surface.

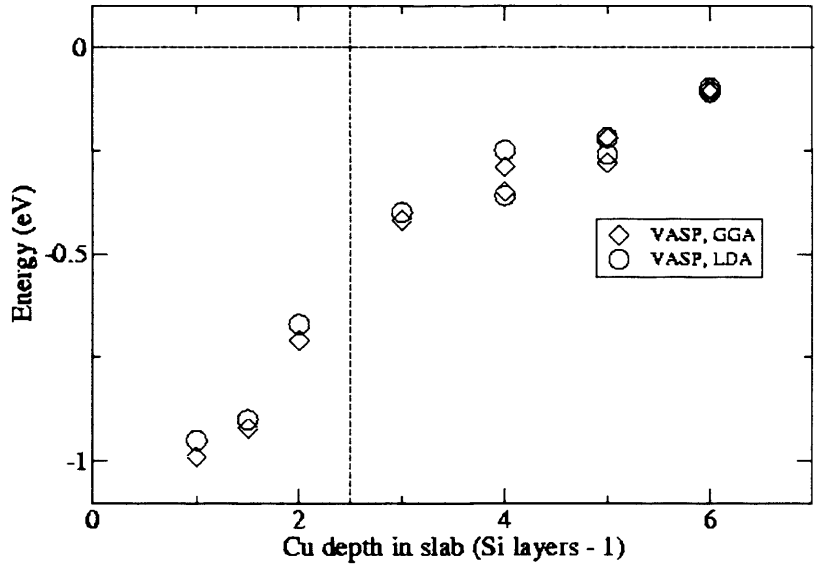

Figure 5.6: Calculated formation energies, relative to bulk Si Cu_i, for the interstitial Cu_i near surface configurations investigated in the present work using VASP. The dashed vertical line in the figure specifies the borderline between the trapping region (Cu within three Si layers of the surface) and attraction region (Cu deeper in the slab) discussed in the text. The dashed horizontal line in the figure specifies the bulk Si Cu_i energy. The close overall similarity between the LDA and GGA results is evident.

Upon optimization of the T_2 and T_3 configurations, Cu moves away from the (approximate) T site by up to 0.2 Å. In all cases this movement is towards the region where the cage has expanded the most before the Cu insertion. Examination of the orbital angular momentum (*s*-, *p*-, *d*-) and site projected character of the wavefunctions for these configurations (described in more detail for bulk Si Cu_i in Sec. 5.2.4) does not reveal any significant changes to the chemistry of Cu in Si compared to the situation for the bulk Si Cu_i configuration: the Cu movements for these configurations are explained by the same mechanisms of interaction that apply for Cu_i in bulk Si.

If we imagined the cage surrounding the bulk Si interstitial Cu atom to be slightly distorted before insertion of the Cu atom, we would indeed expect Cu to move away from the T site and roughly in the direction where the cage had expanded the most, as *(i)* the original T site would no longer correspond to the position where the overlap of the Cu 3*d* shell with the Si wavefunctions was reduced to a minimum and *(ii)* the polarization of the Si environment in conjunction with the relaxations of the Si lattice

due to a Cu off-center movement would tend to drive Cu towards the location where the number of nearest neighbours (NNs) was most easily optimized, i.e., the largest hexagonal face of the cage. As the Cu atom remains at the T site for the bulk Si Cu_i configuration we expect the first of these mechanisms to dominate in the case of the relatively small distortions of the cage (expansion still required upon Cu insertion) encountered near the Si(001) surface. [23]

The main reason for the near surface Cu_i configurations being lower in energy than the bulk Si Cu_i configuration does not appear to be related to a change in the size of the Si cage before Cu insertion or to an increased expansion of the cage upon Cu insertion. [24] The values for the size of the relevant Si cages before Cu insertion have been tabulated in Table 5.6. The size of the cage surrounding the T_3(Dimer) site is 2.352 Å, whereas the values for the cages surrounding the T_2 and T_3(Trench) sites are clearly larger, 2.367 and 2.370 Å, respectively. However, a corresponding difference is not observed between the energies of these configurations (see Table 5.5). The increase in the expansion of the cage upon Cu insertion as Cu moves from the bulk to the near surface region comes close to 20%, but *(i)* this amounts to only a few thousandths of an Å (the expansion of the Si cage for bulk Si Cu_i being 0.036 Å) and *(ii)* there is hardly any variation in this parameter for the Cu_i near surface configurations. [25] These results do not exclude a change in the elasticity of the Si lattice near the Si(001) surface as a way of attracting diffusing Cu_i to this region but it seems unlikely that this is the main reason for the attraction.

In comparison with the expansion of the Si cage due to Cu insertion, the asymmetry of the cage, defined as the rms value for the scatter in the Si-Si distances for the cage before Cu insertion, shows a monotonic (with the T_3(Dimer) configuration as the only, not highly critical, exception) and clearly larger increase as Cu moves towards the surface (see Table 5.6). We therefore conclude that diffusing Cu_i will show a preference to be located near the Si(001) surface for the ideal undoped Si crystal primarily because of an initial asymmetry of the Si cages in this region rather than a change in the elasticity of the Si lattice near the surface. For the near surface configurations, Cu moves towards the region of the cage which has expanded before Cu insertion: as the Si-Si

[23] We have not included the T_4 and T_5 configurations in the above discussion: the distortion of the Si cages before Cu insertion in these cases are so small that the predicted Cu movements are comparable to Cu off-center movements caused by interactions of adjacent Cu atoms, an effect observed previously in our studies of bulk Si Cu_i (see Sec. 8.2.2).

[24] We measure the size of the Si cage (before and after insertion of Cu) by the rms value for the set of Si-Si distances with both atoms belonging to the group comprising the cage.

[25] We have not included the values for the expansion of the Si cages in Table 5.6 as these numbers are related to relaxations of the Si lattice in response to the Cu insertion for two different supercells (bulk, near surface) and convergence with respect to cell size has not been obtained for the Cu_i near surface configurations in the calculations with the Si 10 layer SC slab: this affects the relative difference between near surface and bulk values greatly as all cage expansions are fairly small. A practically converged value for the cage expansion (used for the 20% estimate above) has been obtained for the T_2 configuration in a calculation using a Si 8 layer slab with surface dimensions 15.36 × 15.36 $Å^2$ (see Sec. 8.2.4): this value is only 0.004 Å above the value of 0.038 Å obtained for the same configuration in a calculation with a Si 8 (and 10) layer SC slab. The values for the cage expansion obtained for the Cu_i near surface configurations in the calculations with the Si 10 layer SC slab vary between 0.035 and 0.038 Å.

Table 5.6: Size and asymmetry (see text for details) before Cu insertion for Si cages surrounding the bulk Si T site and various T sites near the Si(001) surface as obtained in the calculations on a Si 10 layer SC slab using VASP and the PW91 GGA to E_{xc}. The near surface sites have been sorted by the formation energy with Cu_i at the site, see Table 5.5.

Site	Size of the Si cage / Å	Asymmetry of Si cage / Å
T_2	2.367	0.020
T_3(Dimer)	2.352	0.012
T_3(Trench)	2.370	0.014
T_4(Dimer)	2.361	0.011
T_4(Trench)	2.359	0.011
T_5(D)	2.360	0.007
T_5(U)	2.360	0.008
Bulk Si	2.351	0

bonds in this region are already stretched, the further increase in these bond lengths required by the presence of the Cu atom are associated with smaller energy changes than observed in bulk Si. We propose this as the main reason for the near surface Cu_i configurations being lower in energy compared to the bulk Si Cu_i configuration. This suggestion accounts for the lowering of the formation energies for the T_2 configuration and all configurations with Cu deeper in the slab (but so close to the surface that the Si cage assymetries due to the surface reconstruction are nonnegligible) relative to bulk Si Cu_i. [26]

When Cu_i moves within two layers of the Si surface dimers (configurations T_1(D), HF(Dimer), and DT), the formation energy decreases rapidly compared to the variation obtained with Cu deeper in the slab (see Table 5.5). Studies of the wave function characters for these configurations reveal that the Cu 3*d* level energies are still hardly changed compared to the situation for Cu_i in bulk Si. The electronic structure near the Fermi energy ε_F is clearly altered but interpretation of the data in this energy range is more difficult. Some tendencies are clear, however: *(i)* the last occupied band is no longer primarily *s* character within the sphere surrounding the Cu atom and *(ii)* this band has moved down in the band gap compared to the Cu_i near surface configurations with Cu deeper in the slab. These results suggest that a Cu-Si bond involving the Cu 4*s* electron has been formed for these configurations.

Charge density plots confirm that Cu-Si bonds are formed for Cu in the trapping region. For the T_1(D) configuration, a weak redistribution of the Si surface dimer charge with accumulation between the Si(D) atom and Cu is observed: compared to the charge density at the center of the Si dimer bond for clean Si(001) (0.55 eV/Å^3), the charge density at the center of the Si dimer and Cu-Si bonds for the T_1(D) configuration have the fractional values 0.96 and 0.63, respectively. The charge redistribution is far

[26] These arguments provide an explanation only to the lowering of the formation energy for Cu in the attraction region. For considerations of the full implications of the above result to the Si(001) surface as a sink for diffusing Cu, i.e., the ability of this sink to attract Cu from the bulk region, we refer to Sec. 5.3.2.3.

more evident for the HF(Dimer) configuration, the corresponding fractional charge density values here being 0.81 and 0.72 (Cu-Si(U)), 0.66 (Cu-Si(D)). The influence of the dangling bonds at the Si(001) surface on Cu for this configuration is also very apparent when one considers structural parameters: Cu does not stay at the T_1(U) site but moves to the hexagonal face between the T_1(U) and DT sites. As this movement corresponds to (part of) the expected diffusion path for Cu in Si, we would expect this structural change for Cu_i in bulk Si to increase the formation energy by almost 0.18 eV, the experimentally reported diffusion barrier for this impurity [50]. The HF(Dimer) configuration, however, is lower in energy compared to the T_1(D) configuration by 0.21 eV, suggesting the presence of a strong Cu-Si bond.

For the DT configuration, significant charge redistribution is obtained as well, along with a large local structural distortion of the Si lattice in response to the Cu atom insertion (explained by the fact that the Si cage surrounding the DT site is clearly smaller than other Si cages). We will not specify any details for this configuration here as the structural parameters change considerably when the cell dimensions are increased in the directions parallel to the surface (see Sec. 5.4.2).

5.3.2.3 A MORE COMPLETE DISCUSSION OF DIFFUSION OF INTERSTITIAL Cu TO THE CLEAN Si(001) SURFACE

While the studies described in Sec. 5.3.2.1 and Sec. 5.3.2.2 have provided us with a great deal of information on the mechanism of the Cu outdiffusion to the Si(001) surface and the detailed properties of this surface as a sink for the diffusing impurity, our chosen approach to investigating this topic also has clear limitations, some of which need to be addressed in order to arrive at a satisfying answer to the question of the behaviour of isolated Cu_i near Si(001): up to now, we have deliberately kept the considerations as simple as possible, partly in order to highlight the main features of our conclusions from the outset but also as a recognition of the fact that we are currently unable to improve the modelling of the larger part of the set of configurations tabulated in Table 5.5 by increasing the cell dimensions in our studies. The discussions of the convergence of the Cu_i near surface formation energies with respect to cell size, while being of considerable importance to the conclusions of the present work (see below), therefore are somewhat challenging and were considered likely to take the focus away from the key conclusions of the actual studies. We have included these considerations in Sec. 8.2.4 but shall discuss the results of the investigations below, when summarizing the conclusions obtained from our theoretical studies of the Si(001) surface as a sink for isolated Cu_i.

Another simplification in our studies concerns the choice of precision in calculations, described in Sec. 5.3.2.1. On the face of it, when comparing with the convergence considerations described for Cu_i in bulk Si in Sec. 8.2.2, we would not expect significant changes in the energies of the Cu_i near surface configurations upon increasing the precision further in our studies (with k mesh convergence being an issue that should be investigated independently). This conclusion, however, is too simplistic as it can presumably be justified only for the configurations with Cu in the attraction region, where the electronic state of the impurity is highly similar to the situation for bulk Si Cu_i. For Cu_i in the trapping region, the electronic state of Cu is changed considerably, with the

formation of an actual Cu-Si bond involving the Cu 4*s* electron and a Si surface dimer: for this situation, on a general level, new convergence studies are required in order to clarify whether the conclusions from Sec. 8.2.2 still apply.

In addition to the above described basic convergence considerations involving the selected system under investigation, the choice of system itself also brings up various issues to be addressed: our theoretical studies have involved the attraction of a diffusing Cu *atom* to the *clean* Si(001) surface in *undoped* Si, with the energies evaluated at *zero* temperature, with all the emphasized terms in the above being potential approximations to the situation for experimentally observed Cu outdiffusion. Destroying the mechanisms of the Cu-Si bond formation by performing calculations on Cu_i^+ or by terminating the dangling bonds at the Si surface through reaction of some overlayer material with the substrate evidently must destroy the trapping region, with only a comparatively weak interaction of Cu to Si(001), depending on the level of cage asymmetries induced by the surface reconstruction in question. In other words, our theoretical studies of Cu outdiffusion to Si(001) neither support trapping of Cu ions at the clean surface nor trapping of Cu at a surface where the dangling bonds are no longer present (unless, perhaps, the lattice distortions near the surface have been considerable increased, see Sec. 5.4.3). It is beyond the scope of this work to discuss these highly relevant issues in full detail here, although we shall make brief comments below on the expected behaviour of Cu at the SiO_2/Si interface on the basis of our studies. We shall clarify below, however, upon discussing the fully converged theoretical results for isolated Cu_i^0 at the clean Si(001), why we do not regard the approximations of an undoped Si sample and zero temperature in calculations as critically affecting the conclusions obtained.

In order to explore theoretically a sufficiently wide range of configurations with Cu_i near the Si(001) surface for the properties of this surface as a sink for diffusing Cu to be fully revealed, we have made the choice, as mentioned in Sec. 5.3.2.1, to perform studies using a Si 10 layer SC slab. As shown in Fig. 5.6, these studies have revealed both *(i)* the long range nature of the mechanism attracting Cu to the surface and *(ii)* the short range of the actual trapping mechanism. We have concluded that the Cu outdiffusion to the Si(001) surface is explained by *(i)* a long range attraction due to surface reconstruction induced asymmetry of the Si cages and *(ii)* Cu-Si bond formation due to the presence of dangling bonds at this surface. However, in order to show that the well defined separation of these two regions in terms of formation energy differences suggested on the basis of these calculations is justifiable, i.e., that the Cu-Si bond formation can actually be regarded as almost solely responsible for the trapping of Cu at the Si(001) surface, we must consider the effect of the choice of surface dimensions on the formation energies for configurations from both regions. Evidently, the supercell used in our studies is too small for the impurity to be regarded as isolated, the separation between adjacent Cu atoms being only 7.68 Å. Our primary concern, however, is not whether increasing the cell dimensions along the surface directions will significantly change the configuration formation energies. Rather, in order to truly verify that Si(001) is a highly efficient sink for an isolated interstitially diffusing Cu atom in the sense described at the end of Sec. 5.3.2.1, we must require knowledge on whether the formation energies in the attraction and trapping regions defined in Sec. 5.3.2 are af-

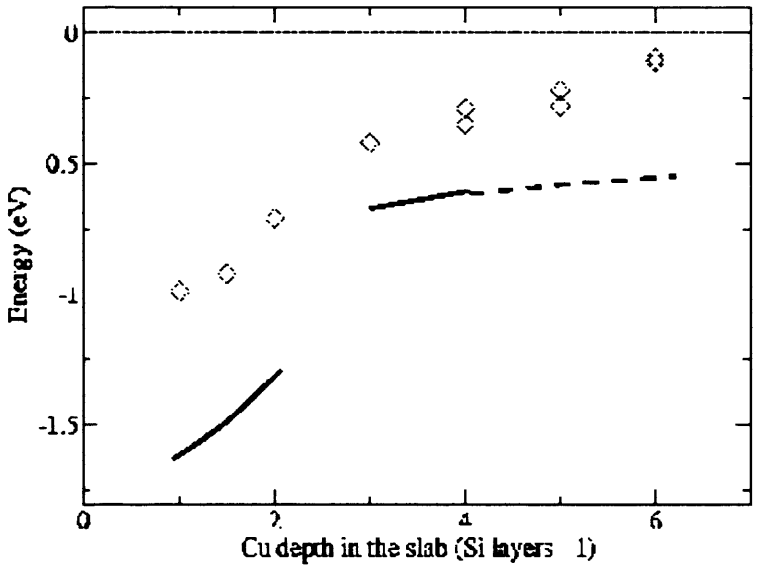

Figure 5.7: Same as in Fig. 5.6 but including only the GGA results of this previous figure. The solid lines represent estimated (see text for details) converged formation energies for the isolated Cu_i near surface configurations as obtained on the basis of the calculations described in Sec. 8.2.4, with the dashed curve emphasizing the extrapolation of the energy variation in this region (where no calculations were actually performed).

fected differently by these changes. In addition, as emphasized at the beginning of this discussion, independent convergence studies with regards to the variable parameters in the code are needed for the configurations with Cu_i in the trapping region.

The investigations into the above described issues have been presented in detail in Sec. 8.2.4 and we shall only summarize in the following the results obtained from these calculations. [27] The studies, performed using VASP within the GGA only (we shall discuss potential limitations in this approach below), have been performed in two stages: firstly, we have obtained practically converged formation energies for all configurations with Cu_i in the trapping region as well as the T_2 configuration (the only

[27] The considerations below in the text will focus only on isolated Cu_i near the Si(001) surface, in accordance with the aim of our studies, presented in Sec. 5.3.2.1. Alternatively, we might use the results obtained with the SC slab to discuss what happens when the Cu concentration near the surface is increased. We shall comment briefly on this issue in Sec. 5.5.

configuration with Cu_i in the attraction region for which such a vastly improved study has been rigorously performed), with fairly precise estimated energies obtained for the T_3 configurations. Secondly, we have performed static calculations for the configurations with Cu_i in the trapping region, increasing the plane wave energy cutoff to 292.2 eV and using the recommended grid for this cutoff value, with the precision in these calculations otherwise being the same as described in Sec. 5.3.2.1. [28] While the cell convergence studies should be practically complete, the studies into the convergence of the total energies with respect to the variable parameters in the code for the above described set of configurations are to be regarded as preliminary, although, as will be discussed below, we do not expect further studies to have a critical effect on the conclusions to be described in the following.

Fig. 5.7 describes the main conclusions obtained, with the very schematic presentation emphasizing that further studies are needed in order to provide rigorous answers to the behaviour of Cu_i in both the attraction and trapping region, discussed in the following. For Cu_i in the attraction region, the studies of Sec. 8.2.4 suggested that the fully converged T_3 configuration energies are lowered relative to the fully converged energy for the T_2 configuration by ~ 0.06 eV. This relatively small energy correction should be compared with the highly similar energy difference of 0.10 eV for the T_2 and T_3 configurations (mean value) obtained on the basis of the calculations performed using the 10 layer SC slab in Sec. 5.3.2.1. In other words, while the initial investigations into Cu outdiffusion to the Si(001) surface performed in the present work within the GGA suggested that the energies for Cu_i in the attraction region would reach the bulk Si Cu_i energy already for Cu within 10 Si layers of the surface (see Fig. 5.7), the calculations of Sec. 8.2.4 suggest a much slower variation for the energies in this region, i.e., a much more long range attraction mechanism, possibly several tens of Si layers. [29] This is a highly important conclusion as it establishes the clean Si(001) surface as a true stable sink for diffusing Cu, with an attraction region that drags the impurity towards the surface from a significant distance into the bulk crystal.

In order to discuss the efficiency of the attraction of Cu_i to the clean Si(001) surface in acceptable detail, we need to address the issue of the energy barrier to diffusion of the impurity between the various T sites for the configurations in this region. A rigorous discussion of this issue evidently would require calculations of the barriers to diffusion of Cu between adjacent sites. Some knowledge can be obtained already, however, from the observations that *(i)* the electronic state of Cu is hardly changed for the Cu_i near

[28] Also, k mesh convergence studies were performed for a selected configuration in the attraction and trapping regions, these calculations suggesting that the convergence had almost been obtained using the (6, 6, 6) k mesh.

[29] As results have been obtained only for the T_2 and T_3 configurations, the schematic curve describing the formation energies for Cu_i near surface configurations in the attraction region in Fig. 5.7 involves extrapolation from only two points: for this reason, we can not justifiably draw any conclusions regarding to depth of Cu in the Si slab where the energy gain relative to bulk Si Cu_i has become truly negligible. The small decay in the energy variation as Cu moves deeper into the slab is justified by the decreasing importance of the Si(001) surface reconstruction on the structural parameters for the Si cage surrounding Cu, i.e., the decreasing strength of the mechanism of the attraction of Cu to the Si(001) surface. The rapid movement of the Cu_i near surface energies towards the bulk Si Cu_i energy obtained with Cu 4 layers or move from the Si(001) surface in the 10 layer SC slab calculations is completely disregarded when drawing the above mentioned curve, as this energy change is believed to be explained by the rapidly increasing importance of confinement effects for Cu moving close to the bottom of slab (see Sec. 8.2.4 for related comments).

surface configurations of Table 5.6 compared to the bulk Si Cu_i configuration and *(ii)* the Si cages for these configurations are only weakly distorted. Both points support the conclusion that the diffusion barriers are very similar to the barrier in bulk Si which has been studied both experimentally [50] and theoretically [57, 59]. All these studies have suggested a very small barrier height, with the most recent theoretical value obtained by Shirai *et al.* [59], obtained within a theoretical framework fairly similar to the VASP LDA studies of this work, being 0.32 eV (see Sec. 5.2.1.1 for details).

We suggest, on the basis of these remarks, that *(i)* the theoretical value for the energy barrier to Cu diffusion in the attraction region would be $\sim$ 0.3 eV according to VASP studies within the GGA and, more importantly, *(ii)* note that with the the difference in formation energies between Cu at adjacent T sites in this region region always being within $\sim$ 0.05 eV (and typically considerably smaller) according to our studies, we find that the Cu RT diffusion coefficient even within a few layers of the Si(001) surface has decreased by no more than a factor of $\sim$ 7 . In other words, the above considerations suggest that Cu is still rapidly diffusing in the attraction region and thus, in summary, dragged very easily towards the clean Si(001) surface where the actual trapping takes place.

The remaining energy differences in Fig. 5.7 between the solid curve and the set of Cu_i near surface configuration energies as obtained with the 10 layer SC have two explanations: *(i)* as discussed in detail in Sec. 8.2.4, the cell convergence studies (calculations performed using an energy cutoff of 234 eV) revealed a very similar lowering in the formation energies of all configurations investigated, by $\sim$ 0.15 eV relative to the energy of bulk Si Cu_i in a 216 Si atom cell (where cell convergence has also practically been reached, see Sec. 5.2.5). Furthermore, however, *(ii)* for Cu_i in the trapping region, the calculations of Sec. 8.2.4 suggested a dramatic lowering, $\sim$ 0.4 eV, in the formation energies upon the increase in the precision in calculations described previously in this discussion (whereas the energies for Cu in the attraction region remained practically unchanged, as expected from the similarities with bulk Si Cu_i for these configurations). We shall not go into details with a discussion of these energy changes as further convergence studies are evidently needed in order to arrive at truly well established values for the energy differences between the configurations with Cu_i in the trapping and attraction regions. Only, we note here that the preliminary convergence studies performed in the present work further support the clean Si(001) surface as a highly efficient sink for diffusing Cu, with an energy gain of more than 1 eV (including the energy barrier to diffusion of Cu between adjacent T sites and using here for simplicity the value of 0.3 eV introduced previously) for Cu moving from the attraction region to the trapping region. Not only does the well defined separation of these two regions in terms of their energy, suggested initially in Sec. 5.3.2.1, remain valid when discussing truly isolated Cu_i at the Si(001) surface at the level of convergence with respect to the variable parameters in the code: the binding energy of the impurity to the trapping region, i.e., within only three layers of the surface, is greatly enhanced.

As mentioned previously in this discussion, we do not believe that the approximations of an undoped Si lattice and zero temperature, employed in the present studies, are of crucial importance to the above described conclusions for the behaviour of Cu_i

at the clean Si(001) surface. The experimental investigations of Cu outdiffusion to Si(001) discussed in Sec. 5.3.1.1 involved *p*-Si, but as the key differences between the behaviour of supersaturated Cu_i in *p*-Si and *n*-Si appear to be explained by changes in the relative importance of the predominant reaction paths (see Sec. 5.3.1.1 for details), we believe that the only issue that we need to take into account in order to verify whether our studies apply to a clean Si(001) surface for moderately doped *p*-Si is the surface band bending discussed already by Flink *et al.* in Ref. [72]. Theoretical modelling into this issue, described briefly by the authors of this paper, suggested that this effect can be taken into account by introducing a repulsive surface potential of ~ 0.05 - 0.1 eV. The influence of this surface potential on the energies in Fig. 5.7 evidently will be small, with the basic conclusions described in the above discussion essentially unchanged.

When an oxide film is grown on the Si(001) surface through cooling of a Si sample in air as in the experiments of Ref. [71], the dangling bonds at the surface are saturated [115]: this removes the reason for Cu trapping at what is now the SiO_2/Si interface, but with the experimental studies by Hozawa *et al.* [113, 114] clearly suggesting that Cu outdiffusion to the surface of the oxide occurs. While we can not go into great detail with this issue on the basis of our studies of Cu outdiffusion to clean Si(001), we note that our explanation for the mechanism of attraction of diffusing Cu to the surface region also appears to apply to the situation where the surface is not clean but covered by a thermally grown oxide: while the structure of the SiO_2/Si interface is still a matter of debate (see references cited in Ref. [115]), very recent theoretical studies by Bongiorno *et al.* [115] strongly suggest, in contrast with previous models (also discussed in that paper), that the interface strain is actually larger than the strain due to reconstruction of the clean Si(001) surface. In other words, thermal growth of a surface oxide film should not destroy the attraction of Cu to Si(001), but rather make it more pronounced.

5.4 Cu AT THE Si(001) SURFACE: CHARACTERIZATION AND MANIPULATION

5.4.1 INTRODUCTION

5.4.1.1 A SURVEY OF PREVIOUS WORK ON Cu AT THE Si(001) SURFACE OF INTEREST TO THE CURRENT STUDIES

Experimental observations suggest that the presence of Cu at the Si(001) surface is associated with the appearance of a $c(8 \times 8)$ surface reconstruction, with apparent contradictions between different results likely to be explained by the fact that only trace amounts of Cu (a few % of a ML) appear to be needed in order to induce formation of this reconstruction. Barbier and Lapujuolade [116] reported a reproducible $c(8 \times 8)$ surface reconstruction of Si(001), as evidenced with thermal energy atom scattering (TEAS), for a clean Si sample in a Cu contaminated UHV chamber upon Ar bombardment cleaning, annealing at 1075 K, and slow cooling to RT. Examination of the near surface constituents with secondary ion mass spectroscopy (SIMS) and X-ray fluorescence (XRF) revealed Cu contamination of the sample: an upper limit of 0.08 ML of Cu on the Si(001) surface was obtained. Upon careful cleaning of the entire equipment, the $c(8 \times 8)$ surface reconstruction was not observed as the experiment was repeated.

More recently, Murray *et al.* [117] reported the $c(8 \times 8)$ reconstruction, using low energy electron diffraction (LEED), upon annealing at 1325 K for a Si sample that once again was shown with SIMS to be Cu contaminated (with no estimations for the amount of Cu at the surface given in this reference). [30] Furthermore, Auger electron spectroscopy (AES) was found to be an insufficient method to reveal this amount of Cu. Hu *et al.* [118] and Kubo *et al.* [119] have reported the $c(8 \times 8)$ reconstruction for a clean Si(001) surface. However, in none of these situations was the surface examined with SIMS. Rather, for the experiments of Ref. [118] (Ref. [119]), AES (electron energy loss spectroscopy [EELS] and thermal desorption spectroscopy [TDS]) was used.

Other experiments have involved deposition of Cu on the Si(001) surface [120, 121, 122, 123, 124]. In the early experiments, [120, 121, 122] several ML of Cu was deposited and various surface reconstructions reported, depending on not only Cu coverage but also annealing and cooling. The first detailed studies of submonolayer deposition of Cu on Si(001), as investigated with STM, were performed by Liu *et al.* [123]. The optimal results for the growth of a $c(8 \times 8)$ surface reconstruction were obtained if Cu was either deposited on the surface at 825 K, with subsequent quenching, or if the surface was annealed at this temperature upon RT deposition.

At very low (below 0.1 ML) Cu coverages, chains of bright features running perpendicular to the Si dimer row direction on the underlying terrace were observed. Each feature was typically found to consist of three bright protrusions along the chain direction, with adjacent features separated by a dark region with the width (along the chain direction) of one dimer row. At Cu coverages only slightly above 0.1 ML, ordering

[30] For these experiments, the surface was also investigated with STM, with the results of these investigations to be discussed further below.

of the chains lead to the appearance of the $c(8 \times 8)$ reconstruction, with the STM images collected for this situation being highly similar to the results obtained in previous experiments by Murray *et al.* [117].

In both the experiments of Ref. [117] and Ref. [123], vacancy defect lines, running perpendicular to the Si dimer row direction, were also observed with STM. The authors speculated that these lines should be attributed either to the presence of Cu [123] or Ni [117] at the surface. More recent experimental studies by Baker *et al.* [124] for a deliberately Cu contaminated Si(001) surface reported chain formation and correlation leading to the $c(8 \times 8)$ reconstruction as described in Ref. [123], but with no mention of the presence of vacancy defect lines on this surface.

As we have performed no theoretical modelling into the $c(8\times8)$ surface reconstruction related features in the present work, we shall describe the details of this surface structure only briefly in the following. Very similar structural models for the $c(8 \times 8)$ reconstruction were suggested by Murray *et al.* [117] and Liu *et al.* [123] on the basis of STM filled and empty state images in the respective experiments: the three protrusions in each (2×8) unit for the reconstruction were explained as either three (Ref. [123]) or five (Ref. [117]) dimers (either Si or Cu) deposited on top of the Si(001) surface, with the Si dimer bonds for the underlying the rows broken at this location. Both models agreed on the dark regions being explained by two Si dimer vacancies along the dimer row. The experiments of Baker *et al.* [124], however, clearly revealed that the dark regions contained four vacancies. [31] The authors of Ref. [124] also reported that subsequent H termination of the Si surface did not destroy the (2×8) units. As previous theoretical studies [125] have suggested that the Si-H bond is much stronger than the Si-Cu bond, the resistance of the islands to H termination strongly supports the suggestion that these islands are comprised by Si rather than Cu.

Liu *et al.* [123] found that there was an almost one-to-one correspondence between the amount of deposited Cu and the amount of atoms in the (2×8) building blocks (within their assumption that each building block contained six atoms). In the experiments by Baker *et al.* [124], the (2×8) building block coverage for a given amount of deposited Cu was clearly below that observed in Ref. [123] (compare Fig. 1 (b) in Ref. [123] and Fig. 1 (a) in Ref. [124]). This might be explained by the fact that the experiments of Ref. [124] involved a somewhat higher growth temperature of 870 K: Liu *et al.* reported in Ref. [123] that the (2×8) building block coverage for a given amount of deposited Cu would start decreasing at temperatures above 875 K, perhaps with the authors speculating that this change was to be explained by Cu diffusion into the sample. Recent experimental studies [126] of the Cu transport along Si(001) in the

[31] On the basis of the information in Ref. [124], the unit for the chains can not, strictly speaking, be described as (2×8) (although we shall keep using this notation for simplicity in the remaining discussion below in the text). We nevertheless speculate that the chain formation, i.e., the initial stages of the formation of the $c(8 \times 8)$ surface reconstruction, might be associated with the experimental TEAS results by Barbier and Lapujuolade [116], where often, in addition to the $c(8 \times 8)$ surface reconstruction of Si(001), a (2×8) surface reconstruction (triggered by quenching) was reported. On the other hand, neither in Ref. [123] nor in Ref. [117] were any comments made on the presence of a (2×8) pattern as obtained with LEED, making it evident that a connection between the (2×8) surface reconstruction as reported in Ref. [116] and the chains of protrusions reported in Ref. [123] can not be fully established at the present level of experimental observation on the Cu contaminated Si(001) surface.

Figure 5.8: Experimental STM image showing chain segments of (2×8) units (one of these units enclosed by the dotted box in the top figure) as well as other assumed Cu related structures (marked by arrows in the top figure) on the Si(001) surface, as obtained upon deposition of ~ 1.2 ML of Cu on this surface. The bottom figure is a close up of part of the area in the top figure, focussing on the structure highlighted by the uppermost arrow in this figure. See text for further details. The images are filled state, with the reported bias voltage in the range 2-3 V. *Image courtesy of L. A. Baker, A. R. Laracuente, and L. J. Whitman.*

temperature range 775 - 925 K, performed using Auger electron spectroscopy (AES) and low energy electron diffraction (LEED), have supported this suggestion, with the reported diffusion path involving Cu moving into the bulk.

In addition to the (2×8) units, the experiments by Baker *et al.* in Ref. [124] revealed previously unnoticed isolated structures that have been associated with a very small number of Cu atoms at the Si(001) surface by the authors: the structure discussed in Ref. [124] consists of a pair of round protrusions, as obtained for a filled state STM image with a bias voltage in the range 2-3 V, clearly smaller than the typical Si dimer protrusion, centered on the middle of the dimer row but offset with respect to the positions of dimers in adjacent rows by half a dimer (see Fig. 5.8). [32] The authors associ-

[32] The authors of Ref. [124] did not distinguish between the two structures marked with arrows in the upper part of Fig. 5.8. These structures, however, appear to be significantly different: the structure at the lower arrow has four pairs of protrusions alligned in the direction perpendicular to the dimer row but the distance between the first and the last pair equals the distance between two (rather than three) dimer rows, making it

ated the protrusions with Cu_i at the surface, but did not suggest any detailed structural model for the observed feature. Comparison [33] of the filled state STM images for the (2×8) units observed in Refs. [117, 123, 124] suggests a higher image resolution in the experiments of Ref. [124]. We speculate, on the basis of this conclusion, that the structure shown in the bottom part of Fig. 5.8 remained unnoticed in the experiments of Refs. [117, 123] even though it might actually have been present as well on the surface in these cases.

5.4.1.2 INTRODUCTION TO OUR WORK

While the theoretical studies performed in Sec. 5.2 and Sec. 5.3 involved a relatively narrow focus (clarifying the electronic state of bulk Si Cu_i and explaining the Cu outdiffusion to clean Si(001), respectively), the discussions in the present section describe the preliminary investigations into the much broader topic emerging from the results of the studies of Sec. 5.3: Cu trapping and manipulation at the Si(001) surface. We shall discuss our view on the potential prospects for this issue in Sec. 5.4.3 (and in more general detail in Sec. 5.5 where we summarize and conclude on the results obtained in our studies of Cu-Si interactions), where we present initial studies into the energies for Cu_i at the Haiku structure under Bi nanolines on the Si(001) surface, this system being our selected candidate in the present work for a nanostructure used for Cu trapping in highly localized region at the surface. For discussions of the results obtained, we refer to Sec. 5.4.3.

Before that point, in Sec. 5.4.2, we shall discuss Cu on the clean Si(001) surface. At a very basic level, this study is to be regarded essentially as a completion of the Cu outdiffusion studies described in Sec. 5.3. The key motivation for these additional investigations, however, is the opportunity thus obtained for comparing the full set of local minimum energy configurations for outdiffused Cu at Si(001) with experimental investigations for Cu at this surface (see Sec. 5.4.1.1). We refer to Sec. 5.4.2.1 for a detailed discussion into this issue. We shall identify in Sec. 5.4.2.2 the set of local minimum energy configurations with Cu on the Si(001) surface, discussing, at a preliminary level, the reasons for discrepancies between the predictions as obtained within the GGA and the LDA for the energies of the full set of local minimum energy configurations for outdiffused isolated Cu_i at Si(001). In Sec. 5.4.2.3, we shall compare theoretical STM images obtained for these configurations with the experimental results of Fig. 5.8, establishing justifiable connections, to be fully investigated in future theoretical and experimental studies, between most of these configurations and experimentally observed structures on the Si(001) surface.

---

clear that this structure is not comprised by four pairs of protrusions on top of Si dimer rows. We have not discussed the larger of these structures further in the present work.

[33] For all experiments, reasonably comparable filled state images are available: the STM images in Fig. 4 of Ref. [123] and Fig. 3 of Ref. [117] were collected at a bias voltage of 2.5 and 2 V, respectively.

5.4.2 ISOLATED Cu ATOMS AND Cu PAIRS ON THE Si(001) SURFACE

5.4.2.1 REASONS FOR STUDYING Cu ON THE Si(001) SURFACE: COMPLETION OF THE STUDY OF Cu OUTDIFFUSION TO Si(001)

The theoretical studies of Cu outdiffusion to the clean Si(001) surface performed in Sec. 5.3 revealed that Cu is trapped (for sufficiently low temperatures, see Sec. 5.3.2.3 for a discussion) within a few layers of the surface, where Cu-Si bond formation involving the Si surface dimers and the Cu 4*s* electron occurs. These studies involved only subsurface Cu, however, thus producing no information about the existence of energetically favourable configurations with Cu *on* the surface: in order to *(i)* complete the outdiffusion study and *(ii)* compare these theoretical results with the experimental results for Cu at Si(001) described in Sec. 5.4.1.1, we need to investigate the energies for isolated Cu on the Si(001) surface.

Restricting our studies to isolated Cu at Si(001), following the same approach as described for the studies of Cu outdiffusion to Si(001) in Sec. 5.3, means that the bulk of the experimental results presented in Sec. 5.4.1.1, i.e., everything concerning the (2×8) units on this surface, represents effectively issues beyond the scope of the modelling to be described later in this discussion. Part of the reason for this choice of simplification of the present theoretical studies is the general challenge in identifying a surface reconstruction where so little is known, at the time of writing, about the connection with Cu at this surface. In addition, even a theoretical study of the $c(8 \times 8)$ reconstruction itself, this system being the smallest in terms of modelling issues (with relatively well isolated (2×8) units or chains of such units requiring considerably larger cells), involves working on a unit cell so large that studies within a different and less time-consuming theoretical framework would seem preferable.

We have decided not to move down the above described path in the present work, i.e, we are not aiming at explaining theoretically in the following the full set of Cu induced structures on the Si(001) surface. Rather, the goal of our studies is to clarify whether the assumed Cu related structure reported in recent experimental studies by Baker *et al.* [124], which appears to be connected to a very low number of Cu atoms (two atoms, presumably, according to the authors of Ref. [124]) on the surface, can be explained by the results of our Cu/Si(001) structural optimization studies, with the candidates for this structure including also, at the outset of the discussion, the Cu_i subsurface configurations in the trapping region obtained in Sec. 5.3.2.1. [34] The conclusions obtained from this study will thus serve, potentially, as an investigation into the reliability of not only the studies to be described in the following but also the conclusions obtained for Cu outdiffusion to Si(001) in Sec. 5.3.

The discussion of Cu at the clean Si(001) surface will proceed as follows: in Sec. 5.4.2.2 we shall describe the energy contours for isolated Cu on the Si(001) surface as obtained in calculations within the GGA (see Sec. 5.4.2.2 for further computational

[34] In addition to this structure, we shall discuss another candidate for a Cu related structure on Si(001), visible in Fig. 5.8 but not discussed by the authors of Ref. [124]. We refer to Sec. 5.4.2.3 for further details on this issue.

details) using a SC and a LC 6 layer Si slab, with this nomenclature explained (and the details of the slab geometries discussed) in Sec. 8.1. As discussed in Sec. 8.2.4, the chosen slab contains a sufficiently large number of Si layers for the energies of the subsurface Cu_i configurations with Cu in the trapping region to be practically converged. [35] Following the above described initial studies, we shall compare fully optimized energies for the configurations with trapped Cu at Si(001) as obtained within both the LDA and GGA (assuming in this approach, on the basis of our interpretations of the calculated energy contours, that the LDA results will resemble closely the GGA results in the sense that the set of local minimum energy regions will be identical). For reasons to be discussed at that stage, these results are to be considered as preliminary, with more to be learned about both *(i)* the electronic structure Cu on the Si(001) surface and *(ii)* the reasons for the differences between the conclusions obtained. With these remarks in the back of our mind, we shall describe in Sec. 5.4.2.3 the results obtained upon comparing theoretical STM images and total energies for the Cu/Si(001) configurations as obtained within the GGA with the experimental results obtained by Baker *et al.* [124] for the structure shown in the bottom part of Fig. 5.8, with these studies involving also structural optimization of configurations with Cu pairs on the Si(001) surface. The promising results obtained from this comparison act as a considerable support for the GGA results being the more reliable ones.

5.4.2.2 LOCAL MINIMUM ENERGY CONFIGURATIONS FOR Cu TRAPPED AT THE Si(001) SURFACE

The study of the Cu/Si(001) surface energy contours was done in two steps: first, the barriers to Cu surface diffusion on Si(001) as well as the local minimum energy regions for the isolated Cu atom on this surface were estimated by construction of an energy contour plot using the SC and the LC slab (with a single Cu atom in these cells, this corresponds to a coverage of 1/4 and 1/16 of a ML respectively). [36] Subsequently, local minimum energy configurations were obtained by performing complete optimizations, starting from configurations at the local energy minima estimated from the contour plot

[35] The DT configuration, as noted in Sec. 8.2.4, represents the single example where convergence is not clear: as will be discussed briefly below in the text, large structural relaxations involving Si atoms two layers from the surface layer are obtained for Cu at the DT site when using cells where the Cu separation has been increased along the Si dimer row direction, compared to the outdiffusion studies of Sec. 5.3. As elastic errors are present also along the dimer row direction for the largest cells used in our studies, we have not investigated the convergence in the DT configuration energy with respect to the number of layers in the slab further, concluding only that the energy evidently is not fully converged with respect to the choice of cell dimension even at this level. For the local minimum energy configurations with Cu on the Si(001) surface obtained in Sec. 5.4.2.2, additional studies (not discussed in the text) revealed that acceptable convergence in the energies and structural parameters with respect to the number of layers in the slab has been obtained at the 6 layer slab level.

[36] We do not suggest comparing these values for the Cu coverage on the Si(001) surface with the experimental coverages discussed in Sec. 5.4.1.1: as *(i)* we focus on only some of the potentially Cu related structures on this surface in our studies and as *(ii)* these structures appear to be relatively well isolated in the experiments of Ref. [124], we should be aiming at studying (locally) isolated Cu configurations on the surface, with the values for the theoretical Cu coverages representing, basically, how well we are able to meet this target.

results. [37]

Calculations were performed using Vanderbilt US PPs [17] as implemented in VASP [23, 24] with the PW91 GGA [12] to E_{xc}. We chose the same precision in these studies as described in Sec. 5.3 for the investigation of Cu outdiffusion to Si(001), using a plane wave energy cutoff value of 233.7 eV, a (6, 6, 1) MP k mesh, and a width of 0.1 eV for the chosen Gaussian smearing scheme (see Sec. 8.2.4 for further details). In addition, however, we performed static calculations for the entire set of optimized configurations considered in the present discussion, increasing in these studies the plane wave energy cutoff value of 292.2 eV and using the recommended grid for this energy cutoff. Our reason for performing these studies was the considerable changes in the formation energies encountered upon such a change in precision for the configurations with Cu_i in the trapping region (see Sec. 5.3.2.3): we wanted to clarify whether similar energy changes would be obtained for the configurations with Cu on the Si(001) surface. These studies produced the same energy changes, within 0.01 eV, for the configurations with Cu on the surface, thus causing hardly any changes of the relative energies of the configurations for trapped Cu at the clean Si(001) surface. As we shall make no reference to the energies of these configurations relative to the energy of bulk Si Cu_i below, the high precision studies will not be discussed further in the following: although it should be kept in mind that rigorous convergence with respect to the variable parameters in the code is yet to be fully investigated, we have found no warning signs from our preliminary studies into this issue that the GGA based conclusions to be described below are importantly affected by these remaining convergence studies.

For the construction of the Cu/Si(001) energy contour plot, calculations need only be performed in the area between two adjacent Si dimers in a dimer row, and (in the direction perpendicular to the dimer rows) between the center of the dimer and the center of one of the trenches next to the dimer row (the dark plus light grey area in Fig. 5.9). We decided to perform calculations in an area with only half the length in the direction along the dimer rows (i.e., the darker area in Fig. 5.9), ignoring the possible influence of Si dimer buckling inversion initially and checking the importance of this effect subsequently in cases where the initial results did not seem clearcut. With the chosen Si lattice constant of 5.43 Å (see Sec. 8.2.2 for comments), the area of the contour plot region is 3.84×1.92 Å^2.

As the contour plot results were meant to be only semi-quantitative, we chose a relatively coarse grid of equidistantly spaced points (0.96 Å in the directions parallel and perpendicular to the dimer row, giving a total of 15 [3×5] points in the contour plot region) as the basis for the contour plot construction. These points specify the Cu x and y coordinates considered in the study. In optimizations, these coordinates were kept fixed while all other coordinates were varied.

[37] Cu dimerization on the Si(001) surface was also investigated, partly inspired by the suggested link between Cu dimers and the $c(8 \times 8)$ surface reconstruction by Liu and Nogami in Ref. [123] (questioned in more recent studies by Baker *et al.* [124]). These investigations, performed using the SC slab and involving a total of 6 Cu dimer configurations with the Cu-Cu bond center located over the Pedestal, Hollow, Dimer Bridge, and Cave sites (using conventional nomenclature), did not suggest that Cu dimerization was energetically favourable and we therefore have made no comments on this issue in the bulk text.

From a general point of view, the LC Cu/Si(001) energy contour plot is considered more reliable than the SC result in the context of an isolated Cu adatom: more relaxations of the Si(001) surface in response to the Cu atom can be included with the larger cell. A comparison of the results suggested, however, that most of the contours are well described with the SC: with the exception of the trench between dimer rows, the changes in the energies relative to clean Si(001) are within $\sim$ 0.1 eV/Cu atom. Most of the differences in the energies for Cu in the trench as obtained with these two cells are explained by the following considerations (with reference to the calculations of this work): with a Cu atom in every trench (SC) and for distances between the impurity and the Si dimer atoms sufficiently short for an appreciable interaction to occur, [38] the dimer bonds will be stretched significantly and a Cu-Si chain will form. On the other hand, for the situation where only every second trench is occupied by a Cu atom (LC), either *(i)* a translation of the Si dimers towards the impurity (creation of a chain segment) or *(ii)* a movement of Cu towards one of the dimers will occur. The grid used for obtaining the LC energy contour plot was too coarse to reveal in full detail the behaviour of Cu in this region, but they correctly specify the chain segment formation as being energetically unfavourable, with further studies (not to be discussed in detail in the present work) revealing that the completely optimized configuration with an isolated Cu atom in the trench between Si dimers is lower in energy (by 0.11 eV/atom) also when compared to the Si-Cu chain. [39] We therefore focus on the LC results below.

The LC energy contours are shown in Fig. 5.9. We find that a barrier of $\sim$ 0.4 eV (height relative to the minimum energy [ME] region with the lowest energies) separates two ME regions, one of them centered around the configuration with Cu in the trench between the dimer rows (trench ME region) and the other centered on the dimer row between Si dimers (dimer ME region). The dimer ME region in fact contains two local minima: *(i)* a configuration with Cu between the centers of the Si dimers (referred to as the pedestal [P] configuration in the following, using conventional nomenclature) and *(ii)* a configuration with Cu at the side of the dimer row, approximately above a second layer Si atom (referred to as the interdimer bridge [IDB] configuration below). These two minima are separated by a barrier of $\sim$ 0.1 eV. The estimated 0.4 eV barrier is the fundamental barrier to Cu diffusion on Si(001): the maximum energy configuration along the minimum energy path for Cu movement along either direction on this surface is located on the minimum energy path connecting the dimer and trench ME regions. This result, which is unaffected if local ME configurations are substituted for local ME regions in the above, suggests that there are no strong restrictions to Cu mobility on the Si(001) surface at RT (we shall discuss Cu diffusion in the complete trapping region in more detail below).

Some of the features described in Fig. 5.9 can be readily explained on the basis of the information gathered for Cu_i in Si in the previous theoretical studies of this work, introducing only a single, but rather essential, difference: the presence of dangling bonds for the Si(001) surface atoms. While for Cu at the T site deep in the Si crystal the overlap of the Cu $3d$ and surrounding Si wavefunctions was the cause of an ex-

[38] Only this situation, of real relevance to the present studies, was considered.

[39] This conclusion is supported by the fact that no Cu-Si chain formation has been reported in experimental studies of Cu on Si(001).

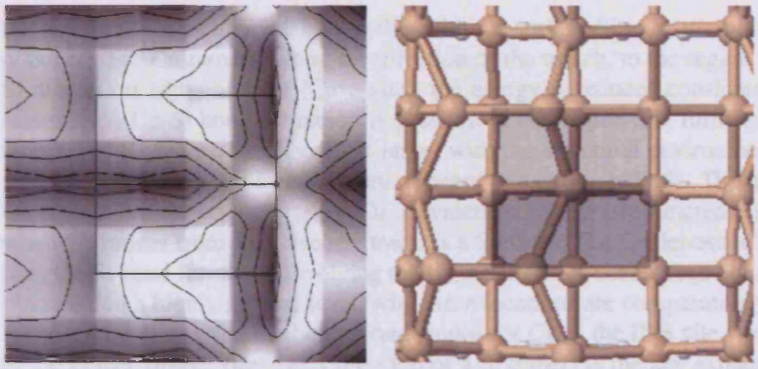

Figure 5.9: Calculated total energy contours (left figure) for the set of configurations with a single Cu atom on the Si(001) $p(2\times2)$ surface as obtained using VASP within the GGA. Calculations were performed with a 6 layer LC slab (see Sec. 8.1 for a description), i.e., the Cu coverage was 1/16 of a ML. The minimum energy regions are the dark regions in the figure. The contour lines are spaced 0.18 eV apart and the difference between the maximum and minimum energies is 0.9 eV. The right figure shows a schematic description of the clean Si(001): the Si atoms are the light brown spheres while the white spheres are the H atoms in the termination layer for the slab. The two rectangular areas in the two figures (see text for a discussion) refer to the same area on the surface.

pansion of the cage, due to Pauli repulsion (see e.g. Sec. 5.2.4.3), for Cu on the clean Si(001) surface, an appreciable overlap between the Cu 3*d* electron wavefunctions and a sufficiently high number of dangling bonds would be expected, on a general level, to potentially lead to Cu-Si bond formation involving the Cu 3*d* states. While we have not discussed the electronic state of Cu for the Cu/Si(001) surface in great detail in the present work, we shall present strong support for such Cu 3*d* - Si 3*sp* hybrization in Sec. 5.4.2.3. For the time being, for clarity in the discussion below, we shall use these results, making cross-references whenever needed, in order to explain the main features of the energy contours for isolated Cu on the Si(001) surface. We believe that these very general considerations to be presented in the following apply to a description of Cu on the Si(001) surface within the LDA as well as the GGA, in the sense that we regard it as justified to conclude that the minimum energy regions for Cu on Si(001) are conceptually the same for these two theoretical descriptions of the system. This, essentially, is our justification for assuming, without actually calculating the energy contours using the LDA, that the set of Cu/Si(001) local ME configurations to be discussed below within both the LDA and the GGA are conceptually the same. [40]

Our discussion of these energy contours starts with Cu near the Hollow site in the trench between dimer rows, i.e., with the same distance to four Si dimers. For this configuration, energies are comparatively high as a consequence of the impurity be-

[40] As will be discussed below, this argument does not apply to the differences between the energies of the Cu/Si(001) local ME configurations, the LDA and GGA studies producing significantly different results.

ing too small for an appreciable overlap with the surface Si atom wavefunctions to be obtained. For Cu moving along the direction of the trench, to the region between two Si dimers on adjacent rows (Cave site), the energy is reduced considerably, for two reasons: *(i)* Cu-Si bond formation is possible in this region and furthermore, *(ii)* the number of Si nearest neighbours is large, with the structural environment highly resembling the hexagonal face between adjacent Si cages in bulk Si. The importance of the high coordination number for Cu is evidenced by the steep increase in the energy when Cu moves from the Cave site towards a Si dimer. For Cu deposited on the dimer row, Cu-Si bond formation involving the Cu $3d$ electrons occurs (see Sec. 5.4.2.3), explaining, on a highly general level, why these locations are comparatively favourable. Finally, we believe that the better bond angles for Cu at the IDB site when compared to the Dimer Bridge site (i.e., Cu on top of a Si dimer) is the key explanation for the relatively large energy difference (of more than 0.2 eV within the GGA) between these configurations shown in Fig. 5.9: for the IDB configuration, Si dimer buckling inversion occurs, resulting in two Si 'Up' atoms on the side of the dimer row where the Cu atom is present. This structural change has the effect of moving Cu away from the surface, i.e., reducing the coordination number, while also moving charge to the region near the adatom, and we therefore regard it as clearly reflecting the comparative importance of Cu-Si bond formation for Cu at the IDB site.

Complete optimization, performed within the GGA, of configurations with Cu located approximately at positions corresponding to minimum energy in the local ME regions discussed previously reveals that the P and IDB configurations as described above in the text remain almost unchanged, whereas for the configuration with Cu at the estimated center of the trench ME region, a movement towards one or the other hexagonal faces at the side of this trench is preferred. This effect, which is not revealed in the contour plot calculations for reasons described previously, is a strong indication that the Cu-Si bond formation involves only the Cu $4s$ electron, with the Cu $3d$ shell remaining closed for these configurations: bond formation with both Si dimer atoms on either side of the trench, leading to a reduction of the coordination number of Cu, produces a configuration with higher energy. We shall argue in Sec. 5.4.2.3 that this argument is supported by actual electronic structure studies. The buckling of the Si dimer involved in the Cu-Si bond formation for the two optimized configurations remains almost unaffected in both situations: in other words, the two configurations are distinguishable, and we shall refer to them as Hexagonal Face (Up) and Hexagonal Face (Down) (or HF[U], HF[D] in shorthand notation), with 'Up' and 'Down' referring to the state of the Si dimer atom closest to Cu (see Fig. 5.10). The HF(D) configuration is the energetically more favourable of the two configurations, [41] being 0.13 eV lower in energy than the HF(U) configuration according to the GGA studies. Furthermore, our studies indicate that there is hardly any energy barrier between the HF(U) and HF(D) configurations, with the energy gain upon moving Cu from the center of the trench ME region to the HF(U) site being less than 0.01 eV, i.e., the HF(U) configuration is unstable according to our studies. We shall comment further on this

[41] Presumably, this is another sign of the importance of increasing the coordination number for the adatom, the Cu-Si distances generally being shorter by 0.04 Å or more for the HF(D) configuration, compared to the HF(U) configuration.

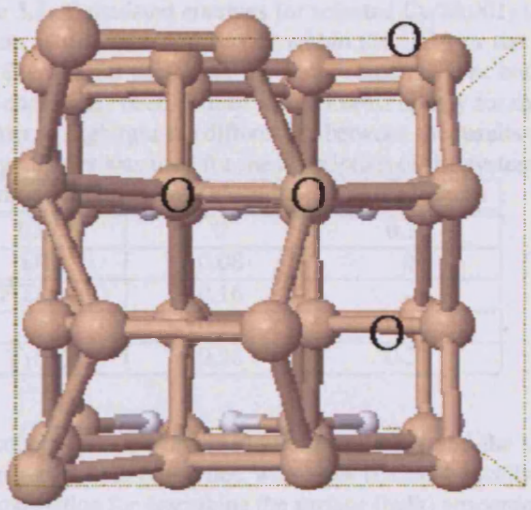

Figure 5.10: Schematic presentation showing the position of Cu for the local minimum energy configurations with Cu on the Si(001) surface (see Fig. 8.1 for details) as obtained in calculations with VASP within either *(i)* the GGA or *(ii)* the LDA (only part of the set). The configurations are (from left to right) the Pedestal, Interdimer Bridge, Hexagonal Face (Up), and Hexagonal Face (Down) configuration. The energies for the configurations investigated within the GGA and the LDA have been included in Table 5.7 while the complete set of GGA energies have been included in Table 5.8.

issue in Sec. 5.4.2.3.

Some of the above described configurations have been optimized as well in an LDA based study. For these investigations, we used only the SC where neither the HF(U) nor the HF(D) configuration can be described according to the GGA studies (see the discussion the SC and LC energy contour plot differences for details). It is clear, however, even without the inclusion of these configurations, that the conclusion of a close similarity between the LDA and GGA results obtained for subsurface Cu_i even in the trapping region (see Sec. 5.3.2.1) can not be extended to include the configurations with Cu on the Si(001) surface: while the GGA studies suggest highly similar formation energies for Cu at the IDB site and at the DT site below the surface, [42] with the IDB configuration being lower in energy by 0.08 eV compared to the DT configuration, the energy difference has been changed by almost half of an eV for the LDA results, the DT configuration in this case being 0.39 eV lower in energy.

Indeed, the Cu subsurface configurations appear to be strongly favoured within the LDA. This is hardly a surprising observation: typically (see e.g. Ref. [8]), differ-

[42] This similarity is not unaffected by changes in the cell dimension towards the point of isolated Cu at the Si(001) surface, see below in the text.

Table 5.7: Calculated energies for selected Cu/Si(001) surface and subsurface configuration as obtained with VASP within the GGA or the LDA using a 6 layer SC slab (see Sec. 8.1 for details on the slab geometry). For both sets of energies, the chosen zero energy has been defined as the lowest energy for the configuration within the set, in order to highlight the differences between the results obtained. In all studies, an SC slab geometry was used for the description of the system. See text for further details.

Configuration	E_{GGA}/ eV/atom	E_{LDA}/ eV/atom
IDB	0	0.39
DT	0.08	0
HF(Dimer)	0.16	-
P	0.25	0.46
T_1(D)	0.38	0.31

ent conclusions are obtained within the LDA and the GGA for surface properties as compared to bulk properties, with LDA (GGA) typically regarded as the more suitable approximation for describing the surface (bulk) properties correctly. While it is beyond the scope of the present work to go into detail with this issue, we speculate that the reason for the differences between the LDA and GGA results is somehow connected with the Cu 3*d* electrons: the results obtained within the LDA and the GGA suggest highly similar energy variations for essentially all subsurface configurations, despite the clear changes in *(i)* the structural environment and *(ii)* the state of the Cu 4*s* electron for the configurations with Cu_i in the trapping region compared to the configurations with Cu deeper in the slab. For this entire set of configurations, the Cu 3*d* shell is still not participating in the Cu-Si bond formation (see Sec. 5.3.2.2), with the DT configuration being a possible exception. [43] For Cu on the surface at the P and IDB sites, however, Cu 3*d* - Si 3*sp* hybridization is obtained, along with significant differences in the prediction of the energies relative to the subsurface configurations within the LDA and the GGA. [44] Unfortunately, LDA based calculations on the HF(U) and HF(D) configurations, which would be expected, on the basis of the above arguments, to resemble the Cu subsurface configurations rather than the Cu surface configurations of Table 5.7, i.e., expected to have highly similar formation energies relative to bulk Si Cu_i according to both the LDA and GGA studies, would be needed in order to gain more insight in this suggestion. [45] We shall focus below and in Sec. 5.4.2.3 almost entirely on the

[43] For this configuration, the Cu 3*d* electrons are clearly more affected by the Si environment compared to the HF(Dimer) and T_1(D) configuration. We have not been able to clarify, from our investigations into the electronic structure of the system, whether the correct interpretation of the electronic state of Cu at the DT site is *(i)* a closed 3*d* shell strongly affected by the reduced size of the surrounding Si cage or whether *(ii)* Cu 3*d* - Si 3*sp* hybridization occurs for this situation. In this respect, the statement made above in the text must be regarded as subject to further studies.

[44] We note that also the energy difference between the P and IDB configurations is strongly affected when moving from the GGA to the LDA based studies, as shown in Table 5.7.

[45] We note that some direct potential support for the above described suggestion for the difference between the LDA and GGA results in Table 5.7 is obtained from a comparison of the Cu-Si distances for the various configurations investigated in both studies: in all cases considered, the expected Cu-Si bond lengths, i.e., the distances involving Si atoms from the uppermost layer, are significantly longer according to the GGA results, with differences in the range 0.03 - 0.11 Å, as one would expect from the suggestion that the Cu 3*d*

Table 5.8: Calculated energies for the set of energetically most favourable configurations for trapped Cu at the clean Si(001) surface as obtained with VASP within the GGA, using a 6 layer LC slab (see Sec. 8.1 for details on the slab geometry). The chosen zero energy corresponds to the energetically most favourable configuration from the set. Comparison with the GGA energies of Table 5.7 shows that the large effects of increasing the cell dimension in calculations (see text for details).

Configuration	E / eV/atom
DT	0
HF(Dimer)	0.18
IDB	0.19
P	0.28
T_1(D)	0.39
HF(D)	0.39
HF(U)	0.52

GGA results, with the rest of the present discussion involving the convergence in the structural parameters and energies of the configurations of Table 5.7 with respect to cell dimension as obtained within this theoretical framework.

Table 5.8 presents the energies of the configurations for trapped Cu at the Si(001) surface as obtained using the LC slab (see Sec. 8.1 for details). Compared to the SC results of Table 5.7, a significant change of the relative energies and even a considerable redistribution of the configurations within the set has occured. Studies into the convergence of the configurations at the LC slab level were performed by investigating the changes in both the energies and structural parameters for each given configuration upon increasing the surface cell dimension from the SC slab starting point, through the LC_x and LC_y slabs (see Sec. 8.1), to the LC. [46] For these considerations we used, in addition, the conclusion from the electronic structure studies described in Sec. 5.4.2.3 that for none of the configurations of Table 5.8 does Cu donate its 4*s* electron to the surroundings, i.e., the convergence considerations of Sec. 5.2.5 do not apply, the key issue in the present discussion being elastic errors (primarily along the Si dimer row).

For the structural parameters, we considered *(i)* the effects of increasing the separation between adjacent adatoms on the lengths of the bonds formed between adatom and substrate and *(ii)* the decay in the substrate structural parameters away from a given adatom. Finally, for configurations with Cu located above or below one dimer row, rather than in the trench between dimer rows, we considered *(iii)* the effect of

orbitals are more extended in the description within the GGA.

[46] In the case of the HF(U) and HF(D) configurations, the information to be obtained from these studies was considerably more limited as these configurations could only be described with the LC_x and LC slab, i.e., cells containing two rather than one Si dimer row. Considering *(i)* the similarity between these configurations and the T_1(D) and HF(Dimer) configurations with regards to the Cu-Si bond formation (discussed briefly above in the text, with more details provided in Sec. 5.4.2.3), and *(ii)* the conclusion that similar convergence characteristics with respect to both energies and structural parameters were obtained for the T_1(D) and HF(Dimer) configurations, we assumed that roughly the same conclusions could be applied to the HF(U) and HF(D) configuration (see below in the text for a discussion of the results obtained).

the presence of Cu on the clean row structural parameters. On the basis of these studies, we concluded that significant elastic errors remained for only the DT, IDB, and P configurations. In particular, the DT configuration was found to be strongly affected by the increase of cell dimension, with the cage surrounding the Cu atom essentially being destroyed, through a significant movement along the dimer row direction of a Si atom in the third layer from the surface, as the separation between adjacent Cu atoms along the dimer row was increased. [47]

We have made the choice not to discuss this structural distortion in further detail in the present work as we regard the result as a suggestion that the energy barrier to a movement of Cu to the DT site is comparatively high, i.e., that a movement of Cu to the DT site is unlikely. This conclusion does gain further support from the comparison with experimental results for Cu on the Si(001) surface in Sec. 5.4.2.3: we shall argue at that point that the remaining set of configurations in Table 5.8 all represent candidates for structures observed with STM in the studies of Ref. [124], whereas for the DT configuration no connection could be established with any such structure (this is not discussed further below). On the other hand, this conclusion only points towards the isolated DT configuration not being observed in experiment. As our comparison with experimental results for Cu at the Si(001) surface excludes the (2×8) units, where the connection with the presence of Cu must be regarded as well established (see Sec. 5.4.1.1), but with both the amount of Cu per unit and the location of the impurity at the surface for this structure being a matter of debate at the time of writing, we can not exclude the DT site as a likely adsorption site for Cu on the basis of the present studies. Indeed, while the present studies of Cu at Si(001) has not involved the calculation of the barriers to diffusion of Cu between adjacent sites for the various configurations in Table 5.8, we regard essentially only the barrier to diffusion of Cu to the DT site as truly significant, compared to the values for bulk Si Cu_i, with alternative diffusion paths involving either Cu moving through hexagonal faces between surface and subsurface configurations (expected low energy barrier) or from a position in the trench between dimer rows to a position on a single dimer row (where the energy contour plot calculations suggested only a low barrier height, as discussed previously). We therefore might argue that the DT site represents the only location at the Si(001) surface where Cu is actually efficiently trapped (as opposed to moving around between various sites in the trapping region), this argument supporting, potentially, a connection between Cu at the DT site and the structure of the (2×8) unit. Another way of stating the above is that our calculations for Cu at the Si(001) surface performed within the GGA essentially suggest that all the configurations of Table 5.8 (perhaps with the exception of the HF(U) configuration, see remarks made previously) are likely to be observed in an STM study of the Cu contaminated Si(001) surface. This provides a key reason for constructing theoretical STM images for the complete set of

[47] For Cu at the IDB site, an additional challenge is present: the optimized configuration is not properly described with the LC as it involves buckling inversion for one of the Si dimers involved in the Cu-Si bond formation, thus forcing the introduction of another pair of Si dimers with 'Up' atoms at the same side of the row elsewhere in the cell. However, test calculations for IDB configurations described using a cell with one Si dimer row containing three dimers suggested that the importance of this restriction is minute (energy differences between the two configurations investigated being well within 0.01 eV). For this reason, we shall not comment further on this restriction below in the text, although it is present whenever a supercell with an even number of Si dimers in the dimer row is used in calculations.

Cu/Si(001) LME configurations in Sec. 5.4.2.3 when comparing the conclusions of our studies with experiment.

5.4.2.3 THEORETICAL STM IMAGES FOR LOCAL MINIMUM ENERGY CONFIGURATIONS WITH Cu TRAPPED AT THE Si(001) SURFACE

In order to compare the results of Sec. 5.4.2.2 for the configurations with trapped Cu at the Si(001) surface with experimental data, we have calculated theoretical STM images for these configurations using the program bSKAN [45, 44] as implemented in VASP. The Tersoff-Hamann approximation was used for the image construction. It is generally expected [44] that qualitative predictions can be made with this approximation for standard situations such as the atom adsorption considered here. As discussed in Sec. 5.4.1.1, recent experimental results by Baker *et al* [124] suggested the presence of structures associated with a very low number of Cu atoms at the Si(001) surface. We shall focus in our studies below entirely on results reported in Ref. [124], but in addition to the configuration discussed by the authors we shall devote attention to an alternative configuration, visible in Fig. 5.8, investigating the connection of this structure with the presence of a single Cu atom at the Si(001) surface (see below for details). We emphasize that both of the experimentally observed structures are isolated and likely to involve no more than two Cu atoms at the surface. Therefore, they should be possible to model using the slab geometry of the present work.

Our approach to comparing the theoretical results obtained in the present work for Cu at the Si(001) surface with the experimental results of Ref. [124] involved calculating theoretical STM images for the entire set of configurations included in Table 5.8, for reasons described at the end of Sec. 5.4.2.2. Calculations were performed only within the GGA, using the same precision as described for the structural optimization in Sec. 5.4.2.2. As discussed previously, the HF(U) and HF(D) configurations can not be described with the SC: in order to ensure a high level of comparability between the various images constructed, we made the choice, therefore, to calculate all theoretical STM images using the LC_x slab (see Sec. 8.1 for details). For optimal comparability with the experimental results (see Sec. 5.4.1.1), we assumed that data were collected with the tip in constant-current mode with a bias of 2.5 V between tip and sample. Sample-tip distances between 1 and 6 Å were considered.

The structure discussed in Ref. [124] was discussed briefly in Sec. 5.4.1.1, with Fig. 5.8 showing an experimental STM image of this structure obtained from this paper. Our model for this structure is shown in Fig. 5.11. On the basis of the appearance of the expected Cu related protrusions for the experimental structure and the results of our calculations for the Cu/Si(001) configurations described in Sec. 5.4.2.2, we suggest that each protrusion is explained by a Cu atom in the P configuration (see Fig. 5.10). We emphasize that our suggested model structure is a Cu pair configuration rather than a Cu dimer configuration. [48] The distance between the Cu atoms without any relaxations of the Si(001) surface considered is a dimer separation, i.e., 3.84 Å, far too large for a Cu-Cu bond to be formed. In practice, our modelling of this structure described

[48] As discussed in Sec. 5.4.2.2, Cu dimerization on Si(001) was found not to be energetically favourable according to our studies within the GGA.

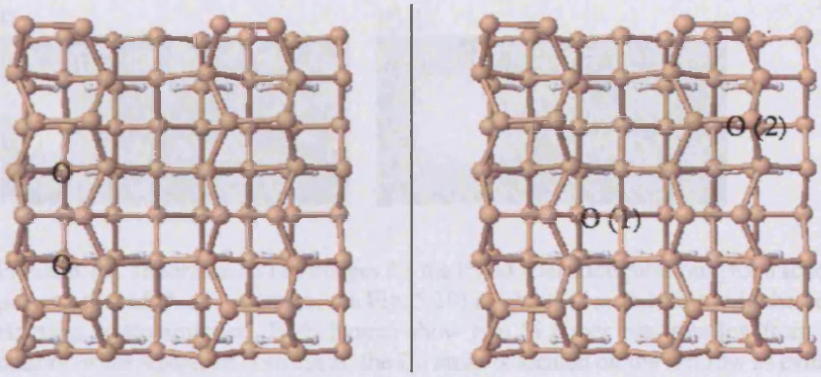

Figure 5.11: Schematic presentation of the Cu/Si(001) configurations put forth as candidates for structures visible in the experimental STM image shown in Fig. 5.8. Both figures show the clean Si(001) surface (see Fig. 8.1 for details), with the circles representing the position of the Cu atoms for the candidate configurations. The numbers in the right figure emphasize that two distinct configurations (which should both be regarded as isolated), each containing only a single Cu atom, have been shown. See text for further details.

below focusses primarily on the P (and IDB) configuration, i.e., a configuration with only a single isolated Cu atom on the Si(001) surface with no theoretical STM images constructed for configurations involving Cu atom pairs. We shall, however, include results of total energy calculations on pair configurations as an initial approach to further analyzing the relevance of the suggested model.

The theoretical STM image obtained for the P configuration is shown in Fig. 5.12. The Cu protrusion is centered on the dimer row and significantly brighter than the Si dimer protrusions. When comparing with the experimental STM image in Fig. 5.8, we find that the P configuration protrusion has both the right shape and orientation, with the long axis of symmetry for this bean shaped feature making at an angle of roughly 45° with the Si dimer row direction. As the brightness of the theoretical protrusion (which clearly exceeds the experimental result) might be explained by the use of the Tersoff-Hamann approximation, we regard this initial modelling result as highly encouraging. We shall discuss below the nature of the protrusion in slightly more detail when discussing the electronic structure near the Fermi level ε_F for the set of Cu/Si(001) configurations obtained in calculations.

In comparison, the theoretical STM image obtained for the IDB configuration, also shown in Fig. 5.12, clearly differs from the experimental result: most importantly, the Cu related protrusion in this case is not centered on the Si dimer row. The conclusion that the IDB configuration is not observed in experiment appears to be at odds with the conclusion in Sec. 5.4.2.2 that the IDB configuration is slightly lower in energy than the P configuration with *(i)* no suggestions of a high energy barrier between these structurally highly similar configurations and *(ii)* fairly comparable amounts of remaining structural relaxations upon increasing the cell size further along the Si dimer

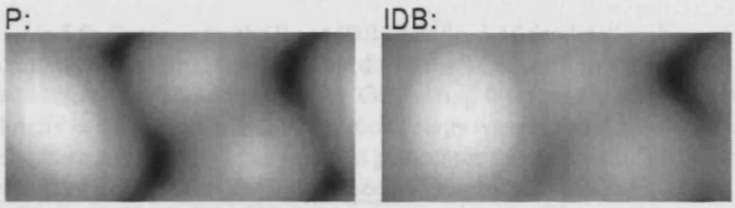

Figure 5.12: Theoretical STM images for the P and IDB configurations (for a schematic presentation of these structures, see Fig. 5.10) as obtained with bSKAN in the Tersoff-Hamann approximation. Both figures show two Si dimer row running from top to bottom in the figure. In both cases, the Cu atom is located on the left row as evidenced by the bright ellopsoidal protrusion in the image. The images are filled-state, with an assumed bias of 2.5 V between tip and sample. See text for further details.

row for both configurations. In this respect, the LDA results, suggesting a lowering of the P configuration energy relative to the IDB configuration by $\sim$ 0.2 eV (see Table 5.7) appear to be in much closer agreement with experiment. On the other hand, the above considerations have involved only structures with a single isolated Cu atom on the Si(001) surface whereas the experimental structure reported by Baker *et al.* in Ref. [124] consists (according to our modelling) of a pair of Cu atoms with no comments made by the authors on the presence of single protrusions on the surface. For this reason, while a complete theoretical modelling (with reference to the suggestions put forth in the present work) of the pair of protrusions reported in Ref. [124] requires investigations into Cu pair configurations on the Si(001) surface, studies of these larger configurations might actually be needed in order to explain why the assumed Cu related protrusions should have a strong preference to be centered on the Si dimer row.

We have investigated the stability of Cu pairing on the Si(001) surface through structural optimization of configurations with pairs of Cu atoms at either (i) the P or (ii) the IDB site. For relaxation effects to be included to a reasonable level for both of these configurations, we considered cells with one dimer row only, but with either 4 or 8 dimers in this row. With the smaller of these cells defined as LC_y in Sec. 8.1, we will refer, for brevity, to the larger cell used in the present studies as XLC_y below. Apart from the choice of k-point grid in these studies, the precision in calculations was the same as described in previous studies. For true comparability of the LC_y and XLC_y results, however, an (8, 4, 1) k mesh ((8, 2, 1) k mesh) was used in the calculations on the smaller (larger) cell. The new set of calculations involved an optimization of the isolated Cu P and IDB configurations as well with the LC_y.

The results of these calculations have been included in Table 5.9. We find that for the P configuration, pairing is actually not an energetically favourable process while this is the case for the IDB configuration. A comparison of the LC_y and XLC_y IDB pair configuration energies and structural parameters strongly suggests that essentially all structural relaxation effects along the dimer row have been included with the XLC_y: this presumably reflects the fact that the buckling inversion obtained for the IDB config-

Table 5.9: Energies for the P and IDB (see Fig. 5.10 for details) plus corresponding pair configurations (adjacent [along the dimer row] Cu atoms in the P or IDB configuration) as obtained with VASP within the GGA using 6 layer LC_y and XLC_y slab (explained briefly in the text). The P configuration energy was chosen as the zero energy in order to emphasize the energy changes upon pairing for this prime candidate for the Cu related structure discussed in Ref. [124]. See text for further details.

Configuration (cell)	E / eV/atom
P (LC_y)	0.00
P pair (LC_y)	0.18
P pair (XLC_y)	0.08
IDB (LC_y)	-0.09
IDB pair (LC_y)	-0.20
IDB pair (XLC_y)	-0.21

uration (see Sec. 5.4.2.2) is not retained for the IDB pair configuration, the disturbance of the original clean Si(001) surface being much smaller, in this sense, for the pair configuration. The estimated energy gain upon Cu pairing for Cu atoms at the IDB site is ~ 0.1 eV per Cu atom. As noted previously in this discussion, we do not regard the IDB configuration as an actual candidate for the structure discussed in Ref. [124]. Without these reservations, however, we would also regard the above mentioned energy gain due to pairing of Cu atoms at IDB sites as too small to truly support a stability of the pair configuration compared to the isolated IDB configuration, i.e., this result does not offer a solution to the problems addressed previously in the discussion when considering modelling of isolated Cu configurations.

Compared to the IDB pair configuration, the P pair configuration involves higher amounts of strain on the Si(001) surface. We shall speculate in the following that this might be the key to interpreting the apparently discouraging result for the energy of this configuration: a study into the Si-Cu distances for the P and P pair configurations reveals that the distance between the outermost Si dimers involved in Si-Cu bond formation for the P pair configuration is increasing by 0.152 Å relative to the corresponding distance for the clean Si(001) surface, in contrast to the situation for the P configuration where the distance between these (in this case adjacent) dimers is decreasing by 0.069 Å. This change of behaviour is explained by the weakening of the Si-Cu bonds for the central Si dimer in the P pair configuration, where there is a Cu atom on both sides of the dimer. [49] This result indicates that the presence of a Si dimer vacancy on each side of the Cu pair along the dimer row might reduce significantly the amount of strain (and the formation energy) for this configuration. Such a dimer vacancy correlation actually appears to be present for the pair of protrusions in Fig. 5.8, but as the authors of Ref. [124] have not commented on this issue, we are unable to draw any further conclusions at the present level of modelling. [50]

[49]The above number for the P pair configuration is a mean value: the Si dimers in question are closer together (by 0.065 Å) on the side of the row involving the comparatively stronger bonds between Cu and Si 'Up' atoms for these dimers.

[50]There appears to be a correlation between the presence of Cu at the Si(001) surface and the distribution of

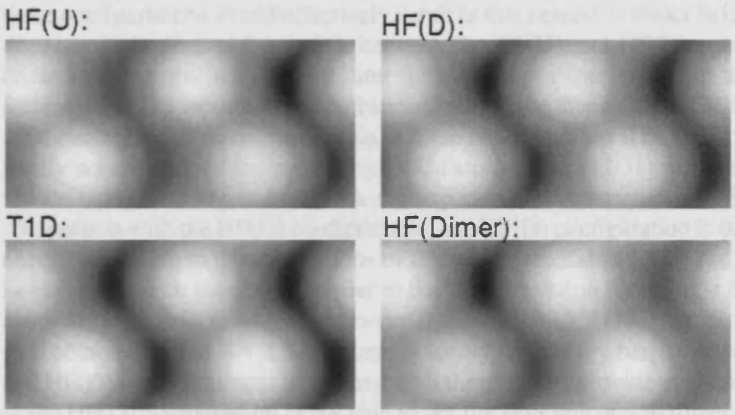

Figure 5.13: Same as in Fig. 5.12 but for the HF(U), HF(D), T_1(D), and HF(Dimer) configurations (for a schematic presentation of these systems, see Fig. 5.10 and Fig. 8.8). All protrusions in these images are at the positions of Si atoms, with the presence of a Cu atom at the Si(001) surface essentially masked according to these results. See text for further details.

In addition to the pair of protrusions disccused above, we shall focus below on a possible relation between Cu at the Si(001) surface and the single Si dimer row segments with pinned dimers visible in Fig. 5.8. Typically, pinning of the Si dimer buckling is observed in the vicinity of defects on the surface or at step edges, but in the present case, there appears to be no such clear cause. We shall clarify in the following our reasons to believe that a single Cu atom might be responsible for the pinning of the buckling of *one* Si dimer and thus in turn for the appearance of a dimer row segment with pinned dimers. These considerations are to be regarded as preliminary as they are based only on the total energy calculations of Sec. 5.4.2.2 and the construction of theoretical STM images on the basis of these results: the aim of the following discussion, therefore, does not go beyond arguing that there might be a connection between the above described experimentally observed structure and the presence of a Cu atom at the Si(001) surface.

The total energy calculations of Sec. 5.4.2.2 revealed a set of configurations (HF(U) and HF(D)) where the presence of the Cu atom did not change the clean Si(001) surface structural parameters significantly, with the result that two conceptually different configurations, distinguished by the state of the Si dimer atom nearest to Cu, could be defined. From a general point of view, a sufficiently large energy difference between

vacancy defects on this surface (which of course might rather be related to the $c(8\times8)$ surface reconstruction discussed in Sec. 5.4.1.1), see Ref. [124] for details. We have not investigated the effect of introducing dimer vacancy defects next to the P pair configuration using the XLC_y as we would expect this structure to be too large for the calculation to yield a reliable result. In particular, on the basis of the experimental STM image in Fig. 5.8, we would not expect the suggested vacancy correlation for the P pair configuration to involve removal of Si dimers immediately adjacent to the Cu atoms but one dimer further along the row.

these configurations would effectively result in this nearest Si dimer being pinned. This does not in itself establish a link between the HF(U) and HF(D) configurations and dimer row segment with pinned dimers observed in experiment, but the idea of such a connection is supported by the observation that the theoretical STM image obtained for the energetically most favourable of these configurations (HF(D)) in Fig. 5.13 bears hardly no evidence of the presence of a Cu atom at the Si(001) surface (with such evidence being in disagreement with the experimental observations in Ref. [124]). In comparison with the HF(U) configuration. the HF(D) configuration is 0.13 eV lower in energy according to the calculations of this work (see Table 5.8). This number should be compared with the energy barrier to buckling inversion for a single Si dimer for the clean Si(001) surface, which is between 0.05 and 0.1 eV [127], but also to the conclusion obtained in Sec. 5.4.2.2 that there is hardly any energy barrier between the HF(U) and HF(D) configurations. In summary, all these results provide evident support for Cu in the HF(D) configuration being able to pin the buckling of a Si dimer. [51]

The T_1(D) and HF(Dimer) configurations constitute another set of conceptually similar configurations (in this case involving subsurface Cu in the cages containing the T_1 sites but 'on either side of the dimer row', as specified by the state of the nearest Si surface dimer atom, see Sec. 8.2.4 for further comments) where pinning of a segment of dimers in a Si dimer row due to the presence of Cu in the energetically most favourable of these configurations might be expected. In comparison with the HF(U) and HF(D) configurations, the two configurations in this set are both *(i)* lower in energy and with *(ii)* a comparatively larger difference, 0.21 eV, in their relative energies (the HF(Dimer) configuration being the most favourable configuration, see Table 5.8). Finally, *(iii)* the Cu atom is not visible in the theoretical STM image constructed for the HF(Dimer) configuration (see Fig. 5.13), making this configuration an even stronger candidate for an explanation to the appearance of the Si dimer row segment with pinned dimers in Fig. 5.8 than the HF(D) configuration.

As mentioned previously in this discussion, all published results [117, 123, 124] of experimental STM investigations following submonolayer deposition of Cu on Si(001) so far have involved relatively high bias voltages of at least 2 V. Our studies of the electronic structure around the Fermi energy ε_F for the Cu/Si(001) local minimum energy configurations of Sec. 5.4.2.2 suggest important changes for some of these configurations upon a reduction of the bias voltage. While interstitial Cu in bulk Si basically donates its 4*s* electron to the environment and otherwise appears to be a 'tiny ball' with an essentially closed 3*d* shell electron configuration according to our calculations (see Sec. 5.2.4.2), hybridization effects become more pronounced as Cu moves to the surface, especially as the configuration changes from involving a large number of weak bonds (which is still the case for the hexagonal face and T configurations) to involve only a few bonds with Si dimer atoms (P and IDB configurations). Our studies suggest

[51] We note that a large energy difference between the HF(U) and HF(D) configurations is not the only possible way to pin the buckling of a series of Si dimers. Alternatively, the energy barrier to dimer flipping for the Si dimer nearest to Cu might be significantly increased due to the presence of this impurity, so that even with a small energy difference between the two configurations from the above set, theory might predict a segment of dimer row with pinned dimers as a result. It is beyond the scope of this work to investigate this issue further.

that the dominant contribution to the Si-Cu bonds for the P and IDB configurations is not from states at ε_F but rather at ~ 0.5 eV or more (outside the energy range included in the present study) below the Fermi level. This implies that for a bias voltage less than 0.5 eV, the protrusions, if they are actually explained by pairs of Cu in the P configuration, will be significantly diminished (while the brightness of protrusions due to Si dimers affected by the presence of the Cu atoms is expected to increase, details not being of importance for the present discussion). Experiments involving submonolayer Cu deposition on Si(001) but with the STM analysis involving such low bias voltages would be of interest for the next step of the modelling of the Cu interactions with this surface.

5.4.3 CONTROLLING THE BEHAVIOUR OF Cu AT THE Si(001) SURFACE: Cu NANOWIRE TEMPLATE STUDIES

Our studies of Cu outdiffusion to the clean Si(001) surface presented in Sec. 5.3 have suggested that Cu is trapped within a few atomic layers of this surface: Si(001), in other words, is a highly efficient sink for diffusing Cu. One promising potential application of this result involves manipulation of these Cu atoms by suitable modification of the properties of the surface: [52] in the following, we shall give examples of two local modifications of the Si(001) surface which we regard, with reference to the results of Sec. 5.3.2, as potential candidates for Cu nanowire templates.

For the clean Si(001) surface, as discussed in Sec. 5.3.2, the trapping mechanism for the Cu atoms is provided primarily by the surface dangling bonds, explaining its short range. If these bonds are saturated by terminating the surface with e.g. H, we expect from our calculations for clean Si(001) that Cu will still be attracted to the Si(001) surface but only spend a larger fraction of time in this region with nothing to efficiently prevent diffusion to other more stable sinks such as extended defects in the bulk crystal. If, however, the H surface termination layer is removed from a local region on the surface, this region, bearing close resemblance to the original clean Si(001) surface, should be able to act as trapping sites for the Cu atoms. This modification of the clean Si(001) surface, which is, essentially, a description of the formation of a dangling bond wire with STM as described in Sec. 4.2.2, thus provides a way of creating, in principle, a Cu nanowire on the Si(001) surface.

Evidently, the quality and stability of the wire produced according to the above line of arguments are issues still to be addressed before the usefulness of the dangling bond wire as a Cu nanowire template can be evaluated. On the other hand, the above consideration serves as a striking example of the simplicity by which a candidate for a solution to a highly challenging problem in current day devices (see Sec. 4.1.1) can be created, according to our theoretical results of Sec. 5.3.2. Furthermore, the truly intriguing part of the discussion is the fact that the above described way of altering the surface properties in order to construct lines of trapping sites for Cu atoms at the Si(001) surface, while possibly being the most simple example, is far from the only one.

[52] We shall discuss on a rather general level a wider range of potential applications of the results of Sec. 5.3 in Sec. 5.5.

In the brief discussion below, we shall consider another potentially interesting structure also introduced in Sec. 4.2.2: the Haiku structure under Bi nanolines on Si(001). This structure provides no dangling bonds for the Cu trapping, but the local reconstruction of the Si(001) surface is so severe that it might act, under appropriate conditions, as a shallow trap for the diffusing impurity, an expectation to be clarified below. Our studies of Cu_i near clean Si(001) in Sec. 5.3 have shown that Cu responds strongly to even the small distortions of the Si cages in this region, with the optimization of the coordination number for the impurity being a key effect. The lowering of the formation energy has been explained by the fact that the movement of Cu towards the expanded part of the distorted cage, along with the expansion of the cage required in order to accommodate the impurity, is associated with a smaller energy penalty for this system as the Si-Si bonds stretched the most due to the presence of Cu have already been stretched due to the surface reconstruction. For the Haiku structure, there appears to be both plenty of room for Cu as well as a possibility of the impurity increasing its coordination number, i.e., Cu might deposit at an energetically favourable position in this environment essentially *without* causing any noteworthy distortion of the host lattice, whereby the formation energy for the configuration would be expected to be considerably reduced compared to the situation for the 'normal' environment. Our theoretical studies to be presented below represent preliminary investigations into this issue.

As a preliminary study into trapping of Cu in the Haiku structure under Bi nanolines on the Si(001) surface, we have structurally optimized a series of configurations with Cu_i inserted in the various nonequivalent cages for this surface reconstruction, comparing the formation energies for these configurations with the energies obtained by depositing Cu at the T_2 site (see Fig. 8.8) for clean Si(001) using a supercell with the same surface dimensions. We emphasize that these investigations are preliminary, with especially the issue of convergence in the energies with respect to the chosen supercell dimensions not being very rigorously addressed in the present approach. For this reason, while these studies do provide some insight into the properties of the Haiku structure as a sink for diffusing Cu compared to the clean $p(2\times2)$ Si(001) surface, we should be cautious about drawing more than general conclusions on this issue when interpreting the energy differences between the various configurations below. We shall clarify later in this discussion on the expected level of reliable information to be obtained from the present investigations.

Fig. 5.14 shows most of the configurations with Cu_i at Si(001), inserted in the Haiku structure under Bi nanolines on this surface, investigated in the present work, with the figure caption presenting the nomenclature used for these configurations in the discussions below: in addition to these studies, also, configurations with *(i)* Cu moved from the position below the center of a Bi-Bi bond to right below a Bi atom and *(ii)* Cu moved along the direction of the Bi nanolines from the position at the approximate center of the Central cage to a position between adjacent Central cages were considered. In both of these situations, Cu could hardly be described as surrounded by a cage, and as our initial studies focussed on this situation for simplicity, we made the choice to omit these configurations both in Fig. 5.14 and in Table 5.10, where the energies of the remaining optimized configurations have been included. The formation

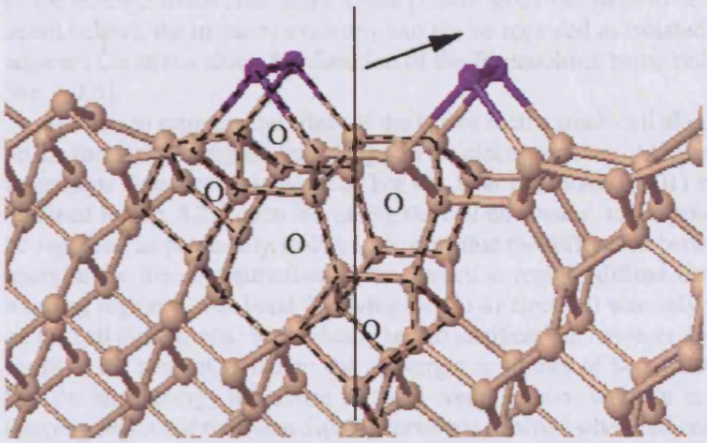

Figure 5.14: Schematic presentation of the expected energetically most favourable configurations with Cu_i at the Si(001) surface, located in the Haiku reconstruction under Bi nanolines. The Bi (Si) atoms are represented by purple (light brown) spheres in the figure while the (approximate) Cu positions have been emphasized with circles. As the Haiku reconstruction shows mirror symmetry with respect to the plane containing the horizontal line in the figure and running along the Bi nanolines (as shown by the arrow in the figure), only configurations on the left side of this plane have been considered. For each Cu position shown in the figure, the surrounding Si cage has been emphasized with dotted lines for clarity. In the present work, these configurations are denoted (from left to right) Edge Pentagonal Cage, Bi Cage, Heptagonal Cage, Central Pentagonal Cage, and Central Cage.

energies for these configurations did not differ very significantly from the energies obtained with Cu at the approximate center of the nearby cage in question, and we shall therefore not comment on these results below. [53]

The cell used in calculations contained a single Si dimer row in the direction along the Bi nanolines, with this row containing 6 dimers. For the Bi nanolines, this choice leads to a separation of only two Si dimers (using the same definition for this term as described for the studies of a conceptually similar Y atomic string candidate structure in Sec. 6.3.2.2), a distance obviously too small for the Bi nanolines to be regarded as well separated but probably not with considerable influence on the results of interest in the present discussion. For Cu, expecting, on the basis of the studies in Sec. 5.3.2.2, that the electronic state of this atom involves a very diffuse 4*s* state for the majority

[53] We emphasize that including only these two subsurface Cu configurations as alternatives to the configurations with Cu at the approximate centers of cages in Haiku structure in the studies does not mean that the complete set of energetically favourable positions for Cu_i at this surface reconstruction (i.e., including both Cu at the approximate center of cages, at faces between adjacent cages, and other alternative positions) has been investigated in the present approach. Only, the two configurations discussed above in the text were included as they represented, in our opinion, good candidates for energetically favourable alternatives to insertion of Cu at the center of the adjacent cage in question.

of the configurations considered in the present study (an issue to be discussed in more detail below), the impurity evidently can not be regarded as isolated, the separation of adjacent Cu atoms along the direction of the Bi nanolines being only 7.68 Å (see e.g. Sec. 5.2.5).

In order to estimate the effect of the use of such a small cell along the Bi nanolines on the formation energies, knowledge on the electronic state of Cu_i for the various configurations investigated is needed. For Cu_i near the clean Si(001) surface, the results obtained in Sec. 8.2.4 upon increasing the cell dimension, to the point where Cu could be regarded as practically isolated, showed that the difference between the formation energies for the configurations in the attraction region (diffuse Cu 4*s* state) and the trapping region (Cu-Si bond involving the Cu 4*s* electron) was only weakly dependent on the cell dimensions. We basically see no justification, however, for generalizing this result to the present situation: the convergence studies of Sec. 8.2.4 essentially show that the large energy difference between configurations with Cu in the attraction and trapping regions at the clean Si(001) surface is retained when cell convergence is taken into account, but the variation in these energy differences with respect to changes in the cell dimension is the result of several effects (Cu 4*s* level dispersion and elastic errors being the most important factors), with the energy variations in the different regions just happening to be very similar for the particular situation considered. On the other hand, we would expect rather similar convergence properties for all of the configurations which can be associated with the presence of a very diffuse Cu 4*s* state, i.e., we would expect remaining energy changes between the configurations for such a set to be within possibly 0.1 - 0.2 eV. Although we have not performed studies to show that the Cu 4*s* state is diffuse for all the configurations with Cu at the Haiku structure considered in this discussion, we would believe this to be the case for Cu in the Heptagonal cage (see Fig. 5.14), the energetically most favourable configuration from the set investigated, while for most of the other configurations, the above approximation should be fairly justifiable.

Calculations were performed using Vanderbilt US PPs [17] as implemented in VASP [23, 24], with the PW91 GGA [12] to E_{xc}. The studies of Sec. 5.3.2 for Cu_i near the clean Si(001) surface revealed that the formation energies relative to the energy for bulk Si Cu_i show hardly any dependence on whether the studies are performed within the LDA or the GGA (whereas the relative energies are found to be clearly dependent on this choice for Cu on the Si(001) surface, see Sec. 5.4.2). As the present calculations involve configurations with Cu_i where no hybridization involving the 3*d* shell for this impurity is expected, we do not believe that choosing the GGA over the LDA has any significant influence on the relative energies of Table 5.10.

The actual calculations, employed a value of 233.7 eV for the plane wave energy cutoff, describing partial occupancies within the Gaussian smearing scheme with a 0.1 eV width, and using a (6, 2, 1) MP *k*-mesh. For a description of remaining essential computational details, we refer to Sec. 8.2.1. This choice of precision in calculations is essentially the same as used for the studies of Cu outdiffusion to the clean Si(001) surface in Sec. 5.3 and we refer to Sec. 8.2.4 for comments on the expected level of convergence of the energies and structural parameters, mentioning only, in the present discussion, that we expect errors due to the choice of supercell to clearly exceed the

Table 5.10: Calculated formation energies (relative to the energetically most favourable configuration from the set investigated) for configurations with Cu_i near the Si(001) surface as obtained with VASP (see text for details). The T_2 configuration refers to a situation where the surface is clean, with a $p(2\times2)$ reconstruction (see Fig. 8.8). For the remaining configurations, Cu has been inserted in the Haiku structure below Bi nanolines on this surface, with the nomenclature used in the Table below being explained in Fig. 5.14.

Configuration	Energy / eV/atom
T_2	0
Heptagonal (H)	0.02
Central (C)	0.12
Bi (Bi)	0.31
Edge Pentagonal (EP)	0.35
Central Pentagonal (CP)	1.00

errors due to the choice of variable parameters for the code.

The results of our studies have been included in Table 5.10. The energetically most favourable configuration from the entire set is the T_2 configuration, a somewhat discouraging result. Studies into the structural parameters for the optimized configurations reveal the expected correlation with especially reduced additional distortions of the host lattice in response to the presence of Cu and lowering of the formation energy of this impurity, but apparently, these effects are insufficient on their own to efficiently attract Cu to the Haiku structure. The almost counterintuitive question arises: are these cages *too large* for Cu?

5.5 SUMMARY AND OUTLOOK: PROSPECTS FOR FURTHER UNDERSTANDING OF THE PHYSICS OF Cu IN Si AND CONTROLLING THIS IMPURITY

The initial aim of our studies into Cu-Si interactions presented in this work was to clarify the electronic state of isolated bulk Si Cu_i, addressing carefully the issue of weak covalent Cu-Si bond formation noted by Estreicher in previous theoretical studies [56] and the evident discrepancies between this conclusion and the experimental picture of the impurity, where diffusing Cu_i^+ is considered as chemically inert, the Cu $3d$ shell remaining closed. As discussed in Sec. 4.1.1, we regard such investigations as needed in order to produce a reliable platform for our subsequent studies of Cu in Si.

Our studies into this issue have revealed that Estreicher's conclusions are based on the use of an incomplete basis set for the Si environment in his pseudo atomic orbital based calculations. The Cu-Si bond formation, we suggested, was actually explained as artificial confinement of electrons to the region around the impurity. Our studies suggested that bulk Si Cu_i is a shallow donor with a very loosely bound $4s$ state (as evidenced in the calculations on bulk Si Cu_i^0) and a $3d$ shell that remains closed, albeit affected by the surrounding environment. For fully converged calculations, Cu was located exactly at the T site in the Si lattice, i.e, at the center of the surrounding Si 'cage'. While our criticism of the results of Ref. [56] must appear well-founded, the reliability of our suggested conclusions for the system under investigation evidently is more difficult to establish on the basis of the studies performed (where, in particular, the energy barrier to Cu diffusion in Si has not been investigated). As will be discussed below, however, our further studies of Cu in Si offer potentially strong support for the above conclusions being justifiable.

Following the studies of bulk Si Cu_i, we have investigated the outdiffusion of this impurity to the clean Si(001) surface. With our work focussing on isolated Cu for simplicity, we found that our total energy calculations suggested the presence of a long range attraction (presumably several tens of Si layers into the bulk) driving Cu_i towards Si(001) while within three layers of the surface, the energies would drop markedly (by more than 1 eV), i.e., the Si(001) surface is a highly efficient sink for Cu_i. For Cu in the attraction region, our studies into the electronic state of Cu_i and the structural details of the Si environment revealed that the predicted diffusion of Cu towards the surface is a consequence of the surrounding Si cages being asymmetric *before* the insertion of Cu at the approximate T site. In other words, the lowering of the formation energy for the impurity compared to the situation for Cu_i in bulk Si is explained entirely by changes in the surroundings, with the electronic state of the impurity essentially remaining unaffected. The cage distortion introduces a movement of Cu towards the region where a local cage expansion has occured, in agreement with the expectation from the conclusions obtained for bulk Si Cu_i that Cu will seek to both *(i)* stay at the approximate center of the given cage and *(ii)* increase its coordination number. The energy lowering, we believe, is connected with the fact that, with Cu moving towards

the region where the cage has expanded the most and with the general requirement that the cage has to expand slightly in order to accommodate the impurity, the energy penalty associated with the latter of these cage expansions is reduced compared to the situation for Cu in a nondistorted cage: the Si-Si bonds being stretched the most in response to the presence of Cu for the near surfae cage are the ones already stretched the most before the Cu insertion. In particular, this conclusion, and the fact that the cage distortions are relatively small, supports the suggestion that Cu is a fast diffuser in the entire attraction region, i.e., there is nothing according to our studies which prevents the impurity from moving towards the clean Si(001) surface. For Cu in the trapping region, our studies reveal that Cu-Si bond formation involving the Cu 4*s* electron and the surface dangling bonds occurs, the Cu 3*d* shell still remaining closed. We believe that the above described mechanisms apply to all the surfaces of the clean Si wafer, with the efficiency of the attraction in particular depending on the level of distortion for the reconstruction of the surface in question. Some support for this argument has been provided by Dolbak *et al.* [126], who reported that the segregration coefficients for Cu to the Si surface showed a dependence on surface orientation. We shall discuss the state of the outdiffused Cu further below.

The results obtained for Cu outdiffusion to Si(001) have important potential implications for the understanding of the physics of Cu_i in Si. Firstly, they offer a highly interesting support for our conclusions for bulk Si Cu_i being justifiable, in the sense that they provide suggestions for explanations to some of the puzzling experimentally observed phenomena for Cu_i near defects in bulk Si, mentioned by Estreicher in Ref. [56] as being incompatible with the behaviour of the impurity as a 'tiny charged ball', unable to interact covalently with the surroundings. [54] The relevance for our theoretical results for Cu near the surface of the Si wafer to issues related to Cu deep in the bulk is clarified by the fact that the explanation for the behaviour of Cu_i in the attraction region near the Si(001) surface is connected with surface properties only through the fact that a localized disturbance (in this case, the surface reconstruction) is the cause of cage assymmetries well into the slab. Essentially the same thing, albeit less pronounced, would be expected to happen in the vicinity of an acceptor in bulk Si. Estreicher [56] noted that the acceptor dependent Cu-acceptor binding energies, along with their magnitude, was to be regarded as a sign of covalent interaction between Cu and the acceptor. We put forth here the alternative explanation that the binding energy variations and surprising strengths are related primarily to a change in the distortion of the Si lattice around the immobile acceptor, i.e., the attraction region around this impurity differs in strength, depending on the disturbance introduced by the particular acceptor in question. This effect (which should be included when comparing with experimental results) would be long range and not possible to model satisfactorily within the theoretical framework used in this thesis. We do note, however, that the argument is supported by an evident correlation between the radius of the acceptor and the experimentally reported Cu-acceptor binding energy (see Sec. 4.1.2 for references), with the binding energy increasing with the size of the acceptor. For the experimentally

[54] We shall argue later in this discussion why there is reason to believe that our theoretical results for Cu outdiffusion to Si(001) are justifiable.

reported Cu trapping at cavities in bulk Si, another system which will be difficult to model satisfactorily with theory, our studies of Cu outdiffusion to the Si(001) surface suggest that the mechanisms for Cu attraction to the cavity and coating of the interior surface are essentially the same as obtained for Cu near the surface. On the basis of these considerations, we have confidence in our general conclusions for the electronic state of bulk Si Cu_i being justifiable.

In order to establish a complete theoretical picture of the behaviour of outdiffused Cu at the Si(001) surface, for comparison with experimental studies of this system, we have calculated the energies for isolated Cu on the surface. The comparison of the experimental and theoretical results for this situation represent the primary verification that our conclusions for Cu near the surface (and thus, in turn, the conclusions described in the above paragraph) are to be regarded as reliable. We have found very promising results for connections between theoretically determined local minimum energy configurations with isolated Cu or Cu pairs at the Si(001) surface and experimentally reported structures by Baker *et al.* in Ref. [124]. Our studies into this issue have focussed on theoretical results obtained within the GGA rather than the LDA and it remains to be clarified whether the similarity between theory and experiment is satisfactorily reproduced within the LDA as well. Furthermore, modelling of larger systems and calculations of relevant diffusion barriers are needed in order to fully establish connections between the theoretical and experimental results. We believe, however, that the present level of comparability provides strong support for the Cu outdiffusion results being reliable.

The Cu outdiffusion results have potential implications for gettering of Cu and, potentially, for Cu nanowire formation on the Si(001) surface: we have performed preliminary studies into the wire formation issue, investigating Cu trapping at Bi nanolines on the Si(001) surface. While the results obtained here were not too encouraging, they do support our expectations for the Cu behaviour near this structure and therefore, we believe, the expectation that the formation energy for Cu in Si can be reduced significantly if a distortion creating an optimal environment for the impurity is introduced. Whether a combination between such a system and a potential wire template (with requirements for the dimensions and straightness of the structure) can be obtained remains to be clarified.

Our theoretical investigations into Cu-Si interactions presented in this thesis have various evident limitations. A fundamental problem is the very low value for the Si band gap obtained with theory (see Sec. 5.2.5). This incorrect description of the host lattice presumably accounts for the surprisingly (i.e., at odds with experiment) efficient screening of the Cu_i^+ and relatively (once again compared to expectations from experimental knowledge of Si) localized $4s$ electron level, but we would regard it as unlikely to affect the key conclusions of our work, essentially as our studies reproduce the experimentally well established conclusion that Cu_i is a shallow donor in Si, suggesting that the theoretically suggested mechanism of Cu trapping at the Si(001) surface is justifiable. The theoretical conclusion of a closed Cu $3d$ shell in a sense is a matter of less concern as we have argued previously in this discussion that the predicted be-

haviour of bulk Si Cu_i on the basis of this conclusion appears to agree in general with the experimental conclusions for this impurity.

Another potential issue is related to finite temperature effects on the relatively small cage distortions driving Cu towards the Si(001) surface according to our zero temperature studies. On a very general level, we do not believe that the increased vibrations of the Si host structure will smear out the effects of the surface reconstruction with the exception of a region within relatively few layers of the Si(001) surface: actually, the lengths of the Si-Si bonds stretched and thus weakened due to the cage asymmetries should probably be expected to oscillate more strongly than other Si-Si bond lengths as a particular change in the bond length is associated with a smaller energy variation for these bonds. Finite temperature corrections, therefore, might enhance the attraction of Cu to Si(001), although also the change in the interaction between impurity and lattice at these conditions would have to be taken into account in order to establish a sensible picture of this situation.

Chapter 6

INTERACTIONS OF RARE EARTH METAL WITH Si(001)

- You might say that fortune smiled at us. I'd say that fortune is something you seek through hard work.

T. Kristensen, 2004 (danish racing driver, on winning the Le Mans 24 hour race by 41 seconds)

6.1 INTRODUCTION

This chapter presents the results of our theoretical studies of the epitaxial growth of RE disilicide nanowires on the Si(001) surface. To our knowledge, the calculations to be described in the following represent the first rigorous theoretical investigations into the substrate/overlayer system. They also represent, more than anything else, a challenge of the generally accepted conclusion (discussed in Sec. 4.2.3), that these wires adopt the vacancy defected AlB_2 structure, with calculations being performed solely on an alternative candidate for the wire structure. The chosen element for the full set of wire studies below is Y, not an actual RE metal, but reported to display the same behaviour with regards to nanowire formation on Si(001). We have also performed preliminary investigations into Er disilicide nanowire formation on the Si(001) surface, but due to time limitations and restrictions to the length of the thesis, it has not been possible to include the results of these studies at a satisfactory level in the final presentation, and we shall make only brief occasional comments throughtout the text to the work performed on this issue. We shall give an overall introduction to the theoretical studies of Y disilicide nanowire growth on Si(001) to be presented in this chapter in Sec. 6.2.1.2, with Sec. 6.2.6 summarizing and evaluating our results obtained on the basis of these studies. In Sec. 6.3 we shall present our preliminary studies into the conceptually difficult topic of Y atomic string growth on Si(001), the motivation being very recent experiments reporting growth of lines of atomic width upon deposition of Y on this surface. For a summary and considerations about future studies in this area, we refer to Sec. 6.3.3. Most computational details in the entire set of studies above have been

postponed until Sec. 8.3. Finally, papers on *(i)* epitaxial growth of the vacancy free Y disilicide nanowire with the AlB_2 structure on Si(001), *(ii)* Y/Si(001) wetting layer formation, *(iii)* Y atomic strings on the Si(001) surface, and *(iv)* the formal valency of Er in Er disilicide are in preparation.

6.2 STABILITY OF VACANCY FREE Y DISILICIDE NANOWIRES ON THE Si(001) SURFACE

6.2.1 INTRODUCTION

6.2.1.1 A SURVEY OF PREVIOUS WORK ON Y DISILICIDE OF INTEREST TO THE CURRENT STUDIES

Y (electron configuration [Kr]$4d^1 5s^2$) is not a RE metal, but it has been reported [128], along with another non-RE metal Sc [129], to form self-assembled disilicide nanowire structures on the Si(001) surface following a deposition and annealing procedure with very clear similarities to the typical recommended procedure for RE disilicide nanowire formation on Si(001) described in Sec. 4.2.3. Katkov and Nogami [128], using STM and LEED, reported wetting layer formation, predominantly with a 2×4 surface reconstruction, for Y coverages of less than 1 ML on Si(001) and annealing at 875 K. At coverages above 1 ML, nanowire growth was observed, with the substrate surface reconstruction changing to 1×3. No details were provided on the wetting layer structures in this brief report. [1]

Compared with the typical coverage and growth temperature values for RE disilicide nanowire formation in Sec. 4.3.3, Y disilicide nanowire formation appears to require significantly higher amounts of Y on the surface (typically, nanowires are observed for coverages of 0.2 ML or even lower, see e.g. Ref. [131, 129]). This might be connected with the experimental observation by Liu and Nogami in Ref. [132] that 3D Y disilicide islands so far have always been reported to grow simultaneously with wires: island growth can not be suppressed simply by quenching following the deposition of Y on the Si(001) surface (in contrast to the situation for Gd and Dy, which were also studied by these authors). [2] This discouraging result explains why no experimental studies have focussed on Y disilicide nanowire growth on Si(001) following Ref. [132]. Very recent experiments by Owen (yet to be published) reporting (assumed) Y nanowire atomic string formation on Si(001) (see Sec. 6.3) might revive interest in Y on the Si(001) surface.

The bulk of the experimental work reported for Y disilicides grown on Si substrates has involved Y disilicide 2D and 3D film growth on the Si(111) surface: it is beyond the scope of this work to describe these studies in detail as they discuss issues of only little relevance to our studies. We note, however, that studies of the 2D RE disilicide films on Si(111) are of potential interest to the studies of RE disilicide nanowires on the Si(001) surface for the following reason: as the former of these systems is *(i)* extremely well described experimentally and *(ii)* possible to model by theory without introducing any severe restrictions, it represents a way of testing e.g., for a chosen 'RE metal', the

[1] In Ref. [128], the surface reconstruction for the above two wetting layers mentioned for Y on Si(001) is denoted '4×2' and '3×1'. For these experiments, however, this notation is of no significance in the sense that the authors made no attempt to distinguish between a 2×4 and a 4×2 wetting layer surface reconstruction [130].

[2] We also note that the appearance of a wetting layer with a 1×3 surface reconstruction, which is not normally observed at the point of RE disilicide nanowire growth (see Sec. 4.2.3), suggests a comparatively higher coverage of Y on the Si(001) surface away from wires and 3D islands.

reliability of theoretical predictions in the case of clearly differing theoretical results for the corresponding bulk RE disilicide with the AlB_2 structure. [3] From this point of view, especially the extensive studies of 2D Y disilicide films on Si(111) performed recently by Martín-Gago and co-workers using both experiment (LEED) and theory (SIESTA) [133, 134, 135], clarifying essentially all structural details of the surface termination Si bilayer for this system, and the MEIS studies by Wood *et al.* [136], confirming the conclusions reported in Ref. [135], stand out as potentially relevant reading for theoretical Y disilicide nanowire studies.

Experimental studies of bulk Y disilicide have produced other results of interest to the present work. The thermal expansion coefficients for Y disilicide in the AlB_2 structure, of importance to nanowire growth considerations as discussed in Sec. 4.2.3, were obtained by Mayer and Felner [137]. Ji *et al.* [97] reported that bulk Y disilicide with the AlB_2 structure is Si vacancy defected, YSi_{2-x}, with $x = 0.228 \pm 0.008$, with no long range ordering of the vacancies (in contrast with experimental results for Y disilicide 3D film growth on Si substrates). This result is strong evidence that bulk vacancy free Y disilicide in the AlB_2 structure is a purely hypothetical system.

From the computational point of view, Y (and Sc) has the great appeal compared to the actual RE metals that it has no f electrons. Structural optimization of YSi_2 and $YSi_{1.67}$ with the AlB_2 structure and, among other structural arrangements, the closely related Th_3Pd_5 structure, respectively, yielding lattice parameters comparing well with experiment for the latter case, were performed already a decade ago by Magaud *et al.* [138], using LDA and *(i)* Vanderbilt US PPs [17] as implemented in VASP [23, 24] as well as *(ii)* the full-potential linearized muffin-tin-orbital (FP-LMTO) method [139]. A study of the same systems was carried out more recently by Rogero *et al.* [140] using LDA and Troullier-Martins NC PPs [101] as implemented in the SIESTA code [108, 27] (see Ref. [135] for basis set details). [4] The structural parameters obtained were reported to differ negligibly from those reported in Ref. [138]. Very recent studies by Szwacki and Yakobson [141], using GGA [12, 13] and Vanderbilt US-PPs as implemented in the Quantum-ESPRESSO package [142], reported values highly similar, once again, to those obtained previously for vacancy free Y disilicide in the AlB_2 structure.

It is typically assumed, on the basis of the structural similarities for the bulk RE/Si systems observed for a large number of the RE metals (including Y and Sc), that general conclusions about the RE-Si bond formation as obtained for one RE metal can be transferred to the other situations where similar structural properties prevail. This suggestion was investigated in the early Y disilicide electronic structure studies by Magaud *et al.* [143, 144], primarily involving vacancy free Y disilicide in the AlB_2 structure. The authors obtained pronounced Y $4d$ - Si $3p$ hybridization near the Fermi level ϵ_F,

[3] We have confirmed the usefulness of such a test for the case RE = Er, where studies employing PAW potentials and VASP have shown that the structural parameters obtained with Er treated as formally trivalent (i.e., assuming promotion of one electron from the $4f$ to the $5d$ shell) are in very good agreement with experimental values. Unfortunately, as discussed in Sec. 6.1, there was neither time nor space to describe these studies in detail in this thesis.

[4] This group have performed studies of bulk vacancy free Y disilicide in the AlB_2 structure using other computational methods as well, but we have made the choice to highlight only the SIESTA results which differ conceptually from the remaining results listed in the paragraph.

similar to the covalent mixing of the Gd $5d$ and Si $3sp$ orbitals at ϵ_F reported in experiments by Braicovich *et al.* [145], on the basis of photoemission data for Gd_3Si_5. More recently, the theoretical studies by Rogero *et al.* in Ref. [135] for a 2D Y disilicide film on Si(111) have revealed bonds with a clear covalent character for Y and a subset of its nearest neighbour Si atoms, involving the Y $4d$ and the Si $3p$ states. This theoretical conclusion has played an important role in the interpretation of experimental STM results for the Y disilicide 3D film grown on the Si(111) surface (see Ref. [140]): the strong covalent character of the Y-Si bonds explains the unexpectedly inefficient screening of subsurface Si vacancies for the metallic film, with these vacancies consequently having a strong influence on the appearance of the STM images.

6.2.1.2 INTRODUCTION TO OUR WORK

The present section describes our work on vacancy free Y disilicide, in the bulk phase and epitaxially grown on the Si(001) surface. The focus of the discussion is on the Y disilicide nanowires on the Si(001) surface reported by Katkov and Nogami in Ref. [128]: we will discuss in Sec. 6.2.2, on the basis of *(i)* our results obtained upon structural optimization of bulk vacancy free Y disilicide in the AlB_2 structure and *(ii)* the experimental knowledge on the structure of the RE disilicide nanowires presently available, why the Y disilicide nanowires might be explained by a vacancy free AlB_2 structure, rather than the commonly assumed vacancy defected AlB_2 structure. In this discussion, we shall emphasize, initially, the importance of treating the epitaxial growth of a RE disilicide structure on Si(001) as a 1D growth phenomenon and argue that for Y disilicide, the vacancy free AlB_2 structure appears naturally as a candidate for an elongated nanostructure on the Si(001) surface if this approach is followed rigorously. Our focus on vacancy free Y disilicide nanowires in the present work will be further justified in Sec. 6.2.2, albeit indirectly, as we argue that there is, at the time of writing, no published experimental results supporting unambiguously the vacancy defected AlB_2 structure over our alternative suggestion as an explanation for the structure of the RE disilicide nanowires.

In Sec. 6.2.3, we shall turn to the actual modelling of a RE disilicide nanowire on the Si(001) surface. On a fundamental level, our approach to this issue assumes an intimate connection between RE/Si(001) wetting layers, typically reported to coexist with the growing wire in experiment, and the wire, with Sec. 6.2.3.1 clarifying the basic details of our suggested wire growth model and Sec. 6.2.3.6 discussing critically the chosen approach to this issue. The studies, as a consequence of the above remarks, involve both wetting layer calculations and wire studies. For the wires, we chose to model wires in an assumed infinitely wide bundle, for reasons to be discussed in Sec. 6.2.3.2. Finally, Sec. 6.2.3.6 discusses, as part of the topic mentioned previously, how to obtain a reliable energy for removing a Si atom from the 'reservoir' of atoms on the substrate for incorporation in the growing wire (with the Y atom reservoir being the wetting layer), needed in order to evaluate the nanowire stability.

Sec. 6.2.4 presents the results of the Y/Si(001) wetting layer studies (including the above mentioned Si atom binding energy), while in Sec. 6.2.5, the results of the Y disilicide nanowire calculations are discussed: it is shown here that for a properly chosen wire profile and surface termination, the vacancy free Y disilicide nanowire is

stable relative to having Y and Si atoms in the appropriate 'reservoirs' on the Si(001) surface. We shall summarize the results in Sec. 6.2.6, arguing, in particular, why there is reason to believe, on the basis of our considerations in Sec. 6.2.3 and Sec. 6.2.3.1 as well as the results of our theoretical studies, that it might just require writing an email in order to clarify whether the Y disilicide nanowire structure is the vacancy defected or vacancy free AlB_2 structure.

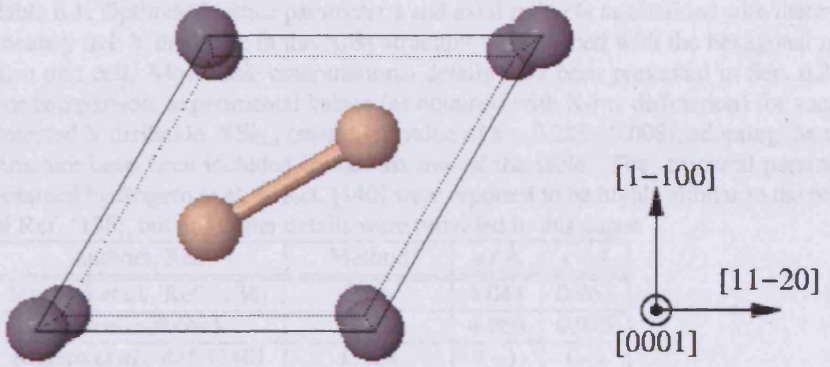

Figure 6.1: The hexagonal primitive unit cell for the AlB_2 structure (perspective view). The c (or [0001]) axis for the structure is directed out of the paper. The choice of lattice parameters refer to the theoretical values obtained for bulk vacancy free Y disilicide adopting this structure as obtained in our studies (see Table 6.2.1 for details). In the figure, the Y (Si) atoms are represented by dark grey (light brown) spheres.

6.2.2 OPTIMIZATION OF VACANCY FREE BULK Y DISILICIDE IN THE AlB_2 STRUCTURE: AN ALTERNATIVE SUGGESTION FOR THE STRUCTURE OF THE RARE EARTH DISILICIDE NANOWIRE

6.2.2.1 VACANCY FREE BULK Y DISILICIDE IN THE AlB2 STRUCTURE AS DESCRIBED WITH THE HEXAGONAL PRIMITIVE UNIT CELL

Vacancy free bulk Y disilicide in the AlB_2 structure as described with the hexagonal primitive unit cell (see Fig. 6.1) has been studied previously with DFT [138, 140, 141]. These studies were described briefly in Sec. 6.2.1.1, but further computational details have been included in Table 6.1. Earlier theoretical studies (see Sec. 6.2.1.1) used experimental values for the Y disilicide lattice parameters whereas all of the above studies involved lattice parameter optimization. As the discussion in this subsection will concentrate on the significance of the optimized lattice parameters for this structure (and other closely related structures) to Y disilicide nanowire growth on the Si(001) surface, only the above three references are of interest as previous work for the time being.

Table 6.1 shows that while the scatter in the optimized theoretical lattice parameters for the structure is quite small, the parameters are clearly different from the experimental results, with the most recently reported values from Ref. [97] included in Table 6.1 for comparison. The difference between experiment and theory is believed to be explained by the fact the theoretical results in Table 6.1 involve a vacancy free structure whereas the structure reported in experiment is vacancy defected, YSi_{2-x}, with the generally mentioned rule of thumb being $x \sim 0.33$, i.e., approximately one out of six Si

Table 6.1: Optimized lattice parameter a and axial ratio *c/a* as obtained with theory for vacancy free Y disilicide in the AlB_2 structure as described with the hexagonal primitive unit cell. Most basic computational details have been presented in Sec. 6.2.1.1. For comparison, experimental values (as obtained with X-ray diffraction) for vacancy defected Y disilicide, YSi_{2-x} (measured value of x = 0.228±0.008), adopting the same structure have been included in the last row of the table. The structural parameters obtained by Rogero et al. in Ref. [140] were reported to be highly similar to the results of Ref. [138], but no further details were provided in this paper.

Authors, Ref.	Method	*a* / Å	*c* / *a*
Magaud *et al.*, Ref. [138]	PWs	4.044	0.967
(same as above)	MTOs	4.066	0.975
Rogero *et al.*, Ref. [140]	PAOs	(-)	(-)
Szwacki *et al.*, Ref. [141]	PWs	4.108	0.960
Our studies	PWs	4.082	0.970
Ji *et al.*, Ref. [97]	Exp. (300 K)	3.842	1.078

atoms in the structure is missing. Ji *et al.* [97] measured a Si vacancy concentration of 11.4±0.4% for Y disilicide in the AlB_2 structure, with no signs of vacancy ordering in the diffraction pattern obtained for this system. We will discuss the reason for the presence of the Si vacancies in Sec. 6.2.2.11 when we analyse our complete set of optimization results for bulk Y disilicide.

Our values for the optimized AlB_2 structure lattice parameters, obtained using the PW91 GGA [12] to the exchange-correlation energy E_{xc} and Vanderbilt US-PPs [17] as implemented in VASP [23, 24], with the Y 4*p* electrons treated as core electrons, compare well with previous theoretical results (see Table 6.1). For a full discussion of the values of the adjustable parameters in the code required for acceptable convergence of the structural parameters and total energy, we refer to Sec. 6.2.2.11 (where, also, a more detailed comparison with previous results will be included). For the time being, we note that including the Y 4*p* semicore states explicitly in calculations employing Vanderbilt US PPs was found to have only a rather weak influence on the optimization results. For this reason, the discussions of our theoretical results in the present subsection will, unless otherwise noted, refer to the studies performed using Vanderbilt US PPs with the Y 4*p* electrons in the core.

Concluding on the above, when discussing the properties of bulk Y disilicide in the AlB_2 structure, the system investigated by theory in Table 6.1 is only relevant as a reference structure for investigation of the relative stability of vacancy defected configurations (see Ref. [138]). When discussing growth of RE disilicide nanostructures on the Si(001) surface, however, the situation is different: we will discuss during the rest of this subsection why the results of Table 6.1 are highly relevant for Y disilicide nanowire growth considerations, arguing that the vacancy free AlB_2 structure should be considered as a new candidate for the wire structure.

6.2.2.2 EPITAXIAL GROWTH OF THE VACANCY DEFECTED AND VACANCY FREE AlB2 STRUCTURES ON THE Si(001) SURFACE

As discussed in Sec. 4.2.3, an explanation for the structure of the RE disilicide nanowires on the Si(001) surface was put forth by Chen *et al.* in Ref. [146], on the basis of experimental investigations of Er disilicide nanowires on Si(001). The authors identified the growth plane for epitaxial growth of Er disilicide with the vacancy defected AlB_2 structure on this surface and argued, from comparison of the lattice parameters along the perpendicular directions in this plane (using the lattice parameters for bulk Er disilicide), that growth of a highly elongated nanostructure on the Si(001) surface was to be expected for Er disilicide adopting this structure. In the present part of the subsection, we shall go through this generally accepted explanation for the structure of the RE disilicide nanowires on Si(001) in more detail, making explicit reference to the Y disilicide nanowire system of key interest in the present work. Furthermore, we shall consider not only epitaxial growth of vacancy defected Y disilicide nanowires with the AlB_2 structure but also the conclusions obtained upon applying the same set of arguments to the situation where the Y disilicide overlayer is assumed to be vacancy free, still adopting the AlB_2 structure, but with the lattice parameters now being significantly changed, as described in Sec. 6.2.2.1. As will be discussed below, there is reason to believe, on the basis of these considerations, that also vacancy free Y disilicide in the AlB_2 structure can grow elongated nanostructures on the Si(001) surface (although, on the basis of the arguments presented in this part of the subsection, we shall not be able to make a definite statement on whether these nanostructures are sufficiently elongated to deserve the name 'nanowires').

The epitaxial growth of RE disilicide nanowires with the AlB_2 structure on a Si(001) surface as explained by Chen *et al.* in Ref. [146] is shown in Fig. 6.2. The orientation relationship of substrate and overlayer is identified initially, in two steps: at first, we note that, when viewed in projection onto the [1-100] plane, the AlB_2 structure is found to be comprised by planes of Si and RE metal atoms, with the atoms in each plane ordered in a rectangular pattern. On the basis of this remark, we conclude that epitaxial growth of the AlB_2 structure on the Si(001) surface should be associated with having the [0001] axis for the overlayer structure parallel to a <110> axis for the substrate and the [11-20] axis for the overlayer structure perpendicular to this <110> axis. This argument reduces the possible relative orientation of substrate and overlayer to two configurations, distinguished by a rotation of 90° around the substrate normal. In order to fully determine the lattice relationship needed to explain the epitaxial RE disilicide growth, we note that the growth of the AlB_2 structure on Si(001) does not involve matching of only one Si plane for the overlayer and substrate structure: from Fig. 6.2, where the usual reconstruction of the Si(001) surface has been ignored, corresponding to Si dimer bond breaking in the process of the RE disilicide growth on the surface, it is evident the [0001] axis for the AlB_2 structure should be in the direction perpendicular to the Si dimer row direction before growth. This essentially is a consequence of the fact that substrate and overlayer structurally have not only one but two layers in common. [5]

[5] We emphasize that the current discussion of epitaxial growth of RE disilicide on the Si(001) surface is

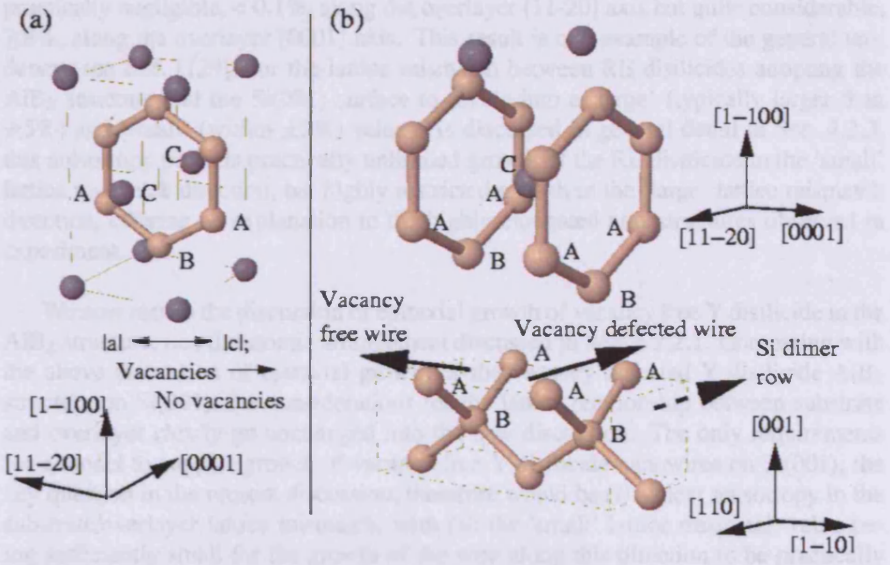

Figure 6.2: Illustration of epitaxial growth of Y disilicide with the AlB_2 structure on a Si(001) surface and how this can explain the appearance of Y disilicide nanowires. Fig. 6.2 (a) shows the AlB_2 structure (see Fig. 6.1 for details). The lower part of Fig. 6.2 (b) shows a selected area (surface dimension 3.84 × 3.84 $Å^2$) on the Si(001) surface containing only atoms from the uppermost three layers of the substrate and with no dimerization of the uppermost atoms (A). The dotted arrow shows the Si dimer row direction obtained with dimerization. The labelling A and B in Fig. 6.2 (b) shows the one-to-one correspondence of the two uppermost two layers for the substrate and the lowest two layers for the AlB_2 structure (upper part of this figure), which explains the epitaxial growth. If the AlB_2 structure is vacancy defected (approximately one out of six Si atoms missing, $YSi_{1.67}$), anisotropic overlayer/substrate lattice mismatch leads to a wire growing parallel to the Si dimer rows on the surrounding terrace (as emphasized by a solid arrow in the figure). For a vacancy free wire, the lengths of the AlB_2 structure lattice parameters in the growth plane are almost perfectly interchanged (Fig. 6.2 (a)) and wire growth perpendicular to the Si dimer rows on the surrounding terrace is predicted.

In order to explain why this growth process should yield highly elongated nanostructures on the Si(001) surface, the experimental lattice parameters for substrate and overlayer in the growth plane are compared: taking Y disilicide as the example here and using RT values (see Table 6.1), [6] we find (with the substrate interatomic distance along the <110> axes being 3.840 Å) that the substrate/overlayer lattice mismatch is practically negligible, < 0.1%, along the overlayer [11-20] axis but quite considerable, 7.8%, along the overlayer [0001] axis. This result is one example of the general tendency (see Ref. [129]) for the lattice mismatch between RE disilicides adopting the AlB_2 structure and the Si(001) surface to divide into a 'large' (typically larger than ±5%) and 'small' (within ±2%) value. As discussed in general detail in Sec. 4.2.3, this anisotropy predicts practically unlimited growth of the RE disilicide in the 'small' lattice mismatch direction, but highly restricted growth in the 'large' lattice mismatch direction, offering an explanation to the highly elongated nanostructures observed in experiment.

We now turn to the discussion of epitaxial growth of vacancy free Y disilicide in the AlB_2 structure, i.e., the atomic arrangement discussed in Sec. 6.2.2.1. Comparing with the above discussion of epitaxial growth of the vacancy defected Y disilicide AlB_2 structure on Si(001), the considerations for the lattice relationship between substrate and overlayer clearly go unchanged into the new discussion. The only requirements for a model to support growth of vacancy free Y disilicide nanowires on Si(001), the key question in the present discussion, therefore would be *(i)* a clear anisotropy in the substrate/overlayer lattice mismatch, with *(ii)* the 'small' lattice mismatch value being sufficiently small for the growth of the wire along this direction to be practically unrestricted. The division into points *(i)* and *(ii)* is deliberate: from the general considerations in Sec. 4.2.3, the anisotropy in the lattice mismatch values is to be considered a necessity for the growth of elongated islands, of which the true nanowires (as defined by the dimensions of the structure, see Sec. 4.2.1) is a subgroup. The requirement on the 'small' lattice mismatch value in point *(ii)*, however, is more uncertain, the ±2% range mentioned previously in this subsection being obtained on the basis of the assumption that the RE disilicide nanowires adopt the vacancy defected AlB_2 structure, with the limits established through the observation that RE disilicides with a larger value for the 'small' lattice mismatch do not form wires on the Si(001) surface (see e.g. Ref. [129, 98]). [7] When discussing growth of nanowires with a different structure, we

not meant to clarify the details of the substrate/overlayer interface. We have assumed in Fig. 6.2 that the lowest layer of the nanostructure relative to the surrounding clean areas of the same terrace of the substrate is a RE metal layer. However, the arguments presented above would still hold true if we assumed that the lowest layer for the nanostructure was a Si layer (followed by a RE metal layer, counting from the bottom of the nanostructure). This change of interface would lead to a change in the growth direction of the nanostructure, but the present discussion is not concerned with this issue either.

[6] We shall discuss below how the lattice mismatch values are affected if the substrate and overlayer lattice parameters are compared at the wire growth temperature.

[7] The authors of Ref. [98] argued that the range of 'small' lattice mismatch values to be associated with RE disilicide nanowire growth on Si(001) was smaller than ±2%. This conclusion was obtained on the basis of the lack of support for wire growth upon deposition of Sm and Yb the Si(001) surface. More recently, wire growth has been reported for both of these elements (see references cited in Ref. [87]). No Nd disilicide wire growth ('small' and 'large' lattice mismatch values of 7.29% and 15.6%, respectively) has been reported in experiment, however, supporting the conclusion that a large anisotropy in the lattice mismatch values is

can only, without further knowledge, require that the 'small' lattice mismatch value is numerically 'within a few percent'.

The key obstacle to determining the substrate/overlayer lattice mismatch values for epitaxial growth of vacancy free Y disilicide in the AlB_2 structure is the fact that bulk YSi_2 has not been observed in experiment. Simply comparing the theoretical lattice parameters for the substrate and overlayer in order to obtain these values does not seem recommendable: one suggestion that this approach is unlikely to yield reliable results can be made on the basis of the results for lattice mismatch values obtained using the theoretical lattice parameters for bulk $YSi_{1.67}$ [138], i.e., the structure discussed at the beginning of this part of the subsection. The study in Ref. [138], which involved using $\sqrt{3} \times \sqrt{3}$ R30 supercells, allowing for various vacancy orderings along the c axis (including the ordering reported in experiment for RE disilicide 3D film growth on Si(001)), gave lattice parameters a = 3.759 Å, c = 4.067 Å. Keeping the Si(001) surface lattice parameter fixed at 3.84 Å for simplicity in this discussion, justified by the fact that the theoretical error is known to be very small (see Sec. 8.1), we obtain small and large lattice mismatch values of -2.2% and 5.9%, respectively. For one thing, this means that, strictly speaking, a purely theoretical study of the epitaxial growth of vacancy defected Y disilicide with the AlB_2 structure on Si(001) does not predict growth of nanowires with this structure, as the numerical value for the 'small' lattice mismatch is larger than 2%. Of more concern, however, the change in the predicted lattice mismatch values in this study compared to the experimental values presented previously in this part of the subsection are so significant, $\sim$ 2.0%, that the conclusions obtained for the substrate/overlayer lattice mismatch values clearly have very little value on their own. Evidently, for the discussion of the growth of vacancy free Y disilicide nanowires with the AlB_2 structure on Si(001), some correction of the theoretical parameters obtained in Sec. 6.2.2.1 must be required. This correction, however, will have to be made on the basis of information obtained from comparison between experimental and theoretical parameters for another RE disilicide structure.

For reasons to be described below, we have not been able to find any structure suitable for this task. Discussing briefly the candidates considered one by one, the vacancy defected AlB_2 structure, being the first of these candidates, has the appeal that it is structurally closely related to the vacancy free AlB_2 structure, although the c/a ratios differ markedly (see Table 6.1). However, with one out of six Si atoms removed from the Y disilicide, the cohesion of the structure will be clearly affected and the difference between the theoretical and experimental lattice parameters will almost certainly change, perhaps significantly. In general, therefore, adjustment of theoretical results obtained for $RESi_2$ on the basis of comparison between theoretical and experimental results for $RESi_{1.67}$ therefore seems questionable.

The 2D Y disilicide film grown on a Si(111) substrate, the second candidate considered, shares the similarity of the presence of graphite-like Si planes with the bulk vacancy free AlB_2 structure. However, it is not a bulk system and the scatter in the interatomic distances is comparatively much larger as a consequence of the increased amount of structural relaxations possible for especially the uppermost layer of the film. This is clearly reflected in the results obtained in calculations by Rogero *et al.* [135]

insufficient for wire growth.

for 2D Y disilicide on Si(111): the calculated Si-Si distances almost perfectly match experimental values (as obtained in the same paper) whereas the theoretical predictions for the Y-Si distances are between 1.4 and 4.4% shorter than measured distances. To our knowledge, comparisons between optimized theoretical and experimental structural parameters for 2D RE disilicide films on Si(111) have not been reported for the actual RE metals (although calculations involving structural optimization have been performed for 2D Er disilicide on Si(111) [147]). However, on the basis of the above discussion for the 2D Y disilicide film, it seems sensible to suggest that in general, obtaining the difference between the theoretical and experimental interatomic distances for the overlayer atoms of the 2D RE disilicide growing on a Si(111) substrate does not provide a well-defined (or at least not a simple) recipe for evaluating the difference between theoretical and experimental parameters for a bulk RE disilicide.

The final candidates considered here are the $ThSi_2$ and $GdSi_2$ structures (discussed very briefly in Sec. 4.2.3), which have both been observed in growth of Y disilicide 3D films on a Si(001) substrate (see Ref. [148]). Apart from being bulk structures they both have the appeal, for the present purpose, of not being vacancy defected. Unfortunately, interpretation of the results of our preliminary theoretical studies of these systems, to be discussed in Sec. 8.3.3, is problematic: optimization yields a $ThSi_2$ structure which is significantly stretched along the *b* axis of the experimental unit cell, the theoretical *b* lattice parameter being 8.3% larger than the experimental result [148], while the theoretical *a* lattice parameter is smaller than the experimental value by 1.6%. [8] We suspect (see Sec. 8.3.3 for details) that this large difference is associated with lack of *k* mesh convergence in our theoretical studies, but the investigations carried out so far are not sufficiently thorough to act as definite support for this suggestion. At present, therefore, while we do not exclude the $ThSi_2$ and $GdSi_2$ structures as reliable candidates for estimating the difference between theoretical and experimental lattice parameters for the bulk vacancy free AlB_2 structure (expecting that the $GdSi_2$ structure might be stabilized according to theory upon increasing the number of *k* points in the IBZ), the results obtained for the theoretical bulk Y disilicide $ThSi_2$ structure lattice parameters in Sec. 8.3.3 appear too uncertain for such corrections to be considered at the present stage. To our knowledge, no results of structural optimization for RE disilicides with the $ThSi_2$ or $GdSi_2$ structure (which could shed further light on this issue) have been published at the time of writing.

In the absence of a reliable correction of the theoretical lattice parameters $a = 4.082$ Å, $c = 3.960$ Å obtained for bulk vacancy free Y disilicide in the AlB_2 structure as described in Sec. 6.2.2.1, we can only discuss growth of vacancy free Y disilicide with this structure on the Si(001) surface, using the epitaxial growth model shown in Fig. 6.2, on the basis of a comparison of these lattice parameters with the Si(001) surface lattice parameter. Assuming, once again, a theoretical Si(001) surface lattice parameter of 3.84 Å for simplicity, the substrate/overlayer lattice mismatch values obtained from this consideration are 3.1% and 6.3%. In other words, there is a clear anisotropy in the lattice mismatch, suggesting growth of elongated nanostructures on the surface and furthermore, the 'small' lattice mismatch value is not far too large for

[8] Optimization of bulk Y disilicide in the $GdSi_2$ structure takes this atomic arrangement into the $ThSi_2$ structure.

these nanostructures to be connected potentially (depending on the above mentioned correction) with nanowires. We regard these results as sufficiently encouraging to include the vacancy free AlB_2 structure in the discussions below in this subsection as a potential candidate for the structure of the Y disilicide nanowire.

The above discussion of epitaxial growth of RE disilicides on the Si(001) surface compared RT values for the substrate and overlayer lattice parameters in order to reach conclusions regarding the possibility of nanowire growth. As noted initially by Nogami *et al.* [98], however, the thermal expansion coefficient for RE disilicides is generally significantly different from that of Si, meaning that at the temperatures of $\sim$ 875 K where the wires actually grow (see Sec. 4.2.3), the lattice mismatch will be different. For Y disilicide, suggestions of the importance of this correction have been made on the basis of experimental results for epitaxial growth of the AlB_2 structure on a Si(111) substrate [149]. The thermal expansion coefficient for Y disilicide in the AlB_2 structure has been measured by Mayer and Felner, see Ref. [137]. [9] Using their reported values, $\alpha_a = 6.8 \times 10^{-6}$ / K, $\alpha_c = 7.1 \times 10^{-6}$ / K, and the value $\alpha = 2.6 \times 10^{-6}$ / K for bulk Si, we find that the 'small' and 'large' lattice mismatch for epitaxial growth of vacancy defected Y disilicide in the AlB_2 structure on Si(001) change from the previously obtained values of '< 0.1' and 7.8% to 0.3 and 8.2%. For vacancy free Y disilicide, the (theoretically obtained) values change from 3.1 and 6.3% to 3.3 and 6.6%. [10] Concluding, the fact that the wires grow at $\sim$ 875 K rather than RT does have an effect on the lattice mismatch values but the conclusions obtained previously for Y disilicide are unaffected by this correction.

6.2.2.3 ON THE IMPORTANCE OF ACKNOWLEDGING RE DISILICIDE NANOWIRE FORMATION AS A 1D GROWTH PHENOMENON

As discussed in Sec. 4.2.3, the RE disilicides have been reported to adopt up to three different structures when growing epitaxially as 3D films on the Si(001) surface. In general, on the basis of substrate/overlayer lattice mismatch considerations, only one of these structures, the AlB_2 structure, can explain nanowire growth (for further details, see Sec. 4.2.3): for the alternatives, the $ThSi_2$ and $GdSi_2$ structures, compact 3D island growth is predicted. In addition to this basic argument, the growth of 3D islands is typically (see e.g. Ref. [151]) reported to dominate wire growth upon increasing the annealing temperature in experiment. [11] This observation, along with the lattice

[9] These results were obtained for YSi_2 according to the authors but we regard them as describing YSi_{2-x} for the following reasons: *(i)* as discussed in Sec. 6.2.2.1 (see Ref. [97]), bulk Y disilicide adopting this structure has been reported to be vacancy defected, YSi_{2-x}, but with no vacancy ordering, the presence of Si vacancies therefore not being revealed in an X-ray diffraction experiment. This can explain why no attention was made to the possibility of vacancies in Ref. [137]. In addition *(ii)*, the results in Ref. [137] for '$ErSi_2$' hardly differ from the results for $ErSi_{2-x}$ recently reported by Yang *et al.* in Ref. [150].

[10] As bulk vacancy free Y disilicide has not been observed in experiment, we use the thermal expansion coefficients for YSi_{2-x} as well for the temperature correction of the YSi_2 lattice parameters. As the key point of the discussion is these corrections being of secondary importance, the errors introduced by this choice should not affect the conclusion.

[11] Experimental observations [152]of compact RE disilicide 3D islands with the AlB_2 structure upon deposition of several ML of RE metal on the Si(001) surface suggest that one should be very cautious about associating a compact island uncritically with the RE disilicide adopting the $ThSi_2$ or $GdSi_2$ structure. We

mismatch considerations, is in good agreement with experimental observations from growth of RE disilicide 3D films on Si(001) where the $ThSi_2$ and $GdSi_2$ structures have been reported to grow preferentially at annealing temperatures well above the nanowire stability range. Thus, starting with this set of structures as the set of possible candidates for the structure of RE disilicide nanowires, it seems well established that the AlB_2 structure is the only realistic candidate.

This line of thought, essentially the one put forth by Chen *et al.* when presenting the AlB_2 structure as the candidate for the Er disilicide nanowire structure in Ref. [146], has the basic flaw, however, that it applies information obtained from 3D film growth to a situation involving 1D growth on the Si substrate. The effect of the substrate/overlayer lattice mismatch on the overlayer structure is acknowledged, but only to the extent that the overlayer structure is assumed to be elastically strained to fit the substrate. The conclusion for the case of Y disilicide, described in Sec. 6.2.2.2, that formation of elongated nanostructures, perhaps true nanowires, with the vacancy free AlB_2 structure is also a possibility according to this model fully emphasizes the limitations of this approach: the vacancy free AlB_2 structure is certainly closely related to the vacancy defected AlB_2 structure but the change of the cell dimensions in the absence of vacancies and its consequences for nanowire growth as described in Fig. 6.2 could not have been predicted on the basis of 3D film growth information.

We can not perform a fully complete study of an epitaxial 1D growth phenomenon by describing the overlayer structure with an extended 3D system, varying the structural parameters for this system in the search for substrate/overlayer lattice mismatch values predicting nanowire growth. In particular, surface termination issues for a given nanowire structure evidently will have to be studied separately for that structure. Keeping this limitation in mind, requiring that our chosen approach to investigating epitaxial growth of vacancy free RE disilicide nanowires on the Si(001) surface suffers from as few restrictions as possible, we find that the optimization of the vacancy free AlB_2 structure as described in Sec. 6.2.2.1 involves a potentially important restriction. The calculations described so far have all involved the hexagonal unit cell for this structure (see Fig. 6.1). When consulting Fig. 6.2, however, it is evident that this choice of cell involves, effectively, a coupling of the nanowire interatomic distances in the direction perpendicular to the substrate (growth) plane to the wire interatomic distances along one direction in the growth plane. When addressing the issue of wire growth, there is no justification for this restriction: optimization involving one or more cells without this coupling present clearly is needed in order to see how the lattice parameters in the RE disilicide nanowire growth plane will be affected.

We have performed two additional optimization studies of vacancy free Y disilicide, starting in both cases at the optimized parameters for the AlB_2 structure, but allowing for various additional distortions of this structural arrangement. The initial study involved a complete optimization of all structural parameters, including cell shape, of the unit cell shown in Fig. 6.1. This study yields information on the registry and interlayer distances for the lowest three layers in the nanowire, assuming that the

still regard inclusion of the above statement as justifiable as we are not aware of any experimental reports on comparatively large elongated RE disilicide nanoislands adopting the $ThSi_2$ or $GdSi_2$ structure.

set of interatomic distances within each layer remains the same for all layers. Additional studies were performed with the orthorhombic cell shown in Fig. 6.2 (a). This cell, containing twice as many layers in the direction perpendicular to the Y disilicide nanowire growth plane, allows, in addition to the properties described for the smaller cell, for further modulation of the interlayer distances. We have not considered extending the cell dimensions along the directions in the wire growth plane, i.e., testing the above mentioned assumption on the intralayer distances: any important structural distortions revealed in such studies should ultimately be revealed when the actual wire growth is studied. These studies did not reveal any structural instabilities and we shall therefore postpone a detailed discussion until Sec. 8.3.2. [12]

It is useful to summarize at this point, as the arguments presented in this part of the subsection have significantly affected our interest in vacancy free Y disilicide with the AlB_2 structure as a potential explanation for the structure of the experimentally reported [128] Y disilicide nanowires on Si(001): when discussing growth of Y disilicide nanowires with this structure in Sec. 6.2.2.2, our main argument for further studies into this issue was the appearance of an anisotropic lattice mismatch with a 'small' lattice mismatch value of only a few percent for epitaxial growth of vacancy free Y disilicide with the AlB_2 structure on the Si(001) surface as obtained using, rather uncritically, the model presented by Chen *et al.* in Ref. [146]. In the above discussion, however, we have shown that when dealing appropriately with epitaxial growth of Y disilicide nanowires on the Si(001) surface by describing this process as a 1D growth phenomenon, [13] the vacancy free AlB_2 structure appears naturally as a potential candidate for the structure of this system, on equal footing with the vacancy defected AlB_2 structure. In other words, the results obtained in Sec. 6.2.2.2 are not to be regarded as some kind of coincidence: epitaxial growth of an elongated vacancy free Y disilicide nanostructure, perhaps a nanowire, adopting the AlB_2 structure makes perfect sense. [14]

As the conclusions obtained for the lattice mismatch in Sec. 6.2.2.2 are still key to the suggestion that the Y disilicide nanowires might adopt the vacancy free AlB_2 structure, we should clearly be cautious about generalizing the above, suggesting that the RE disilicide nanowires on Si(001) might be explained in general by the vacancy free rather than the vacancy defected AlB_2 structure. On the other hand, given the high level of similarity for these wires, this thought is intriguing. The discussions in the rest of this subsection will make this suggestion even more interesting: admitting that the vacancy defected AlB_2 structure can be challenged, in principle, as a candidate for

[12] Our optimization has been started using layer registries and structural parameters appropriate for the AlB_2 structure: thus, we can not make the claim that it is truly 'complete' in the sense indicated in the text. This choice has been made solely on the basis of the remarks at the beginning of this part of the subsection: as the AlB_2 structure is strongly favoured as the candidate for a RE disilicide nanowire structure compared to the other structures observed upon RE disilicide 3D film growth on Si(001), we have, in summary, restricted our current studies of possible nanowire candidate structures essentially to structural arrangements closely related to this structure. For corresponding studies of vacancy defected RE disilicide nanowire growth on Si(001), the same approach as described in the text would apply, but with introduction of vacancies in various 'relevant' orderings.

[13] As appropriately as can be done in a study which uses only information on the overlayer structure obtained from a study of the bulk phase with this structure, see remarks above in the text for details.

[14] Only, for higher RE metal coverages, i.e., 3D film growth, where different growth conditions (bulk conditions, essentially) prevail, the vacancy free AlB_2 structure evidently is not observed.

the RE disilicide nanowire structure, the next logical question to ask is whether any unambiguous experimental support exists for the RE disilicide nanowires adopting this structure. We will go through the various significant comments on this issue made in the literature below and show that in all cases discussed so far, when put to the test, the answer to the above question is 'no': up to this point, as will be fully clarified below, there have been no experimental conclusions reported on the RE disilicide nanowires on the Si(001) surface which clearly support the vacancy defected AlB_2 structure over the vacancy free AlB_2 structure as an explanation for the structure of these systems.

6.2.2.4 A SURVEY OF THE PUBLISHED EXPERIMENTAL CONCLUSIONS ON THE RARE EARTH DISILICIDE NANOWIRE STRUCTURE: INTRODUCTORY REMARKS

With only few exceptions in the literature [153, 154], the suggestion by Chen *et al.* [146] that the RE disilicide nanowires on the Si(001) surface should be explained by a vacancy defected AlB_2 structure has been accepted without any theoretical and fairly little experimental support, with the last point to be evidenced through the rest of this subsection. The main reason for this is the extremely strong experimental support for epitaxial growth of the RE disilicide nanostructures on the Si(001) surface (see Sec. 4.2.3) combined with the fact that, as discussed in Sec. 6.2.2.3, the vacancy defected AlB_2 structure is the only structure from the set of RE disilicide structures growing as 3D films on Si(001) which satisfies the requirements for substrate/overlayer lattice mismatch values to be associated with nanowire growth according to theory (see Sec. 4.2.3).

This support evidently is insufficient, however, when introducing the alternative suggestion (see Sec. 6.2.2.3 for details) that the RE disilicide nanowires, while still adopting the AlB_2 structure, might be vacancy free. Our preliminary theoretical studies of Y disilicide nanowire growth on Si(001) in Sec. 6.2.2.2 have suggested that these two candidates for the nanowire structures differ in an important respect, the wires growing in mutually perpendicular directions for the same choice of substrate/wire interface. The question, however, remains at the present stage of the discussion whether this information is sufficient to choose one candidate for the wire structure over the other, [15] and, if not, whether there are other ways to identify the structure of the wire on the basis of experimental information.

Although we shall eventually address this issue in full detail, the aim of the discussions in the present subsection will be more modest: the focus at this stage will be on the conclusions from experiments on the RE disilicide nanowires on the Si(001) surface which have been used in the literature as support for the wires adopting the vacancy defected AlB_2 structure. We shall critically discuss all these suggestions and ultimately show that in none of these cases does one obtain unambiguous support for this wire structure. These considerations however do provide us with valuable input for the considerations on how to model theoretically the RE disilicide nanowire system. We shall present these initial considerations in Sec. 6.2.3.1. For a full discussion

[15] In addition, one might ask the question whether we are certain that the changes in the lattice parameters predicted by theory for Y disilicide in the AlB_2 structure in the absence of Si vacancies would be observed for the RE metals in general. We shall discuss in Sec. 6.2.2.11 why we believe that this would be the case.

of whether the RE disilicide nanowire structure is more likely to be explained by the vacancy defected or the vacancy free AlB_2 structure, we refer to Sec. 6.2.6.

For clarity, the considerations below are clearly divided according to the general topic of discussion: we shall evaluate below the experimental support for the RE disilicide nanowires adopting the vacancy defected AlB_2 structure made on the basis of observations for *(i)* the wire width (Sec. 6.2.2.5), *(ii)* the wire height (Sec. 6.2.2.6), *(iii)* the wire surface termination (Sec. 6.2.2.7), *(iv)* the wire profile (Sec. 6.2.2.8), and *(v)* the wire growth direction (Sec. 6.2.2.9).

With the exception of the X-ray diffraction studies of Er disilicide nanowires on Si(001) by Harako *et al.* in Ref. [99] and the TEM studies of Dy disilicide nanowires on this surface by He *et al.* in Ref. [154], the discussions in Sec. 6.2.2.5 - 6.2.2.9 will deal with the entire amount of published direct experimental knowledge on structural details for the RE disilicide nanowires on Si(001). [16] We have excluded the experimental results in Ref. [99] as the data were collected for wires growing on a flat substrate, i.e., involving scattering from wires growing in mutually perpendicular directions. Considering that the two nanowire candidate structures presented in Sec. 6.2.2.2, when including the effects of strain due to the wire/substrate interaction, differ primarily by their growth direction (see Fig. 6.2), we do not, from the outset, regard the X-ray diffraction data in Ref. [99] as providing definite support for e.g. the vacancy defected AlB_2 structure over the vacancy free AlB_2 structure as the explanation for the experimentally observed Er disilicide nanowire structure. X-ray diffraction data collected for RE disilicide nanowires growing on vicinal Si(001) might provide support for a particular wire structure, but to our knowledge, the results of such experiments have not been reported at the time of writing. The TEM studies by He *et al.* [154] will be discussed in Sec. 6.2.2.10. We shall argue at that point why we would be cautious about drawing conclusions about the structure of the RE disilicide nanowires on the basis of these studies.

6.2.2.5 A SURVEY OF THE EXPERIMENTAL STUDIES INTO THE RARE EARTH DISILICIDE NANOWIRE WIDTH

The RE disilicide nanowire epitaxial growth model first put forth by Chen *et al.* in Ref. [146] assumes, on a general level, that the overlayer structure is elastically strained in order to fit the substrate, the width of the wire being limited, ultimately, by the continuing increase in wire strain energy (see Sec. 4.2.3 for general remarks). On the basis of this model, one would expect some relation (although not necessarily a very simple one) to be present between the 'large' substrate/overlayer lattice mismatch value for growth of a given RE disilicide nanowire on the Si(001) surface and the typical width(s) observed in experiment for these wires. Such a relation, if obtained to a reasonable level of accuracy and applicable to a variety of RE disilicide structures, would have the appeal that various nanowire candidate structures with sufficiently large

[16] We have also excluded results of experimental studies on the '3D RE disilicide nanowires' on the Si(001) surface [155, 156] from the discussions of this subsection to the extent that we do not regard it as well established that these systems adopt the same structure as the true nanowires (see Sec. 4.2.3 for details).

differences in the value of the 'large' lattice mismatch could be termed likely or less likely candidates simply on the basis of their 'large' lattice mismatch value.

The intuitive assumption of an elastically strained overlayer structure has received direct support from experiment: the mismatch values between the lattice parameters for broad Dy disilicide nanowire $c(2\times2)$ surface unit cells and the Si(001) surface lattice parameter as reported by Liu and Nogami using STM [157] show a clear dependence on the number of layers for the wire with this structure being increasingly well strained to fit the substrate as the number of layers is reduced. [17] These experimental studies did not yield information on the wire strain along the wire width direction for the wires with the lowest number of layers, however.

Chen *et al.* presented a theoretical model for evaluation of the typical width of an Er disilicide nanowire in Ref. [158]. Their approach to this issue assumed only strain along the wire width direction, with the wire treated as particles connected by identical springs influenced by a harmonic substrate potential (corresponding to 'small' distortions of the overlayer structure). Balancing wire strain and sidewall energies, the authors obtained a minimum energy wire width of ~ 27 Å, in fair agreement with experimental observation [146]. The study in Ref. [158] suffered, however, from the fact that a series of unknown RE disilicide related model parameters were approximated. To our knowledge, results obtained on applying this model to a larger number of RE disilicide nanowire systems, with more justifiable choices for the model parameters, have not been reported.

More recently, the growth of anisotropically strained nanostructures on a substrate has been investigated on a more general level by other groups [159, 160, 161]. Pradhan *et al.* [160] have argued that regarding the growth of these nanostructures along the direction of the small substrate/overlayer lattice mismatch as essentially unlimited is too simplistic, the suggested key parameter to explaining the wire dimensions being connected with the ratio of the two lattice mismatch values. This result has received some attention in the RENW community [150], but it remains that the conclusions obtained are yet to be properly tested against experimental results for the RE disilicide nanowires.

A less elaborate test of strain perpendicular to the RE disilicide nanowire growth direction being a key factor for the wire width has involved comparison of the maximum width for the wire and the width obtained by demanding that the accumulated overlayer/substrate lattice mismatch, as measured from the wire centre, can be no greater than half the Si(001) surface lattice parameter (see Fig. 6.3): such a correlation was mentioned by Nogami *et al.* in Ref. [98] where it was noted that both Dy and Ho disilicide nanowires display a behaviour in reasonable agreement with this simple rule. Subsequent studies in Ref. [131, 157] for these elements further supported this suggestion, but other studies have yielded a very different conclusion: the experimental results obtained by Chen *et al.* [129] for RE disilicide nanowire growth on Si(001) with a a series of different RE metals, including Dy, suggest a correlation with the average wire

[17] We note that the mismatch values for islands no. VII and VIII in Table I of Ref. [157] refer to islands at nanowire junctions, possibly with a structure different from the wire structure.

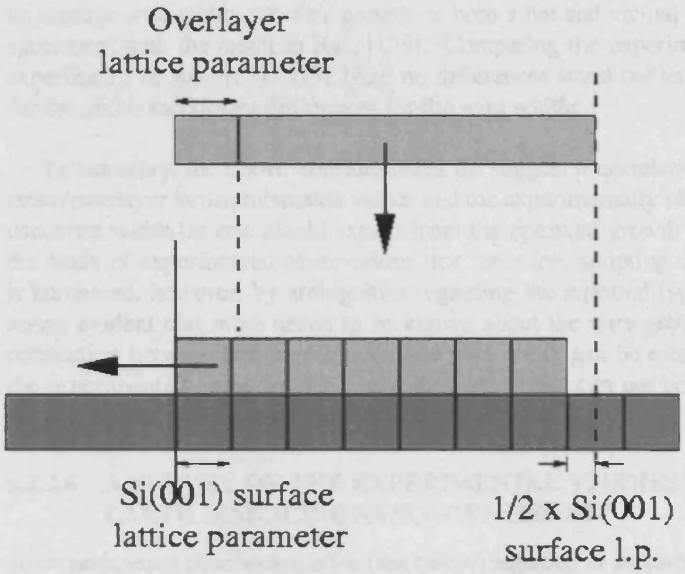

Figure 6.3: Schematic presentation of the model presented by Nogami *et al.* [98] for determination of the maximum width of the RE disilicide nanowire on the Si(001) surface. In the figure, the substrate (overlayer) has been described by a dark grey (light grey) box with the respective lattice parameters indicated for the two structures in the absence of interaction between overlayer and substrate (top grey box in the figure for the overlayer). The wire direction is into the paper. Symmetry of the wire structure with respect to the plane running through the center of the wire, along the wire direction (vertical solid line in the figure) has been assumed, the arrow in the left of figure indicating continuation of the wire structure along this direction. The wire width, according to the model in Ref. [98], is limited by the accumulation of the mismatch between substrate and overlayer along this direction, with the limit obtained at the point where the unit cell for the wire, in the absence of interactions between overlayer and substrate, would be displaced by half a Si(001) surface lattice parameter compared to the situation at the center of the wire. For the actual wire growth, the wire structure is expected to be elastically strained to fit the substrate (bottom grey box in the figure), the model therefore in practice referring to accumulation of strain, rather than change of registry. This model has been supported by some experiments whereas other experiments suggest growth of significantly wider wires (see text for details).

width and the theoretically predicted width obtained by following the guidelines in Ref. [98]. [18] This is clearly at odds with the conclusions obtained in Ref. [131, 157] where the wire widths are accumulated far below the maximum width. More recent studies of Er disilicide nanowire growth on Si(001) by Zhou *et al.* [163] have reported an average wire width, for wire growth on both a flat and vicinal Si substrate, in good agreement with the result in Ref. [129]. Comparing the experimental details for the experiments of Ref. [131, 129, 163], no differences stand out as an easy explanation for the above mentioned differences for the wire widths.

In summary, the above considerations do suggest a correlation between the substrate/overlayer lattice mismatch values and the experimentally observed RE disilicide nanowire width, as one would expect from the epitaxial growth model. Support, on the basis of experimental observations, for the wires adopting a particular structure is hampered, however, by ambiguities regarding the reported typical wire widths. It seems evident that more needs to be known about the wire growth before a reliable connection between lattice mismatch and wire width can be established. At present, the experimentally reported RE disilicide wire widths can not be regarded as reliable support for the wires adopting a particular structure.

6.2.2.6 A SURVEY OF THE EXPERIMENTAL STUDIES INTO THE RARE EARTH DISILICIDE NANOWIRE HEIGHT

An experimental observation often (see below) regarded as support for the RE disilicide nanowires adopting the vacancy defected AlB_2 structure is the measurement of the wire structural parameters in the direction perpendicular to the growth plane. Nogami *et al.* mentioned in their initial studies of Dy and Ho disilicide nanowire growth on Si(001) in Ref. [98] that the only allowed vertical growth of the wires, typically observed upon wire bundle formation, appears to be in steps of three layers (i.e., one RE disilicide structure unit cell dimension, see Fig. 6.2). This suggestion was strongly supported in subsequent studies by the same group [131, 157] of both of these systems. For the Dy disilicide nanowires investigated in Ref. [157], a wire plateau height difference of 3.4 ± 0.2 Å, as obtained with STM, was reported, with an example of a single measurement shown in Fig. 6.4. The authors noted a good agreement between this value and the distance of 3.31 Å between three consecutive layers along the [1-100] direction for the corresponding bulk vacancy defected Dy disilicide in the AlB_2 structure, obtained here using the RT experimental lattice parameters for this structure reported in Ref. [150]. The same conclusion was obtained for the Ho disilicide nanowires [131] and, more recently by Zhu *et al.* [151] in studies of Er disilicide nanowires on Si(001), whereas Preinesberger *et al.* [153] obtained a comparatively higher plateau height difference, 3.9 ± 0.3 Å, in their studies of Dy disilicide nanowires. The determination of height

[18] More specifically, Fig. 4 (a) in Ref. [129], showing the average wire width for the various RE disilicide nanowires studied, reveals a dependence of the wire width on the type of Si terrace on the miscut substrate (supported by more recent studies, see e.g. Ref. [162]), with agreement between the predicted wire widths and the 'narrow wire' set of widths in the figure. The difference in wire widths (and heights) on different terraces might be connected with the adatom diffusion on the two types of terraces displaying different behaviours, leading to different growth rates for the wires. Experiment [162] suggests that these wire dimensional differences almost disappear upon increasing the annealing time.

Figure 6.4: Experimental STM based measurements of the variation in the height of a Dy disilicide nanowire on the Si(001) surface as reported in Ref. [157]. The top figure on the right shows the plateau height difference for the case where both the lower and the higher plateau is part of the wire, while for the bottom figure on the right, the lower plateau refers to the substrate. The experimental STM image on the left, showing the lines along which these heights were obtained, is filled state, bias voltage 1.04 V, and referring to an area of 700 × 700 Å^2 on the surface. *Image courtesy of B. Z. Liu and J. Nogami.*

differences between wire plateaus with STM should be a considerably more reliable way of obtaining wire structural parameters compared to the determination of height differences between wire and substrate, where the electronic structure for the two subsystems involved is significantly different. [19]

In general, though, the above conclusion can not be regarded as an independent support for the nanowires adopting the vacancy defected AlB_2 structure: as noted by He *et al.* in Ref. [154], the distances between three consecutive layers for the various RE disilicide structures growing on the Si(001) surface, as predicted from lattice parameters for bulk RE disilicides, is typically smaller than the uncertainties in the height measurement (see e.g. Table I of this paper for the case of Dy). As discussed at the beginning of this subsection, we see good reason to exclude the alternatives to the vacancy defected AlB_2 structure on the basis of lattice mismatch considerations and recent experimental observations, and we therefore do not regard the above point as shedding real doubt on the conclusion that the nanowire structure is closely related to the AlB_2 structure. The comment nevertheless is important to the present discussion as it suggests that the distance between three consecutive layers for a RE disilicide nanostructure growing on the Si(001) surface is only weakly dependent on the layer registry

[19] As an example, the wire height of lowest layer Ho and Dy nanowires as determined with STM by Nogami *et al.* in Ref. [98] was found to vary between 2.4 and 4.0 Å, depending on voltage bias. See also Fig. 6.4.

and the presence of Si vacancies. In particular, if the wires were actually comprised by vacancy free RE disilicide in the AlB_2 structure, we would expect plateau height differences very similar to those reported above.

The comparison of the given RE disilicide nanowire structural parameters with lattice parameters for a bulk RE disilicide structure assumes that the nanowire is elastically strained only in the growth plane. This seems unlikely to hold true considering the large amounts of strain on the wire along the direction perpendicular to the wire growth. Indirect experimental support for significant changes of the nanowire structural parameters in the direction perpendicular to the growth plane were obtained in recent studies with 3D MEIS by Kobayashi [156] on Er disilicide 3D islands on the Si(001) surface. It was concluded that these islands adopted a monoclinically distorted AlB_2 structure with the distance between three consecutive layers in the direction of the substrate normal being 3.23 Å. This value is not considerably smaller than the value of 3.28 Å obtained for bulk Er disilicide but it is obtained for a structure which undoubtedly contains more layers than the typical wire structure, [20] the effects of the strain on the overlayer structure thus being more 'masked'. The issue of strain effects on the wire structure in the direction perpendicular to the wire growth plane was noted by Preinesberger *et al.* in Ref. [153], but no detailed discussion was provided in this paper.

Concluding, while measurements of RE disilicide nanowire plateau height differences do contain reliable (within the limitations of STM predictions) information on the wire structural parameters, there are strong suggestions from comparison with bulk RE disilicide lattice parameters that a wire adopting the vacancy free AlB_2 structure would have a plateau height difference very similar to a wire adopting the vacancy defected AlB_2 structure. In addition, the interpretation of a measured plateau height difference is complicated by the fact that very little is currently known on the effects of the strain on the wire structure in the direction perpendicular to the wire growth plane (indeed, this is an area where theoretical studies of a RE disilicide nanowire on the Si(001) surface could yield indispensable information). Measurements of the RE disilicide nanowire plateau height differences, therefore, do not stand out as a highly reliable way of supporting a particular wire structure.

6.2.2.7 A SURVEY OF THE EXPERIMENTAL STUDIES INTO THE RARE EARTH DISILICIDE NANOWIRE SURFACE TERMINATION

While a series of different RE disilicide nanowire surface reconstructions have been reported in experiment [153, 157], the $c(2\times2)$ surface reconstruction reported in the original experimental studies of Er disilicide nanowires by Chen *et al.* [146] is the most frequently observed example of a nanowire surface termination. Liu and Nogami [157] reported, on the basis of experimental studies of Dy disilicide nanowires, that for wires more than 4 Si(001) surface lattice parameters wide, a $c(2\times2)$ surface reconstruction is

[20] The experiments of Ref. [156] involved deposition of $\sim$ 1.5 ML of Er on the Si(001) surface. Upon annealing, relatively well separated islands, nanowires, and wire bundles were reported (see e.g. Fig. 4 of this paper). The authors reported, as part of their conclusion obtained from the 3D MEIS studies, an average width of the Er disilicide nanostructures of 46 Å.

typically adopted. [21] Chen *et al.* interpreted their results for the Er disilicide nanowire surface reconstruction in Ref. [146] as being in good agreement with the nanowire epitaxial growth model presented in the same paper, i.e., in particular with the nanowires adopting the vacancy defected AlB_2 structure. No details for this suggestion were provided, however, and the issue of wire surface termination appears to have been largely ignored in the literature, the general assumption being that the wires terminate in a Si layer or a Si bilayer (see e.g. Ref. [157]). [22] Only one model for a nanowire surface termination has been suggested, on the basis of experiments on Dy disilicide nanowires [153]. The surface reconstruction reported by the authors of this paper was not $c(2\times2)$, however, but an example not reported in more recent studies for the same RE disilicide [157].

Considering the explanation for the nanowire structure put forth by Chen *et al.* in Ref. [146] and the fact that the vacancy defected AlB_2 structure has been observed in 3D RE disilicide film growth on the Si(001) surface, it seems reasonable to expect that the structural details for wire and film surface termination should be very similar. Chen *et al.* [164], studying surface reconstructions for Er disilicide nanostructures obtained upon deposition of several ML of Er on the Si(001) surface and annealing at up to 975 K, reported a $c(2\times2)$ surface reconstruction, as evidenced with LEED and STM, for both rectangular islands, identified as a bundle of nanowires, and compact 3D islands on the surface. X-ray diffraction studies revealed that the 3D islands adopted the $ThSi_2$ structure. This suggests that the $c(2\times2)$ surface reconstruction does not require a vacancy defected structure, [23] and thus indicates that this surface termination for the nanowire could also be associated with a vacancy free AlB_2 structure. Of interest to the modelling of nanowires, recent studies of Er disilicide nanostructures on Si(001) by Fujii *et al.* [152], focussing on islands with the AlB_2 structure and a $c(2\times2)$ surface reconstruction, have strongly supported termination of these structures in an Er plane, as evidenced with CAICISS, in contrast to previous assumptions.

In summary, experimental studies of surface structures for RE disilicide islands on the Si(001) surface have suggested that *(i)* the $c(2\times2)$ surface reconstruction, the most common surface structure of the RE disilicide nanowires, is not uniquely associated with the vacancy defected AlB_2 structure but might equally well be connected with the vacancy free AlB_2 structure and *(ii)* the wire surface termination is a RE metal layer rather than a Si layer as commonly assumed. In particular, point *(i)* suggests that the

[21] The authors of Ref. [157] also reported that the $c(2\times2)$ unit cell for the Dy disilicide nanowires is actually rather far from square, in contrast with the remarks in Ref. [146].

[22] Referring to the schematic presentation of RE disilicide nanowires with the vacancy defected and vacancy free AlB_2 structure on the Si(001) surface in Fig. 6.2, we find that, for both of these cases, neglecting both surface relaxation effects and the issue of the location of possible vacancies for simplicity, the uppermost wire layer is either a Si or a RE metal plane (normal vector along the [1-100] direction), with the atoms ordered in a rectangular $p(1\times1)$ pattern. Liu and Nogami reported a $p(1\times1)$ nanowire surface reconstruction in their studies of Dy disilicide nanowires on Si(001) in Ref. [157] and discussed the possible connection with the vacancy defected AlB_2 structure for both this situation and the case of the more common $c(2\times2)$ surface reconstruction. No model was presented on the basis of these considerations, though.

[23] This observation, on the other hand, does not exclude the presence of Si vacancies within the last few layers of the Er disilicide surface in the studies of Ref. [164], see e.g. the discussion in Sec. 6.2.1.1 of the recent work on Y disilicide 3D films on Si(111) by Rogero *et al.* [140].

nanowire $c(2\times2)$ surface reconstruction can not be regarded as support for a particular wire structure.

6.2.2.8 A SURVEY OF THE EXPERIMENTAL STUDIES INTO THE RARE EARTH DISILICIDE NANOWIRE CROSS-SECTIONAL PROFILE

The typically assumed (see e.g. Ref. [151], [141]) RE disilicide nanowire cross-sectional profile is (closely) rectangular with each wire sidewall consisting of a Si graphite-like plane. In the absence of any theoretical modelling of wires on a substrate, this presentation obviously is just an assumption, presumably made on the basis of the intuitive, but potentially misleading, argument that completion of all (vacancy defected) Si 'cages' surrounding a RE metal atom is to be associated with the energetically most favourable wire configuration. [24]

The most detailed experimental studies of nanowire cross-sectional profiles were reported by Nogami and co-workers [98, 131] for Dy and Ho disilicide nanowire growth on the Si(001) surface. For both elements, two different wire morphologies, denoted 'triangular' and 'rectangular' in Ref. [98], were observed in STM studies, with examples of the two profiles shown in Fig. 6.5 for the Ho disilicide nanowires. [25] The wires were found to run along the same direction when growing on the same terrace and reported to be present with equal probability for Ho coverages of 0.2 - 0.3 ML while for coverages of $\sim$ 0.4 ML, where the wires would start forming bundles, the rectangular wires were found to dominate. In other words, the triangular nanowire could not simply be disregarded as a rare growth phenomenon according to these studies. More recently, triangular wires have been reported for Er disilicide nanowire growth on Si(001) [165].

The experimental studies in Ref. [131] did not yield any structural information on the triangular wires. The authors of this paper speculated that these wires might be explained as a minimum width rectangular wire with a different step edge structure. Yang *et al.* [165], on the other hand, suggested that the rectangular wires were 'truncated' triangular wires, i.e., with a wire height one set of layers (see discussion of wire heights in Sec. 6.2.2.6) lower but having the same step edge structure. Fig. 6.5 does appear to suggest that the key difference between the two wire structures is the growth of an additional set of layers for the triangular wire, i.e., that only one type of wires is present on the Si(001) surface in the experiments of Ref. [98, 131, 165], all with a triangular cross-sectional profile which is often incomplete, leading to a 'trapezoidal'

[24] The discussion of the energetically most favourable wire cross-sectional profile is to a high degree connected with minimizing the number of Si dangling bonds for the system. The rectangular wire profile appears a likely candidate on the basis of this consideration but e.g. a step edge structure where the width of the wire is reduced by a Si(001) surface lattice parameter (i.e., a single cage) on both sides of the wire every time one moves three layers further up the wire structure must seem a very reasonable candidate as well. We shall not discuss this potentially complex issue further here, but refer to Sec. 6.2.5.1, where we present the energetically most favourable cross-sectional profile and surface termination for a vacancy free Y disilicide nanowire with fixed width on the Si(001) surface, for further comments.

[25] For the time being, we shall distinguish between these wires using the names given above. We emphasize that we are not making an assumption about the structure of the two wire profiles at this stage of the discussion, however, as we regard the information from Fig. 6.5 as insufficient for such a conclusion to be drawn. For further comments, see below in the text.

Figure 6.5: An example (taken from Ref. [131]) of the 'triangular' and 'rectangular' RE disilicide nanowire cross-sectional profile, as measured with STM, obtained in experiments involving Ho on Si(001) (and other RE metals, see text for details). Part (a) in the figure shows an STM image of the two nanowires described in part (b), (c). The triangular nanowire is the brighter wire on the left in this figure. *Image courtesy of C. Ohbuchi and J. Nogami.*

(rather than a rectangular) wire. [26]

It is tempting to regard the conclusion of a single wire cross-sectional profile and the results in Fig. 6.5 as support for the RE disilicide nanowires adopting the vacancy free AlB_2 structure: certainly, a smooth triangular wire profile would seem much easier to explain with this structure compared to a wire with the vacancy defected AlB_2 structure, considering the change of wire growth direction (see Fig. 6.2). [27] On the other hand, one should be extremely cautious about jumping to conclusions from this result: one can not expect a nanostructure as high as the wire cross-sectional profile in Fig. 6.5

[26] The change of name for this wire profile is deliberate: if the two wires in Fig. 6.5 adopted the same step edge structure, we would regard it is highly unlikely, given the triangular wire results, that the wire sidewalls should consist of a single Si graphite-like plane. In particular, the 'trapezoidal' wire is not necessarily to be explained by a structure with vertical sidewalls in the absence of wire strain effects.

[27] As an example of possible cross-sectional profiles for the RE disilicide nanowire with a vacancy free AlB_2 structure we refer to Fig. 6.12 in Sec. 6.2.3.3.

to be described to a very high precision with STM. More precisely, interpretation of the result in Fig. 6.5 is not only a matter of clarifying whether the wire sidewalls are relatively smoothly sloping or adopting a more well-defined step edge structure but also a question of the correct averaged value for the slope of the wall. In other words, there is a high element of speculation to the above considerations, and we do not consider it justifiable to apply these remarks as support for any particular wire structure.

In summary, experiment indicates, in contrast to usual assumptions, that the general RE disilicide nanowire cross-sectional profile might be trapezoidal or triangular, with these two profiles being closely connected, the trapezoidal wire being an incomplete triangular wire. These considerations, however, should be regarded primarily as a good reason for comparing the stability of various wire cross-sectional profiles in theoretical studies of the RE disilicide nanowires on Si(001), the results obtained in experiment being too uncertain for any real conclusions to be drawn regarding the detailed wire structure.

6.2.2.9 A SURVEY OF THE EXPERIMENTAL STUDIES INTO THE RARE EARTH DISILICIDE NANOWIRE GROWTH DIRECTION

The RE disilicide nanowires on the Si(001) surface typically (see Sec. 4.2.3) grow in the presence of a RE/Si(001) wetting layer. It has often been mentioned in the literature (see e.g. Ref. [98, 166, 167]) that there could very well be an intimate connection between wetting layer formation and wire growth in the sense that they essentially represent different stages of a single growth phenomenon, with the generally accepted structural model for the wetting layer (see Sec. 6.2.3.4) supporting this suggestion. The interest in understanding the structure of the wetting layer when investigating RE disilicide nanowires is evident already on the basis of this remark: if the exact relation between wetting layer formation and wire growth is well established, a definite statement regarding the growth direction of the wire can be made by determining the structure of a wetting layer typically coexisting with the growing wire for the given RE disicilide nanowire system under investigation. Considering that the two candidates for the wire structure presented in Sec. 6.2.2.2 grow in mutually perpendicular directions on the surface, the power of this approach is immense: we can basically exclude one of these candidates.

Despite the potential strength of the above statement, the attempts to understand the growth and structure of RE disilicide nanowires made in the literature so far [146, 98, 151] have largely focussed on a different issue: the wire growth direction relative to the direction of Si dimer rows on the surrounding terrace. The reason for this essentially goes back to the fact that wetting layers were not observed during the Er disilicide nanowire growth in the experiments by Chen *et al.* [146] where the wire epitaxial growth model was presented initially. The authors of this paper reported nanowires growing perpendicular to the Si dimer rows on the surrounding terrace and reasoned that, in order to obtain agreement between this observation and the suggestion that the wires adopted the vacancy defected AlB_2 structure, the lowest layers of the wire (starting from the bottom) would have to be a Si and an Er layer. We emphasize that Fig.

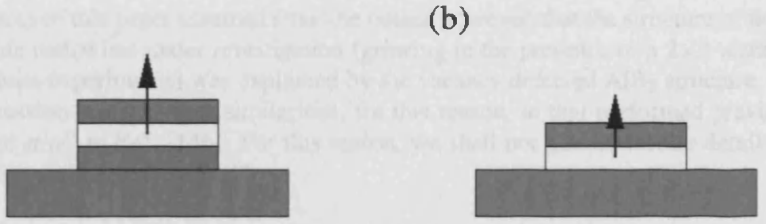

Figure 6.6: Schematic presentation of the assumed wire/substrate interface for RE disilicide nanowire growth on the Si(001) surface for the epitaxial growth model by Chen *et al.* in Ref. [146] (part (a) in this figure) and the model presented in our work, see Fig. 6.2, Sec. 6.2.2.2 (part (b) in this figure). The Si substrate is described by the large dark grey box in both of the figures. For the overlayer, a single Si (RE metal) layer is described by a dark grey (white) box. The arrows indicate further growth of the wire structure by addition of layers (an issue that the present discussion is not concerned with).

3 in Ref. [146], describing the RE disilicide nanowire epitaxial growth model suggested by Chen *et al.*, differs in this respect from Fig. 6.2 in Sec. 6.2.2.2 (see Fig. 6.6): for simplicity, we ignored the wire/substrate interface issue in our presentation, choosing simply, without any argument provided, a RE layer as the lowest layer for the wire. This simplification was justifiable at that particular stage of the discussion, the key point being to emphasize that for the same choice of wire/substrate interface, wires adopting a vacancy free and a vacancy defected AlB_2 structure grow in mutually perpendicular directions on the Si(001) surface.

The RE disilicide nanowire epitaxial growth model presented in Fig. 3 of Ref. [146] has the inherent weakness that it requires knowledge on the wire/substrate interface. To our knowledge, the details of this interface have not been clarified (for related comments, see Sec. 6.2.2.10). Furthermore, on the basis of our considerations in Sec. 6.2.2.3, where we argued that there is reason to take the vacancy free AlB_2 structure into account as a potential candidate for the structure of the wire, there is suddenly no reason to require that the lowest layers of the Er disilicide nanowire observed in the experiments of Ref. [146] should be (starting from the bottom) a Si and an Er layer: indeed, it seems intuitively more straightforward, from the point of view of a wire growing directly on the Si(001) surface, to suggest that the lowest layer of the wire is an Er layer, with the wire adopting the vacancy free AlB_2 structure. We emphasize that this remark is not included here as support for the wires adopting the vacancy free AlB_2 structure, but to emphasize, rather, that a conclusion regarding the wire structure can not justifiably be drawn from the experimental results in Ref. [146]. Indeed, in the absence of any experimental information on the wire/substrate interface, there appears to be no clear reason why one interface in Fig. 6.6 should be preferable to another, as such a suggestion, when put forth without any additional information on the wire/substrate system, would require detailed knowledge on the wire growth process.

To our knowledge, the only attempt to discuss in detail the growth of RE disilicide nanowires in the presence of a wetting layer so far was made by Zhu *et al.* [151]. The

authors of this paper assumed from the outset, however, that the structure of the Er disilicide nanowires under investigation (growing in the presence of a 2×3 wetting layer in these experiments) was explained by the vacancy defected AlB_2 structure, with the discussion bearing close similarities, for this reason, to that performed previously by Chen *et al.* in Ref. [146]. For this reason, we shall not go into further detail with the considerations in Ref. [151].

To summarize, experimental information on the RE disilicide nanowire growth direction on the Si(001) surface appears a highly promising way of gaining further knowledge on the wire structure in the sense that we should be able to exclude one of the two wire candidate structures presented in Sec. 6.2.2.2 as an explanation for the experimentally observed structure simply on the basis of this information. Comparing with the discussions in Sec. 6.2.2.5 - 6.2.2.8 of other experimental observations used previously in the literature as support for the structure of the RE disilicide nanowire adopting the vacancy defected AlB_2 structure, the above conclusion is outstanding as it presents the only unambiguous way of obtaining such knowledge on the basis of the experimental studies performed so far on these systems.

As a consequence of this encouraging conclusion, we shall devote our attention in Sec. 6.2.3.1, when discussing the initial considerations for our theoretical modelling of Y disilicide nanowires on Si(001), to the experimental information on the wire growth direction. We shall focus in that discussion on the nanowire-wetting layer coexistence, which has so far not been used effectively in the literature as a way of gaining knowledge on the wire structure, even though it seems likely that wetting layer formation and wire growth are very closely connected growth phenomena. While we are yet to actually discuss the potential strength of this approach, i.e., whether a well-established connection between the wetting layer formation and the wire structure can be obtained, this approach seems more likely to produce useful results when compared to the experimental observation in e.g. Ref. [146] that the RE disilicide nanowires run perpendicular to the Si dimer rows on the surrounding terrace: we have argued in the above, that, with the lack of experimental knowledge on the wire/substrate interface, this observation essentially can not be regarded, on its own, as definite support for the wires adopting either the vacancy defected or the vacancy free AlB_2 structure.

6.2.2.10 EXPERIMENTAL SUGGESTIONS FOR RARE EARTH DISILICIDE NANOWIRE STRUCTURES DIFFERENT FROM THE AlB_2 STRUCTURE

Cross sectional TEM studies represent a way of obtaining direct structural information on RE disilicide nanostructures on the Si(001) surface. The fundamental reason why this efficient, on the face of it, approach to identifying the structure of the RE disilicide nanowires is pushed to the end of the subsection is that we do not regard it as truly clarified that reliable knowledge on the actual nanowire structures has been obtained with TEM. Ye *et al.* [155], performing cross sectional TEM studies for various Dy disilicide nanostructures on Si(001), found that it was not possible to obtain meaningful results for the true wire structures which were oxidized during *ex situ* TEM sample preparation. For this reason, the investigations in Ref. [155] involved only larger nanostruc-

Figure 6.7: Cross-sectional TEM images of Dy disilicide nanostructures on the Si(001) surface. See text for details. *Image courtesy of Z. He, D. J. Smith, and P. A. Bennett.*

tures (3D nanowires, see Sec. 4.2.3) where the connection with the structure of the true nanowires must be regarded as questionable. Chen *et al.* [146] performed TEM studies of Er disilicide nanowires on the Si(001) surface, but provided hardly any details on this issue. [28] In particular, the authors of this paper did not use these results as a direct support for their epitaxial growth model, the reasons for this decision being unclear to us, but possibly explained by the influence on the capping material in the TEM studie on the structure of the wire (see below for further comments).

More recent cross sectional HRTEM studies of Dy disilicide nanowires by He *et al.* [154] have seriously challenged the suggestion that the wires adopt the vacancy defected AlB_2 structure, as suggested in Ref. [146]. Fig. 4 in Ref. [154] (included as Fig. 6.7) shows two HRTEM images for Dy disilicide nanowires of various widths and heights: the wire in the upper figure has a width of $\sim$ 8 Si(001) surface lattice parameters (counting the number of atomic columns for the wire along the wire width direction) and appears to contain 4 Dy layers while the wire in the lower figure has a width of $\sim$ 13 Si(001) surface lattice parameters and appears to contain 6 Dy layers. Both wires have highly triangular cross sectional profiles, but neither of the wire structures was found to agree with the vacancy defected AlB_2 structure. By contrast, for the wider wire, an apparent mixture between two of the structures observed on RE

[28] The only comment made on the basis of the TEM studies in Ref. [146] was the conclusion that no detectable protrusion of the nanowires below the Si(001) surface was revealed, i.e., that the growth of the wires was to be regarded as epitaxial rather than endotaxial (wires growing into the substrate). As the precision in these studies is unclear to us, we do not regard this experimental result as evidently clarifying the details of the wire/substrate interface discussed in Sec. 6.2.2.9.

disilicide 3D film growth on the Si(001) surface was reported, with the lowest two Dy layers adopting a registry agreeing with the vacancy defected AlB_2 structure but the following four layers suggestion formation of a $ThSi_2$ structure, while for the more narrow wire, the layer registry was reported to agree with a $ThSi_2$ structure.

The cross sectional TEM experiments in Ref. [154] involved capping the substrate and overlayer with $\sim$ 200 Å of Ti at RT in order to prevent structural changes induced by oxidation to occur. The authors argued that, while this process might distort or even destroy some of the wire structure, it was unlikely that a new ordered structure should be occur as a result. We agree with this statement but are nevertheless cautious about regarding the results obtained in Ref. [154] as support for the wires adopting either a mixed RE disilicide structure or the $ThSi_2$ structure, for the following reasons: *(i)* the Dy disilicide nanostructure in the lower part of Fig. 6.7 is evidently higher than the typical nanowires, suggesting that it might structurally belong to a different category of RE disilicide nanostructures grown on the Si(001) surface. *(ii)* The wire in the upper part of Fig. 6.7 could be explained by the vacancy free AlB_2 structure, as it is not unlikely that the distortion reported for the uppermost part of the wire is explained by the interaction with the capping material. Given the limited amount of information on this issue, in particular the fact that He *et al.* [154], did not consider the possibility of growth of vacancy free wires with the AlB_2 structure when discussing their results, we do not regard the result in Fig. 6.7 as well established support for the wires adopting this structure.

6.2.2.11 ELECTRONIC STRUCTURE OF BULK VACANCY FREE Y DISILICIDE IN THE AlB_2 STRUCTURE: WHY THE Y 4*p* ELECTRONS CAN BE REGARDED AS CORE ELECTRONS FOR THIS SYSTEM

When presenting our results for the structural optimization of bulk vacancy free Y disilicide in the AlB_2 structure in Sec. 6.2.2.1, we noted that inclusion of the Y 4*p* semi-core states in our calculations employing Vanderbilt US PPs did not have a very significant effect on the optimized values for the lattice parameters of the system. As the considerations of Sec. 6.2.2 have used only information on the lattice parameters for this system, with the statements that we have been able to make about the epitaxial growth of elongated vacancy free Y disilicide nanostructures with the AlB_2 structure on the Si(001) surface not effectively requiring a highly precise determination of these parameters (see Sec. 6.2.2.2), there has been little reason to discuss this conclusion in detail.

For various reasons, it is recommended to move beyond this stage, however, investigating the electronic structure for vacancy free bulk Y disilicide with the AlB_2 structure: from a general point of view, agreement in structural parameters as obtained in differently based theoretical studies is not a very reliable measure when discussing the properties of the system under investigation. [29] Consequently, in order to clarify whether our results obtained with the Y 4*p* electrons included explicitly in calculations actually differ importantly from the results obtained when keeping these electrons in

[29]The Plato based studies of isolated bulk Si Cu_i discussed in Sec. 5.2.4 provide a good example of how misleading a conclusion about the similarities of different theoretical results for a given system can be when drawn on the basis of a comparison of structural parameters only.

the core, i.e. including them in the pseudopotential, we need to move beyond the simple comparison of structural parameters. The same goes for the comparison of our results with the results reported in previous theoretical studies of bulk vacancy free Y disilicide in the AlB_2 structure (see Sec. 6.2.2.1). On a more specific level, previous theoretical studies by Magaud *et al.* [138] have reported that explicit inclusion of the Y 4*p* electrons is of key importance to the optimization results , in apparent contrast with our results. Thus, there is very good reason to investigate the electronic structure of bulk vacancy free Y disilicide in the AlB_2 structure as obtained in our two theoretical descriptions of this system.

In the discussion below, we shall compare the converged electronic structure for bulk vacancy free Y disilicide in the AlB_2 structure as obtained with the above described theoretical methods. For a full discussion of how the convergence with respect to the variable parameters in the code was obtained, we refer to Sec. 8.3.2 (although we shall make comments in the following on the conclusions obtained in that part of the thesis). We shall comment initially on the issues addressed above, clarifying in this process that explicit inclusion of the Y 4*p* electrons in the calculations has next to no effect on the cohesive properties of the system under investigation: in other words, the Y 4*p* electrons can safely be regarded as core states for the studies of bulk vacancy free Y disilicide in the AlB_2 structure, according to our results. Following these considerations, we shall discuss briefly why we regard the change in the values of the lattice parameters for this system, compared to bulk vacancy defected Y disilicide in the AlB_2 structure, as a conclusion that can be generalized to a reasonable approximation to other RE disilicides.

As mentioned at the beginning of this discussion, previous theoretical studies of bulk Y disilicide [138] reported that explicit inclusion of the Y 4*p* semi-core states was needed for these studies in order to produce reliable results. This conclusion referred to the previous studies of bulk Y by Min and Ho [168], employing NC PPs [16], where it was reported that the 4*p* semicore states were so extended that they would be affected significantly by the crystal environment, thus being of real importance to the lattice parameter optimization results. The studies of bulk Y disilicide by Magaud *et al.* in Ref. [138] were performed using Vanderbilt US PPs as implemented in VASP and the LDA as parametrized by Ceperley and Alder [9] to E_{xc}, thus being highly similar to our chosen theoretical description of the Y/Si system which used VASP and Vanderbilt US PPs but employed the PW91 GGA [12] to E_{xc}. No results of calculations for bulk Y disilicide with the Y 4*p* electrons treated as core electrons were reported in Ref. [138], however. Rogero *et al.* [134] reported, in calculations on 2D Y disilicide on Si(111) based on the same theoretical approach to describing the Y/Si system as used in our work, that the Y 4*p* electrons had to be included explicitly in the calculation, but no details on their results were provided in this paper. Considering the clear differences between bulk Y disilicide and the 2D Y disilicide film, we would be cautious about regarding this result as evident support for explicit inclusion of the Y 4*p* electrons being required for bulk vacancy free Y disilicide in the AlB_2 structure. It appears, therefore, that the question of the importance of the Y 4*p* semi-core states to the cohesive properties of bulk Y disilicide have not been rigorously addressed up to now.

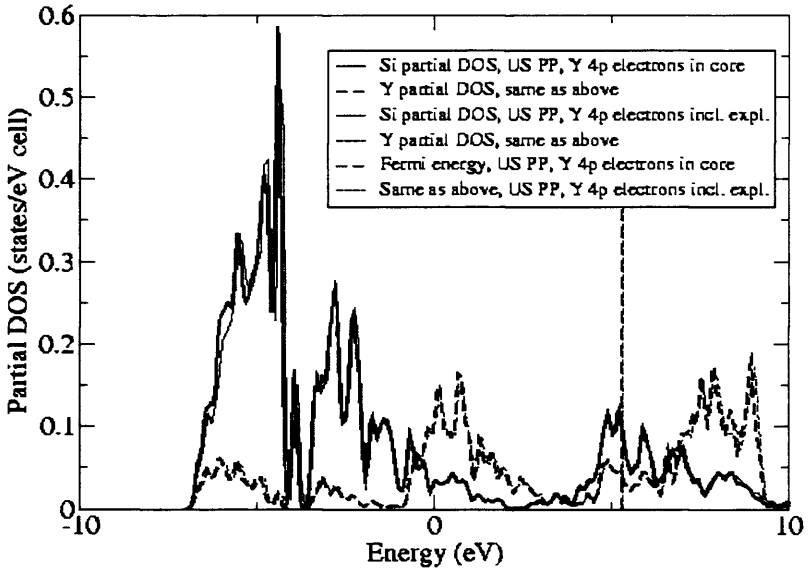

Figure 6.8: Partial density of states for bulk vacancy free Y disilicide in the AlB_2 structure as obtained from calculations with VASP using two different Vanderbilt US PPs, differing as described above. Both this figure and more detailed studies of the electronic structure of the system (see text for details) suggests that the effect of treating the Y 4p electrons as semi-core electrons is very small.

Our results for the electronic structure of bulk vacancy free Y disilicide in the AlB_2 structure, as obtained with and without the $4p$ electrons included explicitly in the calculation, are shown in Fig. 6.8, while the optimized lattice parameters and total energy for this system have been included in Table 6.2. The results in Fig. 6.8 refer to calculations on the same structure, a choice made to separate out the differences in the electronic structure due to the inclusion of the Y $4p$ electrons from the differences connected with the slight variation in the optimized structural parameters (see Table 6.2): we chose the optimized structure as obtained with the Y $4p$ electrons in the core for these studies. As convergence in the total energy and lattice parameters was obtained in both studies for a plane wave energy cutoff of 188.3 eV, a (11, 11, 11) Γ centered k mesh, and a smearing width of 0.1 eV for the chosen Gaussian smearing scheme, this choice of parameters was used for the electronic structure studies.

The results in Table 6.2 show that the change (increase) in the lattice parameters for the bulk vacancy free Y disilicide in the AlB_2 structure obtained upon including the Y $4p$ electrons explicitly in calculations is rather small, 0.012 Å (0.3% relative

Table 6.2: Optimized lattice parameters and total energy for bulk vacancy free Y disilicide in the AlB_2 structure as obtained with VASP using two different Vanderbilt US PPs, differing as described below. See text for details.

Method	a / Å	c / Å	E / eV/atom
Y 4p electrons in core	4.082	3.960	-6.282
Y 4p electrons semi-core	4.094	3.990	-6.231

difference) for the a lattice parameter and 0.030 Å (0.8% relative difference) for the c lattice parameter. As mentioned previously in the discussion, this in itself does not suggest that the Y $4p$ electrons have only a weak influence on the cohesive properties of the system. Clear support for this argument is obtained, however, from the fact that the inclusion of the Y $4p$ electrons hardly changes the total energy of the system (a decrease in this energy by 0.003 eV/atom is obtained upon this inclusion). Furthermore, as discussed in detail in Sec. 8.3.2, the variation of the lattice parameters and total energy with the number of k points in the IBZ for the two studies is highly similar. It seems, already on the basis of these considerations, that the Y $4p$ electrons remain almost unaffected by the details of the surrounding crystal, i.e., that these states can safely be regarded as core states in the calculations on this system.

The results in Fig. 6.8 suggest that, with the exception of the lowest lying Si $3s$ states, the electronic structure is essentially unaffected by the explicit inclusion of the Y $4p$ electrons in the calculations on bulk vacancy free Y disilicide in the AlB_2 structure. Further studies of the electronic structure for the system as obtained within these different theoretical frameworks were performed by projecting the electronic charge density onto ion-centered spherical harmonics within spheres surrounding each ion in the system: for the situation where the Y $4p$ electrons were treated as semi-core states, investigation of the additional states with energies $\sim$ 23 eV below the Fermi level ε_F obtained in this study revealed that *(i)* the wavefunctions for these states have $\sim$ 99% p character with *(ii)* typically more than 98% of the full amount of electrons for these levels recovered within the sphere of the chosen radius 1.98 Å (to be compared with the Y-Si and Y-Y distances of 3.08 Å and 3.96 - 4.08 Å, respectively). Finally, a dispersion of $\sim$ 0.2 eV was obtained for these levels over the range of k-points in the IBZ. We regard the results of these investigations as a very strong suggestion that the Y $4p$ electrons are fully contained within the sphere and hardly affected by the crystal environment. In addition to these studies, comparison of the character of the wavefunctions for higher lying levels as obtained with the Y $4p$ electrons in the core or included explicitly in calculations did not reveal strong differences at any energies investigated (the focus primarily being on the lower energies in Fig. 6.8 where the DOSs as obtained in the two studies were found to differ the most), further supporting the conclusion that the Y $4p$ electrons can be regarded as core electrons for bulk Y disilicide with the AlB_2 structure.

Given the above conclusion, in particular, the difference in the lattice parameters obtained in the two theoretical studies of bulk Y disilicide with the AlB_2 structure evidently remains to be clarified. It is beyond the scope of the present work to go into this issue: we believe that the studies described in the above have clarified that this

difference is not explained by the influence of the Y 4*p* electrons on the cohesion of the structure, the reason for the discrepancy being seemingly more subtle as the conclusions obtained for the electronic structure within these two theoretical descriptions of the system under investigation hardly show any differences at all. As a consequence of the conclusion of the present studies, we shall focus in the rest of this work almost exclusively on the results obtained in calculations with the Y 4*p* electrons treated as core states. We shall, however, include the results of additional optimization studies with the Y 4*p* electrons treated as semi-core states, primarily to highlight, for the sake of future studies, in which situations these theoretical descriptions of the Y/Si system produce conclusions that differ the most. [30]

As the main target of the investigations into Y disilicide nanowire formation on Si(001) presented in this work focusses on the modelling the structure of this wire, leaving an examination of the electronic structure for this system until future studies, we have not devoted considerable attention to investigating the details of the electronic structure of vacancy free bulk Y disilicide in the AlB_2 structure either (although, ultimately, if the Y disilicide nanowires were found to be vacancy free, adopting this structure, such studies of the bulk phase would be the natural starting point of a real understanding of the mechanisms of stabilizing the wire): we did, however, perform very preliminary studies into this topic in order to ensure that we obtained results in acceptable agreement with results of previous theoretical studies. In our results obtained for the Y disilicide electronic structure, we found that the states with energies 6.5 eV or more below ε_F were fairly localized in the Si spheres with predominant *s* character, this conclusion being in very good agreement with the result reported by Magaud *et al.* in Ref. [143]. In the studies of this paper, the experimental lattice parameters for vacancy defected Y disilicide with the AlB_2 structure were used in calculations, explaining why the less localized states at higher energies obtained in these studies do not bear a strong resemblance to our results. There is agreement between our studies and the reported conclusions in Ref. [143] with regards to the wave function having a predominant Y 4*d* and Si 3*p* character close to ε_F. We have not investigated the issue of the reported covalent Y-Si bond formation reported by Rogero *et al.* in Ref. [135] in the present work.

As a closing remark of the initial discussions of vacancy free RE disilicide nanowire growth on the Si(001) surface, we shall discuss briefly why we believe there is good

[30] As noted in Sec. 8.3.2, the difference in the lattice parameters obtained in the two studies of bulk Y disilicide with the AlB_2 structure considered in this work ultimately would be quite important to the discussion of vacancy free Y disilicide nanowire growth on the Si(001) surface in Sec. 6.2.2.2, i.e., to the evaluation of the substrate/overlayer lattice mismatch as described in that discussion, provided that we should somehow be able to find a more reliable approach to drawing conclusions regarding this issue. With regards to total energy calculations, we would believe that the choice of theoretical description of the system is less important as *(i)* the total energy difference in Table 6.2 is quite small and *(ii)* our studies of bulk vacancy free Y disilicide (see Sec. 8.3.2 and Sec. 8.3.3) have suggested that the energy contours are very shallow for these systems, i.e., that an appreciable change in the lattice parameters is not necessarily associated with large changes in the total energy of the system. We shall make further comments on these issues later in this work whenever comparing the results of structural parameters and energies for Y/Si systems obtained using these two theoretical descriptions.

reason to expect that the structural instability obtained for bulk vacancy free Y disilicide in the AlB_2 structure would occur also for at least most of the other elements where RE disilicide nanowire formation on Si(001) has been reported. For bulk RE disilicide with the AlB_2 structure, as noted by Magaud *et al.* in Ref. [138], it is generally believed that the introduction of Si vacancies in the growing structure acts as a mechanism for strain relief in the graphite-like Si planes surrounded by RE metal planes along the [0001] direction in this ionic arrangement (see e.g. Fig. 6.2). The key support for this argument is the conclusion that, when using the experimental lattice parameters for bulk RE disilicide in the AlB_2 structure (see e.g. Ref. [150] for a list of recent results obtained for various elements of key interest to the issue of RE disilicide nanowire growth) and assuming a perfect disilicide, i.e., no Si vacancies, one will typically find Si-Si distances in the plane well below the value, 2.35 Å, of the bond length in bulk Si, with differences for e.g. RE = Er and RE = Dy being 0.16 and 0.14 Å. Y disilicide adds to this group, with a predicted Si-Si distance of 2.22 Åobtained using the above described approach. With the removal of every sixth Si atom in the Si planes and the subsequent (experimentally supported) movement of the Si atoms in these planes, each Si-Si distance can be increased considerably towards a more preferred value.

On the other hand, if we insist, somewhat hypothetically for bulk RE disilicide (we shall return to this point below), on retaining the full set of Si atoms, the alternative choice of strain relief, according to our calculations on Y disilicide, consists in moving all Si atoms in each plane farther apart and moving adjacent Y and Si planes closer together in order to retain fairly unchanged Y-Si distances, i.e., changing the axial *c/a* ratio for the unit cell: the value for the Si-Si distance obtained in our theoretical studies as a result of this change of the lattice parameters is 2.356 Å, very close to the optimized theoretical value (see Sec. 8.1) for the Si atom separation in bulk Si, strongly supporting the above explanation for the appearance of this distortion. Considering the typical close similarity in the experimental lattice parameters for various vacancy defected bulk RE disilicides with the AlB_2 structure (see e.g. Ref. [150]), there is good reason to believe, in conclusion, that the change in the *c/a* ratio reported in the present studies with RE = Y can be generalized, i.e., that highy elongated vacancy free RE disilicide nanoislands adopting the AlB_2 structure can be grown on the Si(001) surface. Our calculations on vacancy free bulk Er disilicide with the AlB_2 structure, not included in the present work for brevity, have produced the same type of distortion as obtained for bulk vacancy free Y disilicide with the AlB_2 structure in Sec. 6.2.2.1, strongly supporting the above conclusion.

Evidently, for bulk RE disilicide, the mechanism of strain relief is introduction of Si vacancies, as verified in recent experiments by Ji *et al.* [97]. For epitaxial growth of RE disilicide nanostructures on the Si(001) surface, however, as discussed in Sec. 6.2.2.3, this selection must be strongly influenced by the properties of the substrate, given that we are dealing with a 1D growth phenomenon. These remarks are at the heart of our interest in vacancy free RE disilicides with the AlB_2 structure as candidates for the structure of the experimentally reported nanowires: if we somehow knew about the details about the above mentioned selection with e.g. Si vacancy introduction being the preferred mechanism also for the growth of RE disilicide nanowires on Si(001), it clearly would not matter that highly elongated vacancy free RE disilicide structures provided an alternative explanation, on the basis of lattice mismatch considerations,

to the wire structure. As discussed previously in Sec. 6.2.2, however, experiment has not devoted a great deal of attention to the potential consequences of not knowing any details on this issue while furthermore, no alternative unambiguous support for a particular wire structure has been put forth up to now in the literature. This explains the importance of testing the vacancy free AlB_2 structure as a candidate for the structure of RE disilicide nanowires on the Si(001) surface.

6.2.3 STRATEGY FOR STUDY OF VACANCY FREE Y DISILICIDE NANOWIRES ON THE Si(001) SURFACE

6.2.3.1 PRESENTATION OF THE BASIC ELEMENTS OF A RARE EARTH DISILICIDE NANOWIRE GROWTH MODEL: INTRODUCTION TO THE MODELLING OF VACANCY FREE Y DISILICIDE NANOWIRES ON Si(001)

When discussing in Sec. 6.2.2.4 - 6.2.2.9 the direct experimental information on structural details for the RE disilicide nanowires on the Si(001) surface, our main aim was to clarify that none of these experimental observations unambiguously support the vacancy defected AlB_2 structure over the vacancy free AlB_2 structure as an explanation for the wire structure. We also noted in Sec. 6.2.2.9, however, that the typical (see Sec. 4.2.3) coexistence between these wires and a RE/Si(001) wetting layer provides, in principle, an extremely powerful method for gaining knowledge on the structure of the RE disilicide nanowires. We did not go into detail with this suggestion in Sec. 6.2.2.9 as, up to now, there has been no real focus on this suggestion from the RENW community. As an introduction to the discussion in the present subsection of the theoretical modelling of vacancy free Y disilicide nanowires on the Si(001) surface, we shall, however, clarify how we interpret the 'intimate connection' between wetting layer formation and wire growth, stated without much further comment in Sec. 6.2.2.9. We shall emphasize, during this discussion, why modelling of the Y/Si(001) wetting layer is of huge potential importance to clarifying the structure of the Y disilicide nanowire.

The discussion below is aimed only at presenting our general ideas for the wire-wetting layer coexistence, making reference to experimental results only when discussing the wetting layer model. Several experimental studies of RE disilicide nanowires growing in the presence of a wetting layer have been reported, but for clarity in the discussion, this issue being concerned with the interpretation of our results rather than the theoretical modelling, we shall postpone a more detailed discussion of these experimental results until Sec. 6.2.3.6.

As the first step towards clarifying how we interpret the previously mentioned 'intimate connection' between RE/Si(001) wetting layer formation and RE disilicide nanowire growth, we shall describe below the basic structural details for the largely accepted model for a 2×4 wetting layer put forth by Liu and Nogami [169], with the discussion in Sec. 6.2.3.4 dealing with this issue in more detail, in particular clarifying the outstanding questions for this model. The authors of Ref. [169] concluded, on the basis of experimental studies of the 2×4 reconstructed Dy/Si(001) wetting layer, that the uppermost layer for this surface structure was comprised by Dy atoms replacing Si dimers on the surface, with each atom deposited at the growth site resembling the structural environment for the AlB_2 structure as closely as possible, i.e., at the same position as the RE metal atom in Fig. 6.2. Moving along the shorter direction of the surface 2×4 unit cell, the uppermost layer was found to alternate between a Dy atom and a vacancy while along the longer direction of the cell, the layer was found to alternate between triplets of Dy atoms and a vacancy. The longer axis of the wetting layer unit cell was found to be parallel to the Si dimer rows on the clean areas on the

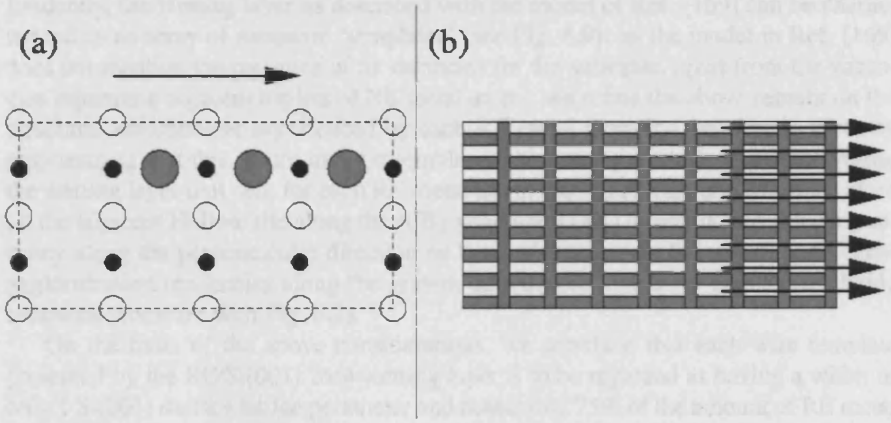

Figure 6.9: Schematic presentation of *(i)* the structural model for a 2×4 RE/Si(001) wetting layer suggested by Liu and Nogami in Ref. [169] and *(ii)* its suggested function as a template for a vacancy free RE disilicide nanowire. Part (a) in the figure shows the uppermost three layers for the reconstructed surface, with only a single 2×4 wetting layer unit cell, as marked by dotted lines, included in the figure: the atoms in these layers, as represented by the spheres in the figure, are distinguished by their colour and the size of the spheres, with the radius of the spheres decreasing as one moves into the bulk substrate. The white and black spheres describe Si atoms while the grey spheres describe RE metal atoms. Each RE metal atom is deposited at a site which structurally resembles the local environment for bulk vacancy free RE disilicide in the AlB_2 structure (see e.g. Fig. 6.2). On the assumption that wetting layer formation is the first step towards constructing a nanowire, we conclude from the above remarks and the discussion in Sec. 6.2.2.2, that this wire should run in the direction of the arrow in part (a) in the figure. Part (b) in the figure shows a larger area of the 2×4 wetting layer, containing several unit cells (a triplet of RE metal atoms being described by a white box). Once again, the connection with wire growth is emphasized by the set of arrows pointing along the direction of the wires that can be grown potentially on the basis of this template. For details on the actual wire growth, see Fig. 6.10.

surrounding terrace, i.e., areas where no replacement of Si with Dy had taken place. A schematic drawing of this wetting layer model is shown in Fig. 6.9.

Considering, in particular, the above mentioned fact that the RE metal atoms for the wetting layer are deposited at the same location as the RE metal atoms for epitaxial growth of RE disilicide on the Si(001) surface, there have been suggestions in the literature [166, 167] that the wetting layer formation is a precursor to wire growth. Evidently, the wetting layer as described with the model of Ref. [169] can be characterized as an array of nanowire 'templates' (see Fig. 6.9): as the model in Ref. [169] does not mention the presence of Si vacancies for the substrate, apart from the vacancies separating adjacent triplets of RE metal atoms, we refine the above remark on the structural environment experienced by each RE metal atom for the wetting layer by emphasizing that this environment resembles the *vacancy free* AlB_2 structure: within the wetting layer unit cell, for each RE metal atom, there is at least one RE metal atom on the adjacent Hollow site along the AlB_2 structure [0001] direction, but always a vacancy along the perpendicular direction on the surface, i.e., the RE metal atoms show agglomeration tendencies along the growth direction of a vacancy free RE disilicide nanowire (compare with Fig. 6.2). [31]

On the basis of the above considerations, we conclude that each wire template presented by the RE/Si(001) 2×4 wetting layer is to be regarded as having a width of only 1 Si(001) surface lattice parameter and containing 75% of the amount of RE metal needed to construct the lowest of wires (assumed to contain only one RE metal layer) of the same width. The only new element in this discussion, compared to the previous considerations referred to above, is the conclusion from the wetting layer model that this layer is to be regarded, on the face of it, as a template for a nanowire with the vacancy free rather than the vacancy defected AlB_2 structure.

The wetting layer model strongly supports the idea that the RE disilicide epitaxial nanowire growth is simply to be regarded as the next stage of the same growth mode: the wire, according to this suggestion (see Fig. 6.10), grows by agglomeration initially of RE metal atoms in a particular area of the wetting layer, covering an area on the surface containing several wire templates (the wires always attaining width of several Si(001) surface lattice parameters), with consumption of RE metal atoms from the immediate vicinity and the Si atoms for the growing wire provided either by the step edges or the immediate vicinity, an issue which we shall discuss in more detail in Sec. 6.2.3.6. [32] These remarks clarify our interpretation of the 'intimate connection' be-

[31] The key support for the suggestion that the growth site for each RE metal atom resembles the structural environment for the vacancy free AlB_2 structure is the experimentally observed agglomeration of the RE metal atoms along the growth direction of a vacancy free RE disilicide nanowire: without this argument, for the *isolated* RE metal atom substituting a Si dimer on the Si(001) surface, we can only conclude, at the outset at least, that the growth site resembles the local environment for a RE metal atom in a bulk RE disilicide structure: in order to remove the ambiguity of this statement, clarifying which RE disilicide structure we are talking about, more precise information on the structural details of the growth site is needed. From this point of view, the vacancy defected AlB_2 structure is not necessarily excluded from the outset of the discussion, as the substrate might be naturally strained to produce structural parameters closer to this environment in the absence of interactions with the RE metal. We shall go into more detail with this issue when discussing the results for isolated Y atoms on the Si(001) surface and Y/Si(001) wetting layers in Sec. 6.2.4.2 , 6.2.4.3 respectively, clarifying why we regard the statement made in the above text as being justifiable.

[32] We emphasize that we are not aiming at presenting an actual model for the RE disilicide nanowire growth in this presentation, i.e., we are drawing no conclusions about the relative stability of various pos-

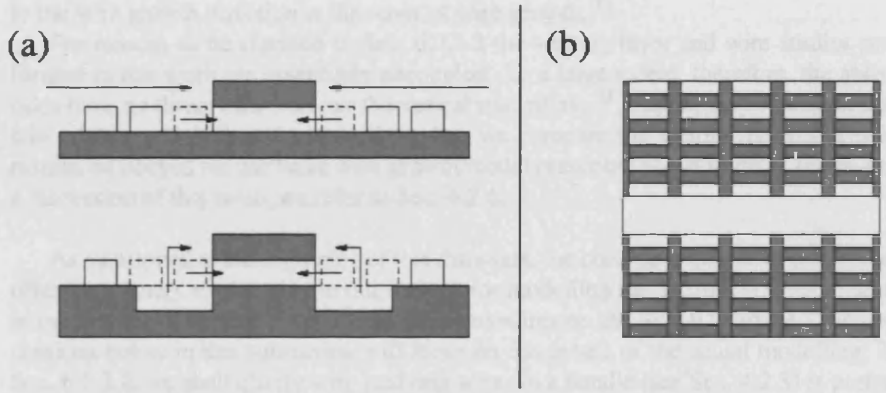

Figure 6.10: Schematic presentation of RE disilicide nanowire growth in the presence of a wetting layer (see Fig. 6.9 for initial remarks on this issue). Part (a) in the figure (cross sectional view of wire/substrate system) shows two suggested wire growth modes: in these figures, the substrate is represented by the large dark grey box while the wetting layer unit cells are represented by small white boxes. The wire is comprised by both a larger white box and a similar sized grey box, emphasizing *(i)* that it is comprised by both RE metal and Si atoms and *(ii)* that it does not necessarily attain the same width as a single wire template (see Fig. 6.9). In the top figure, the wire grows by consuming RE metal atoms from the immediate vicinity while the Si atoms are provided from the step edges, farther away from the wire, as described by the arrows in the figure. In the bottom figure, both RE metal and Si atoms for the growing wire are provided by the immediate vicinity, leading to a different wire/substrate interface. Part (b) in the figure (plan view of the wire/substrate system) shows the coexisting wetting layer and wire for the growth mode described in the upper half of part (a), with new RE metal atoms restoring the wetting layer in the immediate vicinity of the wire, described in this figure by a large white box.

tween wetting layer formation and nanowire growth mentioned initially in Sec. 6.2.2.9: they represent our basic assumption for the overall details of wire growth in the presence of a wetting layer. [33]

The above assumption gives us two essential pieces of information which will be used ultimately in Sec. 6.2.6 for the evaluation of the calculations on the vacancy free Y disilicide nanowires on Si(001) performed in this work: *(i)* at the onset of wire growth, the lowest RE metal layer for the wire and the wetting layer on the surrounding terrace are at level as they are essentially the same layer initially. Furthermore, *(ii)* as clarified in Fig. 6.10, the long axis of the wetting layer 2×4 surface unit cell is always parallel

sible intermediate wetting layer-nanowire configurations. We shall postpone the discussion of why these considerations have not been used successfully in previous work for gaining knowledge on the structure of the RE disilicide nanowire on Si(001) until Sec. 6.2.6.

[33] For brief comments on RE disilicide nanowire growth on Si(001) in the absence of a wetting layer (as reported for RE = Er, see e.g. Ref. [146]) we refer to Sec. 6.2.6.

to the wire growth direction at the onset of wire growth. [34]

For reasons to be clarified in Sec. 6.2.3.2 the wetting layer and wire studies performed in this work are essentially decoupled. To a large extent, therefore, the above rules have no direct effect on our theoretical modelling. [35] Rather, they represent certain criteria which should ultimately, when we compare the wetting layer and wire results, be obeyed for our basic wire growth model presented above to make sense. For a discussion of this issue, we refer to Sec. 6.2.6.

As mentioned at the beginning of this disussion, the considerations described above offer the primary explanation to our reasons for modelling the Y/Si(001) wetting layer in our studies of vacancy free Y disilicide nanowires on the Si(001) surface. The discussions below in this subsection will focus on the details of the actual modelling: In Sec. 6.2.3.2, we shall clarify why studying wires in a bundle (see Sec. 4.2.3) is preferable to studying isolated wires on the surface and, in particular, why studying wires in a bundle means that we effectively decouple the wetting layer and wire studies. In Sec. 6.2.3.3, we shall present the set of wire configurations investigated in this work, discussing the completeness of this set of configurations.

We shall move to the discussion of the modelling of the Y/Si(001) wetting layer in Sec. 6.2.3.4 , 6.2.3.5, discussing initially in Sec. 6.2.3.4 the structural details for the 2×4 wetting layer, with reference to the original model by Liu and Nogami [169] and more recent experimental information on this surface reconstruction, and clarifying subsequently in Sec. 6.2.3.5 our chosen approach to the Y/Si(001) wetting layer structural optimization. Sec. 6.2.3.6 has two purposes: firstly, we shall make introductory comments to the reliability of the chosen theoretical description of the Y disilicide nanowire growth through a discussion of the experimental knowledge on the wire growth modes, this part of the thesis essentially being a precursor to the final evaluation of our results in Sec. 6.2.6. Secondly, we shall discuss how to obtain a reliable value for the energy required to removing the Si atoms from the substrate for consumption by the growing wire.

6.2.3.2 THE WIRE SYSTEM: REASONS FOR STUDYING A WIRE IN A BUNDLE

On the basis of the experimental knowledge on RE disilicide nanowire growth on the Si(001) surface (see Sec. 4.2.3), essentially two possibilities exist for the choice of nanowire system to be modelled by theory: *(i)* an isolated wire and *(ii)* a wire in a bundle of wires. Both of these systems can be described in principle within the supercell approximation (see Sec. 2.3). In practice, this approximation assumes characteristics

[34] As discussed in Sec. 6.2.1.1, the Y disilicide nanowires have been reported to coexist with a 1×3 wetting layer, rather than a 2×4 wetting layer, in experiment. [128] We have made the choice in the above to focus on the 2×4 wetting layer as no structural model has been suggested in the literature for the 1×3 wetting layer. However, ultimately, we shall both suggest a structural model and perform calculations for the 1×3 wetting layer (see Sec. 6.2.3.5 for further comments).

[35] As will be discussed in Sec. 6.2.3.6, the choice of a well defined wire/substrate interface (see Sec. 6.2.3.3) for the Y disilicide nanowires investigated in this work is still to be regarded as an assumption, albeit a reasonable one, with the basic reasoning making reference to the growth model presented in the text above.

for both systems which should be justified when comparing with the respective experimentally observed systems: in the case of the isolated wire, the requirement for a reliable theoretical description when using a supercell is that each wire is well separated from the adjacent wires, in the sense that acceptable convergence in the formation energy for the wire system with respect to wire separation has been obtained. For the wire in a bundle of wires described with a supercell, the fact that the bundle is regarded as infinitely wide in this approach means that the reliability in the theoretical description hinges on the wire being so far from the edges of the bundle that effects related to the bundle termination can be regarded as negligible: in other words, the wire bundle typically should contain many wires, a statement to be discussed further below.

On the basis of the above remarks, it seems clear that modelling a nanowire in a bundle is the preferable option: as the wire formation is associated with a significant substrate/overlayer lattice mismatch in the direction perpendicular to wire growth, the region of the surrounding terrace affected by the presence of the wire will necessarily be several Si(001) surface lattice parameters wide. To eliminate the effect of this wire potential on the adjacent wire, the requirement presented above, we will need large cells which in turn puts a restriction on the wire width, the conclusion being that only very narrow nanowires with an acceptable level of interaction can be studied in the supercell approximation. In practice, we will be likely to study only wires more narrow than the most narrow wires observed in experiment. [36] This is not necessarily detrimental to the theoretical predictions made, but it could have very important implications e.g. for comparisons of various wire cross sectional profiles, as *(i)* edge effects have a comparatively larger influence on the energies of the more narrow wires and as *(ii)* some of these effects might be 'masked' if only one wire width is studied.

For a RE disilicide nanowire in a bundle, the dimension of the supercell perpendicular to the wire growth direction includes only the wire and the narrow trench between wires [157]: studying wires of more than one width therefore should pose no problem. [37] Rather, as mentioned previously, the requirement for this theoretical description of the wire system being reliable is that the typical wire bundle contains a large number of wires. Exactly what number is required here is not a straightforward question: information is to be obtained from experiment and, to our knowledge, this topic is yet to be discussed. In particular, while the wires at the edges of the bundle appear to be more narrow than isolated wires [131, 165], [38] we are not aware of any 'convergence' of the wire width as one moves closer to the wires at the center of the bundle: in other words, there does not appear to be a simple change of the wire width reflecting when the wire is unaffected by the bundle termination. The only statement we can make on this issue

[36] For isolated RE disilicide nanowires on the flat Si(001) surface, the typical minimum wire width appears to be 6 Si(001) surface lattice parameters ($\sim$ 23 Å) [131, 163]. It is not necessarily impossible to describe an isolated wire of this width at an adequate level but the calculations will be time consuming and the problems faced when increasing the wire width further are evident.

[37] It is beyond the scope of the present discussion to consider more detailed modelling issues such as the trench between the wires in a bundle. For comments on this and other relevant issues for the wires in a bundle, we refer to Sec. 6.2.3.3

[38] We note that as we are focussing on wires far away from the edges in the bundle in our theoretical description of the wire system, it is not justifiable, given the remarks in Ref. [131], to conclude that we can study more narrow wires when choosing to model wires in a bundle.

is that bundles containing ten or more wires, a number which ought to be sufficiently large for our theoretical approach to describing the wire system being justifiable, have often been observed in experiment (as evidenced by experimental STM images in e.g. Ref. [98, 157]).

The above discussion has dealt only with studies of the nanowires themselves, without including considerations about the Si and RE metal 'reservoirs' for the growing wire. We shall postpone more detailed comments of our modelling of these reservoirs until Sec. 6.2.3.5 , 6.2.3.6 and make only a few remarks of relevance to the present discussion in the following.

The experimental observation that wires and wetting layers are found to coexist for the case of the Y disilicide nanowire growth on Si(001) [128] means that with both a wire and an intermediate region of variable size between adjacent wires present for the theoretical system under investigation, i.e., the situation for the isolated Y disilicide nanowire on Si(001), the intermediate region ought to be covered with a wetting layer rather than being clean Si(001). While this has the potential advantage that wetting layer formation and wire growth is described within a single system, with the effect of one system on the other modelled to some extent, this further complicates the theoretical description of the isolated wire system: *(i)* even if the wetting layer with the most frequently observed reconstruction at the point of isolated nanowire growth is chosen as default for the reconstruction of this intermediate region, a series of configurations, where the wetting layer unit cell is displaced relative to the wire in the direction perpendicular to wire growth, will generally have to be compared for a given wire separation in order to evaluate the importance of the relative position of wetting layer and wire. Furthermore, *(ii)* as mentioned in Sec. 6.2.3.1, with both wetting layer and wire described within a single system, we have to deal with the question of the structural details of the wire/substrate interface (see Sec. 6.10). And finally *(iii)*, if one actually wishes to take full advantage of this description of a coexisting wetting layer-wire system, configurations where RE metal atoms are removed from the wetting layer should be studied, making this approach to studying the wire-wetting layer system seem both rather naive and horrendously complex.

In comparison, for wires in an infinite bundle, the wire system in principle covers the whole substrate. In practice, this has the effect that the wetting layer and wire studies are decoupled in the sense that, in the assumed wire growth process, RE metal atoms are removed for consumption from somewhere in the bulk wetting layer region, far from the wires (or, to put this in another way, we perform calculations on the two systems separately). This decoupling, and the experimental support (to be discussed in Sec. 6.2.3.3) for the structural details of the intermediate region, i.e., the trench, between adjacent wires being fully resolved, simplifies the description of the wire bundle system tremendeously compared to the modelling of the isolated wire. [39] Once again, therefore, a RE disilicide nanowire in a bundle appears considerably easier to model satisfactorily compared to an isolated wire on the Si(001) surface. [40] We shall clarify

[39] As will be discussed in Sec. 6.2.3.3, the wire/substrate interface remains a topic of discussion for a RE disilicide wire in a bundle of wires.

[40] We do not focus in the present work on the differences in the assumptions made in the description of the RE metal consumption by the growing RE disilicde nanowire for the two wire systems considered: as a

in Sec. 6.2.3.6 why we believe that the decoupling of the wire and wetting layer system is not of crucial importance to the description of wire growth.

6.2.3.3 MODELLING THE WIRE STRUCTURE

The vacancy free Y disilicide nanowire studies have been carried out in various stages. Initial studies have focussed on 3×1 wires, i.e., wires with a unit cell covering an area of dimensions 3 (1) Si(001) surface lattice parameters perpendicular to (along) the wire growth direction. [41] For this set of wires, a practically exhaustive search for the energetically most favourable wire cross-sectional profile has been performed [42] within the restrictions that *(i)* the registry of each layer of the wire agrees with the registry obtained within the assumption that the wire is only elastically strained by the substrate and *(ii)* the lowest layer of the wire is a RE metal layer. In particular, the first choice of restriction above means we have not investigated various wire surface terminations for a given wire profile. We will discuss both of these approximations and their importance below, with a full discussion of the wire/substrate interface assumption postponed until Sec. 6.2.3.6.

Following these studies, we have increased the wire unit cell surface area for the most relevant 3×1 wire profiles along and perpendicular to the wire growth direction, in order to investigate (for a 3×2 wire) the completeness of the 3×1 optimization procedure and (for 5×1 and 7×1 wires) the dependence of the wire stability on wire width. The results of these studies will be described in Sec. 6.2.5. On the basis of experimental results [157], to be discussed further below, we choose a width of one Si(001) surface lattice parameters for the trench between wires. For the supercells used for the wire studies, this means that the surface dimensions considered, in units of Si(001) surface lattice parameters, are 4×1, 4×2, 6×1, and 8×1.

A general modelling issue, regardless of the particular choice of wire structure, concerns the trench between the wires in a bundle. Liu and Nogami reported that all measured trenches in their experiments on Dy disilicide nanowires on Si(001) in Ref. [157] adopted a width of one Si(001) surface lattice parameter. Although, to our knowledge, there have been no other detailed investigations into this issue, we regard the results in Ref. [157] as sufficiently strong evidence for the conclusion that the trench always has the above mentioned width to be justifiable. Another essential detail when

natural consequence of the supercell approximation, these descriptions are both hugely simplified compared to the experimental situation where the RE metal atoms bind primarily to the ends of the wire.

[41] Conventionally, the notation $n\times1$, $n > 1$, refers to a surface unit cell with the shorter length along the Si dimer row direction on clean areas on the surrounding terrace. Considering the remarks in Sec. 6.2.3.1 on the ambiguity for the wire/substrate interface, however, additional remarks are needed in order to clarify the meaning of the wire $n\times1$ unit cell. In our studies of Y disilicide nanowires, we have chosen a RE metal layer as the lowest layer for the wire (a discussion of this issue is provided below in the text). The notation '$n\times1$' refers to the fact that, with this choice of wire/substrate interface, the Si dimer rows appearing upon removal of the wire structure (see e.g. Fig. 6.10) would run perpendicular to the direction of wire growth. In other words, the n refers to the chosen width of the wire. For brevity, we shall use the nomenclature '$n\times1$ (or $m\times2$, see below in the text for details) nanowire', with the explanation defined by the above, frequently below.

[42] We shall not elaborate on this bold statement here, but return to the justification of the comment when we present the results of the vacancy free Y disilicide wire studies in Sec. 6.2.5.

discussing the trench between wires in a bundle is the observation that, in situations where termination of one wire away from the edges in a bundle is observed (see e.g. Fig. 4, 5 in Ref. [157]), the surrounding wires apparently can easily change their width, this process being seemingly similar to the kinks in isolated wires often observed in the experimental STM images of isolated wires. This suggests that the trench region itself is not explained by a structure with a large kink energy.

On the basis of these experimental observations and our RE disilicide nanowire growth model presented in Sec. 6.2.3.1, we believe that there is strong support for the conclusion that the trench between wires in a bundle, whatever the details of the wire/substrate interface, is simply to be regarded as an area on the substrate where no overlayer has been deposited, i.e., while the Si-Si bond lengths in this region are affected by the strain on the substrate due to the wire growth, this effect does not lead to bond breaking and reordering of the atoms in a new 'wire trench structure'. [43] We shall discuss the function of the trench further below, but only note, for the time being, that the structural details of this part of the wire system appear to be fully clarified. We shall therefore not refer to our choice of trench structure as a modelling assumption below.

When discussing the choice of wire/substrate interface for the Y disilicide nanowires on Si(001) investigated in the present work, the onset of growth of wires in a bundle, and the function of the trench between wires in this respect, become fundamental issues. On the very basic level, the RE disilicide nanowires in the bundle must nucleate either *(i)* simultaneuously, i.e., like a single very broad wire, where the trenches appear naturally as strain relief (see the discussion in Sec. 6.2.2.5 for details), or *(ii)* independently, where the wire widths are limited by the nearby growth of other wires. For the growth scenario where all wires nucleate simultaneously, we would expect the Si atoms for continuing growth of these wires to be provided from outside of the bundle region, i.e., we would assume that the trenches between the wires remain unaffected. [44] In other words, on the basis of our growth model of Sec. 6.2.3.1, regardless of the particular growth scenario from the pair of scenarios presented in Fig. 6.10, now applied to the complete wire bundle (see Fig. 6.11), we would expect the wire/substrate interface for a wire well within the bundle to be the same.

If the wire bundle formation involves wires nucleating independently, a different wire/substrate interface can be obtained by using the wire growth mode in Fig. 6.10 where the Si atoms are consumed from the immediate vicinity of the growing wire: each wire now has a Si layer as its lowest layer, with a RE metal layer as its next layer. This suggestion is not at variance with the trench width being one Si(001) surface lattice parameter, only it suggests different structural details for the wire profiles. It therefore seems that, by neglecting the possibility of this alternative wire/substrate interface, we essentially remove half of the potential candidates for the structure of the

[43] Fig. 6.12 shows examples of this situation (strain effects ignored) for situations where the lowest layer of the wires is assumed to be a RE metal layer.

[44] Removing Si atoms from the trench between wires would involve breaking Si-Si bonds for Si atoms forming part of the wire structure, a process that would be associated with the edge of the wire structure for the wires around the trench to be 'destabilized'. Such a suggestion does seem at odds with the experimental observation [157] that the trench width is always one Si(001) surface lattice parameter.

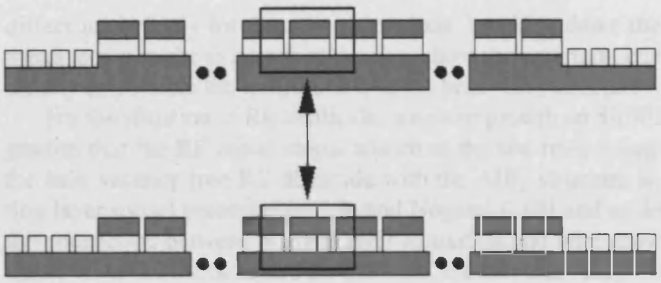

Figure 6.11: Schematic presentation showing how a RE disilicide nanowire well within a bundle of wires on the Si(001) surface is believed to be unaffected by the details of the wire growth mode (as emphasized by the identical contents within the black frames in the top and bottom figure) for the situation where all wires in a bundle are assumed to nucleate simultaneously. The two figures above describe the two wire growth modes presented in part (a) of Fig. 6.10, the boxes at the sides of the top and bottom figure describing the edges of the wire bundle and the central boxes in the figure describing the bulk region of the bundle, with the presence of an intermediate region between the edge and bulk of the bundle emphasized by the black dots between the boxes. See text for further details.

vacancy free Y disilicide nanowire. For reasons to be discussed in Sec. 6.2.3.6, we regard our chosen wire/substrate interface as a considerably more likely option.

The assumption about the registry of the various layers for the nanowire structure mentioned at the beginning of this discussion has an appeal similar to the assumption on the wire/substrate interface discussed above, in that it greatly simplifies the wire studies, reducing immensely the number of (ingeniously chosen) configurations which would otherwise have to be considered for completeness. In order to discuss the justifiability of this assumption, we consider the 2D RE disilicide growth on the Si(111) surface, where the structure of the overlayer (including the registry with the substrate) is well known (see e.g. Ref. [170]). For this system, optimization of the registry of the whole film with respect to the substrate is important, with the energetically most favourable structural arrangement not being obtained in an approach similar to the above, i.e., by assuming that the lowest RE metal layer for this system occupies the sites where the structural environment is most similar to the environment in the bulk AlB_2 structure.

On the face of it, the conclusion for the 2D RE silicide structure on Si(111) supports the need to go beyond the approximation of an elastically strained, but otherwise undistorted structure for the studies of Y disilicide nanowires on Si(001). The expectation that the RE atoms for the 2D film should deposit at the above mentioned site, on the other hand, is rather naive as it disregards the fact that the hybridization of the Si atoms for the substrate plane is sp^3 rather than sp^2, as obtained in bulk RE disilicide. In other words, not only is this surface plane distorted compared to the graphite-like Si plane for bulk RE disilicide with the AlB_2 structure [170], but also, the electronic structure

differs importantly for these two situations, breaking down the argument that the RE metal atoms ought to adsorb at the site where the structural environment resembles as closely as possible the environment in the bulk AlB_2 structure.

For the situation of RE disilicide nanowire growth on Si(001), by contrast, the suggestion that the RE metal atoms adsorb at the site resembling the local environment for bulk vacancy free RE disilicide with the AlB_2 structure is supported by the wetting layer model presented by Liu and Nogami [169] and as discussed in Sec. 6.2.3.1 the connection between wetting layer formation and wire growth appears highly intimate. [45] As for the Si layers for the wire, the fact that AlB_2 structure [0001] axis (the normal vector to the Si graphite-like planes for the bulk structure) is along the direction of wire growth (see e.g. Fig. 6.12) means that for a given added Si layer there should be a strong preference for the Si atoms to be located close to the highly directional dangling bonds of the Si atoms from the lower Si layer. [46] Concluding, therefore, the assumption of an elastically strained nanowire structure chosen in our studies, while being highly convenient for the reasons mentioned at the beginning of this paragraph, appears, in addition, to be justifiable.

The various wire profiles investigated for the 3×1 vacancy free Y disilicide nanowire have been included in Fig. 6.12. We are not aware of any information on the range of Y disilicide nanowire widths observed in experiment. However, considering the discussion in Sec. 6.2.3.2, it seems unlikely that the 3×1 wire should actually have been observed far from the edges in a wire bundle for Y disilicide nanowire growth on Si(001). The 5×1 and 7×1 wire studies are indispensable from this point of view as they represent wire widths which might actually have a counterpart in experiment.

In addition to the assumptions for the wire structure presented previously in this discussion, the profiles shown in Fig. 6.12 involve the additional simplification that the wire is assumed to be symmetric with respect to the AlB_2 structure [11-20] plane running through the center of the wire, i.e., a vertical line through the wire centers in Fig. 6.12 (not shown). This assumption is justified by the fact that no asymmetric wire profiles have been reported in experiment.

The wire profiles studied divide into four groups: for each group, we have consid-

[45] This remark ignores the fact that for the RE/Si(001) 2×7 surface reconstructed wetting layer often reported [131, 166, 167] to coexist with the 2×4 wetting layer and the RE disilicide nanowires for RE metal deposition on Si(001), protrusions with two different registries with respect to the Si dimers on the surrounding clean areas on the terrace are observed, i.e., some of the assumed [166, 167] RE metal atoms for this wetting layer do not adsorb at the site on the Si(001) surface which resembles the local environment in the AlB_2 structure as closely as possible. Considering the suggestion in Sec. 6.2.3.1 that the wetting layer is essentially an array of nanowire templates this observation could be regarded as a suggestion that the nanowire structure has a similar division for the lowest layer RE metal atoms into two subsets, with the complete wire structure being much more complex than assumed in the present discussion. Essentially, given the present level of experimental and theoretical knowledge on the RE disilicide nanowires on Si(001), we can not rule out the possibility of such alternative wire structures. Our basic reason for ignoring this issue in the present work (only Sec. 6.2.6, discussing future work on the Y disilicide nanowires, will include further comments on this issue) is one of simplicity in the theoretical studies.

[46] We note that this argument does not determine the Si layer positions in the added layer unambiguously for all layers. The initial alternative structures produced, however, are the other RE disilicide structures observed upon RE disilicide 3D film growth on Si(001) (see Sec. 4.2.3): as discussed in Sec. 6.2.2.3 , 6.2.2.4, these structures are of little interest to the present discussion.

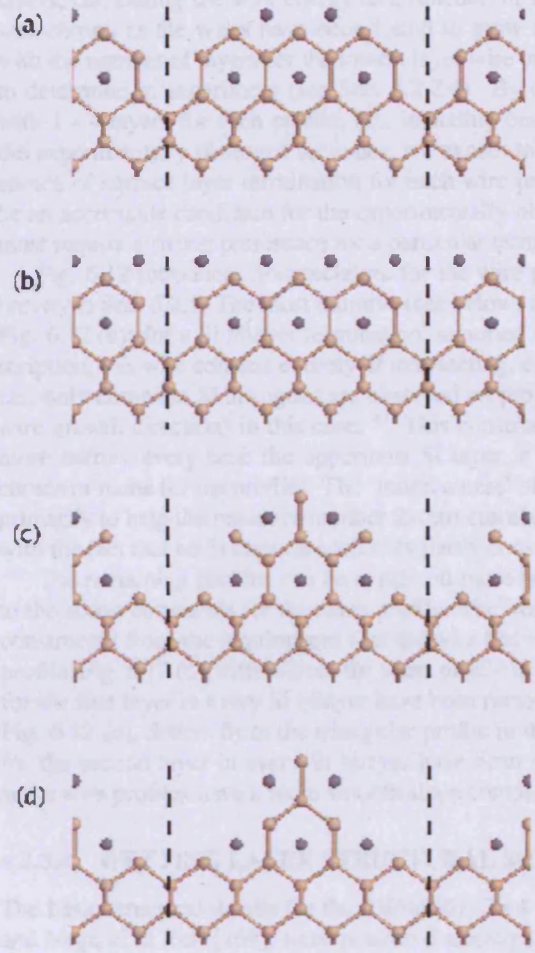

Figure 6.12: Schematic presentation of the complete set of wire cross sectional profiles investigated for the studies of the stability of the vacancy free Y disilicide nanowire with the AlB_2 structure. Y (Si) atoms have been represented with dark grey (light brown) spheres in the figure. The wire growth direction is into the paper. The vertical dotted lines in the figures show the edges of the supercell used for the modelling, with adjacent wires in the assumed wire bundle at the edges of each figure. The cross sectional profiles investigated are (a) 'stairs', (b) 'rectangular', (c) 'triangular', and (d) 'spike'. For each of these profiles the total energy variation with numbers of layers for the wire was evaluated for all numbers up to the choice shown in the figures (4 layers for the first two profiles, 5 layers for the last two), for reasons discussed in the text.

ered addition of layers to the wire until the point where the wire contained at least four layers, calculating the wire energy as a function of layers in all cases. This approach was chosen as the wires have been found to grow in steps of three layers [157] but with the number of layers for the lowest layer wire unknown, being a quantity difficult to determine in experiment (see Sec. 6.2.2.6). By calculating the energies for wires with 1 - 4 layers for each profile, i.e., including one more layer than the number for the experimentally observed sequence, we expect to reveal any trend towards a given choice of surface layer termination for each wire profile. For a given wire profile to be an acceptable candidate for the experimentally observed Y disilicide nanowire, we must require a strong preference for a particular termination layer for this profile.

Fig. 6.12 introduces nomenclature for the wire profiles to be used for clarity and brevity in Sec. 6.2.5. The most intuitive (see below) wire profile is the 'stairs' profile of Fig. 6.12 (a): for a Si bilayer termination, assumed here only for simplicity in the description, this wire consists entirely of intersecting, complete Si AlB_2 structure 'cages', i.e., only complete Si hexagons are observed on projection onto the [0001] plane (the wire growth direction) in this case. [47] This construction results in a wire which gets more narrow every time the uppermost Si layer in a Si bilayer is added (hence the choice of name for the profile). The 'intuitiveness' of the construction, mentioned here primarily to help the reader remember the structural details of this profile, is connected with the fact that no Si cages are left only partly constructed for this wire growth mode.

The remaining profiles can be explained more briefly, two of them with reference to the above comments for the stairs profile. The 'rectangular' profile, Fig. 6.12 (b), is constructed from the requirement that the wire has vertical sidewalls. The 'triangular' profile, Fig. 6.12 (c), differs from the stairs profile in that the Si atoms at the wire edges for the first layer in every Si bilayer have been removed. Similarly, the 'spike' profile, Fig. 6.12 (d), differs from the triangular profile in that the Si atoms at the wire edges for the second layer in every Si bilayer have been removed. Both the triangular and spike wire profiles have a more smooth slope compared to the stairs profile.

6.2.3.4 WETTING LAYER STRUCTURAL MODELS: PREVIOUS WORK

The basic structural details for the RE/Si(001) 2×4 wetting layer, as proposed by Liu and Nogami in Ref. [169], were presented already in Sec. 6.2.3.1 when we discussed the reasons for modelling the Y/Si(001) wetting layer as part of our studies of vacancy free Y disilicide nanowires on the Si(001) surface. In the present discussion, we shall give a more detailed account of these considerations, clarifying the extent to which the structural model presented in Ref. [169] is to be regarded as well established. We shall focus almost entirely on the 2×4 wetting layer below, making only brief comments on the also frequently observed 2×7 surface reconstructed wetting layer. For comments on the 1×3 wetting layer reported for Y on Si(001), we refer to Sec. 6.2.3.5 where we shall discuss our strategy for modelling the wetting layers of relevance to the Y disili-

[47] We emphasize that this and the following descriptions of the wire profile structures completely disregard relaxation effects, their sole purpose being to connect, on the most basic level, the chosen names for the wire profiles with the wire structures shown in Fig. 6.12 (where effects of relaxations, unknown at the present stage of the discussion, are also excluded).

cide nanowire studies. [48]

The studies by Liu and Nogami in Ref. [169] of the 2×4 Dy/Si(001) wetting layer represent the first experimental studies of wetting layer 2×n surface reconstructions. These experiments reported small more or less connected areas of clean Si(001) and reconstructed surface as shown in Fig. 3 of Ref. [169]. Each 2×4 surface unit cell for the reconstructed area was found to contain three protrusions, in registry along both directions with the Si dimers on the clean areas. Along the short axis of this unit cell, the reconstructed part of the surface would alternate between a protrusion and a dark area, assumed to be a vacancy, while along the perpendicular direction on the surface, the alternation would involve triplets of protrusions separated by an assumed vacancy. The long axis of the 2×4 unit cell was found to be along the direction of the Si dimer rows on the clean Si(001) areas.

Minor structural details in the experiments of Ref. [169] involved an observed division of the triplets of protrusions on the reconstructed area into two subsets, distinguished by different brightness in the experimental STM images. A local ordering of either a bright protrusion between two less bright protrusions, or vice versa, was always reported in empty state images. The relative brightness of the protrusions for a given unit cell showed a strong dependence on applied bias, the brighter protrusions changing into the less brighter ones for voltages above 1 V. Some short range ordering of these two types of triplets, with pairing of dissimilar structures along the Si dimer row direction, was reported on the basis of the STM studies. The surface reconstruction as reported on the basis of results obtained with LEED, on the other hand, was 2×4.

The authors of Ref. [169] concluded that each protrusion was most likely to be associated with a single Dy atom, [49] i.e., that the reconstructed areas were Dy/Si(001) wetting layer segments. Furthermore, on the basis of *(i)* the relative intensity of the reconstructed and clean areas in the experimental STM images and *(ii)* the registry of the protrusions for the reconstructed areas with respect to the Si dimers on the clean areas, it was suggested that each Dy atom replaced a Si dimer on the surface. In other words, the Dy atoms were concluded to adsorb at a site on the Si(001) surface bearing as close resemblance as possible to the structural environment for Dy in bulk Dy disilicide with the AlB_2 structure. Fig. 6.9 summarizes these conclusions in a schematic presentation of the resulting 2×4 wetting layer model, neglecting possible structural differences for the Dy atoms within a given unit cell.

More recent studies of 2×4 wetting layers, performed on the basis of experimental observations for Ho [131], Er [171], and Gd [167] deposition on the Si(001) surface, have basically supported the model presented by Liu and Nogami in Ref. [169],

[48] Within the discussion of the 2×4 RE/Si(001) wetting layers, a subtle element of potential confusion arises from the fact that often, wetting layers with a 4×2, rather than a 2×4 surface reconstruction are reported in the literature. We have investigated this issue only for the Y/Si(001) wetting layers (see Sec. 6.2.1.1), otherwise ignoring it in our present discussions, partly as a consequence of the conclusion obtained from the above mentioned investigation.

[49] This conclusion was drawn with some reservation: as a consequence of the nanowire-wetting layer coexistence, a correlation between the amount of deposited Dy atoms and the density of wetting layer unit cells on the surface was difficult to establish in the experiments of Ref. [169]. As will be discussed below, one of the outstanding questions for the current wetting layer model indeed is whether one or both of the two types of protrusions mentioned previously can be associated with a RE metal atom.

the only remaining question addressed by Ohbuchi and Nogami in Ref. [131] being whether all protrusions for the wetting layer corresponded to Ho atoms. It was concluded by the authors, on the basis of comparisons between wetting layer/nanowire coverage and the deposited amount of Ho on the Si(001) surface, that only one of the two protrusions should be associated with Ho. On the other hand, Harrison *et al.* [167] suggested, on the basis of the STM images collected in their experimental studies of the Gd 2×4 wetting layer that each protrusion was most likely to be associated with a Gd atom, the key arguments being the identical registry of the protrusions and their similar bias voltage dependence. [50] Finally, Yang *et al.* [171] associated each protrusion for their reported Er 2×4 wetting layer with an Er dimer, rather than an Er atom, on the basis of considerations similar to those in Ref. [131]. As an additional support for the conclusion made from the experiments of Ref. [171], Er disilicide nanostructures were found not to grow at the chosen coverage ($\sim$ 0.5 ML). Considering the clear similarities between the 2×4 wetting layers for these different RE metals as observed with STM, the interpretation of the protrusions for the wetting layer must be regarded as an unsolved issue at present.

In addition to the 2×4 wetting layer investigations, 2×7 wetting layers have also been studied in considerable detail for Ho [131], Gd and Dy [166], and Gd [167] deposition on Si(001). The 2×7 wetting layer always coexists with the 2×4 wetting layer with the onset of formation being at comparatively higher RE metal coverages. The fractional coverage for the two layers and the onset of 2×7 wetting layer formation relative to wire nucleation appears to show a strong dependence on the RE metal in question [166]. For this surface reconstruction, the ordering is evident in both filled and empty state images, in contrast to the 2×4 wetting layer where the ordering is much clearer in the empty state images. Models for this 2×7 wetting layer, suggesting a structure with clear similarities to the 2×4 wetting layer, have been proposed [166, 167]. However, it is beyond the scope of the present discussion to go into details with this issue, as our wetting layer modelling, to be presented in Sec. 6.2.3.5, is not focussed on the 2×7 wetting layer. [51].

The key assumption made by Liu and Nogami in Ref. [169] when presenting the RE/Si(001) 2×4 wetting layer model is the suggestion that each RE metal atom replaces a Si dimer during wetting layer formation. While the complete 2×4 wetting layer has been studied theoretically for Gd on Si(001) [167], [52] this 'substitutional wet-

[50] Harrison *et al.* also chose to refer to the Gd/Si(001) wetting layer under investigation in Ref. [167] as a 2×8 surface reconstructed wetting layer, on the basis of the fact that also for this wetting layer, the experimental STM images suggested short range ordering of the two types of protrusions along the Si dimer row as reported previously for the Dy/Si(001) 2×4 wetting layer by Liu and Nogami in Ref. [169]. For simplicity, we shall postpone a discussion of this issue until the presentation of our Y/Si(001) 2×4 wetting layer optimization results in Sec. 6.2.4.3.

[51] We are not aware of any experiments reporting coexistence of only a 2×7 wetting layer with a growing wire at the onset (with regards to RE metal coverage) of wire growth. For this reason, we do not regard, on a general level, modelling of the 2×7 wetting layer as crucial for obtaining reliable relative wire energies. In the case of Y disilicide nanowire growth on Si(001), no 2×7 wetting layers have been reported at all, see Sec. 6.2.1.1.

[52] We shall discuss these results when presenting our results for the structural optimization of the Y/Si(001)

ting layer growth mode', i.e., the gradual replacement of Si with RE metal, is yet to be investigated by theory.

Experimentally, the changes of the Si(001) surface observed upon deposition of very low coverages ($\sim$ 0.1 ML) of RE metal have been studied for Gd on Si(001) by Harrison *et al.* [167]. These studies, involving deposition of Gd during annealing at temperatures in the range 675 - 975 K, revealed a strong interaction between RE metal and substrate for Gd coverages below 0.1 ML, with the appearance of long lines of vacancies on the Si(001) surface, running along the direction perpendicular to the Si dimer rows on the terrace. The authors of Ref. [167] connected the appearance of these vacancy lines with the presence of Gd on the surface, the lines being absent before the Gd deposition. Furthermore, they argued, on the basis of experimental and theoretical results for other impurities such as Ni on Si(001), that this phenomenon might be associated with Gd atoms occupying dimer vacancies, i.e., the same (locally) adsorption site as suggested by Liu and Nogami [169] for the RE/Si(001) 2×4 wetting layer, reducing the mobility of these vacancies considerably and thereby affecting the general accumulation of vacancies not containing a Gd atoms.

For slightly higher Gd coverages ($\sim$ 0.1 ML), triplets of protrusions, with the same characteristics as those obtained for the Gd/Si(001) 2×4 wetting layer, were observed. These triplets showed some tendencies of clustering, with isolated triplets always being of the type with a single brighter protusion between two less bright protrusions in an empty state image collected for a relatively small voltage bias ($\sim$ 0.5 V). Further studies showed that, upon increasing increasing the bias voltage, the relative brigthness of the protrusions was reversed for the isolated protrusion (see Fig. 3 of Ref. [167]), as reported previously for both the Dy and Gd 2×4 wetting layers on Si(001) [169, 166]. For both types of triplets, including isolated triplets, vacancies adjacent to the protrusions along the Si dimer row direction were reported. [53] We note that these experimental results, while providing a great deal of knowledge on the initial stages of wetting layer formation, did not rigorously show that the suggestion by Liu and Nogami [169] that the Si dimers are replaced by RE metal atoms as part of this process is correct.

6.2.3.5 MODELLING THE WETTING LAYER

The theoretical studies of the RE/Si(001) 2×4 wetting layer so far have been limited to a study by Harrison *et al.* in Ref. [167] of the fully constructed layer for Gd on Si(001), within the assumption that the wetting layer model presented initially by Liu and Nogami in Ref. [169] was correct. In the present theoretical study of the Y/Si(001) 2×4 wetting layer, [54] we shall move beyond this assumption in various ways, although

2×4 wetting layer in Sec. 6.2.4.3.

[53] The 'vacancies' adjacent to the protrusions along the perpendicular of the surface were 'naturally' present, being the trenches on either side of the Si dimer row in question.

[54] As discussed in Sec. 6.2.1.1, two different wetting layer surface reconstructions, a 2×4 and a 1×3 wetting layer, have been reported in experiment for Y on Si(001) [128]. We shall focus on the modelling of the former of these wetting layers here, as no model has been presented so far for the 1×3 wetting layer. Theoretical studies of this wetting layer however will be considered as well (see below in the text), as it is the 1×3 wetting layer, rather than the 2×4 wetting layer, which has been reported [128] to coexist with the Y disilicide nanowires on the Si(001) surface.

our studies will also in some senses be preliminary, in ways to be clarified below. In the process of presenting our chosen approach to studying Y wetting layer formation on Si(001), we shall analyse the experimental observations for the RE/Si(001) wetting layer presented in Sec. 6.2.3.4, in the attempt to clarify what can be concluded from the various observations, i.e., what must be regarded as essential requirements for the wetting layer structure. We shall, however, postpone the full discussion of these issues until Sec. 6.2.4.3, where we analyse the results of the Y/Si(001) wetting layer structural optimization, i.e., where rather complete theoretical information on the formation of a RE/Si(001) wetting layer is actually available. Also, a discussion of the previous theoretical results for the RE/Si(001) 2×4 wetting layer [167] is postponed until Sec. 6.2.4.3

Liu and Nogami suggested, on the basis of their experimental results for Dy on Si(001) in Ref. [169], that each protrusion for the 2×4 wetting layer observed in these studies should be explained by a Dy atom replacing a Si dimer on the surface. This suggestion has been challenged in more recent experimental studies (see Sec. 6.2.3.4 for a full discussion): suggestions have been made that *(i)* only half of the protrusions should actually be associated with RE metal atoms [131] and *(ii)* that the Si dimers are replaced by RE metal dimers rather than atoms [171]. The basic conclusion in Ref. [169] regarding the position of the RE metal atoms for the wetting layer has not been questioned, though. As will be discussed below, this choice of adsorption site for the RE metal atoms on the Si(001) surface indeed would be likely to be associated with a significant binding energy, but clearly, such an argument is not a truly satisfactory answer to a question on which a great deal of the theoretical modelling of the wetting layer rests. A detailed theoretical study of the RE/Si(001) 2×4 wetting layer should clarify, at the outset, which adsorption sites are the energetically most favourable for the RE metal atom in question when deposited on the Si(001) surface.

While our approach to modelling the Y/Si(001) 2×4 wetting layer rests on the basic assumption that each protrusion for the wetting layer is explained by either an Y atom or an Y dimer, we aim at constructing this wetting layer on the basis of calculations for isolated Y atoms and dimers rather than the experimental knowledge on the registry of the protrusions with respect to the Si dimers on the surrounding terrace discussed in Sec. 6.2.3.4: we shall neglect in these initial studies the essential (within the assumption that each protrusion is to be associated with a RE metal atom/dimer) experimental information about the registry of the protrusions with respect to Si dimers on the surrounding clean areas on the Si(001) surface, testing, thus, at the very basic level whether the wetting layer model presented by Liu and Nogami in Ref. [169] (i.e., with each protrusion associated with RE metal as opposed to more recent variations) agrees with theoretical results for the current case of Y on Si(001).

On the basis of our results for the isolated Y atoms/dimers on Si(001), we shall construct wetting layers on the basis of the energetically most favourable such 'wetting layer units' (a term which will be used frequently below to describe the assumed theoretical explanation for a single wetting layer protrusion, in order to avoid confusion with the experimentally observed protrusions, where the registry requirements are present) in a manner described for a particular choice of wetting layer unit in Fig. 6.13. Also for the construction of the wetting layers, we shall test the modelling by Liu

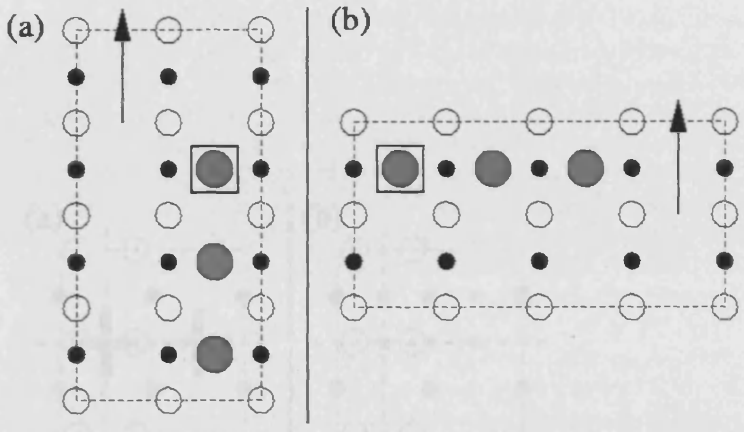

Figure 6.13: Schematic presentation of the construction of RE/Si(001) 2×4 and 4×2 surface reconstructed wetting layers on the basis of a RE/Si(001) wetting layer unit (see Fig. 6.9 for basic comments on the presentation). The figure shows a 2×4 and 4×2 wetting layer unit cell, part (a) and (b) respectively, where e.g. the '2×4' notation refers to the long axis of the unit cell being parallel to the Si dimer row direction on the surrouding clean areas on the terrace. For the present wetting layer, the unit, being the large grey atom enclosed by a black frame, is deposited at the Hollow site on the Si(001) surface, i.e., in the trench between dimer rows. The 2×4 cell therefore has the RE metal atoms agglomerating along the Si dimer row direction (the black arrow in the figure). For simplicity in the presentation, the Si dimer bonds have been broken. For the 4×2 wetting layer, the RE metal atoms agglomerate along the perpendicular direction on the surface.

and Nogami [169] by constructing both Y/Si(001) 2×4 and 4×2 wetting layers. In other words, within the assumption that each protrusion for the experimentally observed RE/Si(001) 2×4 wetting layer is explained by a RE metal atom or dimer, our modelling comes close to being complete. We shall postpone discussions of the limitations of our studies until Sec. 6.2.4.3, where the results of our Y/Si(001) wetting layer calculations are discussed.

As mentioned in the above presentation of our theoretical modelling of the Y/Si(001) 2×4 wetting layer, for the investigation of the adsorption of single Y atoms and dimers on the Si(001) surface we have paid no attention to the experimentally observed requirements for the registry of these adatoms/addimers with respect to Si dimers on the clean terrace that must be satisfied for a connection with the protrusions of the wetting layer unit cell to be justifiable. We shall discuss this requirement in some detail in the following, however, in order to fully clarify which of the Y atom/dimer adsorption sites can actually be associated with the protrusions for the experimentally observed wetting layer.

Fig. 6.14 shows the configurations with a single Y atom or Y dimer on the Si(001)

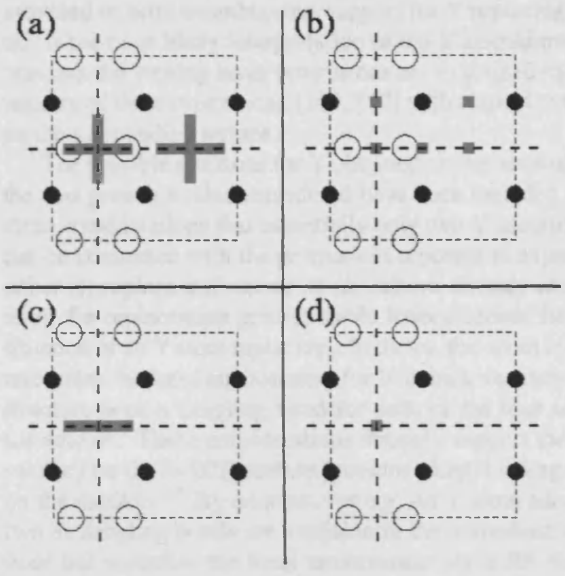

Figure 6.14: Schematic presentation of the selected adsorption sites for Y atoms and dimers on the Si(001) surface in the present studies. The two uppermost layers for the clean surface are represented by white and black spheres respectively, with the size of the spheres decreasing as one moves into the substrate. Dimerization of the uppermost Si atoms has been shown while buckling has been ignored. The selected Y adsorption sites have been represented with grey squares for the case of Y atoms and grey rectangular boxes for the case of Y dimers, with the long axis of the box along the dimer bond. In part (a), (b) in the figure, Y is deposited on the otherwise unchanged surface while in part (c), (d), Y replaces a Si dimer. The dotted lines in the figure show the experimental requirements for the registry of a 2×4 wetting layer protrusions with respect to Si dimers on the surrounding clean areas on the surface: only Y atoms located at (Y dimers with the dimer bond centered at) the site where the horizontal and vertical dotted lines meet are allowed on the basis of these experimental observations. See text for further details.

surface which have been investigated in the present work. [55] In addition to considering both Y atom and dimer adsorption on this surface, we have also considered substitutional as well as additional growth modes, i.e, Y replacing a Si dimer as well as Y adsorbing on the otherwise unaffected surface. This choice is made in order to achieve a fairly complete picture of the Y adsorption sites on Si(001). Furthermore, we note that the experimental studies of the wetting layers described in Sec. 6.2.3.4 have not provided us with unambiguous support for Y replacing Si dimers on the surface: only, this is the most likely interpretation of the Y atom/dimer positions, within the assumption that the wetting layer protrusions are explained by Y, on the basis of the reported registry of these protrusions [169, 167] with respect to the Si dimers on the clean areas on the surrounding terrace.

The possible positions for Y obtained on the basis of these registry requirements for the two growth modes considered have been included in Fig. 6.14. It is evident from these considerations that essentially only two Y adsorption sites on the Si(001) surface can be connected with the protrusions reported in experiment: the Y atom/dimer must either *(i)* replace a Si dimer or *(ii)* adsorb directly above a Si dimer. [56] On the face of it, the replacement growth mode indeed seems the more sensible option: for the situation of an Y atom replacing a Si dimer, this atom is located at a site that structurally resembles the local environment for Y in bulk vacancy free Y disilicide with the AlB_2 structure with a dangling bond for each of the four second layer atoms surrounding the adatom. These considerations strongly support the suggestion that a single dimer vacancy on the Si(001) surface provides a high binding energy for an Y atom deposited on the surface. [57] By contrast, for e.g. an Y atom adorbed on top of a Si dimer, only two Si dangling bonds are available in the immediate vicinity, and the adsorption site does not resemble the local environment for a RE disilicide structure. We refer to Sec. 6.2.4.2 for a discussion of which of these sites is the more favourable one for Y on Si(001) according to our studies.

Another requirement from experiment is that the long axis of the 2×4 wetting layer unit cells should be parallel to the Si dimer row direction on the clean areas on the surrounding terrace [169, 167]. On the basis of this observation, we find that, within the above mentioned set of experimentally acceptable wetting layer units, the acceptable Y/Si(001) wetting layer constructed on the basis of the studies of Y atoms/dimers on Si(001) as described previously should be a 2×4 wetting layer for the situation where Y is replacing Si but a 4×2 wetting layer for the situation where Y is adsorbed on the otherwise unchanged surface, the wetting layer in this case being raised by one Si layer relative to the clean surface and therefore rotated by 90°. We shall refrain from discussing this issue for the remaining potential wetting layer units in Fig. 6.14 but return to it in Sec. 6.2.4.3, when discussing the results of the wetting layer studies.

[55] For simplicity, we shall not go into detail with the description of these configurations in the present discussion. We refer to Sec. 8.3.4 for detailed comments on this entire set of configurations.

[56] For the Y dimer configurations, 'directly above' refers to the center of the Y dimer bond: as clarified in Fig. 6.14 (a), we have considered two configurations that might satisfy this requirement, depending on the effects of the structural optimization.

[57] For the Y dimer replacing a Si dimer, this argument appears to make less sense. We shall leave this point for now, returning to it in Sec. 6.2.4.2 when discussing the results of the calculations for Y atoms and dimers on the Si(001) surface.

Our initial theoretical studies, to be discussed in Sec. 8.3.4, of the entire set of Y atom/dimer configurations on the Si(001) surface shown in Fig. 6.14, employed a supercell containing a single Si dimer row with two dimers in it (like the cells shown in Fig. 6.14). As mentioned previously in this discussion, the aim of this study is to separate out the realistic candidates, from the point of view of the calculated formation energies, for wetting layer units forming the basis of the Y/Si(001) 2×4 and 4×2 wetting layer construction, with an example shown in Fig. 6.13. In order to compare the formation energies for these layers with the formation energies of relatively isolated wetting layer units, however, [58] we performed calculations for larger cells for these units, increasing the surface cell dimension by a factor two along or perpendicular to the Si dimer row direction initially and along both of these directions for the largest cell considered, in all cases with only one wetting layer unit in the cell. We shall discuss in Sec. 6.2.4.2 the convergence in the structural parameters and total energies for these wetting layer units with respect to the above described changes in the separation between adjacent units.

When considering substitution of Y for Si on the Si(001) surface, we must include, in order to evaluate the energy of the configurations considered, an energy for binding the removed Si atoms somewhere else on the substrate. We have chosen the binding energy for Si atoms at a step edge on the surface, obtained as described in Sec. 6.2.3.6, for this energy. While experiment suggests that very low coverages ($\sim$ 0.1 ML) of RE metal on the Si(001) surface is the cause of the formation of long vacancy lines on this surface [167], with the amount of vacancies on the surface reported to increase considerably upon RE metal adsorption (suggesting that Si atoms are moved from the terrace to the step edges), there are no comments by the authors on the RE metal considerably altering the surface step edge structure at these coverages. For reasons to be clarified in Sec. 6.2.3.6, we regard our evaluation of the Si binding energy described in that discussion as applicable to the above situation.

For Y/Si(001) wetting layers, where the uppermost Si layer for the substrate has been either removed or covered completely, the distinction between a substitutional growth mode and a growth mode involving adsorbing Y at the corresponding site on the Si(001) surface without removing any Si essentially does not apply and the binding energy for a Si atom at the step edge on the surface is not required. [59]

As mentioned previously in this discussion, the Y/Si(001) 2×4 wetting layer is not the wetting layer reported to coexist with the growing Y disilicide nanowires [128]: the relevant wetting layer for a theoretical investigation of a coexisting wire-wetting layer system for this element is a 1×3 wetting layer. We have focussed on the Y/Si(001) 2×4 wetting layer in the above discussion as *(i)* it represents a situation which has been reported for Y on Si(001) [128] and *(ii)* it has been studied in detail experimentally,

[58] A comparison of the wetting layer formation energies with energies for configurations with relatively well isolated Y atoms or dimers on the Si(001) surface (an experimentally observed situation [167]) is considered useful in the present studies as it offers yet another way to address the justifiabilty of the wetting layer model presented by Liu and Nogami in Ref. [169]. We shall discuss this comparison of energies in Sec. 6.2.4.3.

[59] We note that this also holds true in general when comparing different wetting layers (see discussion below in the text) which are distinguished, essentially, by a redistribution of the Y atoms on the substrate.

leading to the suggestion of a structural model for this surface reconstruction [169] and a wealth of indispensable experimental information for the evaluation of the results of a (relatively) unbiased theoretical study of this system.

For the Y/Si(001) 1×3 wetting layer, by contrast, essentially no experimental information has been published. We shall nevertheless present a structural model for this layer on the basis of our Y/Si(001) 2×4 wetting layer studies in Sec. 6.2.4.3 and structurally optimize this wetting layer as well in order to clarify the Y disilicide nanowire stability relative to this system. As the model presented is strongly connected with the results of the 2×4 wetting layer studies, we shall not go into detail with this issue in the present discussion but refer to Sec. 6.2.4.3 for further details.

6.2.3.6 ON THE SELECTED ATOM RESERVOIRS FOR THE GROWING RARE EARTH DISILICIDE NANOWIRE: INTRODUCTORY COMMENTS TO THE EXPERIMENTAL KNOWLEDGE ON RARE EARTH DISILICIDE NANOWIRE GROWTH

In the presentation of our chosen approach to modelling the vacancy free Y disilicide nanowires with the AlB_2 structure on the Si(001) surface in Sec. 6.2.3.2 , 6.2.3.3 , 6.2.3.5, we have occassionally emphasized the fact that while the modelling of various Y/Si(001) wetting layers, expected highly useful for the evaluation of not only the wire stability but also the discussion of the wire structure (see Sec. 6.2.3.1), and the Y disilicide wires are essentially decoupled in the present studies, there are certain issues to be addressed carefully in this respect in order to justify this modelling scheme: when choosing to study wires in an assumed infinitely wide bundle in Sec. 6.2.3.2, we assumed (effectively, by choosing to perform the wetting layer calculations for a system where the wetting layer is assumed to cover the entire surface) that the RE metal atom supply for the growing wire is not the immediate vicinity of the wire, but an area for the wetting layer where the influence of the nearest wires can be neglected. In Sec. 6.2.3.3, when presenting the detailed candidates for the nanowire structure, i.e., discussing the wire cross-sectional profile and surface termination, we assumed that the details of the wire/substrate interface for the wire well within a bundle were well established, the lowest layer for this wire being a RE metal layer. Finally, we have deliberately postponed the discussion of how to obtain a reliable energy for the Si atoms consumed by the growing wire as this issue requires a discussion of the experimental knowledge on the effect of the wire on the substrate.

In order to discuss in thorough detail the issues addressed above, we need to look into the experimental information on the growth of RE disilicide nanowires on the Si(001) surface in the presence of a wetting layer. The present discussion will provide the basic remarks needed in order to clarify the reliability of our chosen approach to modelling the Y disilicide nanowire on the Si(001) surface.

When presenting our basic model for the growth of a RE disilicide nanowire in the presence of a wetting layer in Sec. 6.2.3.1, we considered only two possible scenarios for the wire growth mode: in the first case considered, the RE metal atoms were provided by the immediate vicinity of the wire while the Si atoms were provided by the step edges on the substrate while for the other case, both RE metal and Si atoms

Figure 6.15: Experimental STM images showing two different growth modes for Dy disilicide nanowires on the Si(001) surface. See text for details. *Image courtesy of B. Z. Liu and J. Nogami.*

were provided by the immediate vicinity of the wire (see Fig. 6.10). Both of these wire growth modes appear to be supported by experiment, with the most detailed studies of this issue carried out by Liu and Nogami for Dy disilicide nanowire growth on the Si(001) surface [157]. Fig 8 (included here as Fig. 6.15) and Sec. III D of this paper discusses the above mentioned scenarios. Short nanowires were observed in these experiments both near a step edge and on a flat terrace far from step edges, suggesting, in particular, that the step edge does not play a vital part to the nucleation of the wire. The growth mode of the wires however appears to depend on where they nucleate, the authors of Ref. [157] reporting Si atom consumption from the region adjacent to the wire for wires nucleating on a flat terrace, as clearly evidenced from the STM image in the left part of Fig. 6.15 but with no such changes reported for the wires growing near a step edge: in this case, with an example shown in the right part of Fig. 6.15, the typically reported phenomenon of the step edges conforming drastically to the growing wire was observed. [60]

Both terraces in the left part of Fig. 6.15 were found to be covered by a Dy/Si(001) 2×4 wetting layer, with the relative orientation of the unit cell rotated by 90° [130]: this suggests that an uneven number of Si layers was removed in the process of Si consumption for this wire growth mode. We would regard this number being one as far more likely than the number being three. The essential support for this suggestion is the fact the details of the surface reconstruction for the terrace adjacent to the wire are still visible in the STM image. Another, more indirect but no less strong support can be made the basis of the comments made in Sec. 6.2.2.6, where we discussed measurements of the height of the RE disilicide nanowires on the Si(001) surface with STM. Assuming a wire growth mode where three Si layers of the surrounding substrate are removed leads to a height for the lowest layer wires clearly above any reported val-

[60] We emphasize that while the right part of Fig. 6.15 shows a long Dy disilicide nanowire, the discussion in Sec. III D of Ref. [157] shows that investigations into the growth mode for wires near a step edge involved studies of wires in their early stages of growth. In other words, both growth modes discussed above must be regarded as well established.

ues. [61] This explains our choice of wire growth modes in Fig. 6.10.

On the basis of the experimental studies of Dy disilicide nanowires on Si(001) discussed in Ref. [157], the RE disilicide wire growth modes described in Fig. 6.10 appear to be well supported with regards to the areas on the substrate providing Si and RE metal atoms for the growing wire: [62] the only outstanding question not answered directly by experimental observation in Ref. [157] is whether the RE metal atoms are consumed from the immediate vicinity of the wire also for the growth mode where the Si atoms are provided by the step edge. As there is no clear difference between the state of the RE metal atoms for the growth scenarios, we see no reason, however, why the RE metal reservoirs should differ for these two situations.

On the face of it, the above conclusion for the details of the RE metal reservoir for the growing wire appears to suggest that the simplification made when decoupling the wire and wetting layer theoretical studies as described in Sec. 6.2.3.2 is unjustifiable: according to experiment, the RE metal atoms consumed by the growing wire are removed from the region right next to the wire rather than a region farther away, where the effects of the wire on the wetting layer can be safely neglected as assumed when modelling the coexisting wire-wetting layer system. The experimental studies of Dy disilicide wires on Si(001) in Ref. [157] also suggest, however, that new RE metal atoms keep diffusing to the region around the growing wire to occupy effectively all the empty sites from where the RE metal atoms have been removed for consumption by the wire: consequently, in the experimental STM images of Fig. 4 of Ref. [157] and Fig. 6.15, left part, there is no sign of a region devoid of RE metal around the wires (in constrast to the situation for the Si atoms, see below). This additional observation from experiment supports our theoretical description of the wire-wetting layer system being justifiable, albeit slightly simplified: from experiment, we suggest that RE metals are consumed from the region right next to the wire, with the reservoir for the RE metal atoms for this part of the wetting layer being a region for the wetting layer farther away from the wire. In the theoretical modelling of the system, we skip the step where atoms are moved from one region of the wetting layer to the other, assuming that the RE metal atoms are 'somehow' removed from a region of the wetting layer clearly away from the wire for incorporation in the growing wire structure. While this description does not describe the actual growth process in great detail, according to the experimental knowledge on the system, it does not get this process clearly wrong for any stage of wire growth. In this sense, the decoupling of the wire and wetting layer theoretical studies appears acceptable.

---

[61] This argument assumes that the wire growth mode involving Si consumption from the immediate vicinity of the wire is a scenario often encountered, or, more precisely, that measurements of the height difference between a wire and a substrate have involved wires growing by this mode. Strictly speaking, this assumption has not been rigorously justified given the current level of knowledge on this issue. On the other hand, the discussion for Dy disilicide nanowires in Ref. [157] does not contain any support for one growth mode over the other from the above discussed pair, and we would therefore hold it as rather unlikely that the above mentioned wire height measurements (often involving Dy disilicide nanowires on Si(001)) refer only to wires growing by one of the two modes.

[62] We shall focus later in this discussion on the issue of how well the choice of wire/substrate interface in Fig. 6.10 is supported by experiment.

In comparison with the above discussion for the choice of Y atom reservoir in the Y disilicide nanowire theoretical studies presented in this work, the choice in Sec, 6.2.3.3 to simplify these studies by assuming a well defined wire/substrate interface, with the lowest layer for the wire essentially being the wetting layer present on the Si(001) surface at the onset of wire growth (see the RE disilicide nanowire growth model decribed in Sec. 6.2.3.1 for details), is not justified to the same extent by experimental observation, essentially as it involves details close to the point of wire nucleation not captured in experimental studies due to the rapid growth of the RE disilicide wires. As discussed in Sec. 6.2.3.3, we distinguish, on the very basic level, between two growth modes for wires in a bundle: *(i)* simultaneous and *(ii)* independent nucleation of these wires. On the basis of our wire growth model presented in Sec. 6.2.3.1 it seems safe to conclude, as discussed in Sec. 6.2.3.3, that the first scenario above will lead to a wire/substrate interface for a wire well within the bundle where the lowest layer of the wire is a RE metal layer, as assumed in our theoretical modelling. The challenge to this picture thus is the second scenario, the argument being that if the growing wires consume Si atoms from the immediate surroundings, at the point when their growth along the width direction is eventually terminated by the presence of adjacent wires in the bundle, the wire/substrate interface will be different from what has been assumed in Sec. 6.2.3.3, the lowest layer for each wire in this case being a Si layer.

While it is beyond the scope of this work to discuss the complex issue of the very early stages of RE disilicide nanowires on the Si(001) surface in detail (see Sec. 6.2.2.5 for brief general remarks on this issue), we shall point in the following important inherent, in our opinion, weaknesses to the second scenario presented above. Firstly, while arriving at a bundle with all trenches between adjacent wires having the width of one Si(001) surface lattice parameter, as suggested by experiment [157], is not impossible according to this wire growth scenario, there appears to be no reason why the trench should always attain this width, given an independent nucleation of each wire in the bundle and the expected restrictions on the wire width by the substrate/overlayer lattice mismatch. Secondly, while the growth scenario is clearly supported for an isolated wire as discussed in the above, it seems counterintuitive that it should apply to the stages of wire growth where the wire is yet to reach its final width, as a layer which is eventually to be incorporated in the growing wire is removed in the process of the wire growth according to this suggestion when the wire width has not converged (see Fig. 6.10). Finally, the suggestion that wire bundle growth to a good approximation is to be regarded as a coincidental agglomeration of independently nucleating wires on the surface is unable to explain the experimental observation that wire bundles appear to grow at the expense of isolated wires (see Sec. 4.2.3). While the second of the above three arguments is clearly highly speculative, and thus comparatively weaker than the first and last argument, we regard these various objections to the relevance of a wire bundle growth scenario where each wire in the bundle nucleates independently, when combined, as a strong support for the onset of wire bundle growth being much more likely to involve simultaneous nucleation of the wires. In other words, these considerations point towards the simplification of the wire studies by the assumption of a well-defined wire/substrate interface in Sec. 6.2.3.3 being justifiable.

The experimental information on the coexisting wire-wetting layer system for the

case of Dy disilicide nanowires on Si(001) presented in Ref. [157] clearly suggests that the Si atom reservoir for the growing wire is not unique. While this adds a certain level of complexity to the discussion of the details of the wire growth, it is a potential advantage for a theoretical study of the wire as there is more than one acceptable way of modelling the coexisting wire-wetting layer system with regards to the treatment of the Si atoms consumed by the wire. When studying a wire well within a bundle of wires, we can, in principle, assume either of the two wire growth modes described in Fig. 6.10, where Si atoms are either provided by the step edge or by the immediate vicinity of the edge of the bundle: in either case, the effect on the wire well within the bundle is negligible. As will be discussed further below, this consideration is of considerable potential importance to the application of our evaluated energy for removing a Si atom from the substrate to the present problem.

Regardless of the wire growth mode chosen from the pair in Fig. 6.11, the task of obtaining the binding energy of a Si atom for consumption by the wire amounts to a good approximation to calculating the binding energy of a Si atom at a step edge on the Si(001) surface. For the growth mode where the Si atoms are removed from the step edges already present on the substrate during wire growth this is evident, but the same holds true for the wire growing by consuming Si atoms from the immediate vicinity of the wire: in this case, the wire effectively creates two new step edges around it, as both the wetting layer and the uppermost Si layer for the substrate retracts. Apart from the early stages of this growth mode, where, on the average, a comparatively higher number of Si atoms has to be broken to remove a Si atom, the association of this situation with removing Si atoms from a step edge on the substrate appears acceptable.

Our chosen approach to obtaining the energy of the Si atom at a step edge follows the strategy of previous theoretical studies of nanostructure formation on a Si(001) surface [172]. For clarity, however, we shall go through the key assumptions made in this approach below. The line of arguments preceding the actual calculations performed are as follows: *(i)* we aim at calculating the average energy required for removing a Si atom at the step edge, where the average is over the actual step edge structure, i.e., we remove a line of Si atoms from the step edge but keep the detailed structure unchanged. Furthermore, *(ii)* we regard adjacent step edges as being so far apart that their interactions can be neglected. Fig. 6.16 explains how these assumptions being justified to an acceptable approximation means that the total energy change for the system changed as described above (ignoring, for simplicity, considerations about where the removed Si atoms are adsorbed subsequently) is obtained, regardless of the details of the step edge structures, by removing a straight line of Si atoms at the center of the terrace, far away from both step edges. The actual calculation, therefore, does not have to involve step edges on the substrate, but simply investigates the energy change upon adding a layer of atoms to a perfectly flat substrate, i.e., the average energy for removing a group of Si atoms from the system as described above is equal to the binding energy of Si in the bulk structure (see Ref. [172]). [63] We shall describe the details of the actual study

[63] Incidentally, this simple result makes it evident that the present considerations are not affected by the details of the RE metal coverage on the surface. For this reason, and given the remarks in Sec. 6.2.3.5 on the lack of importance of the evaluation of the binding energy for the Si atoms to the RE/Si(001) wetting layer studies, we conclude that, within the assumptions presented above for the Si atom binding energy evalualtion, the Si and RE metal atom reservoirs can be dealt with independently. Wetting layers therefore will not be

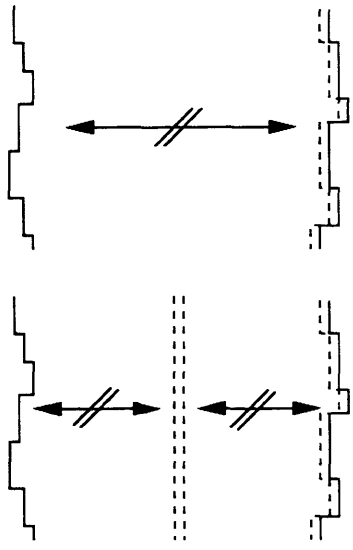

Figure 6.16: Schematic presentation of our approach to obtaining the step edge averaged binding energy for a Si atom at a step edge structure, within certain assumptions (see below), on the Si(001) surface. The two solid lines in the top figure show adjacent step edges on the substrate, the structural details of each structure being unimportant to the discussion below. Assuming that the interaction between these step edges can be neglected (as emphasized by the crossed out pair of arrows in this part of the figure), removing a line of Si atoms from the step edge on the right, changing it into the dotted curve in the top figure, amounts to removing a straight line of Si atoms from a central area on the terrace (assumed to be so far from both step edges that interactions with either of these structures can be neglected).

carried out to obtain this energy in Sec. 6.2.4.1.

The key issue when discussing the reliability of this approach is the assumption that the step edge structure is unchanged by the formation of the nanostructure in question on the surface. [64] In the present work, we use the averaged binding energy for a Si atom at the step edge on the Si(001) surface when discussing both *(i)* the relative stability of isolated Y atoms and dimers on this surface (see Sec. 6.2.3.5) and *(ii)* the relative stability of the Y disilicide nanowire to the Si and Y atom reservoirs on Si(001). As discussed in Sec. 6.2.3.5, there are no suggestions from experiment that this assumption should be significantly off the mark for coverages below what is required for wire growth for the particular RE metal under investigation. For wire growth, on the other

discussed below.

[64] For adjacent step edges on the terrace to affect each other, the step edges will have to be quite close. This certainly happens for relatively well isolated RE disilicide wires on Si(001), where the substrate conforms to a high degree to wires growing out over a step edge (see Sec. 4.2.3), leading to a pileup of step edges at the end of the wire. However, as this situation also involves the breakdown of the step edge structure being unaffected by the wire growth, for simplicity, we shall not discuss the issue of close step edges below.

hand, and in particular for growth of isolated wires on the Si(001) surface, the assumption breaks down completely, with the step edges conforming to a very high degree to the growing wires (see Sec. 4.2.3).

For wires growing in a bundle, the step edge structure generally appears less affected, an observation that makes sense on the basis of very general arguments: for low RE metal coverages and growth of RE disilicide nanowires on a flat substrate, the wires can grow longer before being stopped by a wire growing in the perpendicular direction on the adjacent terrace. In addition, the consumption of Si atoms from the substrate is relatively low, the main effect of wire growth on the Si substrate being, rather, the step edges conforming to the wires. For higher RE metal coverage, at the point where wire bundles form, the above situation is reserved, in particular with the wires now experiencing a higher tendency to be stopped by a growing wire on the adjacent terrace.

The above arguments can hardly be used as support for the step edge structure in general being 'almost unaffected' by the wire growth for RE metal coverages associated with wire bundle formation, and indeed, our approach to evaluating the energy required to remove a Si atom from the substrate for incorporation in the growing RE disilicide wire must be regarded as a key potential weakness in our theoretical modelling of the wire system. On the other hand, these considerations clearly do suggest that the assumption of an unchanged step edge structure is closer to being fulfilled for the situation of wire bundle growth on the surface, compared to lower RE metal coverages. In particular, as the experimental results in Ref. [157] for a wire growth mode involving Si atom consumption from the immediate vicinity on the terrace appears to suggest a fairly homogeneous removal of Si atoms along the wire growth direction (see Fig. 8 (a) in this paper), we consider it possible that a wire bundle growing by this mode, while consuming more Si atoms from the vicinity compared to the situation of the isolated wire in Ref. [157], keeps these wire created step edges fairly straight. Thus, with all the level of speculation that this last consideration involves, our theoretical modelling of a RE disilicide wire in a bundle might actually be associated to a good approximation with an experimentally observed growth scenario with respect to entire set of assumptions made in this study. [65]

[65] The above discussion focusses on flat Si(001) substrates. Experiment, on the other hand, has also involved vicinal Si(001) to a large extent. We have refrained from getting into this issue, however, as we are not aware of highly detailed experimental studies of wires grown on this type of surface.

6.2.4 Y/Si(001) WETTING LAYER FORMATION STUDIES: 2×4, 4×2, AND 3×1 SURFACE RECONSTRUCTIONS

6.2.4.1 BINDING ENERGY OF A Si ATOM AT A STEP EDGE

For reasons discussed in Sec. 6.2.3.5 , 6.2.3.6, evaluation of the energy for binding a Si atom at the step edge on the clean Si(001) surface is needed in order to evaluate the relative stability of both *(i)* the vacancy free Y disilicide nanowire with the AlB_2 structure on the Si(001) surface (to the atom reservoirs for the growing wire) and *(ii)* the full set of candidates for a protrusion in a Y/Si(001) 2×4 wetting layer investigated in this work. As reference will be made to the present studies of the clean Si(001) surface in both Sec. 6.2.4.2 and Sec. 6.2.5.1 below, we have made the choice to include the results obtained at the onset of our discussion of the complete set of calculations related to the studies of Y disilicide nanowires on Si(001).

The strategy for obtaining this energy has been described in Sec. 6.2.3.6 but is briefly summarized here for clarity: we calculate the binding energy of a Si atom in the bulk diamond structure within the supercell approximation used for the studies of the Y disilicide nanowires, i.e., by increasing the number of layers for a Si(001) surface slab geometry until the added layers resemble bulk Si to an acceptable approximation. As discussed in Sec. 6.2.3.6, this energy corresponds to the binding energy of a Si atom at the step edge on the Si(001) surface, averaged over the step edge structure and within the assumptions of *(i)* negligible interaction between the step edges and *(ii)* the structural details of the step edge structures being practically unchanged upon Si atom removal. In the presentation below, for simplicity, we shall refer to the result of the studies presented in the following as the energy of a Si atom in the bulk diamond structure, although our interest is in Si atoms at the step edge structure, as described in Sec. 6.2.3.6.

Fig. 6.17 describes how the total energy of a Si(001) slab geometry changes upon addition of one layer to the slab, for slabs containing 4 - 11 Si layers. For clarity, the energy has been presented in units of eV/Si atom, making no specific reference to the geometry used. The actual calculations involved slabs with a surface cell dimension 7.68 × 7.68 $Å^2$, i.e., with one Si dimer row containing two dimers within each cell, the chosen surface reconstruction being $p(2\times2)$. For a more complete description of the slab used, we refer to Sec. 8.1.

Calculations employed Vanderbilt US PPs [17], as implemented in VASP [23, 24], and the PW91 GGA [12] to the exchange-correlation functional E_{xc}, i.e., the same theoretical description used when studying Y on Si(001) (see Sec. 8.3.1 and Sec. 8.3.4). The chosen value for the plane wave energy cutoff was 200.0 eV and a smearing width of 0.1 eV was chosen for the Gaussian smearing scheme. (N, N, 1) Monkhorst-Pack (MP) k meshes were used in calculations, with N attaining the values 2 and 6. As discussed in Sec. 8.1, acceptable convergence in the structural parameters and total energies was found to be obtained with this choice of parameters and the (6, 6, 1) k mesh.

As shown in Fig. 6.17, calculations using the (2, 2, 1) k mesh were performed using both *(i)* slabs with an approximately fixed vacuum gap width (13.8 Å) between the

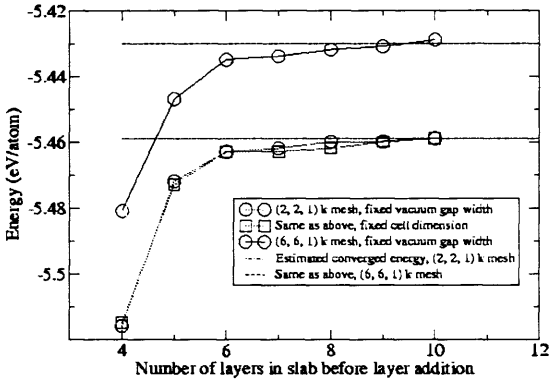

Figure 6.17: Change in the total energy for a Si(001) $p(2\times2)$ slab geometry (normalized units, eV/Si atom) upon adding a Si layer to the existing slab, as a function of the initial number of Si layers for the slab. The method for containing the converged values (included in Table 6.3) for this energy change has been described in the text.

actual surface layer and the bottom layer of the adjacent slab along the surface normal in the supercell approximation and *(ii)* a fixed cell dimension along all directions, i.e., a vacuum gap width that increased as the number of layers for the slab decreased. In these studies, the largest slabs considered, containing 11 Si layers, were identical. The difference between the energies obtained in these two studies was found to be minute: for the studies with the (6, 6, 1) k mesh therefore, only the computationally slightly less demanding set of calculations with a fixed vacuum gap width were performed.

The convergence in the energy change of the Si slab geometry upon addition of a layer to the slab is evident from Fig. 6.17: already for a slab containing 6 layers initially, addition of a Si layer leads to an energy change per Si atom for the system which is well within 0.01 eV of the estimated (see below) fully converged value, i.e., the value for a slab containing so many Si layers that the surface effects on the lowest layers in the slab are truly negligible. On the other hand, the energy change is not evidently fully converged for the situation where the slab contains 10 layers before the addition of yet another layer: [66] on the basis of the results alone, an evaluation of the converged

[66]In particular, the more important k mesh converged calculations in Fig. 6.17 show an almost linear behaviour (with nonzero linear coefficient!) in the variation of the energy change for the largest slabs considered, making a direct evaluation of the converged value for this energy change problematic. A large part of this apparent linear behaviour is presumably connected with the fact that the results have not been restricted to slabs containing e.g. an even number of layers. The inclusion of both slabs with even and uneven numbers of Si layers is expected, on a general level, to yield to some zigzagging in the total energies, due to slight differences between the systems related to the different orientation of the H termination layer for the two types of systems: according to these considerations, the above mentioned 'linear behaviour' in the variation of the energy change in Fig. 6.17, is actually a combined decay of the energy towards the converged value

Table 6.3: Evaluated (by fitting, see text for details) converged value of the binding energy for a Si atom in the bulk diamond structure, as obtained using the approach described in Fig. 6.17. This energy corresponds to the binding energy for a Si atom at a step edge on the Si(001) surface, averaged over the step edge structure and assuming approximations described in Fig. 6.16. The energy in the table refers to the converged energy obtained on the basis of the results using a (6, 6, 1) MP k mesh.

Configuration	Energy / eV/atom
Si atom in bulk diamond	-5.430

energy change would probably only yield a value which is correct to within a few hundredths of an eV/atom within the present theoretical description, whereas a higher precision in this choice of obtaining the converged value would require calculations on slab containing more Si layers.

While the above mentioned potential error in the evaluation of the converged energy change might appear relatively small, a very high precision in this evaluation is strongly desired for the Y disilicide nanowire calculations: as the wire structures presented in Sec. 6.2.3.3 typically contain a fairly large (up to ten or more) number of Si atoms, the above mentioned potential error in a fairly crude estimate of the converged energy change in the present studies will be scaled by this factor and suddenly appear relatively, or at least, unnecessarily, large. For this reason, we considered fitting the results in Fig. 6.17 with an appropriate curve in an attempt to evaluate the converged average value for the binding energy of the Si atom at the Si(001) step edge with more certainty. We shall discuss the results of this approach below.

At the outset of discussing the fitting of the results in Fig. 6.17, we emphasize that physical relevance is hardly the key target of this procedure: indeed, the sole aim of the fitting is to find a curve displaying a behaviour which matches the set of energies obtained in the above studies, with only small overall deviations and, in particular, with no trends towards increasingly large differences between the original energies and the fitted curve upon increasing the number of layers in the slab. The number of slabs investigated are considered sufficiently large for the chosen curve satisfying these requirements to present a reliable way of evaluating energies beyond the point where calculations have been performed. Considering the lack of physical justification for the choice of curve, however, we shall not discuss this selection, but focus only on the errors in the fitting and the uncertainty in the estimated value for the converged averaged binding energy for the Si atom to the step edge on the Si(001) surface.

Upon testing various functions for the fitting curve, we found that a polynomial of the type $y = ax^{-n}+b$ provided, for a properly chosen value of n, a very good description of the results in Fig. 6.17, with *(i)* χ^2 values down to less than 10^{-4} (obtained by varying a and b for a given n) and *(ii)* an acceptable description of the results over the entire range of slab considered. The estimated values for the binding energy of a Si atom

and the above mentioned zigzagging, rather than a sign of convergence requiring slabs with a much larger number of layers. Including only half of the energies in Fig. 6.17 does not solve the problem, however, the number of points now being very low for any highly reliable conclusions to be obtained about the converged value of the energy change.

in the bulk diamond structure obtained on the basis of fitting curves to the two sets of calculations on systems with different numbers of layers but approximately fixed vacuum gap width (see Fig. 6.17) are -5.459 eV and -5.430 eV, referring to the results using a (2, 2, 1) and a (6, 6, 1) MP k mesh, respectively. The latter of these results has also been included in Table 6.3. [67]

For the (2, 2, 1) k mesh results, the best fitting was obtained with the choice n = 6, while for the (6, 6, 1) k mesh results, n = 5 produced the better results. While this clarifies the obvious limitations to the interpretation of the fitting, we note that the variation in the estimated average binding energy varied only weakly, by 0.003 eV/atom or less, upon changing n by the value of 1 around the optimal values referred to above. As the fitting curves obtained for these choices of n failed to describe the entire set of original energies properly, we are fairly confident, on the basis of these investigations, that the error in the estimated energies of Table 6.3 is within $\pm$0.003 eV/atom.

6.2.4.2 ISOLATED Y ATOMS ON THE Si(001) SURFACE

The calculations on the complete set of wetting layer unit candidate configurations introduced when discussing our strategies for modelling the Y/Si(001) 2×4 wetting layer in Sec. 6.2.3.5 (see Fig. 6.14) have been discussed in Sec. 8.3.4. With reference to the conclusion in that discussion that only four configurations (all involving Y atoms rather than dimers) out of this set make realistic candidates, on the basis of energy considerations, for the wetting layer units, the current discussion will involve only the calculations on these configurations. Fig. 6.18 shows a schematic presentation of these configurations, included for clarity in the discussion below. With the exception of the Cave configuration, all Y atoms adsorb at a site showing close similarities to the local structural environment for an Y atom in a bulk vacancy free RE disilicide structure. [68]

The total energies obtained upon structural optimization of the Y/Si(001) configurations shown in Fig. 6.18 have been included in Table 6.4. For simplicity, following the notation introduced when discussing adsorption of Cu on the Si(001) surface in Sec. 5.4.2.2 and explained in Sec. 8.1, we shall refer to the various cells used for the studies of these configurations as the SC, LC_x, LC_y, and LC. The calculations for the Y/Si(001) configurations employed Vanderbilt US PPs [17] as implemented in VASP [23, 24], using the PW91 GGA [12] to the exchange correlation functional E_{xc}. For the full set of calculations described in Table 6.4, the Y 4p electrons were treated as core states, i.e., included in the PP. Explicit inclusion of these states in calculations was considered as well for the smallest cells (SC), however, Table 6.5 including the

[67] The seemingly strange suggestion in Fig. 6.17 that the estimated converged value for the Si atom binding energy for the k mesh converged results is numerically higher (rather than lower) compared to the result of the calculation on the largest slab considered is explained by the discussion included previously for the apparent linear behaviour for the variation in the energy change for these results obtained for the larger slabs.

[68] We shall discuss further the properties of the properties of the growth site for most of these configurations below when we consider the change in the structural parameters and total energies upon increasing the surface cell dimensions in our studies, i.e., increasing the distance between adjacent adatoms in the supercell approximation.

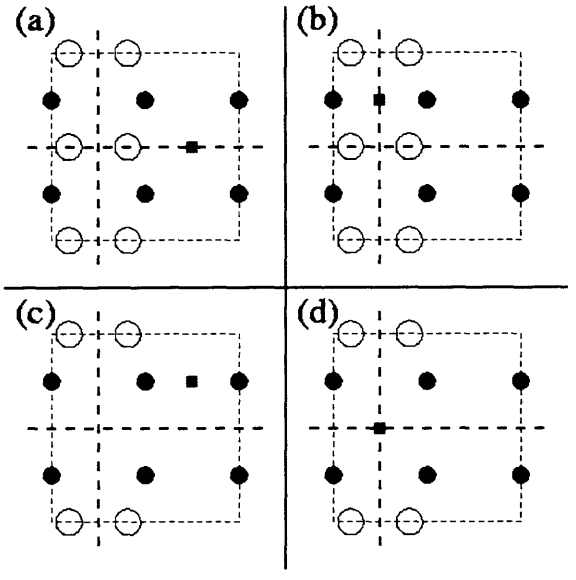

Figure 6.18: Schematic presentation (see Fig. 6.14 for general comments) of the selected wetting layer units obtained on the basis of structural optimization of the entire set of configurations shown in Fig. 6.14. The selected configurations are, using conventional notation for adatoms on the Si(001) surface, the (a) Cave, (b) Pedestal, (c) Hollow, and (d) Substitutional configuration, respectively. The choice of name for the latter of these configurations is justified by the fact that only one configuration involving substitution of Y for Si on the Si(001) surface is considered in the present discussion. Energies for these configurations obtained using the cell shown in the figure as well as larger cells have been included in Table 6.4.

optimized total energies obtained in these studies. Convergence in the structural parameters and energies for these configurations with respect to variation in the variable parameters for the code was obtained for a plane wave energy cutoff value of 200.0 eV, a smearing width for the chosen Gaussian smearing scheme of 0.1 eV, and a (6, 6, 1) MP k mesh, regardless of the treatment of the Y $4p$ electrons, with Sec. 8.3.1 and Sec. 8.3.4 providing further details on the convergence issues.

As a first thought, we would be using the results of Table 6.4 to obtain information on the well converged energies for isolated Y atoms on the Si(001) surface (see Sec. 6.2.3.4 for information on the experimental support for the relevance of this situation) for comparison with the Y/Si(001) wetting layer results to be discussed in Sec. 6.2.4.3. In the following, however, we shall be focussing, rather, on the tendency for the Y atoms to agglomerate. The agglomeration tendency of Gd on the Si(001) surface appears to be evident on the basis of the experimental results obtained by Harrison *et al.* [167] which clearly suggest that triplets of assumed Gd atom protrusions form at relatively low adatom coverages on the Si(001) surface, a result which we believe

Table 6.4: Total energies (in eV/Y atom) for the energetically most favourable Y/Si(001) configurations from the set in Fig. 6.14, relative to the energy of clean Si(001). All configurations involve a single Y atom on the Si(001) surface, with the adsorption sites explained in Fig. 6.18. Variations in the energies with Y coverage have been studied by changing the surface cell dimensions, with the choice of notation for the various cells used explained in Sec. 8.1. See text for details.

Configuration	E (SC) / eV	E (LC_x) / eV	E (LC_y) / eV	E (LC) / eV
Cave	-7.26	-7.26	-7.43	-7.42
Pedestal	-7.13	-7.17	-7.14	-7.17
Hollow	-7.32	-7.67	-7.54	-7.57
Substitutional	-7.37	-7.46	-7.19	-7.26

can be generalized to other RE metals, including Y. We shall clarify below that considerations into the agglomeration tendencies for Y atoms on Si(001) offer very strong support for only one of the configurations from the set in Table 6.4 being connected with the Y/Si(001) 2×4 wetting layer unit.

The results of Table 6.4 suggest that for Y at the Pedestal site, no strong agglomeration tendencies are obtained, while for the Cave configuration, adjacent Y atoms along the direction of the Si dimer row are repelling each other. For Y at the Hollow site, some separation between adjacent adatoms appears to be preferred both along and perpendicular to the dimer row direction, while only for Y replacing a Si dimer, a very clear preference for agglomeration of Y atoms, along the Si dimer row direction, is obtained. This result basically supports the most likely scenario for the early stages of wetting layer formation obtained on the basis of the present experimental knowledge on the system: as discussed in Sec. 6.2.3.5, and given the results for the complete set of configurations with Y on the Si(001) surface investigated (see Sec. 8.3.4), the only acceptable candidate for a single protrusion (explained by Y) in a 2×4 wetting layer unit cell, is an Y atom replacing a Si dimer. The considerations above point towards Y adsorbing initially at the position of a Si dimer vacancy on the terrace, with the wetting layer unit cells forming at sufficiently high coverage as a natural consequence of a tendency for Y to agglomerate on the Si(001) surface.

In order to gain further insight in the above result, we consider the structural details for the local environments of the adsorbed Y atoms. We noted at the beginning of this discussion that, with the exception of the Cave configuration (which will not be discussed in the following, see below for further remarks), the growth sites for Y resemble the local structural environment for this atom in a bulk vacancy free Y disilicide structure. This statement, as noted in Sec. 6.2.3.1, is somewhat ambiguous: we have to investigate the structural parameters for the growth site in order to clarify whether this site can be regarded as a preferable growth site, in terms of substrate/overlayer lattice mismatch considerations, for an overlayer adopting the AlB_2 structure (as opposed to the $ThSi_2$ and $GdSi_2$ structures). Focussing initially on the Substitutional configuration, we have calculated the distances, along and perpendicular to the Si dimer row, between the Si atoms in the second layer from the top surrounding the adatom. [69] For

[69] These atoms correspond to the four atoms of type 'A' for the substrate in Fig. 6.2, with only the direction

all the cells considered in Table 6.4, the Si atom separation perpendicular to the Si dimer row direction is clearly longer than the distance along the dimer row, the values obtained for the SC slab being 3.92 Å and 3.49 Å, respectively, with the results obtained upon increasing the Y atom separation along the dimer row reducing this scatter considerably, yielding values of 3.85 Å and 3.60 Å for these distances.

The clear anisotropy in these distances, along with the conclusion that the shorter of these distances is along the [0001] direction for the overlayer structure (in this case with the overlayer being a single atom) evidently makes the growth site resemble the vacancy free AlB_2 structure, with the significant differences between the above values and the overlayer lattice parameters in the growth plane for epitaxial growth of this structure on Si(001) (see Sec. 6.2.2.2) presumably being explained primarily by the stronger Y-Si interactions for the situation of a single Y atom on the surface, where only the 'lower half' of the surrounding Si cage is present compared to the bulk Y disilicide case. With reference to the considerations in Sec. 6.2.3.1, this supports the suggestion that the Y/Si(001) wetting layer should be associated with the early stages of growth of a vacancy free Y disilicide nanowire with the AlB_2 structure, i.e., with the Y atoms showing a tendency to agglomerate along the Si dimer row. In addition, the conclusion that the second layer Si atoms on either side of the Y atom in the direction along the dimer row are moved together compared to the situation for the clean Si(001) surface (where the mean value for the Si-Si distance is 3.84 Å) offers an explanation to the frequent introduction of Si dimer vacancies, containing no Y atom, along the dimer row, i.e., why the experimentally observed unit cell is a 2×4 cell and not $2\times n$ with, in principle, no limits to n: on the face of it, when presenting the ideas of the wire-wetting layer 'intimate connection' in Sec. 6.2.3.1, the frequent interruption of the nanowire template by Si dimer vacancies made little sense. The above considerations suggest, however, that this is essentially a method of strain relief, needed as the Y-Si interactions for the wetting layer are stronger than what is obtained in bulk vacancy free Y disilicide with the AlB_2structure.

For the Hollow and Pedestal configurations, the situation is very different, the structural parameters for the growth site being dominated to a much higher extent by the fact that the four Si atoms corresponding to the atoms of the type 'A' for the substrate in Fig. 6.2 are all involved in Si dimer bond formation. These growth sites, by comparison with the growth site for Y adsorbing at a Si dimer vacancy, bear little resemblance to the lattice parameters in the growth plane for any situation of epitaxial growth of a RE disilicide structure on the Si(001) surface, with the anistropy being not 7 - 12% as obtained for the Substitutional configuration but 25% or more, providing some explanation to the lack of agglomeration tendencies for Y at these sites. [70]

Finally, in the above discussion, the Cave configuration was excluded, primarily for simplicity, but also on the basis of the fact that this configuration is *(i)* structurally very similar the Hollow configuration and *(ii)* above this configuration in energy for all cells considered in Table 6.4. While we have not investigated the energy contours for Y on the surface, we would consider it as likely that the energy barrier between these two configurations is relatively low. Furthermore, for larger Y coverages we would expect

of the Si dimer row rotated by 90° in the current discussion compared to the situation described in the figure, as a consequence of the atoms now not being from the uppermost layer.

[70]We shall discuss the structural details for the Hollow site on the Si(001) in further detail in Sec. 6.3.2.1.

Table 6.5: Same as in Table 6.4 but including SC results only, as obtained using VASP and Vanderbilt US PPs differing for Y as described below. See text for details.

Configuration	E(SC), Y 4*p* in core / eV	E(SC), Y 4*p* semi-core / eV
Cave	-7.26	-7.15
Pedestal	-7.13	-7.22
Hollow	-7.32	-7.31
Substitutional	-7.37	-7.44

the adatoms to prefer being located at an environment bearing close resemblance to a bulk Y disilicide structure. This criterion can be satisfied for Y at the Hollow site, through breaking of Si dimer bonds, whereas there is no easy way to arrive at the desired structural environment with Y remaining at the Cave site. For this reason (and as the protrusions for the Y/Si(001) 2×4 wetting layer can not be associated justifiably with Y atoms at the Cave site, within the assumption that they are explained by Y atoms), we do not regard an exclusion of the Cave configuration in the above as critical.

The above considerations offer a very strong support for the wetting layer unit, i.e., the protrusion in a wetting layer unit cell, being an Y atom adsorbed at a Si dimer vacancy site. While this conclusion appears to be in contrast with the results of the total energy calculations presented in Table 6.4, where isolated Y adsorbed in the trench between dimer rows (Cave or Hollow site) appears to yield energetically considerably more favourable configurations (by up to $\sim$ 0.3 eV, assuming relatively well isolated Y atom configurations at the LC level), we do add that the modelling performed in the present work on isolated Y atoms on Si(001) is incomplete in various potentially important respects: *(i)* we have not investigated vacancy correlations with the adsorbed Y, an issue which might be important for Y replacing a Si dimer as even for the LC configuration, a considerable strain (see previous discussion for details) is present along the dimer row for this configuration. Furthermore, *(ii)* we have not fully investigated the effects of Y atom agglomeration for adatoms in this configuration, with more to be learned if we considered moving gradually two Y atoms, each replacing a Si dimer, together on a Si dimer row, using a cell sufficiently large to accommodate the most important elastic relaxations. These issues offer potential explanations for the apparent contradiction between the conclusions for the most likely wetting layer unit obtained on the basis of *(i)* the calculated energies for isolated Y atoms on the Si(001) surface and *(ii)* the agglomeration tendencies for adatoms in the various configurations. For further discussions into the issue of the most likely unit for the Y/Si(001) 2×4 wetting layer, we refer to Sec. 6.2.4.3.

Table 6.5 compares the energies obtained for the configurations with Y atoms on the Si(001) surface included in the present discussion, as obtained treating the Y 4*p* electrons as either *(i)* core states (the approach in the above) or *(ii)* semi-core states. For reasons discussed in Sec. 6.2.2.11 we shall not discuss in detail the differences between these results. Only, we note that the change in the energies of the various configurations obtained upon including the Y 4*p* electrons explicitly in calculations is

neither negligible nor a simple displacement of the entire set of energies, as one might have expected on the basis of the results for vacancy free bulk Y disilicide with the AlB_2 structure as obtained using these two theoretical descriptions of the Y/Si system (see Sec. 6.2.2.11 and Sec. 8.3.2).

6.2.4.3 Y/Si(001) WETTING LAYERS

The strategy for constructing Y/Si(001) 2×4 and 4×2 wetting layer candidate configurations on the basis of the calculations with single Y atoms/dimers on the Si(001) surface (the 'wetting layer units', i.e., suggested candidates, on the basis of calculations only, for a single protrusion of the experimentally observed wetting layer) has been described in Sec. 6.2.3.5. On the basis of the results presented in Sec. 6.2.4.2 we have narrowed the set of realistic (in terms of formation energies) candidates for such wetting layer units down to four configurations, all with a single Y atom on the Si(001) surface. [71] On the face of it, this would yield eight different wetting layer configurations to be structurally optimized. However, as the chosen supercell in these studies is a wetting layer unit cell, i.e., as the wetting layer is assumed to cover the whole substrate, wetting layers constructed from Y atoms adsorbed at the Hollow and Pedestal sites as well as Y atoms replacing a Si dimer should essentially yield the same configuration, as these adsorption sites are to be regarded as equivalent for the high coverages of Y atoms considered. [72] In the presentation of the theoretical studies of the Y/Si(001) 2×4 and 4×2 wetting layer candidate configurations below, therefore, we shall make reference only to wetting layers constructed by depositing each Y atom at the Cave site or at a Si dimer vacancy site on the Si(001) surface, with the latter of these configurations chosen over the Pedestal or Hollow configurations for reasons described in Sec. 6.2.4.2. We emphasize that the Substitutional configuration 2×4 wetting layer unit cell includes a Si dimer vacancy along the dimer row by construction, i.e., the model for this wetting layer candidate structure is essentially the same as the one used by Harrison *et al.* in Ref. [167] for their theoretical investigations of the Gd/Si(001) 2×4 wetting layer.

The total energies as obtained upon structural optimization of the Y/Si(001) 2×4 and 4×2 wetting layer candidate configurations have been included in Table 6.6. Calculations were performed using two different theoretical descriptions of the Y/Si(001) system, *(i)* Vanderbilt US PPs with the Y 4*p* electrons in the core and *(ii)* included explicitly in the calculation. We shall comment briefly on the differences between these results below. All results in Table 6.6 refer to calculations with values of 200.0 eV for the plane wave energy cutoff and 0.1 eV for the smearing width in the chosen Gaussian smearing scheme. For the 2×4 and 4×2 wetting layer studies, a (6, 3, 1) *k* mesh and a (3, 6, 1) *k* mesh was used, respectively. As discussed in Sec. 8.3.4, convergence in both structural parameters and total energies is expected to be obtained for these con-

[71] We shall discuss below that other considerations in Sec. 6.2.4.2 have produced very strong support for choosing one of the wetting layer units over the alternative candidates from this set.

[72] In practice, we have tested various distortions for the wetting layers constructed by depositing Y atoms at the Hollow site, in order to make sure that the most energetically favourable configuration was identified in these studies.

Table 6.6: Optimized total energies (eV/Y atom) for the Y/Si(001) 2×4 and 4×2 wetting layer candidate configurations as obtained using VASP. The third and fourth column refer to energies using Vanderbilt US PPs with the Y 4*p* electrons in the core and included explicitly in the calculations, respectively. The third and fourth row refer to two structurally quite different wetting layer unit cells. See text for details.

Unit	Unit cell	E_I / eV	E_{II} / eV
Y atom, Cave site	2×4	-7.407	(-)
(same as above)	4×2	-6.431	(-)
Y atom replacing Si dimer	2×4	-7.480	-7.524
(same as above)	2×4	-7.482	-7.493
(same as above)	4×2	-7.676	-7.648

figurations with the above mentioned choice of values for the variable parameters in the code. [73]

The results of Table 6.6 show that only the Cave configuration based Y/Si(001) 4×2 wetting layer is clearly energetically unfavourable: this is an expected consequence of the fact that this layer involves one Y atom at the DB site, as defined by the method of construction, a configuration which is clearly higher in energy than the configurations of Table 6.4 (see Sec. 8.3.4). The remaining wetting layer candidate configurations are fairly close in energy: in order to interpret the results of our wetting layer studies, therefore, we turn to the considerations of Sec. 6.2.4.2 for isolated Y on the Si(001) surface, the experimental knowledge on the RE/Si(001) wetting layers discussed in Sec. 6.2.3.4, and more general considerations about the configurations of Table 6.6.

When comparing only the formation energies for the various configurations in Table 6.6 we find that a Substitutional configuration 4×2 wetting layer is the energetically most favourable configuration. This is clearly at odds with the experimental results [169, 167] where the wetting layer is 2×4, i.e., the long axis of the unit cell is along the Si dimer row rather than perpendicular to it. We do not need this knowledge, however, to regard the Substitutional configuration 4×2 wetting layer unit cell as an unlikely structure to actually be observed on the Si(001) surface: this configuration involves *(i)* Y atoms replacing Si dimers at the same position on adjacent dimer rows while furthermore, *(ii)* an Y atom has to adsorb in the trench between these two rows in order to complete the triplet of protrusions, a sequence of processes which must be regarded as unlikely to occur very often. [74]

[73] We did not perform spin polarized calculations for the wetting layers as such calculations performed for isolated Y atoms on the Si(001) surface did not introduce any significant changes in the structural parameters or energies for these configurations.

[74] Fig. 2 of Ref. [167] showing an experimental STM image of Gd/Si(001) wetting layer unit cells formed on the surface, also reveals apparent agglomeration of 2 - 4 protrusions along the perpendicular direction on the surface, i.e., with the assumed Gd atoms located at the same position of adjacent dimer rows. For these structures, however, no protrusions are visible in the trench between the dimer rows, making it unclear whether these structures are to be associated with a Substitutional configuration n×2 wetting layer unit cell. Several examples of this type of structure are visible in the figure, but as the authors of Ref. [167] made no comments on a generally observed agglomeration tendency for Gd perpendicular to the Si dimer rows, we have got insufficient information to discuss this issue in further detail.

By contrast, the Substitutional configuration 2×4 wetting layer unit cell, [75] being above its 4×2 counterpart in energy by $\sim$ 0.2 eV/atom, must be considered a much more likely configuration to occur: for one thing, the agglomeration of Y atoms is confined within a single dimer row, but furthermore, as discussed in Sec. 6.2.4.2, this tendency is clearly supported by the calculations for an isolated Y atom in the Substitutional configuration (as opposed to the other alternative, the Cave configuration 2×4 wetting layer unit cell.). A further, potentially very strong support for a connection between this wetting layer candidate structure and experimentally reported RE/Si(001) 2×4 wetting layers is provided by the conclusion from our calculations that two structurally clearly distinguishable 2×4 wetting layer unit cell candidates, based on Y atoms replacing Si dimers, are obtained on optimization: for one configuration, the Y atom at the center is clearly raised above the surface relative to the surrounding Y atoms, while for the other configuration, the opposite situation occurs, with hardly any difference in energy between these two structures. The apparent connection with experimental results is evident: generally (see e.g. Ref. [169, 167]), two different types of 2×4 wetting layer unit cells, described by either a bright protrusion surrounded by two darker protrusions or vice versa in empty state STM images (with the relative brightness of the protrusions reversed upon changes in the bias voltage), have been reported for this surface structure (see Sec. 6.2.3.4 for details). On a general level, as we would expect the surface structure image collected with STM for the higher bias voltage to bear a closer resemblance to the ionic structure, [76] and consequently, we would regard the unit cell with two brighter protrusions for these voltages (denoted 'T' in Ref. [167]) to be associated with the configuration where two Y atoms are raised from the surface.

The appearance of two structurally different Substitutional configuration 2×4 wetting layer unit cells, a result which goes beyond that reported by Harrison *et al.* [167] in their preliminary theoretical studies of a Gd/Si(001) 2×4 wetting layer, is an extremely intriguing starting point for further comparison with experimental conclusions. We shall comment on future studies into this issue in Sec. 6.2.6. For the time being, we shall only note that, although making frequent reference to experimental results in both the present discussion and the considerations for isolated Y on the Si(001) surface in Sec. 6.2.4.2, we can summarize the Y/Si(001) wetting layer studies as follows: on the basis of *(i)* the calculated agglomeration tendencies (and their experimentally verified importance) for isolated Y atoms on Si(001) and *(ii)* the conclusion that agglomeration of adatoms along the Si dimer row must be considered a much more likely event compared to adatom agglomeration along the perpendicular direction on the surface, our investigations have produced strong support for the Y/Si(001) wetting layer reported by Katkov and Nogami [128] being explained by Y atoms replacing Si dimers on the surface with each protrusion for the wetting layer unit cell corresponding to a single Y atom, i.e, support for the wetting layer model presented by Liu and Nogami in Ref. [169]. [77] Apparently, the chosen restrictions of our theoretical modelling (see

[75] As shown in Table 6.6, there are two such cells, an issue to be discussed further below in the text.

[76] For very low bias voltages, the STM image is obtained from only few bands around the Fermi level, leading to an expected important influence of the electronic structure on the resulting image. The electronic structure influence is to some extent smeared out at higher bias voltages where lots of bands contribute to the current flow between tip and sample.

[77] For reasons discussed in Sec. 6.2.4.2, it is difficult to draw conclusions about the Y/Si(001) wetting layer

Sec. 6.2.3.5) are not of importance, although the comparability of our resulting wetting layer configuration with experimental results remains to be fully clarified, through construction of theoretical STM images. We emphasize that, in particular, the results of our calculations support the suggestion in Sec. 6.2.3.1 that the Y/Si(001) wetting layer formation is to be regarded as the initial stage of the growth of a vacancy free Y disilicide nanowire with the AlB_2 structure on the Si(001) surface.

On the basis of the above, for the Y disilicide nanowire stability studies in Sec. 6.2.5, we shall use either the Substitutional configuration 2×4 wetting layer energy or the 1×3 wetting layer energy (to be discussed briefly below) as the reference energy for the Y atoms consumed by the growing wire.

Explicit inclusion of the Y 4*p* electrons as semi-core states in calculations does not change the energies of configurations investigated (see Table 6.6) appreciably: in particular, the two different Substitutional configuration 2×4 wetting layer unit cells remain structurally different with an energy difference of $\sim$ 0.03 eV/Y atom between the two configurations (the configuration with only one raised Y atom being lower in energy), i.e., these calculations also suggest that both configurations should be observed on the Si(001), in agreement with the conclusions of experimental studies for other RE/Si(001) 2×4 wetting layers.

On the basis of the results for the Y/Si(001) 2×4 wetting layer described above, we have performed studies into both Y/Si(001) 3×1 and (for completeness, see below) 1×3 wetting layer formation. This wetting layer surface reconstruction is of potential importance to the studies of Y disilicide nanowire growth on Si(001), with Katkov and Nogami [128] reporting growth of wires for this element in the presence of a 1×3 wetting layer rather than the above discussed 2×4 wetting layer. To our knowledge, there have been no suggestions of structural models for a RE/Si(001) 1×3 wetting layer in the literature. Furthermore, we do not know the exact details for this wetting layer, i.e, no information was provided in Ref. [128] about the registry of the protrusions with respect to Si dimer positions on clean areas on the surrounding terrace. With these limitations in the back of our mind, [78] we have made the choice to model the wetting layer assuming a rearrangement of the Y atoms but without any change of the choice of growth site compared to the 2×4 wetting layer. The authors of Ref. [128] made no comments about coexistence of the two wetting layers observed, and it is therefore not clear to us whether the 1×3 surface reconstruction reported in that paper along with a 2×4 surface reconstruction, should be interpreted as the wetting layer being associated (within our choice of modelling) with a Substitutional configuration 1×3 wetting layer unit cell (as opposed to a 3×1 cell). On a more basic level, however, we would expect agglomeration of Y atoms along the dimer row to be favourable also for the present

stability relative to isolated Y atoms on the surface. As comparison of the energies for the Substitutional configuration in Table 6.4 and the 2×4 wetting layer based on this configuration (see Table 6.6) does not appear to lead to a directly incomprehensible conclusion, we have made the choice not to comment further on this issue.

[78] These remarks essentially clarify why we do not regard it is fully justifiable, at the present level of theoretical modelling, to use solely the result to be described below in the text as an Y atom reference energy for the Y disilicide nanowire growth studies in Sec. 6.2.5.

Table 6.7: Optimized total energies (eV/Y atom) for the Y/Si(001) 3×1 wetting layer candidate configuration as obtained using VASP. The third and fourth column refer to energies using Vanderbilt US PPs with the Y 4*p* electrons in the core and included explicitly in the calculations, respectively. See text for details.

Unit	Unit cell	E_I / eV	E_{II} / eV
Y atom replacing Si dimer	3×1	-7.369	-7.307

situation, the expectation therefore being that the calculations should definitely include a Substitutional configuration 3×1 wetting layer unit cell.

For completeness, structural optimization was considered for both the Substitutional configuration 3×1 wetting layer unit cell and its 1×3 counterpart, but convergence could not be obtained in calculations on the latter. We speculate that this conclusion is a suggestion of the agglomeration along the direction perpendicular to the dimer rows requiring Si vacancies for the substrate, in order to make the growth site resemble the local structural environment for an Y atom in bulk vacancy defected (rather than the vacancy free) Y disilicide with the AlB_2 structure, but no investigations have been performed into this issue. In addition to the 3×1 wetting layer unit cell calculations, also a 3×2 unit cell was structurally optimized, i.e., we doubled the cell size along the specified direction and allowed for modulations of the Y atoms. On optimization, however, these modulations were suppressed, or, in other words, the unit cell returned to being a 3×1 cell.

Compared with the Y/Si(001) 2×4 wetting layer, the 3×1 wetting layer is higher in energy by 0.11 eV/Y atom. We regard this result as comprehensible, with the Y atoms choosing 2×4 wetting layer formation when the adatom coverage on the surface is sufficiently low, i.e., with a full wetting layer coverage being possible in practice for this choice of wetting layer. For Y coverages above 0.375 ML, in the absence of nanowire growth (which was reported to set in only at considerably higher coverages, see Ref. [128]), decreasing the mean distance between adjacent Y atoms on the surface is the only option, and the 1×3 wetting layer appears. [79] We shall discuss this result in more detail in Sec. 6.2.5.1 in the context of Y disilicide nanowire growth on the Si(001) surface.

[79] In particular, this result indicates that the energy barrier to constructing an Y disilicide nanowire at the above mentioned coverage is higher than the barrier to changing the wetting layer surface reconstruction. As we shall not be discussing in detail the actual wire growth process but consider only stability of various wires in Sec. 6.2.5, we shall not discuss this issue in further detail below.

6.2.5 STRUCTURAL OPTIMIZATION OF VACANCY FREE Y DISILICIDE NANOWIRES ON Si(001)

6.2.5.1 WIRE CROSS SECTIONAL PROFILE AND SURFACE TERMINATION

Our chosen strategy for the structural optimization of Y disilicide nanowires with the vacancy free AlB_2 structure (referred to as 'Y disilicide nanowires' for brevity below) has been described in Sec. 6.2.3.3. In this initial discussion of the theoretical studies of the wires, we shall present the results of our calculations for the narrowest wire investigated (width of 3 Si(001) surface lattice parameters, '3×1' and '3×2' wires, see Sec. 6.2.3.3). This part of the study has focussed (3×1 wire studies) on identifying the most favourable wire cross sectional profile and wire surface termination (with the studies of wider wires yielding important additional information on both issues). Furthermore, by increasing the surface area of the wire in the supercell calculation along the wire growth direction (3×2 wire studies), we investigate whether all crucial relaxation effects for the wire have been included for the 3×1 and, more generally, the n×1 wire studies. As the bulk of our studies involve n×1 wires, the 3×2 wire studies are of huge importance to the question of the reliability of the nanowire studies.

Table 6.8 presents the complete set of energies for the 3×1 Y disilicide nanowires investigated, relative to the energy required to remove the number of Y and Si atoms in the wire segment from the respective reservoirs for the growing wire, with Fig. 6.19 showing the variation of the energies with the number of wire layers for each 3×1 wire profile. For reasons discussed in Sec. 6.2.4.3 when we presented the results of our structural optimization of various Y/Si(001) wetting layers, the assumed Y atom reservour for the growing wire, we have included both of the wetting layers reported in experiment [128] for Y deposition on the Si(001) surface, even though only the Y/Si(001) 3×1 wetting layer has been reported to coexist with the wires [128]. We shall comment further on this issue below when evaluating the stability of the Y disilicide nanowires relative to the Si and Y atom reservoirs. For each of the wire profiles presented in Fig. 6.12, the wire relative energies have been obtained for wires containing up to at least four layers, for reasons described in Sec. 6.2.3.3 when discussing the strategy for the wire studies. For the 'triangular' and 'spike' profiles, energies for wires containing five layers were calculated, for reasons to be discussed later on this subsection.

The results in Table 6.8 refer to calculations performed using Vanderbilt US PPs [17] with the Y 4p electrons treated as core states. Computational details, with expection of the k mesh used in calculations, are the same as described for the studies of isolated Y atoms on the Si(001) surface in Sec. 6.2.4.2. For the present studies, we used a (12, 3, 1) MP k mesh, corresponding to a density of k points in reciprocal space sufficient for the results of Sec. 6.2.4.2 to be converged. [80] We did not test k mesh convergence explicitly but noted that, compared to the initial wire studies performed using a (8, 2,

[80] As noted in Sec. 6.2.3.3, the 3×1 wire unit cell is a 4×1 cell, as the trench between adjacent wires has the fixed width of one Si(001) surface lattice parameter in our modelling. In other words, the surface cell dimensions for the structures of Table 6.8 is 15.36 × 3.84 Å^2.

Table 6.8: Total energies for the optimized vacancy free Y disilicide nanowires with the AlB_2 structure on the Si(001) surface and a chosen width of 3 Si(001) surface lattice parameters, relative to the binding energies when depositing the same amount of Si atoms at a step edge on the surface and Y atoms in (I) a Y/Si(001) 2×4 or (II) 3×1 wetting layer (see Sec. 6.2.4 for details on these calculations). The wire unit cell in these studies has a length of one Si(001) surface lattice parameter along the wire growth direction. The first column in the table refers to the number of layers in the wire, with the second column specifying the choice of wire cross-sectional profile (see Fig. 6.12 for details). The third and fourth columns specify the number of Si and Y atoms, respectively, in the wire unit cell.

Layers	Profile(s)	Si	Y	E_I / eV/atom	E_{II} / eV/atom
1	(all)	0	3	0.17	0.06
2	Stairs/Rect.	4	3	0.17	0.12
2	Triang./Spike	2	3	-0.24	-0.30
3	Stairs/Rect.	7	3	0.19	0.15
3	Triangular	5	3	0.23	0.19
3	Spike	3	3	-0.14	-0.19
4	Stairs	7	5	-0.03	-0.07
4	Rectangular	7	7	0.01	-0.05
4	Triangular	5	5	-0.09	-0.14
4	Spike	3	5	0.03	-0.04
5	Triangular	6	5	-0.14	-0.19
5	Spike	4	5	-0.09	-0.16

1) k mesh, both total energy and structural parameters showed only a weak variation when increasing the density of k points as specified above. We shall discuss later the results of calculations employing a Vanderbilt US PP with the Y 4p electrons treated as semi-core states.

All calculations were performed using a cell with the same dimensions along the surface normal, i.e., the vacuum gap width varied quite dramatically for the set of configurations investigated in Table 6.8: for the clean Si(001) surface, a vacuum gap width of 13.84 Å was obtained (see Sec. 8.1) while for the wires containing 5 layers, the width had decreased by more than 4 Å, attaining values of 9.58 and 9.41 Å for the optimized spike and triangular profiles, respectively. Test calculations for some of the highest wires suggested, however, that even the smallest gap width was sufficiently large for the interaction between the uppermost wire layer and the artificial H terminated layer at the bottom of the slab geometry to be negligible.

Finally, while we did expect the chosen number of 6 Si layers for the substrate as sufficient for the effects of the strain introduced by the interactions with the overlayer to be accommodated at an acceptable level by the slab geometry, we did investigate, for a few selected configurations, the effects on the energy and structural parameters upon increasing the number of Si layers for the slab to 8. These studies did not suggest any important changes to the wire structure or formation energy, the discussions below therefore involving a 6 layer Si slab geometry.

Finally, The relative energy for each wire configuration, ΔE_{NW}, has been obtained using the following equation:

$$\Delta E_{\mathrm{NW}} = E_{\mathrm{NW}} - N_{\mathrm{Y,\,NW}}\Delta E_{\mathrm{Y}} - N_{\mathrm{Si,\,NW}}\Delta E_{\mathrm{Si}} - \eta E_{\mathrm{Si(001)}} \qquad (6.1)$$

This general statement makes no reference to the details of the Y and Si atom reservoirs, E_{Y} (E_{Si}) specifying simply to energy required to remove an Y (Si) atom from somewhere on the surface for incorporation in the growing wire, with $N_{\mathrm{Y,\,NW}}$ ($N_{\mathrm{Si,\,NW}}$) specifying the number of such atoms per wire segment, i.e, contained in the wire unit cell. As discussed in Sec. 6.2.4.3, we have concluded that the Y atom reservoir is to be regarded in the present studies either as a Y/Si(001) 2×4 wetting layer or as a 3×1 wetting layer, in both cases obtained by replacing Si dimers on the Si(001) surface with Y atoms. The Si atom reservoir has been described in Sec. 6.2.4.1 and we refer to that discussion for details on this issue. In order to make Eq. 6.1 entirely general, i.e., applying to all $n\times m$ wires discussed in the present work, we have introduced the variable η in connection with the reference energy $E_{\mathrm{Si(001)}}$, describing the energy of the clean $p(2\times2)$ Si(001) surface as obtained using a 6 layer SC Si slab (see Sec. 8.1 for details). As noted above, the chosen clean surface slab geometry involves the same number of Si layers as the slab used for the wire calculations, but with the chosen fixed surface cell dimension for the clean substrate, the number of Si atoms for the substrate is not necessarily the same for the system referred to with E_{NW} and $E_{\mathrm{Si(001)}}$. [81] The parameter η correct for this potential error, being defined as the wire surface cell dimension divided by the clean Si(001) surface cell dimension. With this parameter included, Eq. 6.1 applies to all the Y disilicide wire calculations discussed in the following.

The information contained in Fig. 6.19 provides us with sufficient information to basically exclude the rectangular and stairs profiles of Fig. 6.12 as realistic candidates for the Y disilicide nanowire structure, regardless of the fact that wires this narrow have not been reported in experiment. Furthermore, of the remaining two wire profiles, in particular, the triangular profile wire energies display a behaviour upon addition of layers to the wires which appears to be in agreement with the experimental observation that wires do not grow in a layer by layer addition mode but in steps of three layers. For this reason, before interpreting in detail the main features of the variation in the energies obtained for the various wire profiles in Fig. 6.19, we emphasize that the results of these calculations offer support for the triangular wire profile explaining the experimentally observed wire structure, with the spike profile being the only possible alternative from the set of configurations in this work. We shall discuss this issue in more detail in Sec. 6.2.5.2 when investigating wider wires. [82] For simplicity in the discussion below, we shall focus on energy differences between wire profiles as obtained assuming that

[81] The choice of a well-defined system the clean Si(001) reference energy is not only one of simplicity but also necessity, as e.g. there is no clean Si(001) surface 4×1 unit cell with a $p(2\times2)$ surface reconstruction. Studies of clean Si(001) cells with different surface dimensions but the same surface reconstruction suggest that this approximation is not of great importance for converged k-point grids.

[82] The discussions below in the text are meant to provide an overall understanding of the results in Fig. 6.19. By choosing to include such considerations on the basis of the 3×1 wire results only, we are silently passing the potential importance of increasing the wire unit cell dimension along the wire growth direction, allowing for modulations of the wire structure and, most importantly, saturation of Si dangling bonds present for some of the 3×1 wires. As will be discussed later in the text, the energy changes for the 3×2 wires compared to

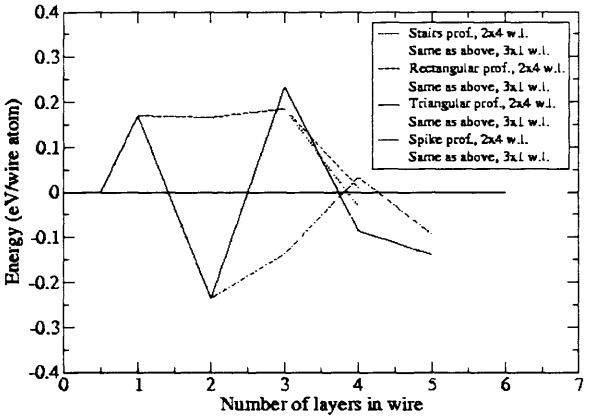

Figure 6.19: Total energies for the optimized vacancy free Y disilicide nanowires with the AlB_2 structure on the Si(001) surface and a chosen width (unit cell length) of 3 (1) Si(001) surface lattice parameters, as a function of the number of layers in the wire. The zero energy is defined at the point where there is no energy gain or penalty for constructing the wire on the basis of the selected initial Y and Si atom configurations (with introductory comment on these systems provided in Table 6.8). See text for details.

the Y atoms for the growing wire are provided by a 2×4 wetting layer. At the end of this discussion, we shall comment on the consequences to the wire stability discussion when using the 3×1 wetting layer as the Y atom reservoir.

For the wires containing only the lowest assumed (see Sec. 6.2.3.3) RE metal layer, all profiles are equal (see e.g. Fig. 6.12). The agglomeration of RE metal, presented as the onset of wire growth in Sec. 6.2.3.1, when discussing our general ideas for the growth of a RE disilicide nanowire in the presence of a wetting layer, is not a favourable process on its own, the wire being stabilized, however, by the addition of the next layer of Si atoms, a possibility also mentioned in Sec. 6.2.3.1. The first of these conclusions, which strongly suggests that the lowest layer Y disilicide wire is not at level with the wetting layer, bears close similarities to the conclusion to be obtained from the studies of Y/Si(001) 2×4 and 3×1 wetting layers in Sec. 6.2.4.3. We only discussed this issue briefly previously, and therefore, we shall go into further detail with both results in the following: the result that the 3×1 wetting layer was higher in energy by 0.11 eV/Y atom compared to the 2×4 wetting layer can be connected with the increased Y atom agglomeration leading to significant amounts of strain on the substrate along the long

the wires in Fig. 6.19 are generally found to be surprisingly small, according to our studies. For now, we shall regard this conclusion as sufficient justification for regarding essentially all the 3×1 wire energies as practically converged for this choice of wire width.

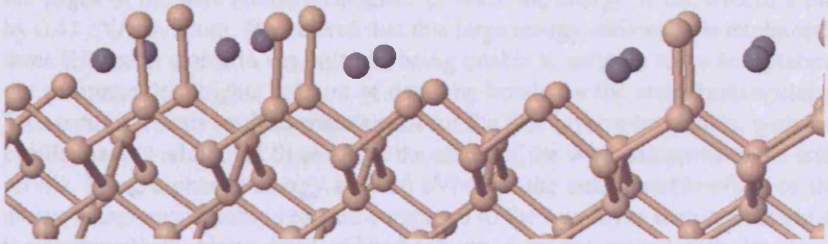

Figure 6.20: The optimized 3×1 vacancy free Y disilicide nanowire in a bundle of wires as obtained in calculations with VASP. Each wire runs into the paper and contains three (two) 'rows' of Y (Si) atoms, described by dark grey (light brown) spheres in the figure. See text for details.

axis of 3×1 wetting layer unit cell. This conclusion is further supported by the present studies, the one layer wire effectively being a 4×1 wetting layer with the energy per Y atom increased compared to the 2×4 wetting layer by 0.17 eV (reflecting the fact that it is even more difficult to create an optimal growth site for each adatom for this configuration) and similar values for the compression of the part of the surface not covered with Y. The conclusion does also appear to be in agreement with experiment in the sense that the lowest layer RE disilicide nanowires growing in the presence of a wetting layer have been reported (see e.g. Ref. [98]) to be clearly higher than this layer.

The second of the above conclusions, the stabilization of the wire structure by addition of Si atoms, holds some surprises. The suggestion that the one layer wire structure formation energy is reduced by addition of a single layer of Si atoms is not unexpected: this Si atom addition involves the introduction of a high level of dangling bonds, each wire Si atom forming only a single Si-Si bond with an atom from the substrate for the 3×1 wire, but the wire structure is presumably stabilized by the fact that these dangling bonds make it energetically favourable for the RE metal atoms to move away from the substrate, closer to the center of each of the partly completed Si AlB_2structure 'cages', occupying sites resembling more closely, with reference to both the ionic and electronic structure, the local environment for Y in bulk vacancy free Y disilicide with the AlB_2structure. We shall discuss the differences between these two configurations in more detail for the case of the triangular wire profile below. These considerations, when viewed on their own, might be regarded as pointing towards the completion of the AlB_2structure cages reducing the wire formation energy even further. However, as will be discussed below, this is not generally the case. Indeed, the two layer triangular/spike wire is the energetically most favourable of all the 3×1 wire configurations investigated.

For the two layer wire profiles, the two configurations investigated have markedly different formation energies: the triangular/spike profile, which involves only addition of Si atoms in two 'lines' around the central line of RE metal atoms (see Fig. 6.20) is

by far the energetically most favourable configuration: with Si atoms added as well at the edges of the wire (stairs/rectangular profile), the energy of the structure increases by 0.41 eV/wire atom. We believe that this large energy difference is explained by the three RE metal atoms in the unit cell being unable to saturate to an acceptable extent the comparatively higher amount of dangling bonds for the stairs/rectangular profile. This pattern repeats itself to some extent for the four layer wire studies, with the stairs profile, having additional Si atoms at the edges of the wire compared to the triangular profile, being higher in energy by 0.06 eV/atom, the unfavourable effect of the edge atoms being considerably reduced compared to the two layer wire considerations, by the comparatively higher level of bond saturation for the energetically less favourable four layer wire (see Fig. 6.12). [83] In other words, the 3×1 wire studies suggest that the wire formation energies in general are reduced by having Y atoms rather than Si atoms at the edges of the wire. This is the first suggestion that the rectangular and stairs profiles are generally higher in energy than the triangular and spike profiles.

As mentioned above, the intutive completion of the Si AlB_2 structure cages, obtained by adding a second layer of Si atoms to the wire, does not reduce the wire formation energy: in particular, in the case of the spike profile, where any reduction of the energy would make this three layer wire structure energetically more favourable than any of the two layer wire structures, the formation energy increases by a fairly large amount, 0.10 eV/wire atom. This result shows to point out crucial differences between bulk vacancy free Y disilicide in the AlB_2structure and the wire structure: *(i)* the stoichiometry for the latter system, especially for a wire as narrow as the 3×1 wire, is typically far from the bulk value (see Table 6.8), making the two systems highly dissimilar, and *(ii)* the majority of the atoms for the three layer wire structures of the chosen width belong to either the edge or the surface of the wire, which means that the electronic structures must be far from comparable. In other words, thinking in terms of completion of Si AlB_2structure cages as a way of reducing the wire energy is fundamentally misleading for the very narrow wires. The present results also apply to the wider wires, however: as the width increases, the relative energies of different wire profiles are determined to an increasing extent, for a wire containing a given number of layers, by the differences in the structural details at the wire sidewalls, the atoms aways from the edges of the wire experiencing highly similar surroundings for all profiles studied. As, in particular, the rectangular/stairs profile is far above the spike profile in energy for the three layer wire (0.33 eV/wire atom), with the basic difference between these profiles being the details of the wire sidewalls, the spike profile must also be the clearly more energetically favourable profile compared to these profiles for considerably wider wires. [84]

[83] The comparison of the formation energies per wire atom for these four layer wire configurations to some extent tends to mask the conclusions about the binding energy for the Si atoms at the edge of the wire profile. If, instead, the total energies for the two configurations are compared, we obtain a binding energy of 5.20 eV for the Si atoms at the edge of the wire structure for the stairs profile, significantly lower than the calculated average binding energy of 5.43 eV for a Si atom at a step edge on the Si(001) surface (see Sec. 6.2.4.1). Using the same approach for the two layer wire configurations, on the other hand, gives a binding energy of only 4.26 eV for the Si atoms at the edges of the wire, justifying the conclusions of the less elaborate discussion above in the text.

[84] Also, the 3 layer triangular wire profile is found to be energetically highly unfavourable. For this con-

On the basis of the above considerations, which add to the conclusion previously that a wire sidewall comprised by Si atoms is energetically unfavourable according to our calculations, and the conclusion (see below) that the addition of the next layer for the wire has a similar effect on the formation energies for most of the wire profiles investigated, we can complete our argument for excluding the rectangular and stairs profiles as realistic candidates for the vacancy free Y disilicide nanowire on Si(001): as these two profiles are energetically unfavourable compared to other candidates for wires containing 1 - 4 layers, they basically will not be favourable upon addition of further layers to the wire, where varations in the formation energies similar to those described above are expected to be repeated to a good approximation for the various profiles. [85]

Adding a fourth layer, comprised by Y atoms, to the wire structures typically (with the spike profile as the only exception, see below) leads to a considerable lowering of the energy, to the point where construction of any of the wires in no cases involves an energy penalty higher than 0.01 eV/wire atom. When looking at the schematic presentations for the various wire profiles in Fig. 6.12 this result does appear to make a lot of sense: for both the stairs and triangular profiles, all the Y atoms in the added layer experience a local structural environment highly similar to bulk vacancy free Y disilicide with the AlB_2 structure, the key difference between this situation and the adsorption of the initial layer of Y atoms on the substrate for the one layer wire being that the wire structure can relax to a much higher extent in order to produce almost optimal growth sites for the Y atoms. For these situations, we obtain energies of 8.60 and 8.84 eV/Y atom for the stairs and triangular profiles, respectively, much lower (more than 1 eV) than the binding energy for Y in any configuration on the clean Si(001) surface investigated previously in the text. For the rectangular wire, a significantly lower binding energy, 7.91 eV/Y atom, is obtained, explained by the fact (see Fig. 6.12), that the Y atoms at the edge of this wire structure do not experience the same favourable surroundings. This suggestion is further supported by the fact that spike profile, involving addition of Y atoms at similar growth sites, is the only configuration where the energy increases significantly, by 0.17 eV/wire atom, upon addition of the fourth layer.

In summary, while the binding energies for the Y atoms in the fourth layer differ significantly from the situation for the one layer wire, for reasons described above, the considerations when adding this layer to the wire are highly similar (with the exception of wire edge issues) to the one layer wire considerations. On the basis of this remark, we would believe that adding a fifth layer (Si) to the wire should lead to a lowering in the wire energy for both the triangular and spike profiles, i.e., a similar trend (but not necessarily similar energy changes) to the situation encountered when adding the second layer to these profiles. For the five layer wire studies, only the triangular and spike profiles were investigated, as the alternative profiles were expected (see above) to be higher in energy. As shown in Fig. 6.19, addition of a Si layer does lead to an appreciable energy gain for both wire profiles, supporting the above suggestion.

Although the set of wire cross-sectional profiles examined in the present work does

figuration, however, the wire sidewalls do not have the same appearance as the rectangular/stairs sidewall, and we shall therefore postpone a discussion of this issue until later in the text.

[85] We shall investigate this assumption for the triangular and spike five layer wire profiles below.

Table 6.9: Total energies for the optimized vacancy free Y disilicide nanowires with the AlB_2 structure on the Si(001) surface and a chosen width (unit cell length) of 3 (2) Si(001) surface lattice parameters, relative to the binding energies when depositing the same amount of Si atoms at a step edge on the surface and Y atoms in a Y/Si(001) 2×4 wetting layer. The energy gain in the parentheses in the third column is relative to the corresponding 3×1 wire configuration (see Table 6.8).

Layers	Profile(s)	Energy / eV/atom (Energy gain)
1	(all)	0.15 (0.02)
2	Stairs/Rect.	0.17 (0.00)
3	Triangular	0.23 (0.00)

not include the complete set of possible wire profiles for this choice of wire width, we would argue, on the basis of the above considerations, that the remaining profiles left out of this study will not produce configurations with energies comparable to the lowest energies from the set in Table 6.8. As discussed above, addition of Si atoms at the edge of the structure in general is found to clearly increase the formation energy of the wire structure. When going through the entire set of symmetrical, vacancy free Y disilicide nanowire cross-sectional profiles which can be constructed for a wire width of 3 Si(001) surface lattice parameters and wire heights between 1 and 4 layers, we find that only profiles which differ compared to profiles already investigated by the addition of such Si atoms have been excluded from the study, justifying the above conclusion. In other words, as claimed originally in Sec. 6.2.3.3 when presenting the various wire structures investigated, we are performing, effectively, an exhaustive search into the choice of wire profiles for the chosen wire width and wire/substrate interface.

The above discussion involved only 3×1 wires. For some of the configurations encountered in these studies, a high level of dangling bonds were present: consequently, we would regard it as likely that the energies of these particular wire configuration would be lowered, possibly considerably, when allowing for reduction of the number of dangling bonds by performing calculations on 3×2 wires. Table 6.9 shows the results of the investigations performed into this issue. [86] We have focussed only on wires containing up to three layers as we believe that any distortions revealed in studies of an appropriately chosen configuration within this set can be used to explain distortions for wires containing more layers. For the selected configurations, we generally generally performed optimization using either *(i)* the same starting point as in the corresponding 3×1 wire study or *(ii)* introducing slight modulations (movements by a few tenths of an Å of selected atoms) of the previously optimized 3×1 wire configuration structural parameters. Surprisingly, even for the stairs/rectangular 2 layer wire, where the presence of dangling bonds are expected to explain the high energy of this configuration, as discused previously, these optimizations did not reveal any significant instability, with the structural parameters only changed appreciably for the single layer wire: for

[86] For simplicity, only wire energies relative to one wetting layer have been included in this table, the key issue being the gain in the formation energy of the wire structure upon the increase of cell dimension, rather than the wire stability.

this configuration, every second triple along the wire growth direction had the Y atoms raised relative to adjacent triples by $\sim$ 0.4 Å. We can not exclude that our approach to triggering structural instabilities is insufficient for revealing the presence of a very significant distortion of the wire. On the other hand, it is also possible that the large distortions required to saturate dangling bonds are somehow prevented by the combined effect of *(i)* having Y atoms in the partly or completely constructed Si cages for the overlayer (affecting the electronic structure in ways not predicted by our very general previous analysis) and *(ii)* growing the wires on a substrate, leaving part of the wire structure fairly rigid. Szwacki and Yakobson [141] reported a high level of saturation of dangling bonds for isolated Y disilicide nanowires, i.e., with no considerations of interactions with a substrate. This type of structure evidently is more easily deformed than a wire growing on a substrate, however. Further studies, in particular studies of the electronic structure for the wires, are needed in order to clarify whether it is justifiable to conclude that the 3×1 (and, more generally, $n\times1$) wires represent practically completely optimized configurations. We shall not discuss this issue further in Sec. 6.2.5.2 where we draw conclusions solely on the basis of $n\times1$ wire energies.

When the 3×1 Y/Si(001) wetting layer is substituted for the 2×4 wetting layer as the Y atom reservoir for the growing wire, the relative stability of all wire configurations are increased, with the wire profiles involving a comparatively high amount of Y being favoured the most in this process. This last addition to the statement is important only for relatively narrow wires, however, with the stoichiometry for the fairly narrow 7×1 wires to be discussed in Sec. 6.2.5.2 already coming quite close to the bulk vacancy free Y disilicide value with two Si atoms per Y (including the uppermost layers of Si atoms for the substrate in this calculation). Most importantly, for the 3×1 wires the change of Y atom reservoir does not have the effect of changing qualitatively the arguments described above. The most crucial issue is the relative energy of the triangular and spike wires for the situations where the wires contain two and five layers. We shall postpone a discussion of this issue until Sec. 6.2.5.2 where we shall draw conclusions regarding the choice of wire profile for the vacancy free Y disilicide AlB_2 structure nanowire on the Si(001) surface as obtained in our studies.

6.2.5.2 INCREASING THE WIRE WIDTH

The studies of the 3×1 wires in Sec. 6.2.5.1 has left us with the conclusion that the rectangular and stairs profiles can not be associated with the cross-sectional profile of a vacancy free Y disilicide nanowire with the AlB_2 structure, epitaxially grown on the Si(001) surface: compared to these profiles, energetically more favourable alternatives, the triangular and spike profiles, exist for a range of wire heights sufficiently large for the exclusion of the initially mentioned profiles to be justifiable. In order to gain further information on which of the remaining wire profiles is our prime candidate for the structure of the Y disilicide nanowire, we have performed structural optimizations of selected 5×1 wires with the triangular and/or spike profile. Initially, we focussed on the 2 layer triangular wire and the 3 layer spike wire, in order to clarify whether the latter of these structures would remain close in energy to the former for a wider wire. Our studies suggested that the energy difference between these two configurations in-

Table 6.10: Same as in Table 6.8 but for selected profiles with a chosen width (unit cell length) of either 5 or 7 (1) Si(001) surface lattice parameters. See text for details.

Unit cell	Layers	Profile(s)	E_I / eV/atom	E_{II} / eV/atom
5×1	2	Triang./Spike	-0.22	-0.28
(same)	3	Spike	-0.05	-0.10
(same)	5	Triangular	-0.16	-0.20
7×1	2	Triang./Spike	-0.21	-0.27
(same)	5	Triangular	-0.16	-0.21

creases with wire width, from 0.10 eV/wire atom for the 3×1 wire to 0.17 eV/wire atom for the 5×1 wire, i.e., moving from the 2 layer triangular/spike wire to a 3 layer wire always involves an appreciable energy penalty, which is also obtained if we substitute the Y/Si(001) 3×1 wetting layer for the Y/Si(001) 2×4 wetting layer as the Y atom reservoir in the above (in this case, energy differences of 0.11 and 0.19 eV/wire atom are obtained for the 3×1 and 5×1 wires, respectively). We regard this result as establishing the 2 layer wire with the triangular/spike profile as a stable wire structure.

In addition to this conclusion, as the 3×1 wire studies suggested a significant energy difference (considering the considerably higher number of atoms in the wire segment) of 0.06 eV/wire atom (0.04 eV/wire atom for the Y/Si(001) 3×1 wetting layer based calculation) between the triangular and spike profiles, with the triangular profile being lower in energy, we conclude from our studies that *(i)* a vacancy free Y disilicide nanowire with the AlB_2 structure on the Si(001) surface will adopt the triangular profile (described in general detail in Sec. 6.2.3.3) with *(ii)* the presence of the experimentally reported (see e.g. Ref. [157]) set of 'magic numbers' for the number of layers in the wire being verified in our calculations, the lowest wire being comprised by an Y and a Si layer and the next wire containing three additional layers, in agreement with experiment. In particular, our studies suggest that the wire surface termination layer is a single Si layer, in contrast with the recent conclusions obtained by Fujii [152] on the basis of studies of Er disilicide films grown on Si(001). We emphasize that these conclusions do not involve considerations about the details of wire growth in the sense that it remains to be clarified how to grow the next plateau of the wire, moving from a wire containing 2 layers to one containing 5 layers.

The remaining studies of n×1 wires, with n being either 5 or 7 (see Table 6.10), have focussed on how an increase in the wire width affects the relative energies of the 2 layer and 5 layer triangular wire, i.e., the two lowest stable wires, according to our studies, with Fig. 6.21 providing a perhaps more illuminating illustration of these variations. We found that the 2 layer wire is gradually becoming energetically less favourable compared to the 5 layer wire, suggesting that wider wires show a tendency to be higher according to our studies. This result is in agreement with experimental conclusions where a fairly high RE metal coverage, leading to the growth of comparatively broad wires, and, in particular, wire bundle formation, has been found to be needed for the next plateau of layers for the wire to be observed. On the other hand, as our calculations involve only wires in a bundle, we would be cautious about reading to much into the present result.

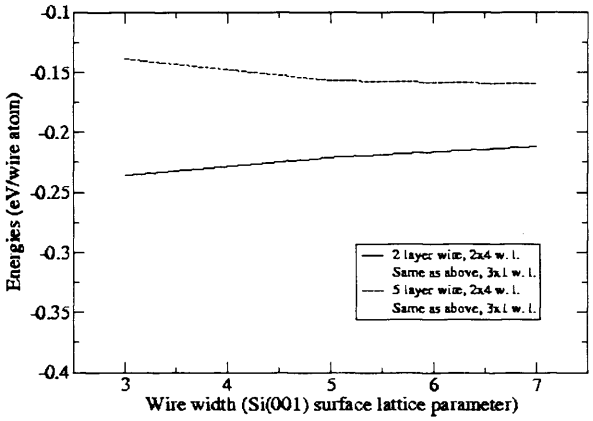

Figure 6.21: Total energies for the optimized vacancy free Y disilicide nanowires with the AlB_2 structure on the Si(001) surface, with a triangular cross sectional profile and containing either 2 or 5 layers, as a function of wire width. All wires have a unit cell length 1 Si(001) surface lattice parameter. See text for details.

Ultimately, and more important for the conclusions of the Y disilicide nanowire discussions, the wires clearly appear to remain stable for wire widths which can arguably be connected with experimentally reported wire widths: the decrease in stability is an expected consequence of the increasing amount of strain introduced by the overlayer/substrate lattice mismatch. While we do not necessarily expect e,g, the 2 layer wire energies to reach positive values relative to the Y and Si atom reservoirs, evidently suggesting instability of the wire structure, comparison with wire systems containing two narrow wires covering the same surface area as a single broader wire (the additional trench between wires included) would be expected to reveal stability of the 'wire pair' for a sufficiently large single wire width. We believe that the gradual increase in the wire energy for the two layer wire in Fig. 6.21 should be interpreted primarily in this fashion.

6.2.6 SUMMARY AND OUTLOOK: A MODEL FOR THE INITIAL STAGES OF RARE EARTH DISILICIDE NANOWIRE GROWTH ON Si(001)

The key motivation of the calculations performed on Y disilicide nanowires in the present work goes back to the structural optimization results for bulk vacancy free Y disilicide with the AlB_2 structure. Our theoretical studies of this system, as well as previous calculations, suggest that the axial *c/a* ratio is changed dramatically when Si vacancies are not present in the system. As discussed in Sec. 6.2.2.11, we believe that

this is an alternative mechanism of strain relief (which can be generalized to other bulk RE disilicides adopting this structure) with the effect of increasing the distances between the Si atoms in the graphite-like planes for the AlB_2 structure to a value fairly close to bulk Si. For bulk RE disilicides, introduction of Si vacancies (approximately one out of six Si atoms are missing according to experimental studies) has essentially the same effect and is the energetically preferred solution to the strain relief issue. For the epitaxial growth of RE disilicide nanostructures with the AlB_2 structure on the Si(001) surface, however, the situation is considerably less clear. We have argued that the line of arguments used by Chen *et al.* [146] for the suggestion that the RE disilicide nanowire on Si(001) surface adopts the vacancy defected AlB_2 structure (i.e., the structure of bulk RE disilicide) is based on an approach to the growth phenomenon which is not truly justifiable: lattice mismatch values for the overlayer and substrate in the growth plane have been compared using an *extended*, i.e., 3D, overlayer structure, whereas the actual wire growth must be regarded as a 1D phenomenon, with the substrate having a considerable influence on the details of the wire structure. In particular, preliminary studies into the growth of a *vacancy free* RE disilicide AlB_2 structure on Si(001) (being preliminary in the sense that they are based on calculations alone, with no known corrections for comparison with experimental values being available at the time of writing) have supported growth of highly elongated nanostructures, possibly nanowires, adopting this structure.

On the basis of further calculations confirming the stability of the AlB_2 structure for bulk vacancy free Y disilicide, we regard the above considerations as quite well-founded support for the vacancy free RE disilicide nanowires adopting the AlB_2 structure being a realistic candidate for the experimentally observed wires on the Si(001) surface. A critical examination of the published experimental support for the wires adopting the vacancy defected AlB_2 structure has revealed that none of the experimental conclusions can be regarded as providing rigorous support for one particular wire structure, further establishing the vacancy free AlB_2 structure as a potential explanation for the structure of RE disilicide nanowires on Si(001).

A crucial point to the discussion of the wire structure below is the following: the epitaxial growth model for the two RE disilicide wire candidates presented in the above predict wires growing in mutually perpendicular directions for the same choice of wire/substrate interface. We shall argue later in this discussion why this conclusion could very well provide sufficient information to determine the structure of the RE disilicide nanowires on Si(001).

Our theoretical studies have involved only Y disilicide nanowires with the vacancy free AlB_2 structure. These investigations represent the first rigorous theoretical studies of RE disilicide nanowire growth on Si(001), i.e., the first studies involving an interacting wire/substrate system. In our approach to modelling the Y disilicide nanowire, we have focussed our attention on the wire-wetting layer coexistence typically reported in the literature: we have put forth the basic details of a growth model which essentially suggests that the RE/Si(001) 2×4 wetting layer formation is to be regarded as the formation of a 'wire template', each wire in this wire bundle running along the Si dimer rows on the surrounding clean areas on the same terrace and furthermore *(i)* being only a single Si(001) surface lattice parameter wide, *(ii)* containing only a single

layer (RE metal), and, finally, *(iii)* being defective, every fourth RE metal atom in each chain missing (leading to the 2×4 unit cell as these vacancies are adjacent in the direction perpendicular to the wire chains). We shall discuss below the further implications of this model, focussing, for the time being, on the bulk of the wetting layer studies performed in the present work.

To our knowledge, the above presentation of the wetting layer as a wire template is conceptually new, but the structural model for the wetting layer has been put forth previously by Liu and Nogami [169]. We have performed the first detailed theoretical studies of this model, our investigations into the 2×4 wetting layer formation for Y on Si(001) suggesting that Y occupies a Si dimer vacancy site on the surface initially, with adatoms at adjacent sites along the Si dimer row direction showing a tendency to agglomerate, in line with the arguments presented in Ref. [169]. The apparent connection with wire growth has also been further established through these studies: the structural environment for an isolated Y atom replacing a Si dimer on the Si(001) surface has evident similarities with the local structural environment for Y in bulk vacancy free Y disilicide with the AlB_2 structure, meaning that the agglomeration tendency along the dimer row can justifiably be described as the growth of a wire (with the details described in the above) with the vacancy free AlB_2 structure. With only a single layer of RE metal on the substrate, the Y-Si bonds are significantly shorter than the values for the bond lengths expected for the actual wire (more closely resembling bulk vacancy free Y disilicide): the introduction of defects in the wire template is regarded as a mechanism of strain relief, explained by the large amount of strain on the surface imposed by the wire template.

Our RE disilicide nanowire growth model, discussed in Sec. 6.2.3.1 and Sec. 6.2.3.6 suggested that the wire should grow initially by agglomeration of RE metal atoms in a local region of the wetting layer, possibly with the addition of Si atoms required in order to stabilize this structure. More precisely, we can extract the key suggestion from this growth scenario that, at the very early stages of wire growth, the wire and the 2×4 wetting layer unit cell must be running along the same direction as they represent different stages of the growth of the same structure on the substrate. This growth scenario, while being extremely simplistic (we shall provide some additional information when evaluating the results of the calculations on the Y disilicide nanowire on Si(001) later in this discussion), is highly intuitive, as opposed to an alternative wire growth scenario discussed for Er disilicide nanowires on Si(001) in the presence of an Er/Si(001) wetting layer by Zhu *et al.* in Ref. [151]: the authors of this paper introduced an additional Si layer *under* the first layer of wetting layer Er atoms in the region where the wire grows, a suggestion which was not accompanied by any explanation other than the conclusion, in agreement with our remarks above and at the end of the opening part of this discussion, that the wire having its lowest Er layer at level with the wetting layer would otherwise be growing in a direction perpendicular to the direction predicted for an epitaxially grown wire with the vacancy defected AlB_2 structure.

Evidently, we can not argue, on the basis of the comparative intuitiveness of our growth model, that the structure of the RE disilicide nanowires should be the vacancy free rather than the vacancy defected AlB_2 structure, but arguably, the amount of support for our growth model is stronger, in particular when taking into account the con-

clusion (to be described below) that stable vacancy free Y disilicide nanowires with the AlB_2 structure are obtained from our theoretical studies. Before discussing these calculations, however, we shall argue below why we believe that experimental results are already available for clarifying, within our suggested wire growth scenario, whether one of the two above candidates for the wire structure can be excluded. [87]

As the growth of RE disilicide nanowires is extremely fast, information on the early stages of wire growth, the focus of our wire growth model, generally has not been extracted from experimental studies. The investigations by Liu and Nogami [157] for Dy disilicide nanowire growth on Si(001) represent an extremely interesting exception, in a sense to be clarified below: as discussed in Sec. 6.2.3.6, an experimental STM image was collected for a growth scenario where the wire nucleates on a flat terrace, consuming both Dy and Si atoms from the immediate vicinity, but leaving most of the terrace unaffected. [88] Within our RE disilicide wire growth model, this experimental result should be interpreted as the wetting layer on the unaffected part of the terrace being the 'wire template'. In other words, although this wire is not at the early stages of growth, we can still obtain unambiguous information about the wire structure, within our suggested growth scenario, simply from getting the answer to the question: 'does the long axis of the wetting layer unit cell on the unaffected area on the terrace point along the direction of wire growth?'. If the answer to this question is yes, say, the wires *can not* adopt the vacancy defected AlB_2 structure, for reasons clarified in the above. We are planning to contact the authors of this paper in order to get the answer to this extremely interesting question.

Our investigations into vacancy free Y disilicide nanowires with the AlB_2 structure on the Si(001) surface have involved optimization of the wire cross sectional profile and the number of layers in the wire. For the Si and Y atom reservoirs for the growing wire, needed in order to determine the wire stability, we used *(i)* Si atoms at the step edge on the substrate for a step edge structure assumed to be unchanged during wire growth and (ii) Y atoms from 2×4 and 3×1 wetting layers (chosen on the basis of experimental information [128]). We regard these choices as being sufficiently justifiable for reliable conclusions for the wire relative energies to be obtained (see Sec. 6.2.3.6 for further discussions).

We have concluded from these studies that the wires adopt a profile, described as the 'triangular' profile in the text, which involves stacking AlB_2 cages with the wire width decreasing for every new set of added cages along the surface normal, but leaving

[87] This experimental result, while of interest on its own, also emphasizes the possibly biggest limitation of our nanowire studies: calculations have been performed only on one out of two arguably realistic candidate for the structure of RE disilicide nanowires on Si(001). While there appears to be a clear connection between Y/Si(001) 2×4 wetting layer formation and vacancy free Y disilicide with the AlB_2 structure it is not at all impossible that this connection applies only to the wetting layer, with the wire for some reason, unknown to us at the time of writing (and, in particular, not described by our wire growth model which in this case must be regarded as incorrect) but presumably connected, on a very general level, with the introduction of Si vacancies during the initial stages of wire growth, adopts the vacancy defected rather than the vacancy free AlB_2 structure.

[88] As discussed in Sec. 6.2.3.6, the experimental studies of Ref. [157] clearly suggests two different scenarios for wire growth, not (presumably) with regards to the initial stages discussed above in the text, but definitely with regards to the areas from where Si and RE metal atoms are removed for inclusion in the growing wire.

out the outermost Si atoms for the cages at the wire edges (see Fig. 6.20). Our studies have suggested that, for this wire profile, the wires containing 2 and 5 layers (starting with an Y layer on the substrate as a consequence of the wire growth model) are stable configurations. We have performed only very preliminary studies into the understanding of wire stabilization, but note that the above conclusion for the difference between the number of layers for stable wire configurations is in agreement with experimental conclusions. Most of our studies have involved wires considerably narrower than experimentally observed wires, but with test calculations on wider wires supporting the reliability of the above described conclusions.

The target of the theoretical studies of Y disilicide nanowires on Si(001) performed in the present work has been to investigate the stability of vacancy free wires with the AlB_2 structure. Our calculations have revealed a wealth of information which should be interpreted in a more careful analysis in future work: electronic structure studies are expected to fully clarify whether our conclusions for the Y/Si(001) 2×4 wetting layer compare well with experiment while also providing real information on the stabilization of the nanowires. We have touched only briefly on these issues in the present work, and the main target in future studies is completing the studies initiated as presented above. Inclusion of real RE metals, where, most importantly, more experimental information is available on both wetting layers and wires compared to the situation for Y on Si(001) (an interesting example is provided below), would be highly useful. We have initiated such studies for the choice RE = Er, where formation of elongated RE disilicide nanostructures adopting the vacancy free AlB_2 structure is also predicted.

Another issue concerns the justifiability of the suggested wire growth model and its application to Er disilicide nanowire growth, the only situation where wires have sometimes been reported to grow in the absence of a wetting layer. We speculate here that this apparently very different growth scenario might be explained by much more rapid consumption of the wetting layer for certain growth conditions in experiment, i.e., connected with the Er disilicide wires being comparatively either more stable or with the growth associated with lower energy barriers compared to the situation for Y on Si(001). This is another good reason to focus on Er in future studies. Finally, as mentioned previously in the discussion, comparison with the experimental results in Ref. [157] could provide extremely strong support for our wire growth discussions in this thesis being justifiable. We will investigate this issue first thing.

6.3 STRUCTURAL OPTIMIZATION OF Y ATOMIC STRINGS ON THE Si(001) SURFACE

6.3.1 EXPERIMENTAL OBSERVATION OF SELF-ASSEMBLED ATOMIC STRINGS UPON DEPOSITION OF RARE EARTH METAL ON THE Si(001) AND Ge(001) SURFACES: A NEW CLASS OF RARE EARTH METAL NANOWIRES?

6.3.1.1 EXPERIMENTALLY REPORTED ATOMIC STRINGS UPON DEPOSITION OF Y ON THE Si(001) SURFACE: SUGGESTED CONNECTION WITH THE A TYPE AND HAIKU STRUCTURES

Recent experiments by Owen, yet to be published, involving deposition of Y on the Si(001) surface in UHV conditions, followed by annealing at the typical temperatures for Y disilicide nanowire growth, have revealed a new and very interesting structure not previously reported for RE metal interacting with this surface: [89] for Y coverages below 1 ML and annealing at 875 K for 30 - 40 min, several examples of seemingly defect free and perfectly straight nanostructures with atomic width and lengths of several hundred Å, apparently limited by the presence of other nanostructures on the substrate, were observed in addition to the appearance of elongated islands, presumably comprised by Y disilicide (see Fig. 6.22). These experimental results are distinguished from previously reported results for Y disilicide nanowire growth on Si(001) [128] not only by the appearance of these 'atomic strings' on the surface, but also by the fact that no Y/Si(001) wetting layer formation was observed in the more recent studies. While the annealing time for Y disilicide nanowire growth in the experiments of Ref. [128] was not reported, we would hold it as likely that the typical (see Sec. 4.2.3) annealing times, a few min, for growth of RE disilicide nanowires on Si(001) were employed in these experiments. The lack of a wetting layer in the experiments by Owen might be connected with the comparatively much longer annealing times. Furthermore, while the presumed Y disilicide nanostructures on the Si(001) surface in the experiments by Owen are clearly elongated, they do not have an aspect ratio which makes it evident that they are to be interpreted as Y disilicide nanowires. Due to these complexities, and given the very limited amount of experimental information at present on the growth of Y disilicide nanostructures on the Si(001) surface, we shall focus in the present discussion only on the appearance of the atomic strings.

The atomic strings reported in the experiments by Owen have a series of interesting properties. Firstly, they appear to be stable, showing resistance to coarsening and breaking even upon annealing times of $\sim$ 1 h. Secondly, as mentioned above, they have not only a large aspect ratio but atomic width, perfect straightness and an apparent absence of defects. In this sense, the structures bear a close resemblance to the Bi nanolines on Si(001) reported by Miki *et al.* [91] and discussed briefly in Sec. 4.2.2. This resemblance is further emphasized by the fact that both of these systems grow perpendicular to the Si dimer rows on the surrounding terrace, although comparison

[89] As will be discussed in part B of this subsection, seemingly similar nanostructures have previously been reported in experiment involving deposition of Ho on the Ge(001) surface. [86]

Figure 6.22: Experimental STM image (area: 1000×1000 Å^2) showing various nanostructures observed upon deposition of a submonolayer of Y on the Si(001) surface. In particular, as specified by the white arrows in the figure, two examples of strings of atomic width, running perpendicular to the Si dimer rows on the surrounding terrace, are present in this figure. The STM image is filled state, with a bias voltage of ~ 2 V. *Image courtesy of J. H. G. Owen.*

also reveals structural differences, most importantly the fact that Bi nanolines always occur in pairs, whereas, apparently, the fully grown atomic strings observed upon Y deposition on the Si(001) surface do not. We shall discuss the structural similarities and differences between these two systems further below. For the time being, we emphasize that the preliminary theoretical study of the atomic strings observed upon deposition of Y on Si(001), to be presented in Sec. 6.3.2, will be highly focussed on the similarity between these systems and the Bi nanolines on Si(001), with Sec. 6.3.2.1 clarifying on this statement. In particular, we shall make the basic assumption that the atomic strings are comprised by Y atoms, and refer to these nanostructures, for simplicity, as 'Y atomic strings' in the discussions below.

Apart from the above mentioned features of the Y atomic strings observed by Owen, the experimental STM image in Fig. 6.22 reveals only little information on these systems. Fig. 6.23, however, shows an experimental STM image, also obtained in the studies by Owen, of three different nanostructures on the Si(001) surface, some of which might be connected with the fully grown atomic strings, in the sense that they represent the early stages of string growth. [90] In these experiments, a great deal of the deposited Y (more than 1 ML initially) was evaporated from the Si(001) surface by flashing at 1425 K and the Y coverage therefore is unknown. The surface in Fig. 6.23 is not covered by a wetting layer. This, and the fact that all the nanostructures in the

[90] All these structures are clearly shorter than the strings observed in Fig. 6.22, the typical lengths of the features in Fig. 6.23 being 100 - 200 Å.

Figure 6.23: Experimental STM image (area: 1000×700 Å^2) showing three different types of nanostructures, as labelled with numbers in the figure, observed upon deposition of Y on the Si(001) surface. These structures might be connected (see text for details) with the atomic strings shown in Fig. 6.22. The STM image is empty state, with a bias voltage of ~ 2 V. *Image courtesy of J. H. G. Owen.*

figure have a width of only a few Si(001) surface lattice parameters makes a connection with Y disilicide nanowire growth somewhat questionable, at least on the basis of the growth model discussed in Sec. 6.2.3.6. On the other hand, upon annealing at 875 K of the sample shown in Fig. 6.23 for ~ 30 min, no Y atomic strings were reported. Rather, the structures in Fig. 6.23 appeared to coarsen into nanostructures without very well defined widths, along with the appearance of dark vacancy lines running perpendicular to the Si dimer row direction on the surface, similar to the situation reported by Harrison *et al.* [167] for very low coverages of Gd on the Si(001) surface. Considering these observations, one should be cautious, at the current level of experimental knowledge on the fully grown Y atomic strings, to establish connections between the structures in Fig. 6.23 and the atomic strings in Fig. 6.22. The basic reasons for drawing a parallel between these nanostructures are the evident straightness and atomic width of all these features and the fact that they all run perpendicular to the Si dimer row on the surrounding terrace. In the rest of this part of the subsection, we shall discuss the structural details of the nanostructures in Fig. 6.23, including, on the basis of these arguments, how these structures might be connected with the Y atomic strings. As we shall only be using very limited amounts of this information for our modelling of the strings, to be described in Sec. 6.3.2.1, the discussion will be fairly brief, primarily aimed at clarifying where we might be making important (i.e., unjustifiable) simplifications in our theoretical description of these systems. [91]

Fig. 6.23 shows three different nanostructures, as labelled with numbers, on the

[91] We shall return to this issue in Sec. 6.3.2.3 6.4.3 when the results of our theoretical studies of the Y atomic strings on Si(001) have been presented.

Si(001) surface. We shall discuss the first two structures, as defined by this labelling, initially and return to the third structure, which appears less easy to connect with the theoretical models to be presented in Sec. 6.3.2.1, at the end of this discussion. The first and second structure in Fig. 6.23 appear to be closely related, representing a single string and a set of strings, respectively, of the same width. Comparison with Si dimers on the adjacent terrace suggests that the width of a single string is $\sim$ 1 Si(001) surface lattice parameter while the distance across the pair of strings is between 2 and 3 Si(001) surface lattice parameters. This observation, along with the above mentioned similarity of the strings, appears to be in agreement with the suggestion that the single string (pair of strings) can be explained by a chain (pair of chains) of Y atoms on an A Type (Haiku) structure. [92] In further support of this suggestion, the experimental STM image in Fig. 6.23 shows brightening around these nanostructures, which was found to disappear at higher voltages [173], and a comparatively lower amount of Si vacancies on the surface in the immediate vicinity of these structures. These observations suggest that the string formation is associated with the appearance of an appreciable tensile strain field on the surface. Similar observations have been reported for the Bi nanolines on Si(001), see e.g. Ref. [85]. We shall discuss in more detail in Sec. 6.3.2.1 how these observations appear, in addition, to make sense from the point of view of Y adsorbing on the A Type and Haiku structures.

There is also an evident difference between the structural details reported for the Bi nanolines on Si(001) (see e.g. Ref. [85]) and the pair of strings in Fig. 6.23. For the latter configuration, the Si dimers on the surrounding terrace immediately next to the string display features not observed for the Si dimers farther away from this nanostructure: at the edge of every pair (typically, see below) of Si dimer rows running towards the string, a dark area appears at the point where the dimer row meets the nanostructure. This behaviour might be explained by the buckling of the Si dimers right next to the string being fixed, with the Si 'up' atoms on two adjacent Si dimer rows not being located on the same side of the row. One might argue, on the basis of such an explanation, that the Si dimers farther away from the nanostructure should also be affected, but a detailed discussion of this issue would probably require theoretical modelling of the particular system in question, in order to clarify the energy difference between a configuration where the buckling of the second Si dimer (and all Si dimers farther away) from the nanostructure is inverted relative to the Si dimer with a fixed buckling right next to the nanostructure. We have performed no such theoretical modelling in the present work and therefore we will not go into further detail with this issue at this point (although we shall discuss alternative explanations for this phenomenon in Sec. 6.3.3). Only, we note that the appearance of the dark features around the strings are observed for both the single string and the pair of strings in Fig. 6.23. Typically, as mentioned above, each dark feature is separated by two Si dimer rows, but sometimes the separation is larger, or there is a whole range where the features apparently disappear. This, and the observation that the presence of dark features on either side of the nanostructure does only sometimes show signs of correlation, suggests that it might be regarded as a phenomenon which is not crucial to the formation of the nanostructure. In particu-

[92] While the single strings in Fig. 6.23 appear at a higher frequency than the pair of strings, no pairs of fully grown atomic strings have yet been observed for Y on Si(001). We shall leave this issue for now and return to it in Sec. 6.3.2.1.

lar, of key importance to the present discussion, we see no reason why this observation should be at variance with the suggested connection between these nanostructures and the A Type and Haiku structures.

In addition to the two nanostructures discussed above, a third nanostructure is present in Fig. 6.23. This feature on the Si(001) surface shows some resemblance to the single atomic string discussed above, but in various important respects, it seems to differ from the other nanostructures in Fig. 6.23. In comparison with the single string discussed previously, this string is clearly wider and furthermore surrounded on either side by dark lines, rather than isolated dark features. It appears that the presence of Si vacancies around this string is also reduced compared to elsewhere on the terrace but the clear brightening observed for the more narrow string in the experimental STM image is not observed for this nanostructure. On the basis of these observations, we are cautious about drawing a parallel between the wider string and the more narrow strings discussed above. We have not attempted to do any modelling of the wider atomic string in this work.

In summary, recent experiments by Owen (yet to be published), involving deposition of submonolayers of Y on the Si(001) surface, have revealed atomic strings that remain stable upon annealing at 875 K and attain a length of several hundred Å. Such nanostructures have not previously been reported for RE metal on the Si(001) surface (although a similar structures has been observed in experiment [86] upon deposition of Ho on Ge(001), see below). While little is currently known on the atomic strings, several observations suggest a close connection with the A Type structure (see Sec. 4.2.2): the strings grow perpendicular to the Si dimer rows on the surrounding terrace and they are both perfectly straight and apparently defect free. Other observations for presumed immature string structures add further support to this suggestion while furthermore suggesting that also pairs of atomic strings, connected (in continuation of the above suggestion), with the Haiku structure, exist. In our theoretical modelling of these systems, to be described in Sec. 6.3.2, we shall assume that *(i)* the strings are comprised by Y atoms and *(ii)* that the appearance of the string (pair of strings) is connected with the formation of the A Type (Haiku) structure.

In Sec. 6.3.1.2, we shall discuss the recent experimental observation [86] of Ho atomic strings on the Ge(001) surface in the attempt to *(i)* clarify similarities and differences between this system and the Y atomic string on Si(001) and *(ii)* gain more knowledge on the latter of these systems.

6.3.1.2 EXPERIMENTALLY REPORTED ATOMIC STRINGS UPON DEPOSITION OF Ho ON THE Ge(001) SURFACE

While RE metal atomic strings on Si(001) have not been reported prior to the recent observations by Owen, discussed in Sec. 6.3.1.1, nanostructures with similar dimensions have been reported by Bonet and Tear [86] for deposition of Ho on the Ge(001) surface. As RE metal atoms deposited on Si and Ge do display conceptually similar properties, with self-assembly of RE disilicide structures and RE germanide structures, respectively, reported in 3D film growth studies, [174, 175] there are suggestions that conclusions for the growth of RE metal related nanostructures on the Ge(001) surface

can be transferred to the situation where the substrate is Si(001), although no detailed knowledge on this issue is available at the present stage. This remark is the key motivation for discussing the above mentioned assumed Ho atomic strings on Ge(001) reported in the experiments by Bonet and Tear [86] in the present context of the assumed Y atomic strings on Si(001), as, in addition, the former of these systems has been studied experimentally in comparatively more detail. Below, we shall emphasize similarities and differences between these two systems, discussing the extent to which they might bear a relation and what can possibly be concluded for the Y atomic strings on Si(001) on the basis of this discussion.

The assumed Ho atomic strings on Ge(001) reported in Ref. [86] were observed by the authors with STM upon deposition of 0.1 ML of Ho on this surface in UHV conditions and annealing at 715 K. The strings run perpendicular to the Ge dimer rows and are perfectly straight, with lengths up to $\sim$ 1000 Å and a well-defined width of $\sim$ 15 Å, i.e., almost 4 Ge(001) surface lattice parameters. [93] Only single strings have been reported in these experiments. On the basis of these structural data, a close similarity with the Y atomic strings on Si(001) discussed in Sec. 6.3.1.1 does seem like a possibility. The perfect straightness of the Y strings lead us to the suggestion that these strings might be closely connected with the A Type or Haiku structures. While it seems clear from the experimental STM images in Fig. 6.22 and Fig. 6.23 that the Y strings are more narrow than the Ho atomic strings, the connection with the same local surface reconstruction might still hold true, in view of the above experimental results, with the Ho atomic strings simply being comprised by a larger number of parallel chains of RE metal atoms on the surface.

There are also clear differences between the Ho atomic strings on Ge(001) and the Y atomic strings on Si(001), though. Ge vacancies are found to accumulate around the Ho atomic strings, whereas vacancies appear to be expelled from a region in the vicinity of the Y atomic strings. [94] As the A Type and Haiku structures are associated with a tensile strain field on the surface, this observation does weaken the connection between the Ho strings on Ge(001) and these particular local surface reconstructions. This link seems to be further weakened by the observation by Bonet and Tear [86] that the Ho strings do not remain stable upon annealing at 715 K but coarsen into larger rectangular islands, presumably comprised by Ho germanide. By contrast, the Y atomic strings were found to remain stable upon annealing in the experiments by Owen. Finally, while the observation of perfectly straight trenches without adsorbed Ho on the Ge(001) surface in the experiments of Ref. [86] must be regarded as a strong support for the Ho atomic strings being connected with a local reconstruction of the Ge(001) surface, the width of these vacancy lines was reported to be 4 Ge(001) surface lattice parameters in Ref. [86], clearly larger than the values which can be associated with either the A Type or the Haiku structure.

[93] The Ge(001) surface lattice parameter RT value is 4.00 Å.

[94] As this conclusion for the Y atomic strings on Si(001) is based on the experimental STM image in Fig. 6.23 rather than the image of the fully grown string in Fig. 6.22, we should be cautious about putting too much emphasis on this argument: as discussed in Sec. 6.3.1.1, the strings in Fig. 6.23 did not grow into the long strings observed in Fig. 6.22 upon annealing of the substrate.

In summary, while the Ho atomic strings observed in the experiments of Ref. [86] do appear to be connected with a local reconstruction of the Ge(001) surface, this reconstruction does not satisfy basic structural properties required in order to associate it with the A Type or Haiku structures. As discussed in Sec. 6.3.1.1, it is a basic assumption in the current work that the Y atomic strings on the Si(001) surface are associated with these local surface reconstructions. As this assumption does appear to be well supported by experimental observation, we conclude, on the basis of the current level of experimental information on the Ho atomic strings on Ge(001) and Y atomic strings on Si(001), that the growth processes of these nanostructures are conceptually quite different. We shall therefore not attempt to transfer any information from the experiments of Ref. [86] to our current theoretical studies of the Y atomic strings.

6.3.2 STRUCTURAL OPTIMIZATION OF SELECTED Y ATOMIC STRINGS ON THE Si(001) SURFACE

6.3.2.1 BASIC REASONS, FROM THE POINT OF VIEW OF THEORY AND EXPERIMENT, FOR CONNECTING THE Y ATOMIC STRINGS WITH THE A TYPE AND HAIKU STRUCTURES

The preliminary theoretical studies of the (assumed) Y atomic strings observed by Owen upon deposition of Y on the Si(001) surface basically can be summarized as follows: we are aiming at clarifying whether these strings are closely connected with the A type and Haiku structures, both of which have been presented in Sec. 4.2.2 (see also Fig. 6.25 for a picture of the A Type structure). The discussion in Sec. 6.3.1.1 of the experimental results for the Y atomic strings clarified some of the reasons for drawing parallels between these systems and the Bi nanolines on Si(001) (and thus, in turn, with the Haiku structure): the straightness and well defined width of the Y atomic strings appears very difficult to explain on the basis of the Y disilicide nanowire epitaxial growth mode described in Sec. 6.2.2.2. Indeed, typically (see Sec. 4.2.3), the RE disilicide nanowires have a range of widths, always at least a few Si(001) surface lattice parameters, approximately, and kinks are not infrequent (see e.g. Refs. [98, 157]). For the Bi nanolines on Si(001), however, the atomic width of the structures and their straightness is explained, as discussed in Sec. 4.2.2, by the major local reconstruction of the Si(001) surface, the Haiku structure, below the Bi atoms. Furthermore (see Sec. 6.3.1.1), the Bi nanolines and the Y atomic strings run along the same direction on the Si(001) surface. On a more basic level, the fact that the Haiku structure provides local strain relief, with the reconstruction involving only the substrate, suggests that the same phenomenon might occur upon deposition of Y on the Si(001) surface, provided that the strain experienced by the substrate upon Y deposition can be relieved to a major degree by this particular surface reconstruction. We shall discuss this issue in more detail below.

In this initial discussion, we have not mentioned a key point addressed in Sec. 6.3.1.1: while the Bi nanolines on the Si(001) surface always grow in pairs, the Y atomic strings apparently do not. This has little consequence to the above line of arguments, though: as discussed briefly in Sec. 4.2.2, the Haiku structure is closely connected to the A Type structure, with the key difference being that the latter of these structures is more likely to be associated with the presence of only a single atomic string (we shall discuss this in more detail for Y on Si(001) below). Furthermore, the A Type structure is connected with both local strain relief on the Si(001) surface and the perfect straightness (see Ref. [93]) required in order to be a justifiable candidate for a template for the Y atomic strings. We can therefore, it appears, justifiably substitute the A Type structure for the Haiku structure in the discussion at the beginning of this part of the subsection. This does not mean, however, that we are not interested in including the Haiku structure in our theoretical modelling. We shall clarify on this in the discussion below.

As mentioned in passing in Sec. 6.3.1.1, the fully grown Y atomic strings on the Si(001) surface apparently do not tend to appear in pairs, in contrast to the Bi nanolines on the Si(001) surface. On the other hand, the experimental STM image in Fig. 6.23

clearly shows what appears to be immature single atomic strings as well as pairs of strings on this surface. If there is a relation between the nanostructures in Fig. 6.23 and the Y atomic strings in Fig. 6.22, we are faced with the question why, apparently, no pairs of fully grown strings have been reported so far in experiment. The answer to this question might be connected with the fact that the Haiku structures represent a much more complex local reconstruction of the Si(001) surface compared to the A Type structure and consequently tend to appear at significantly higher temperatures. The Bi nanolines on Si(001) have been reported (see Sec. 4.2.2) to grow in a narrow temperature range, the lower limit of 845 K presumably being strongly connected with the creation of the Haiku structure (although also the diffusion of Bi on the Si(001) surface must be regarded as a key factor). [95] This temperature is very close to the typical annealing temperature of 875 K in experiments involving RE disilicide nanowire growth. In particular, the experimental STM image in Fig. 6.22 refers to annealing at this temperature. In the experiment leading to the nanostructures shown in Fig. 6.23, however, the sample was flashed at much higher temperatures. It is not unlikely, on the basis of these considerations, that the appearance of a pair of atomic strings in Fig. 6.23 only is explained by the onset of growth of this nanostructure being above 875 K. While these remarks are speculative (in particular, they do not explain why no fully grown Y atomic strings were observed upon further annealing at 875 K of the sample in Fig. 6.23), they represent one of our key arguments for regarding the set of narrow strings in Fig. 6.23 and the strings in Fig. 6.22 as closely connected. [96] In essence, these comments explain why, when making reference to the experimental results discussed in Sec. 6.3.1.1, we include the Haiku structure as well as the A Type structure in our theoretical modelling. The basic theoretical reason for including both of these local surface reconstructions in our studies will be presented in the following discussion.

Up to now, in the discussions in this part of the subsection, we have emphasized the interest in the A Type and Haiku structures as explanations for the Y atomic strings due to fact that these local surface reconstructions offer a way of growing straight nanostructures with atomic width on the Si(001) surface. On a more specific level, we should be asking whether there is any good reason to believe that a configuration involving e.g. a chain of Y atoms adsorbed on an A Type structure should be energetically favourable. The answer to this question is 'yes', with the details provided below. Fig. 6.24 shows a schematic presentation of configurations with an Y atom at the Hollow site on the (slightly modified, see below) Si(001) surface and an Y atom at the similar Hollow site [97] along an A Type structure on this surface. Each of these growth sites represent the structural environment most similar to the AlB_2 structure for the given local environment in question, and as such, this choice of growth site for Y on

[95] The A Type structure has been reported to grow at significantly lower temperatures in experiments involving deposition of As on Si(001). [93]

[96] The other arguments for drawing parallels between these nanostructures are the various experimental observations discussed in Sec. 6.3.1.1 that appear to connect all of the structures with either the A Type or the Haiku structure.

[97] For simplicity, in the discussions of this subsection, we have chosen the name Hollow site for this growth site on the A Type structure. We shall follow the same convention below for the very similar growth site obtained for the Haiku structure.

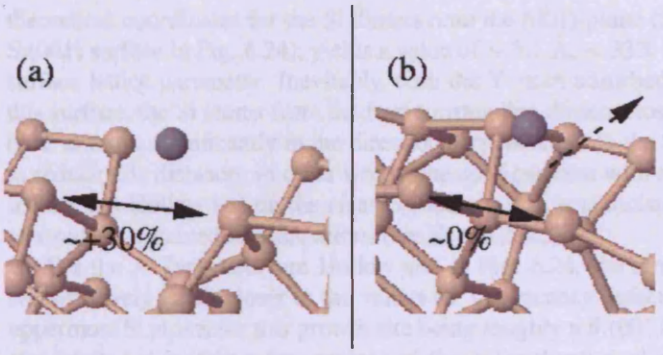

Figure 6.24: Schematic figure showing (a) an isolated Y atom adsorbed at a Hollow site on the clean Si(001) surface and (b) on the A Type structure, respectively. The buckling of the Si dimers for the clean Si(001) surface has been neglected for simplicity. An estimate of the ratio of the distance between the nearest Si atoms on adjacent dimer rows to the Si(001) surface lattice parameter (3.84 Å) has been included in the figure. The dotted arrow shows the direction of the fully grown Y atomic string on the A Type structure.

the A Type structure would be expected to be the most energetically favourable choice for this particular system, compared to other configurations obtained by moving the Y atom within the locally reconstructed area. For Y on clean Si(001), the calculations described in Sec. 6.2.4.2 have shown that the Hollow site is the most favourable configuration for isolated Y atoms on this surface when substitutional configurations have been excluded.

In order to clarify which of these local growth sites is expected to be the energetically more favourable, we recall the conceptually similar discussion in Sec. 6.2.2.2 where the matching of Y disilicide in the AlB_2 structure (rather than a single Y atom) on a Si(001) surface with the Si dimer bonds broken was considered. Referring to the considerations in that subsection, the growth site in Fig. 6.2 would structurally resemble the vacancy defected AlB_2 structure the most if the distance between Si atoms in the direction perpendicular to the Si dimer row direction were $\sim$ 8% larger than the Si(001) surface lattice parameter (we shall postpone the explanation why the vacancy defected AlB_2 structure is chosen over the vacancy free AlB_2 structure until later in this discussion). This still holds true (to a reasonable approximation, with the differences, discussed in Sec. 6.2.4.2, not being crucial to the arguments below) when we consider the adsorption of an isolated Y atom on the clean Si(001) surface, the key difference, however, being that the dimer bonds are not broken for this situation. [98] The Si atom dimerization has major consequences for the present discussion. For the clean Si(001) surface with an isolated Y atom at a Hollow site, the nearest Si atoms on adjacent dimer rows are very far apart compared to the Si(001) surface lattice parameter: a gross estimate of the distance between these atoms, obtained upon projecting typical

[98] Indeed, this consideration in Sec. 6.2.2.2 was justified by the fact that an extended structure was growing on the Si(001) surface, the Si dimer bonds being broken in this growth process.

theoretical coordinates for the Si dimers onto the (001)-plane (the modification of the Si(001) surface in Fig. 6.24), yields a value of ~ 5.1 Å, $\sim 33\%$ larger than the Si(001) surface lattice parameter. Inevitably, with the Y atom adsorbed at the Hollow site on this surface, the Si atoms from the four surrounding dimers closest to this Y atom will have to move significantly in the direction perpendicular to the Si dimer rows in order to reduce this distance: in other words, the configuration with an isolated Y atom adsorbed at a Hollow site on the clean Si(001) surface is associated with a large degree of strain, as obtained in calculations (see Sec. 6.2.4.2).

For the A Type structure Hollow site in Fig. 6.24, the structural parameters are comparatively much closer to the values for the vacancy defected AlB_2 structure, the uppermost Si atoms for this growth site being roughly a Si(001) surface lattice parameter apart, i.e., within a few percent of the optimal value when comparing with the vacancy defected Y disilicide AlB_2 structure lattice parameters. Consequently, with an Y atom adsorbing at the Hollow site for the A Type structure, we would expect the resulting strain on the substrate to be clearly less significant compared to the situation for the clean Si(001) surface. Structurally, the A Type structure Hollow site is clearly more similar to the local vacancy defected AlB_2 structure environment than the Hollow site on the clean Si(001) surface. [99]

These arguments evidently establish the A Type structure Hollow site as an energetically more favourable adsorption site for an Y atom compared to the Hollow site on the clean Si(001) surface. This conclusion should not stand alone, however, for two reasons. Firstly, there is an energy penalty to pay in order for the A Type structure (or the Haiku structure, where an argument equivalent to the above applies) to be created. Ultimately, the stability of the complete chain (pair of chains) of Y atoms on the A Type (Haiku) structure is evaluated through balancing this energy penalty against the large binding energy of the deposited Y atoms expected on the basis of the suggestion that a chain (pair of chains) of growth sites, each resembling closely the local environment for the vacancy defected AlB_2 structure, has been created by this reconstruction of the Si(001) surface. Indeed, the purpose of the above discussion has not been to discuss the relative stability of e.g. the two structures in Fig. 6.24 as this issue can not be clarified on the basis of the arguments used. Rather, our considerations serve as the key theoretical argument for establishing a connection between the A Type and Haiku structures and atomic strings comprised by Y on the Si(001) surface. A second addition to the above discussion relates to the question why the focus was on comparison with the structural parameters for the vacancy defected (rather than the vacancy free) AlB_2 structure. The answer to this question is simple, but the potential consequences are complex, and we will postpone a full discussion of this issue to Sec. 6.3.3. For the time being, we shall only note that as the Y atomic string obtained by e.g. adsorbing Y atoms at the chain of Hollow sites on the A Type structure will grow along the direction of the white arrow in Fig. 6.24, we would require, in addition to adsorbing the Y atom at a site as similar as possible to the local environment for the AlB_2 structure, that there is as little strain as possible along this direction. This requirement selects the growth

[99] When comparing the two growth sites in Fig. 6.24, also the second layer of Si atoms for the A Type structure Hollow site resembles more closely the local structural environment in the bulk AlB_2 structure. This is presumably less important, though, as these Si atoms have no dangling bonds for any of the two configurations considered.

site with strong similarities to the bulk vacancy defected AlB_2 structure over the above mentioned alternative, as clarified in Fig. 6.2 of Sec. 6.2.2.2.

In summary, we have argued that, from the point of view of experiment and theory, there are a series of reasons why the Y atomic strings might be connected with the A Type and Haiku structures. On a very basic level, both of these local reconstructions serve as potential templates for growth of Y strings with perfect straightness as the templates themselves are known to be extremely straight and with atomic width. Further considerations reveal that the growth sites presented by these templates have a very close similarity to the local structural environment for the vacancy defected AlB_2 structure. Consequently, while there is an energy penalty to pay in order for the A Type and Haiku structures to be created, the deposited Y atoms might have a sufficiently high binding energy when adsorbed at these structures to more than compensate for this penalty. On the basis of these considerations, and the suggestion that both the single and paired narrow strings in Fig. 6.23 of Sec. 6.3.1.1, are connected with Y atomic strings, we have chosen to include the Haiku structure along with the A Type structure as the basis for our theoretical modelling of the Y atomic strings. We shall describe our strategy for this modelling Sec. 6.3.2.2, presenting in this process the series of candidate structures investigated in this work.

6.3.2.2 MODELLING OF THE Y ATOMIC STRINGS

With reference to the discussion in part A of this subsection, our chosen candidate structures for the Y atomic strings (see Fig. 6.25) involve chains of Y atoms adsorbed on either an A Type or a Haiku structure, with two different registries of the Y atoms relative to the Si dimer rows on the surrounding terrace, described more clearly for the A Type configurations in Fig. 6.25: in one situation, each Y atom is in registry with the center of the Si dimer bond, whereas in the other situation, all Y atoms have been translated along the Y chain direction by half a Si(001) surface lattice parameter, with the above mentioned registry thus being changed by the same amount. We name these configurations 'Hollow' and 'Cave', respectively, adopting the normal nomenclature for adatoms on the clean Si(001) surface. The Haiku, Cave configuration has the same registry for the adatoms with respect to the Si dimers on the surrounding terrace as obtained for the Bi atoms of the Bi nanolines on Si(001). The Haiku, Hollow configuration is expected to be energetically more favourable for the case of Y on Si(001), though, on the basis of the discussions in Sec. 6.3.2.1, where we concluded that the Hollow site bears a strong similarity with the local structural environment for the vacancy defected AlB_2 structure.

As discussed in Sec. 6.3.1.1, the Y atomic strings have been reported to grow on a locally clean Si(001) surface. This simplifies our theoretical modelling of these structures as the region between adjacent strings/pairs of strings within the chosen supercell approximation (see Sec. 2.3) can justifiably be described by clean Si(001). As no agglomeration of the Y atomic strings have been noted in the experimental STM images discussed in Sec. 6.3.1.1, we aim at describing isolated strings/pairs of strings in our theoretical studies. The convergence in the formation energy with respect to the separation of adjacent Y atomic string candidate structures has been studied for all the

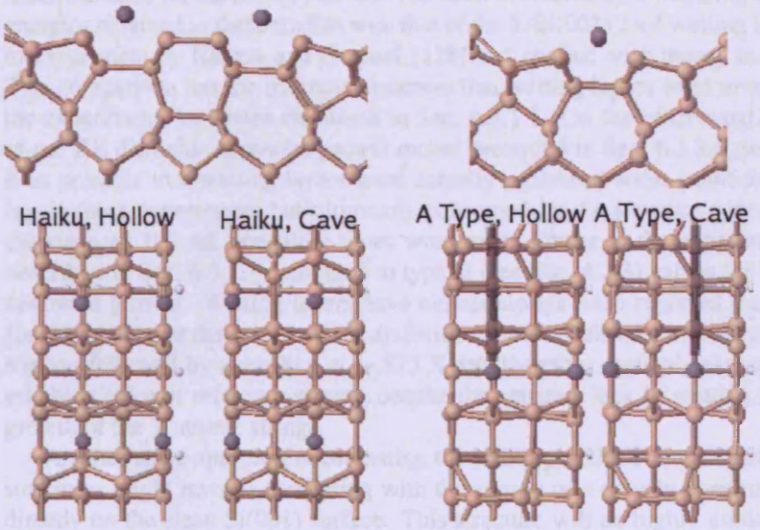

Figure 6.25: Schematic figure showing the Y atomic string candidate structures investigated in this work. Pairs of Y chains on a Haiku structure (figures on the left) and single Y chains on A Type structures (figures on the right) have been optimized. Within each group, two different registries for the Y atoms with respect to the Si dimers on the surrounding terrace (as emphasized by the dark grey rectangular boxes in the top view images of the A Type related configurations) have been chosen.

configurations described in Fig. 6.25 by increasing the number of Si dimers in the row between adjacent nanostructures. For all configurations considered, cells containing 4, 6, and 8 Si dimers for the reference energy clean Si(001) system (i.e., in the absence of both surface reconstruction and deposited Y), have been studied. In order to convert this information into a separation between adjacent string candidate structures for the configuration under investigation, we note that a cell containing n Si dimers along the dimer row for the clean Si(001) surface contains n - 2 and n - 4 dimers along the row for the A Type and Haiku related structures, respectively. On the basis of this information, we define the separation of the adjacent A Type (Haiku) based configurations in Fig. 6.25 as 2, 4, and 6 (0, 2, and 4) Si(001) surface lattice parameters for the supercells employed in this work.

The supercells investigated contain only a single Si dimer row (see Fig. 6.25). As discussed in Sec. 6.3.1.1, there are strong suggestions from experiment that a more proper description of the Y atomic string structure is obtained by including a second dimer row for the supercell and as such, the current choice of cell is not truly justifiable. We have avoided investigating this issue further for the current preliminary studies of the Y atomic strings, however, and we shall return to it only when we discussing future work on these structures in Sec. 6.3.3.

The stability of the Y atomic string candidate structures relative to other Y related nanostructures on the Si(001) surface has been evaluated by comparing the formation energies obtained in these studies with that of the Y/Si(001) 2×4 wetting layer reported in experiment by Katkov and Nogami [128] and studied with theory in Sec. 6.2.4.3. This comparison has the inherent weakness that wetting layers were never reported in the experiments by Owen discussed in Sec. 6.3.1.1. On the other hand, on the basis of our RE disilicide nanowire growth model presented in Sec. 6.2.3.1, we would hold it as possible that wetting layers were actually present at some point during annealing in these experiments but ultimately consumed by the growing nanostructures on the surface. Indeed, annealing times were much longer in the experimental studies described in Sec. 6.3.1.1 compared to typical (see Sec. 4.2.3) values for RE disilicide nanowire growth. Wetting layers have almost always been reported (see Sec. 4.2.3) for submonolayer deposition of RE disilicide nanowire related elements on the Si(001) surface followed by annealing at $\sim$ 875 K and therefore arguably serves as the most reliable choice of reference energy, despite the apparent lack of wetting layers during growth of the Y atomic strings.

An alternative approach to evaluating the stability of the Y atomic string candidate structures might involve comparing with the energy of a naively constructed Y chain directly on the clean Si(001) surface. This structure will be highly unlikely to satisfy the requirements for either straightness or well defined width [100] required for a realistic candidate for the Y atomic strings observed in experiment. It might nevertheless be worth including the most favourable Y chain/pair of chains from this set of structures in the current studies as an additional reference energy, the energy of a realistic candidate for the Y atomic strings expected to be significantly lower than the energy of any such naive chain structure. We have not performed such studies in the present work, though, and we shall therefore not discuss this issue further.

Finally, we might consider comparing the stability of the Y atomic string candidate structures with some of the presumed Y disilicide elongated nanostructures observed in addition to the atomic strings in the experiments by Owen (see Fig. 6.22). As discussed in Sec. 6.3.1.1, however, we regard the structure of these nanostructures as rather uncertain, given the present level of information, this issue consequently being rather complex. We have not discussed this possibility further below.

As discussed in Sec. 4.2.2, the number of Si atoms upon construction of the Haiku structure from clean Si(001) is not locally conserved: for the supercells considered in the present work for the optimization of the Haiku structure related configurations in Fig. 6.22, four Si atoms have been removed and evaluation of the relative energy for these configurations therefore requires an evaluation of the energy for binding these Si atoms elsewhere on the substrate. We have made the choice to use the binding energy for a Si atom at a step edge as calculated in Sec. 6.2.4.1 for this energy. As the present theoretical studies are only preliminary, we shall not go into details with a discussion

[100] For the Y atomic string candidate structures presented in Fig. 6.25, these requirements are satisfied through the local reconstruction of the Si(001) surface. In the absence of such a reconstruction there appears to be no strong tendency, on the basis of the calculations for isolated Y atoms on the Si(001) surface described in Sec. 6.2.4.2, for a chain of Y atoms to form, remain straight, or repel additional Y atoms to diffusing to the side of the chain.

of the justifiability of this choice. [101]

In this part of the subsection, we have presented the strategy for the theoretical modelling of the isolated Y atomic string candidate structures investigated in the present work. Four different configurations, distinguished by *(i)* the choice of reconstruction of the Si(001) surface (A Type or Haiku structure) and *(ii)* the registry of the Y atoms with respect to this reconstruction (all Y atoms at either Cave or Hollow sites), have been investigated. The intermediate region between adjacent configurations in the supercell approximation is clean Si(001), in agreement with experimental observation. The stability of the structures is evaluated by comparing with the energy of the Y/Si(001) 2×4 wetting layer. For the evaluation of the formation energy for the Haiku structure related configurations, we assume that the Si atoms removed locally in the process of the surface reconstruction adsorb at a step edge elsewhere on the substrate. In Sec. 6.3.2.3, we shall discuss the results obtained upon optimization of these Y atomic string candidate structures.

6.3.2.3 RESULTS OF THE OPTIMIZATION OF THE Y ATOMIC STRING CANDIDATE STRUCTURES

The total energies, relative to the clean Si(001) surface, for the optimized Y atomic string candidate structures described in Sec. 6.3.2.2 have been tabulated in Table 6.11. The results in this table refer to calculations performed using Vanderbilt US PPs [17] as implemented in VASP [23, 24], with the Y 4*p* electrons included in the core. The PW91 GGA [12] to the exchange correlation functional was employed in the theoretical studies. A plane wave energy cutoff of 200.0 eV, as determined (VASP default value) by the presence of H atoms in the system (the H termination layer for the Si slab in the supercell calculation) was used on the basis of results obtained in previous calculations for Y on the Si(001) surface (see Sec. 6.2.4). For partial occupancies, the studies employed the Gaussian smearing scheme with a smearing width of 0.1 eV, this once again being the same choice as in the studies of Sec. 6.2.4. The k mesh convergence was tested independently for each supercell, and we refer to Sec. 8.3.5 for comments on this issue as well as a more complete discussion of computational details. The relative energies of the Y atomic string candidate structures have been included in Fig. 6.26, along with the energy of the Y/Si(001) 2×4 wetting layer, as obtained in Sec. 6.2.4.3.

In general, with the limitation to interpretation that only three different nanostructure separations have been investigated for each Y atomic string candidate structure, the variation in the formation energy of all configurations in Table 6.11 shows reasonable convergence with respect to the separation of adjacent configurations within the supercell approximation. In other words, for all Y atomic string candidate structures investigated, the relative energy as obtained with the largest cell is a reasonable estimate of the energy of the truly isolated configuration, the remaining changes presumably being within 0.1 eV for the A_C, A_H, and H_H configurations and clearly smaller for the H_C configuration. These energy changes are much smaller than the energy differences between the various configurations investigated. Indeed, it is evident, by comparison

[101] We refer to Sec. 6.2.3.6 for comments on this issue made in relation to RE disilicide nanowire growth on Si(001).

Table 6.11: Total energies of the optimized Y atomic string candidate structures described in Fig. 6.25, relative to the energy of the clean Si(001) surface, as obtained in the calculations of the present work (see text for computational details). The subscripts in the first row refer to the length of the unit cell in the direction perpendicular to the atomic string direction, as specified by the number of Si dimers for the corresponding clean Si(001) slab geometry with the same surface dimensions. The energy variation with nanostructure separation has been shown in Fig. 6.26.

Configuration	$E_{4\ d.c.}$/ eV/atom	$E_{6\ d.c.}$/ eV/atom	$E_{8\ d.c.}$/ eV/atom
A Type, Cave (A_C)	-5.48	-5.65	-5.71
Haiku, Cave (H_C)	-6.27	-6.31	-6.32
A Type, Hollow (A_H)	-6.87	-7.01	-7.07
Haiku, Hollow (H_H)	-7.22	-7.38	-7.43

with the energy of the Y/Si(001) 2×4 wetting layer (see Fig. 6.26), that all energies but the H_H configuration energy will be clearly above energies which can be associated with stability of the structure in question. As will be discussed below, this does not necessarily rule out any connection between the A Type structure and the structure of the Y atomic string. The results of Table 6.11 strongly suggest, however, that the candidate structures with Y atoms at the Cave site are energetically unfavourable.

For both the A Type and the Haiku structure related configurations, the simple translation of all Y atoms along the chain direction which moves each Y atom from the Cave to the Hollow site is associated with a huge decrease, between 1 and 1.5 eV, in the configuration formation energy. We regard this result as a very strong support for the argument in Sec. 6.3.2.1 that the connection between the A Type and Haiku structure and the Y atomic strings observed in experiment can be explained to a large degree by the fact that these substrate reconstructions lead to the creation of highly favourable growth sites for the deposited Y atoms. In comparison, when the isolated Y atom is moved from the Cave site to the Hollow site on the clean Si(001) surface (see Sec. 6.2.4.2), the energy gain is minute, 0.14 eV.

Investigation of the optimized structural parameters for the Y atomic string candidate structures with Y at the Hollow site show that the nearest Si atoms on opposite sides of the Y chain for the uppermost layer of the substrate are farther apart for the Haiku related structure by ~ 4 %, the mean value for this distance being 3.864 Å (with some scatter in this parameter, see below). This further supports the significance of the creation of an 'optimal growth site' for each Y atom as a key reason for the energy differences obtained between the different configurations in Fig. 6.26, the Hollow site for the H_H configuration clearly being more similar to the local structural environment for the vacancy defected AlB_2 structure compared to the A_H configuration. The most important interatomic distances for the A_H and H_H configurations have been tabulated in Table 6.12. [102] We note that a large amount of the scatter in the interatomic distances

[102] A comparison of the Y-Si distances in Table 6.12 with the Y-Si distances obtained by Magaud *et al.* [138] for bulk vacancy defected Y disilicide in the AlB_2 structure is not regarded as highly informative, primarily as the bonds for the Y atomic string configurations must be comparatively stronger with both the uppermost Si atoms for the substrate and the Y atom at a given growth site being involved in the formation of a fewer

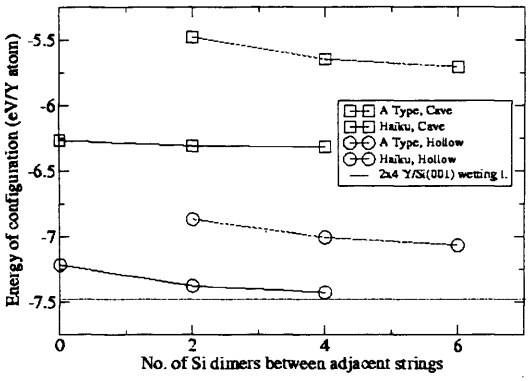

Figure 6.26: Total energies (relative to clean Si(001)) for the Y atomic string candidate structures shown in Fig. 6.25 as a function of the separation of adjacent strings (see Sec. 6.3.2.2 for details). The energy of the Y/Si(001) 2×4 wetting layer, as obtained in Sec. 6.2.4.3, presents a reference energy for evaluation of the stability of these string candidate structures (see text for details).

for the Haiku structure is probably connected with the clear structural differences for this reconstruction in the region between the Y chains and the region on the other side of a given chain.

More information on the Y-Si bond formation for the A_H and H_H configurations would require a study of the electronic structure for these systems. We have avoided going into this discussion for two reasons: *(i)* the above mentioned support for the formation energies of these systems being closely connected to the creation of favourable growth sites for the adsorbed Y atoms appears to be so strong that this link can be regarded as well established. More importantly, we shall discuss below that *(ii)* there is reason to believe that these systems have not been fully optimized. This, and the fact that none of the Y atomic string candidate structures are energetically favourable relative to the Y/Si(001) 2×4 wetting layer, makes a detailed discussion of the electronic properties of the strings seem rather irrelevant at the present stage of theoretical progress in understanding these systems. [103]

On comparing the formation energies for the Y atomic string candidate structures with the energy of the Y/Si(001) 2×4 wetting layer, we find that none of the string configurations are stable, although the energy of the truly isolated H_H configuration might drop slightly below the wetting layer energy. The A_H configuration, the prime candidate for the Y atomic string in Fig. 6.22 in the present theoretical studies, is above

number of bonds.

[103] In particular, we shall not discuss here whether the Y atoms prefer to deposit on all the adsorption sites along a given chain for the A Type or Haiku structure, although in particular the discussion in Sec. 6.3.3 will touch on related issues.

Table 6.12: Interatomic distances for the two energetically most favourable Y atomic string candidate structures in Fig. 6.26. For the Si-Si distances, the label *I* (*II*) refers to the Si atoms on either side (the same side) of the Y chain, while for the Y-Si distances, the label *I* (*II*) refers to the Si atoms in the uppermost layer (second layer from the top) for the substrate.

Distances	A Type, Hollow / Å	Haiku, Hollow / Å
$\|Si - Si\|_I$ / Å	3.71	3.872 - 3.932
$\|Si - Si\|_{II}$ / Å	3.812	3.793 - 3.857
$\|Y - Si\|_I$ / Å	2.877 - 2.921	2.918 - 3.005
$\|Y - Si\|_{II}$ / Å	2.731 - 2.735	2.745 - 2.775
|Y - Y| / Å	3.84	3.759; 3.920

the wetting layer in energy by 0.3 - 0.4 eV. While this result is discouraging, there are indications that neither of these two string configurations have been fully optimized: for both configurations, a slight buckling of the Y chain is obtained, with differences in the Y-Si distances for the Si atoms in the uppermost layer of 0.02 - 0.03 Å for the A_H configuration, the corresponding values being slightly smaller for the H_H configuration. We expect that this buckling is associated with strain relief, with a similar behaviour observed in the calculations on the vacancy free Y disilicide nanowire structures, in particular the wire comprised by an Y layer only, discussed in Sec. 6.2.5.1. Furthermore, the entropy terms for the A_H and H_H configurations are significantly larger than the entropy term for the A_C configuration, where no Y atom buckling is obtained, indicating the presence of a structural instability for the configurations with Y atoms at Hollow sites. On the face of it, the presence of significant strain along the Y atom string direction is rather surprising, considering the growth site discussions in part A of this subsection. We shall attempt to clarify this issue in Sec. 6.3.3, postponing a discussion of the implications of the apparent Y chain instability until that point.

In summary, the theoretical studies of Y atomic string candidate structures performed in the present work has strongly supported the suggestion that the Hollow site for the A Type and Haiku structure is a highly favourable growth site for the deposited Y atoms. The studies also show, however, that the energy cost for creation of the Haiku structure is only just balanced by the energy gain when adsorbing Y atoms on the chains of Hollow sites, the formation energy for this configuration being within 0.1 eV/Y atom of the Y/Si(001) 2×4 wetting layer formation energy. For the A Type, Hollow site configuration, the energy is 0.3 - 0.4 eV higher. The calculations have employed unit cells containing only two Y atoms along each chain and there are suggestions, both from experiment (see Sec. 6.3.1.1) and theory, that this cell is too small to describe satisfactorily the string structure. We shall discuss this and other issues further in Sec. 6.3.3 where we shall evaluate the suggested connection between the Y atomic strings and the A Type and Haiku structures on the basis of the theoretical studies performed so far and make suggestions for further studies to be performed.

6.3.3 OUTLOOK: ON MISSING KEY INGREDIENTS IN THE THEORETICAL MODELLING OF Y ATOMIC STRINGS ON THE Si(001) SURFACE

The theoretical studies of Y atomic string candidate structures presented in Sec. 6.3.2.3 have verified, on one hand, that adsorption of Y atoms at the Hollow site for the A Type and Haiku structures is highly favourable. On the other hand, none of the string candidate structures have been found to be lower in energy than the Y/Si(001) 2×4 wetting layer, the current studies therefore not supporting formation of Y atomic strings adopting any of the structures described in Fig. 6.25. We are thus, still, at the end of the preliminary studies performed in this work, faced with the question whether there is actually a relation between the Y atomic strings observed in the experiments by Owen as discussed in Sec. 6.3.1.1 and the A Type and Haiku structures. The discussion in the present subsection will focus on the reasons for continued interest in this relation, but we emphasize at the outset that this choice of presentation is to be regarded as an attempt to clarify the incompleteness of the theoretical studies performed so far rather than an unambiguous support for the strings being somehow explained by these local reconstructions of the Si(001) surface. Indeed, any alternative model which can explain the straightness and atomic width of the Y atomic strings while furthermore (with the importance depending on the energy required to create this string template) presenting a favourable growth site for the deposited Y atoms must be considered a potential candidate for the structure of the Y atomic strings on Si(001) as well, considering the present level of experimental information on these systems. With these remarks in the back of our minds we continue to evaluating the relevance of the A Type and Haiku structures to the theoretical modelling of the Y atomic strings on the Si(001) surface. [104]

The theoretical results presented in Sec. 6.3.2.3 revealed a significant energy difference between configurations differing by the choice of growth site for the Y atoms: the formation energy of the configurations with Y atoms at the Hollow site on either the A Type or Haiku structures were found to be lower in energy by an impressive 1 - 1.5 eV/Y atom compared to the corresponding configurations with the Y atoms at the Cave site (see Fig. 6.26). This supports the suggestions made in Sec. 6.3.2.1 that the Hollow site is the most favourable growth site for the Y atoms for these structures, but it obviously does not serve as a proof. A more elaborate study of the Y atomic string candidate structures, even within the assumption that these structures were explained by the A Type and Haiku structures, would involve calculating the formation energy of configurations with Y atoms at other relevant adsorption sites on these local reconstructions. Fig. 6.27 shows potential candidates for such alternative adsorption sites for the A Type and Haiku structure related configuration. The seemingly most interesting suggestion is the pairs of Y chains on the A Type structure, where each Y atom is adsorbed on a growth site which resembles the Pedestal site for clean Si(001) but with

[104] In the discussions below in the text, we shall not mention construction of theoretical STM images for comparison with the experimental results as a way of supporting one string candidate structure over another. This does not mean that we do not recommend construction of these images for the present studies but rather that the problem at hand at the present stage is essentially more basic, the studies in Sec. 6.3.2.3 not providing us with a single truly justifiable candidate structure for the Y atomic strings.

the distance between Si atoms along the Si dimer row direction being significantly increased, leading to the creation of a growth site which is structurally rather similar to the local environment for the bulk vacancy free AlB_2 structure. This configuration offers an alternative explanation to the pairs of Y atomic strings in Fig. 6.23, both the single string and the pairs of strings now being explained by the A Type structure. Such an argument has the appeal that it is comparatively much more easy to change a growing pair of strings into a single string: thus, if the Y atom strings and pair of strings are actually both explained by the A Type structure, the pair of strings might simply typically be unstable with respect to the Y atoms moving to the Hollow sites (we shall discuss this suggestion further below). We regard the alternative Y adsorption sites for the Haiku structure in Fig. 6.27 as comparatively less interesting, primarily as the creation of this huge local reconstruction seems difficult to explain on the basis of any of these assumed alternative string structures. [105]

As discussed in Sec. 6.3.2.3, there are suggestions that the unit cells used for describing the Y atomic string candidate structures investigated so far are too small for the description to be truly satisfactory. The problem is not connected with the separation between the nanostructures, where good convergence in the formation energies have been obtained, but in the fact that there are only two inequivalent Y atoms along the chain direction with this choice of cell. Both the A_H and H_H configurations show clear signs, in *(i)* the band structure, through the appearance of a large entropy term for the optimized structures, as well as *(ii)* the ionic structure, through buckling of the Y atoms along the chain, of an inherent structural instability, with the fully optimized structure presumably requiring a larger unit cell along the string direction. The strain along the Y chain direction, as mentioned previously, is somewhat surprising. We shall discuss an expected reason for the appearance of this strain below but note beforehand that, on a very basic level, this could be an indication of a configuration with full occupancy of Y atoms at all Hollow sites, i.e., a proper atomic string, being energetically unfavourable. Indeed, suggestions have been made [173] that the occurence of dark features around the experimentally observed Y atomic strings in Fig. 6.23 and typically separated by 4 Si(001) surface lattice parameters might be connected with strain relief as obtained by not depositing an Y atom at the growth site for the string next to this feature. [106] It is also possible, though, referring to the suggested explanation for the dark features made in Sec. 6.3.1.1, that complete optimization of these configurations requires simply increasing the size of the unit cell along the Y chain direction by a factor two, choosing complete occupancy for the Y atoms at the Hollow sites. In

[105]The above considerations do not involve substitutional Y as we have basically found it difficult to see how a favourable growth site for Y can be connected in this way with either of the local reconstructions. We did perform preliminary studies of an A Type related configuration where the innermost two lines of Si atoms along the chain direction were replaced by Y (with the Y atom thus forming three bonds with the Si atoms, in agreement with the generally expected trivalent nature of this element). This configuration, however, was found to be energetically highly unfavourable and we shall not discuss in further detail the results obtained from these studies. We also note that the above considerations have involved Y atomic string candidate structures with each Y atom adsorbed at an equivalent growth site. We believe that this simplification is reasonably well supported by the experimental information obtained already for the Y atomic strings, where no evident 'zigzagging' in the string structure has been reported.

[106]This suggestion has the inherent weakness, though, that the dark features are only often, not always, present at the same point on either side of the string.

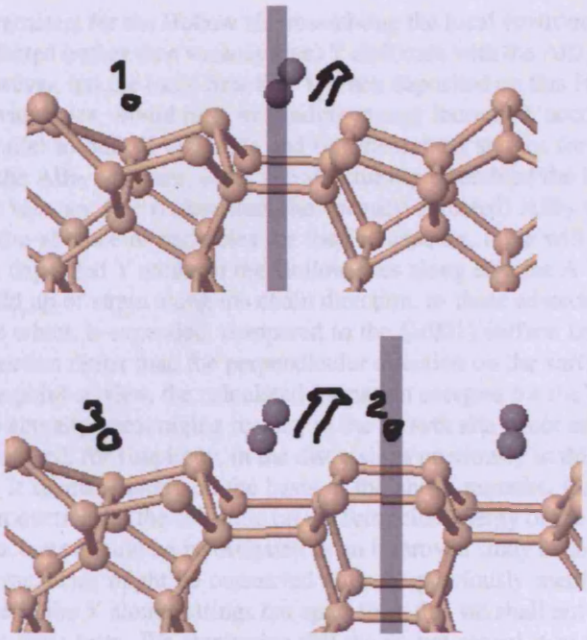

Figure 6.27: Schematic presentation of suggested alternative Y atomic string candidate structures, as obtained within the approximation that every Y atom is deposited at the same type of growth site. For each alternative structure, only one growth site has been pointed out and labelled in the figure. The white arrows in the figure refer to the growth direction of the atomic strings while the vertical lines show the centre of the symmetric reconstructions on the Si(001) surface.

any case, studying Y atomic string candidate structures with an incomplete occupancy of the Y atoms on the growth sites along the string will be useful for investigating the tendency for the Y atoms to both agglomerate and dimerize. Such studies therefore would be recommended for a more complete theoretical investigation of the A_H and H_H configurations.

The above mentioned dark features themselves are an indication that the unit cells used in Sec. 6.3.2 for the theoretical studies of the Y atomic string candidate structures are too short along the Y chain direction. In the above, we briefly discussed how this might be connected with the chosen occupancy of Y atoms at the Hollow sites for the A Type and Haiku structures being unfavourable. In the present discussion, we shall focus on the presence of Si vacancies for the substrate. When discussing in Sec. 6.3.2.1 the basic theoretical reasons for connecting the experimentally observed Y atomic strings with the A Type and Haiku structures we argued that in order for each Hollow site for these local reconstructions of the Si(001) surface to be both *(i)* as optimal a growth site for the deposited Y atoms as possible and *(ii)* connected with as little strain as possible along the growth direction of the Y atomic string, we would require structural

parameters for the Hollow site resembling the local environment for Y in bulk vacancy defected (rather than vacancy free) Y disilicide with the AlB_2 structure. This argument, however, has the basic flaw that Y, when deposited on this Hollow site, with no nearby Si vacancies, would have its binding energy increased, according to above mentioned parallel to bulk Y disilicide and our theoretical studies for vacancy free Y disilicide in the AlB_2 structure, if the site structurally resembled the local environment for Y in the vacancy free (rather than the vacancy defected) AlB_2 structure. In other words, in the absence of vacancies for the Si substrate, there will be a natural tendency for the deposited Y atoms at the Hollow sites along e.g. the A Type structure to lead to a build up of strain along the chain direction, as these adatoms actually prefer a growth site which is expanded, compared to the Si(001) surface lattice parameter, along this direction rather than the perpendicular direction on the surface. [107] Incidentally, from this point of view, the calculated formation energies for the A_H and H_H configurations are actually encouraging results, as the growth site is not as close to being optimal as presented, for simplicity, in the discussions previously in this section.

It seems evident, on the basis of the above remarks, that the effect of Si vacancy introduction for the substrate on the formation energy of the Y atomic string candidate structures should be investigated in an improved study of these systems. We note that Si vacancies might be connected with the previously mentioned dark features at the side of the Y atomic strings but apart from this we shall not go into further detail with this issue here. We emphasize that we do not regard it as unlikely, given the energy penalty for vacancy creation, that the Y atomic string is actually explained rather by a compromise between creating a truly optimal growth site for the deposited Y atom in the absence of Si vacancies and reducing the amount of strain along the chain direction which occurs as a result of this optimization process. [108]

In summary, the results of our calculations on Y atomic string candidate structures appear to support a connection between the experimentally reported Y atomic strings and the A Type and Haiku structures: while the isolated Y chains with each Y atom at a Hollow site for these local reconstructions of the Si(001) surface are not below the Y/Si(001) 2×4 wetting layer in energy according to our studies, there are theoretically well founded suggestions that fully optimized structures require larger cells along the Y chain direction. The Y chain formation as presented with our theoretical modelling can be regarded as a compromise between creating an optimal growth site for the Y atoms and reducing the resulting, in the absence of vacancies for the substrate, build up of strain along the chain direction. Throughout this section we have presented various possible ways of reducing this strain accumulation: on a very basic level, our main suggestions are *(i)* distortion of the substrate surrounding the Y chain, *(ii)* removal of a fraction of the Y atoms from the chain growth sites, and *(iii)* introduction of Si vacancies, presumably in the reconstructed area of the substrate. All these suggestions are

[107] We note, in an attempt to remove any potential confusion that might appear on comparing Fig. 6.2 and Fig. 6.24, that the Hollow site for the A Type structure has been rotated by 90° relative to the Si dimer row direction on the surrounding terrace compared to the situation for clean Si(001), as a result of this local reconstruction.

[108] It is interesting to note that for the pair of Y chains on the A Type structure discussed previously in this subsection, there should be no build up strain along the chain direction.

loosely related to the experimentally reported dark features surrounding the assumed Y atomic strings in Fig. 6.23. While further studies are clearly needed in order to verify which (if any) of these structural changes leads to the creation of an energetically favourable Y atomic string candidate structure, we regard the present theoretical results and the above considerations as good theoretical support for the experimentally observed Y atomic strings being explained by the A Type and the Haiku structure. Future studies should also investigate alternative growth sites for the Y atoms on the A Type and Haiku structures: we regard especially a configuration involving a pair of Y chains on the A Type structure as potentially interesting.

Chapter 7

SUMMARY AND CONCLUSION

- This album was a hard one to get through, physically, mentally, and emotionally: we really worked our asses off on this one.
T. Hamilton, Aerosmith (on the completion of 'Pump')

The thesis has discussed, as its first main topic, *ab initio* modelling of the interaction of Cu with the Si lattice, with emphasis on the Si(001) surface. The electronic configuration of isolated bulk Si interstitial Cu (Cu_i) has been investigated, motivated by disagreements between experiment and theory. We have found that Cu in Si is a shallow donor with a closed $3d$ shell. The experimentally reported Cu outdiffusion to the Si(001) surface has been explained by two mechanisms: *(i)* Cu is *attracted* to this surface solely due to the distortions of the Si environment introduced by the surface reconstruction. *(ii)* At the surface, outdiffused Cu is trapped due to Cu-Si bond formation due to the presence of dangling bonds on the surface. For Cu subsurface configurations, only the Cu $4s$ electron is involved in the bonding while for Cu on the surface Cu $3d$ - Si $3sp$ hybridization occurs. Comparison between theoretical STM images constructed for the outdiffused Cu configurations and experimental STM results for the Cu contaminated Si(001) surface has produced apparent support for our conclusions, these studies however being ongoing. Finally, we have performed preliminary studies into the issue of Cu trapping at Si(001) by calculating the formation energies for Cu_i at the Haiku structure under Bi nanolines on this surface.

The second main topic of the thesis has involved theoretical studies into the growth of rare earth (RE) metal disilicide nanowires on the Si(001) surface, with the focus being on the situation RE = Y. It is well established that these wires grow epitaxially on the surface, with the high aspect ratios explained by highly anisotropic surface/overlayer strain. Up to now, with very few exceptions in the literature, it has also been regarded as well established that the wires adopt the vacancy defected AlB_2 structure. We have argued, on the basis of calculations on vacancy free bulk Y disilicide, that the vacancy free AlB_2 structure should be considered a fully realistic candidate for the wire

structure. We emphasize that this structure differs fundamentally from the defective alternative, with the epitaxial growth model predicting wire growth in mutually perpendicular directions for these candidates. Our studies of Y disilicide nanowire growth on Si(001) have involved the vacancy free structure only. We have predicted stability of this wire structure relative to the Si and Y atom reservoirs on the surface and furthermore established a highly basic wire growth model which might be able to clarify, through comparison with experiment, which of the above wire candidate structures is the correct one. Finally, we have performed preliminary studies into (assumed) Y atomic strings observed in very recent experiments upon deposition of Y on the Si(001) surface.

Chapter 8

APPENDICES

- We don't have to converge everything to the edges of our toenails.
D. R. Bowler, 2007

8.1 THE CLEAN Si(001) SURFACE

8.1.1 GENERAL COMMENTS

Most of the theoretical studies performed in the present work have involved adatoms or even nanostructures on the Si(001) surface. At the outset of the detailed discussions of these calculations we shall therefore provide a very brief introduction into the properties, modelling, and studies of the clean substrate. We shall describe in Sec. 8.1.2 the details of the Si slab geometry most frequently used, discussing subsequently the convergence tests performed on this system, using the various theoretical descriptions employed throughout this work (see below). Furthermore, we shall extend this description to include slab geometries frequently used in our studies, introducing nomenclature used for brevity in those discussions.

All our studies of clean Si(001) performed in this work have involved the $p(2\times2)$ reconstructed Si(001) surface shown in Fig. 8.1. We shall make only a few brief remarks on the properties of this surface, providing a basic introduction to nomenclature used throughout the text. The very evident distortion of the uppermost layer for the surface in Fig. 8.1, with the detailed structure suggested originally by Chadi [176] and verified in low temperature experiments with STM by Wolkow [177], is fundamentally explained by the desire of the semiconductor surface to reduce the number of dangling bonds, even if this requires the introduction of a significant distortion of the surface geometry: upon bulk cohesion, Si (electron configuration [Ne]$3s^2 3p^2$) forms bonds with tetrahedral symmetry through sp^3 hybridization, leading to crystallization in the open diamond structure consisting of overlapping Si 'cages', each comprised by 12 Si atoms (see Fig. 8.1). in the absence of a surface reconstruction, the bonds between the Si atoms in the uppermost layer and the second layer atoms would be vertical in the left part of Fig. 8.1, and each atom in the uppermost layer would form a total of only

two bonds, each bond with the atoms from the lower layer and thus have two dangling bonds (unpaired electrons).

The most basic part of the surface reconstruction is the dimerization of Si atoms from the uppermost layer: the energy gained by this bond formation is sufficiently high to pay the penalty associated with the significant movement of the two members of the dimer. The far more complex issue, and a matter of debate for years before the experiments of Ref. [177], is whether the surface reconstruction was to be regarded as 2×1 (flat dimer, two Si atoms in the unit cell along the [1-10] direction), $p(2\times2)$ (buckled dimer, i.e., with one dimer atom raised from the surface ['Up'] relative to the other ['Down'], with the buckling alternating along the dimer row, i.e., into the paper in the left part of Fig. 8.1), or a more complex reconstruction. For brevity, we shall only note here that experiment and theory points towards the $p(2\times2)$ surface reconstruction as providing a reliable description of clean Si(001). The buckling has the effect on the electronic structure that the lower lying Si atom is to regarded as forming approximate sp^2 bonds (as Si in graphite-like planes) while the bonds for the upper atom are much closer to having sp^3 character. On the clean Si(001) surface, the $p(2\times2)$ reconstruction is only evident at low temperatures, with the energy barrier being too low to pin the dimers, i.e., fix the buckling. The 'Up' and 'Down' atoms cannot be distinguished with STM at RT except in situations where e.g. defects pin the dimers, and the apparent surface reconstruction is 2×1.

All the theoretical studies of this work involving the Si(001) surface have been based on DFT [5, 6, 7] but otherwise separate into essentially four different sections: for the studies of Cu at Si(001), calculations used Vanderbilt US PPs [17] as implemented in the plane wave code VASP [23, 24], employing either *(i)* the LDA (using the parametrization by Perdew and Zunger [102] of the results obtained by Ceperley and Alder [9]) or *(ii)* the PW91 GGA [12] to the exchange-correlation functional E_{xc}. The basic computational details for these studies have been described in more detail in Sec. 8.2.1.

For the studies of *(iii)* Y on Si(001) (basic computational details described in Sec. 8.3.1), GGA calculations using the same theoretical framework as the Cu/Si(001) investigations were performed for the clean Si(001) surface, the plane wave energy cutoff however being comparatively lower (see Sec. 8.2.1 and Sec. 8.3.1 for further comments).

8.1.2 DESCRIPTION OF THE VARIOUS SLAB GEOMETRIES USED

Fig. 8.1 shows the Si(001) surface slab geometry most frequently used in the studies of the present work. We emphasize at the outset that the choice of model system is a supercell, i.e., periodicity has been imposed along the directions on the surface as well as in the direction perpendicular to the surface. This has important implications for the studies of e.g. adatoms on the surface (where, on a very general level, each adatom might feel the presence of adjacent adatoms unless the cell is sufficiently large), whereas for the clean surface, the center of attention in the following, the key task is to

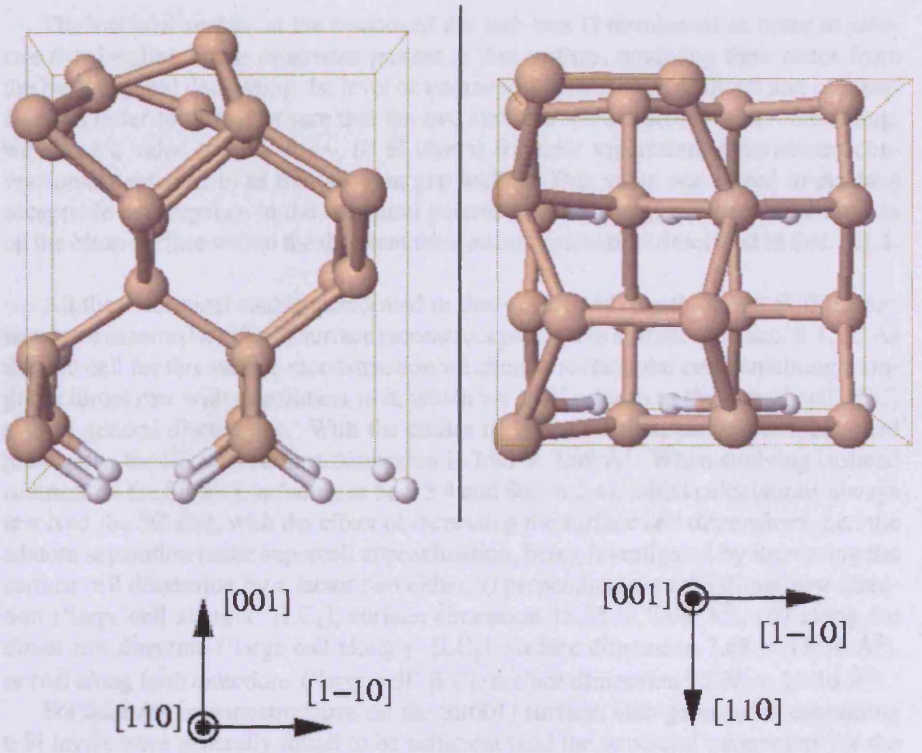

Figure 8.1: Schematic presentation of a typical supercell slab geometry used for the description of the clean Si(001) surface (vacuum gap ignored). See text for details. In the present work, we shall refer to this particular choice of geometry as the Si 6 layer SC slab.

ensure that the unphysical interaction between the real surface and the artificial surface at the other side of the slab is reduced to an essentially negligible level. We shall comment further on this issue below.

Along the z or [001] direction in Fig. 8.1, i.e., the normal to the Si(001) surface, the system consists of 6 layers of Si and 1 layer of H. In optimization, the coordinates of the five uppermost Si layers were always varied while for the sixth layer, they were kept fixed at the values for bulk Si, with the choice 5.43 Å (experimental value) for the Si lattice parameter. In order to clarify the importance of this assumption for the bulk Si conditions, we calculated the pressure on bulk Si as obtained using Vanderbilt US PPs as implemented in VASP, with the studies performed within the LDA as well as the GGA. The results of these calculations, discussed in Sec. 8.2.2, suggested only weak differences between the chosen value for the Si lattice parameter and the fully optimized results. [1]

[1] For simplicity, these calculations involved only the plane wave energy cutoff used with Cu present in the system, the cutoff for the calculations on Y/Si systems being lower. On the basis of the results of the studies

The artificial surface at the bottom of the slab was H terminated in order to saturate the dangling bonds otherwise present at this surface, removing their states from the band gap and decreasing the level of interaction between the artificial and real surface. In order to further ensure that the two surfaces were essentially noninteracting, we chose a value of 13.9 Å ($\sim$ 10 Si layers) for their separation, a parameter conventionally referred to as the 'vacuum gap width'. This value was found to produce acceptable convergence in the structural parameters and energies for test calculations on the clean surface within the different theoretical frameworks described in Sec. 8.1.1.

All the theoretical studies performed in this work involving the clean Si(001) surface have assumed a $p(2\times2)$ surface reconstruction for this surface (see Sec. 8.1.1). As the unit cell for this surface reconstruction we chose a rectangular cell containing a single Si dimer row with two dimers in it, which we shall refer to as the 'small cell' (SC) slab in general discussions. With the choice of bulk Si lattice parameter mentioned previously, the SC slab surface dimension is 7.68 $\times$ 7.68 Å^2. When studying isolated adatoms on the Si(001) surface (see Sec. 5.4 and Sec. 6.2.4), initial calculations always involved the SC slab, with the effect of increasing the surface cell dimensions, i.e., the adatom separation in the supercell approximation, being investigated by increasing the surface cell dimension by a factor two either *(i)* perpendicular to the dimer row direction ('large cell along x' [LC_x], surface dimension 15.36 $\times$ 7.68 Å^2), *(ii)* along the dimer row direction ('large cell along y' [LC_y], surface dimension 7.68 $\times$ 15.36 Å^2), or *(iii)* along both directions ('large cell' [LC], surface dimension 15.36 $\times$ 15.36 Å^2).

For adatoms or nanostructures on the Si(001) surface, slab geometries containing 6 Si layers were generally found to be sufficient (and the structural parameters for the uppermost layers for the clean slab were found to be converged with respect to the number of layers in the slab), whereas for the studies of subsurface configurations (see Sec. 5.3), slab containing a larger of Si layers were used.

---

of Sec. 8.2.2, we would expect the conclusions to be only very weakly changed by the relevant energy cutoff change, however.

8.2 COMPUTATIONAL DETAILS FOR CALCULATIONS INVOLVING Cu/Si SYSTEMS

8.2.1 GENERAL COMMENTS

The theoretical studies of Cu-Si interactions performed in this work divides into two categories: studies of *(i)* of isolated interstitial Cu in bulk Si and *(ii)* Cu near the Si(001) surface. While all calculations have been based on DFT [5, 6, 7] the studies performed for Cu in bulk Si, to be discussed in Sec. 8.2.2 and Sec. 8.2.3 have employed both the plane wave based code VASP [23, 24] and the pseudo atomic orbital based code Plato [28], for reasons described in Sec. 5.2.4, whereas the investigations of Cu near Si(001), to be discussed in Sec. 8.2.4, have been carried out using VASP only. All VASP studies used Vanderbilt US PPs [17] for the description of the Cu/Si system, with the $3d^{10}\ 4s^1$ ($3s^2\ 3p^2$) electrons included explicitly in the calculation for Cu (Si). Investigations of bulk Si Cu_i were performed within this theoretical framework using both the LDA (employing the parametrization by Perdew and Zunger [102] of the results of Ceperley and Alder [9]) and the PW91 GGA [12] to the exchange-correlation functional E_{xc} at an equal level, i.e., convergence of the energy and structural parameters was tested extensively for both situations. LDA calculations were also typically performed for the configurations with Cu near the Si(001) surface, but in these cases, the studies were performed as an addition to GGA studies where convergence had been tested more rigorously, assuming, on the basis of the studies of bulk Si Cu_i (see below for details), the same convergence properties for these two situations. We shall comment further below on the level of convergence in the various calculations performed. For the Plato studies, various basis sets were used, and we refer to Sec. 8.2.3 for a proper introduction to this issue. These calculations employed the parametrization of LDA by Goedecker, Teter, and Hutter [20].

Initial VASP based calculations for bulk Si Cu_i employed a 233.7 eV plane wave energy cut-off, the default value in the code for a system containing Cu and Si. Furthermore, a grid more coarse that the recommended one for the above setting was used with the chosen setting (referred to as 'medium precision' in the code). On examining the effect of varying both of these parameters for the above mentioned system, we learned (see Sec. 8.2.2) that, in particular, the use of a fine grid was crucial if very precise structural parameters and energies were desired (whereas for more general conclusions, the errors encountered were not critical). Essentially the same corrections were found to be needed for the LDA and GGA based calculations. We shall postpone specifying the fully converged values for the parameters of the code (including k mesh requirements) until Sec. 8.2.2.

As one of the key objectives of the Plato based studies of bulk Si Cu_i was to produce results at the same level of precision as a practically converged VASP LDA calculation for this system (see Sec. 5.2.4 for further remarks), convergence tests for these studies concerned only 'independent' variable parameters for this code, i.e., parameters where no direct comparison with the VASP result could be made, with the choice of k mesh and smearing scheme details being the same as obtained in the VASP studies

throughout this part of the work. We shall describe the Plato convergence studies in Sec. 8.2.3.

For the bulk of the studies of Cu near the Si(001) surface, we used the values for the initial bulk Si Cu_i studies in calculations, essentially in order to reduce the amount of time needed for each calculation to be performed. As the main aim of these studies was to clarify the energy variations (including their explanation) for Cu moving towards the Si(001) surface, we did not require rigorously converged formation energies and structural parameters: in addition, such a requirement was generally prohibited by the restrictions on the dimension of the supercell used in the calculations (see Sec. 8.2.4 for further comments). Preliminary convergence studies were performed, however, with the plane wave energy cutoff increased to 292.2 eV and the recommended grid associated for this energy cutoff (choices of values that would be expected to produce almost complete convergence regardless of the specific structural details of the Cu/Si system). These investigations revealed that the initial choice of precision was found to be well justified only for the Cu_i subsurface configurations where the electronic state of Cu did not differ appreciably from the situation with the impurity located in the bulk. For Cu within a few Si layers of the clean Si(001) surface, where actual Cu-Si bond formation was found to occur, the increase of precision lead to a significant lowering in the energies. As these studies were not entirely rigorous convergence studies, we have included in the discussion of the results to Sec. 5.3.2.3, where we summarized the conclusions for Cu outdiffusion to Si(001) as obtained from the studies of the present work. For remarks on the results of k mesh convergence studies (investigated for the calculations performed within the GGA, with the same k-point grid expected to produce acceptable precision for the LDA based studies), we refer to Sec. 8.2.4.

As discussed in Sec. 4.1.2, Cu_i in bulk Si is a shallow donor, the diffusing impurity therefore being positively charged, Cu_i^+ for all practical purposes. While the bulk of our calculations involved the interstitial Cu *atom*, Cu_i^0, the effect on the ionic and electronic structure when substituting Cu_i^+ for Cu_i^0 in calculations was investigated for the studies of bulk Si Cu_i. As *(i)* these discussions are closely connected with understanding the electronic state of Cu and *(ii)* as only relatively few Cu_i^+ calculations were performed, we have made the choice not to comment on this issue below, but to focus entirely on it in Sec. 5.2. The studies of Cu near the Si(001) surface did not involve the charged impurity, and we shall make only relatively brief comments on this issue in Sec. 5.3.2.3 when discussing the results of the bulk of these studies.

Finally, spin polarized calculations will not be discussed in the discussions below. Such calculations were performed both for bulk Si Cu_i and for a few of the configurations with Cu at the Si(001) surface, but in no cases were any significant effects of the structural parameters and total energies revealed. We concluded from these studies that spin polarization can be ignored for the Cu/Si systems under investigation in the present work.

8.2.2 INTERSTITIAL Cu IN BULK Si: VASP STUDIES

The results obtained from the VASP based studies of bulk Si Cu_i performed in the present work have been discussed in Sec. 5.2.3 with the present discussion clarifying how we arrived at these conclusions for the investigations involving the charge neutral impurity (for comments on bulk Si Cu_i^+, see Sec. 5.2.3). Both the initial GGA and LDA based studies of bulk Si Cu_i^0 (for brevity, we shall drop below the superscript denoting the charge state of the impurity), performed using Vanderbilt US PPs [17] as implemented in VASP [23, 24], employed a supercell geometry for the description of the system: a Cu atom was deposited close to a tetrahedral site in an otherwise clean, undistorted Si 64 atom cell with dimensions 10.86 × 10.86 × 10.86 $Å^3$ (i.e., a lattice constant of 5.43 Å), and all coordinates of the atoms were optimized subsequently. The chosen Si lattice parameter is the experimental value at ambient conditions. In both studies, we calculated the pressure on the clean Si cell for the choices of variable parameters in the code where acceptable convergence in the formation energy had been obtained (see below), this set of calculations resulting in suggested corrections of the lattice parameters by -0.024 Å and 0.039 Å for the GGA and LDA based studies, respectively. [2] These results show that the simplification of using a single lattice parameter throughout in the various studies of bulk Si Cu_i does not impose a critical restriction when considering comparison of the two sets of VASP results obtained, as we shall do below. As the studies of Cu_i near the Si(001) surface (performed within both the LDA and the GGA) described in Sec. 8.2.4 involved the VASP default value of 233.7 eV for the plane wave energy cutoff for a Cu/Si system, with only k mesh convergence being rigorously checked, we also calculated the pressure on the clean Si cell for the same of precision and using a (4, 4, 4) k mesh yielding acceptable convergence in the formation energy of bulk Si Cu_i at this level of precision regardless of the approximation to E_{xc} used. The lattice parameter corrections produced from these calculations differed negigibly from the above mentioned pair of results.

For the structural optimization of bulk Si Cu_i, focussing on the GGA based studies for the time being, we considered initially various starting points with Cu atom displacements away from the T site in the undistorted lattice towards one of the nearest neighbour Si atoms by up to 0.38 Å, where the number of next nearest neighbour Si atoms increased from 3 to 6. [3] In these calculations, a plane wave energy cutoff value of 233.7 eV and a (2, 2, 2) k mesh was chosen, with Sec. 8.2.1 providing further essential details on the basic computational details (we shall discuss these issues further below). On optimization, Cu moved back to a position very close to the T site, with insignificant differences between the structural parameters and energies for the various

[2] These values were obtained from including only the lowest order terms in a linear expansion of the expression for the bulk modulus, i.e., B = -V(ΔP/ΔV), with ΔV = V(3Δa/a), a being the lattice constant and Δa being the desired correction. This expansion was justified in both cases by the small calculated pressures of 10 - 20 kB on the cell. For B, we used the experimental value of 0.98 MB.

[3] As discussed in Sec. 5.2.3, we aimed at clarifying, through this approach, whether a structural instability similar to the one obtained in previous theoretical studies by Estreicher [56] of this system (see Fig. 5.1) could be reproduced in our studies. As no significant distortions of the Si lattice in response to the Cu movement were reported in Ref. [56], we made the choice to keep the Si lattice parameters unchanged at the onset of optimization, regardless of the initial Cu position.

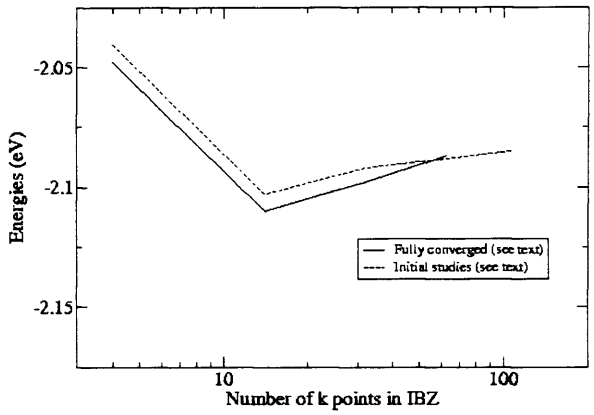

Figure 8.2: Total energies (relative to clean bulk Si) for Cu_i in a Si 64 atom supercell, as obtained in VASP calculations within the GGA, as a function of k-point density. The Cu-Si distances for the configurations are shown in Fig. 8.3. See text for details.

optimized configurations, but with a general scatter of ~ 0.03 Å in the Cu-Si distances. The optimized configuration showed a clear dependence, however, on the choice of T site in the supercell, with other choices leading to essentially no scatter in the Cu-Si distances (but hardly any difference in the formation energy, variations being within 0.005 eV). This result evidently pointed towards the precision in calculations being too low for the configurations to be described satisfactorily.

In order to determine the cause of the above described error, we investigated the effects of *(i)* increasing the plane wave energy cutoff and *(ii)* using a finer grid in calculations (see Sec. 8.2.1 for further comments), focussing on bulk Si Cu_i at the T site where the more significant scatter in the Cu-Si distances had been obtained in initial studies. These calculations revealed that the error is essentially eliminated if the grid mesh spacing was increased to the generally recommended value for a given value of the plane wave energy cutoff: Cu moves almost exactly to the T site for this choice of precision already when the energy cutoff is increased to 248.3 eV (see below for further details), whereas for the setting used in the initial studies described above, the scatter remains even for the highest energy cutoff value of 292.2 eV tested. For further discussions into this issue, we refer to Sec. 5.2.4.3.

Fig. 8.2 shows the variation in the formation energy of bulk Si Cu_i with k mesh density obtained using a plane wave energy cutoff of 248.3 eV and including the entire set of relevant electronic charge density components, while Fig. 8.3 describes the Cu-Si distances obtained in the same studies. The optimization results obtained at the level of precision described for the initial studies at the onset of this discussion have been

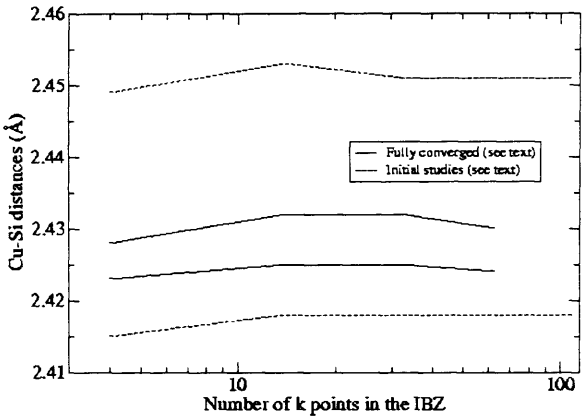

Figure 8.3: Optimized Cu-Si distances for Cu_i in a Si 64 atom supercell, as obtained in VASP calculations within the GGA, as a function of k-point density.

included as well in these figures, for reasons discussed in Sec. 8.2.1. We conclude from these results that, in both cases, acceptable convergence in the energy and structural parameters has been obtained at the (4, 4, 4) k mesh level. [4] In both studies, Gaussian smearing with a chosen width of 0.1 eV was used. Changing this smearing width in the high precision calculations generally was found not to affect the structural parameters of the configuration, with changes in the total energy being well within 0.01 eV in the (4, 4, 4) k mesh studies.

In summary, we conclude that fully converged results for bulk Si Cu_i in the GGA based studies involving the Si 64 atom supercell work have been obtained for a plane wave energy cutoff of 248.3 eV, including the entire set of relevant plane wave components for the evalations of the electronic charge density, and using Gaussian smearing with a chosen width of 0.1 eV and a (4, 4, 4) MP k mesh. The optimized configuration has Cu located almost exactly at the T site with the Cu-Si distances separating into three shorter distances of 2.425 Å and one longer distance of 2.432 Å, compared to the four distances of 2.351 Å obtained for Cu at T site for a nonrelaxed Si lattice. We shall discuss the convergence of the structural parameters with respect to cell dimension in Sec. 5.2.3.

For the LDA based studies of bulk Si Cu_i, calculations conceptually similar to those described above for the GGA based studies were performed. For brevity, we shall fo-

[4] As discussed in Sec. 5.2.3 and Sec. 5.2.5, the energy of bulk Si Cu_i is not converged with respect to cell dimension at the 64 Si atom supercell level with changes of a few hundredths of an eV obtained upon moving to a 216 Si atom supercell. For this reason, we have not used (N, N, N) k meshes with $N > 5$ to test rigorously the convergence of the total energy in particular.

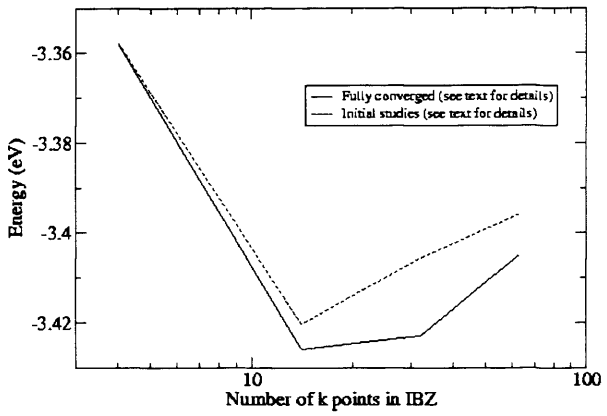

Figure 8.4: Same is in Fig. 8.2 but for VASP calculations performed within the LDA. Note the comparatively much lower energies (relative to clean bulk Si) . For comments on this issue, see Sec. 5.2.3.

cus in the following only on the key differences obtained between these two situations. Firstly, using the same level of precision as described above for the initial GGA studies, the structural parameters for the optimized configurations obtained within the LDA were found to be considerably less dependent on the choice of T site in the supercell, with the scatter in the Cu-Si distances obtained for a given configuration in these studies never being larger than 0.01 Å. This scatter was not reduced for the particular configuration investigated more closely by increasing the precision in calculations as described for the GGA studies (where the change in the total energy upon a reduction of the smearing width to 0.05 eV was found to be so important that this choice of width, rather than the value of 0.1 eV for the GGA studies, was used in the calculations of Fig. 8.4 and Fig. 8.5). However, on the basis of the clear similarities in the convergence properties of both energy and structural parameters for the LDA and GGA based studies, as evidenced when comparing the results in Fig. 8.4 and Fig. 8.5 with the corresponding GGA conclusions above, we did not investigate this issue further.

In summary, fully converged results for bulk Si Cu_i in the LDA based studies involving the Si 64 atom supercell work have been obtained for a plane wave energy cutoff of 248.3 eV, including the entire set of relevant plane wave components for the evalations of the electronic charge density, and using Gaussian smearing with a chosen width of 0.05 eV and a (4, 4, 4) MP k mesh, i.e., the same choices of parameters as obtained from the studies within the GGA, with exception of the smearing width only. The optimized configuration has Cu located almost exactly at the T site with the Cu-Si distances separating into one shorter distance of 2.408 Å and three longer distances of 2.416 Å.

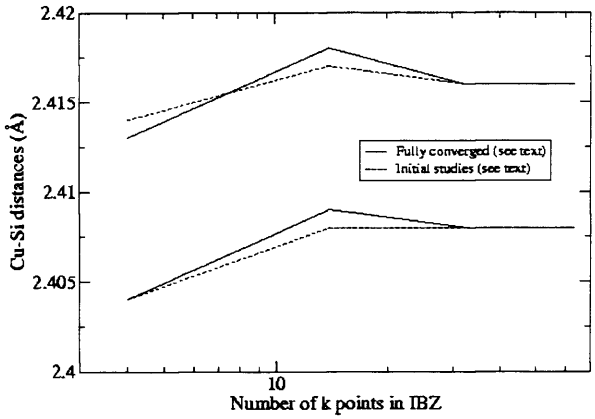

Figure 8.5: Same as in Fig. 8.3 but for VASP calculations performed within the LDA. Note the slight reduction in the Cu-Si distances (greatly exceeding the scatter in these distances) as obtained within this theoretical framework.

8.2.3 INTERSTITIAL Cu IN BULK Si: PLATO STUDIES

The key targets for the Plato based studies of bulk Si Cu_i performed in the present work have been indicated at the beginning of Sec. 5.2.4: *(i)* we wanted to perform a population analysis using a fully converged basis set, i.e., results with expected close similarity to the VASP LDA studies described in Sec. 8.2.2. Furthermore, *(ii)* we wanted to study results obtained with a basis set highly similar to that used by Estreicher *et al.* [56] in the theoretical studies of bulk Si Cu_i^+ performed using the SIESTA code. As discussed in Sec. 5.2.3, the close similarity between the results obtained for Cu_i^0 and Cu_i^+ in bulk Si in the studies performed within the LDA using VASP suggests that it is not crucial to study the charged impurity in the Plato studies, even though this was the choice in Ref. [56]. This issue has been discussed further in Sec. 5.2.4 where a more rigorous justification for the similarity of the results obtained for these two systems has been provided. For this reason, all the studies discussed in the following involve charge neutral Cu_i in bulk Si. In the following, we shall provide an introduction to the various basis sets used in the Plato based calculations, focussing subsequently on the choices of variable parameters for the code yielding acceptable convergence in the structural parameters and energies. Further interpretation of the various results described below has largely been included in Sec. 5.2.4.

In order to meet the above described targets, the Plato calculations have involved four different basis sets. The first two were single numeric (one set of *s* and *p* orbitals, *s* and *p* in shorthand notation, for the Si atoms, and *d* and *s* for the Cu atom), differing only in the choice of cutoff radius r_c for the basis functions (the values 5.5 and 6.0

a_0 have been used). We will refer to these sets as $SN_{5.5}$ and SN_6, respectively, below, and in the discussions of Sec. 5.2.4. Inclusion of these basis sets served two purposes: *(i)* a single numeric basis set was useful for evaluating the level of convergence for the expected fully converged (see below) basis set. In addition, *(ii)* the dependence on the ionic and electronic structure of the configuration on the extension of the orbitals was investigated using these sets, for which calculations were comparatively less time-consuming. As noted in Sec. 5.2.1.1, the orbital cut-off radius in the calculations of Ref. [56] was even shorter than the above values, 5.0 a_0 (we shall comment further on this difference below).

A double numeric plus polarization basis set (s, p, s^*, p^*, d^* for the Si atoms, [5] d, s, d^*, s^*, p^* for the Cu atom) with r_c = 6.0 a_0, referred to as DNP below and in Sec. 5.2.4, was used in order to obtain results sufficiently reliable for a population analysis. A basis set of this type but with r_c = 7.0 a_0 has been shown to give results with the desired accuracy (comparing with results of plane wave based calculations) for both bulk Si and Al, [28]. We emphasize that this does not rigirously justify the chosen Si basis set being fully converged, these results indicating, rather, that the number of orbitals for a DNP basis set add a sufficiently large degree of freedom for the modification of the electronic charge density upon bulk condensation to be described to an acceptable level of precision for both metallic and semiconducting systems. On a more basic level, but also more specific to the present situation, there is very good reason to include a p^* orbital for the Cu basis set, considering that an atom located at the T site in the Si lattice (the situation for Cu_i in Si according to our VASP LDA studies of this system, see Sec. 8.2.2) should experience some degree of distortion of its charge with tetrahedral symmetry. The choice of a shorter range for the orbitals for the DNP basis set employed in the present work, compared to the DNP basis sets discussed in Ref. [28], was made primarily to reduce the time needed to perform the structural optimization, but also, this made comparison with the results obtained with the SN_6 basis set more justifiable. We shall comment further on the completeness of this basis set in Sec. 5.2.4.1.

Finally, a basis set similar to that used by Estreicher in the SIESTA calculations described in Ref. [56]was constructed. Following the information in this paper (see also Sec. 5.2.1.1), the Si atoms in the 'cage' surrounding the Cu atom were treated differently from the other Si atoms: for the former (latter), the chosen orbitals were s, p, s^*, p^*, d^* (s, p, s^*, p^*), i.e., a larger basis set was used for the Si atoms closer to the impurity. For the Cu atom the chosen orbitals were d, s, p, s^*, p^*. A cutoff radius of 5.5 a_0 was chosen for this basis set. This value is larger than Estreicher's choice of 5.0 a_0. However, since the extension of the Plato orbitals in practice had to be slightly shortened (through multiplication by the function $s(r) = 1 - \exp[-(r-r_c)^2/2\sigma^2]$, [6] see Ref. [28, 178]for details) in order to obtain convergence in optimizations, this difference is not regarded as severe. We shall refer to this basis set as DN/DNP below and in Sec. 5.2.4.

For optimal comparability of the results of the Plato studies with the fully converged bulk Si Cu_i configuration obtained in the VASP LDA studies of Sec. 5.2.3,

[5] The orbitals with an asterisk were calculated for the Si^{2+} and Cu^{2+} ions (see Ref. [28] for further remarks).

[6] In our calculations, we chose the value of 1.2 a_0 for σ.

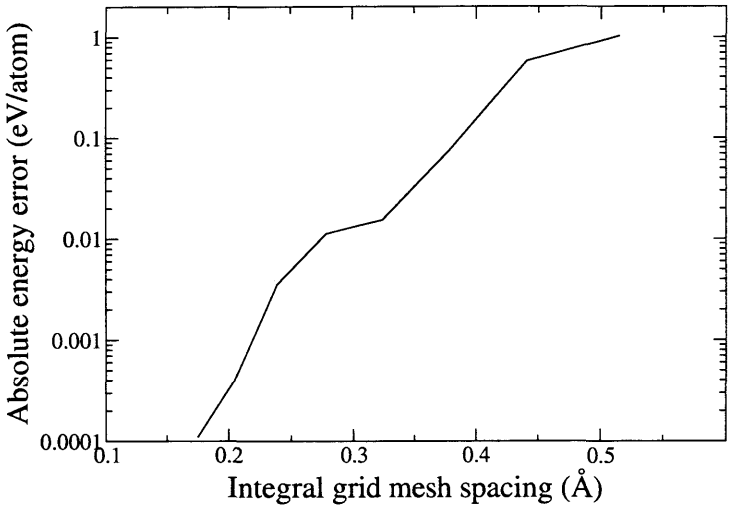

Figure 8.6: Absolute energy error (logarithmic scale) as a function of integral grid spacing for the unrelaxed 8 Si atom cell with a Cu atom at the tetrahedral site according to the Plato studies (see text for details). Zero energy error is defined here as the energy for the system obtained with the lowest integral grid spacing of 0.150 Å investigated.

we employed the same supercell geometry, depositing a single Cu atom near a T site for a Si 64 atom supercell with a chosen lattice constant of 5.43 Å as previously. [7] Furthermore, in all calculations, we chose the Gaussian smearing scheme with a 0.05 eV width and a (3, 3, 3) MP k mesh, these choices of parameters producing almost fully converged structural parameters and formation energy in the VASP studies (see Sec. 8.2.2). Finally, the same tolerance of 0.01 eV/Å to each component for the forces on the ions at the point of convergence in optimizations was chosen.

In order to fully determine the precision for a given Plato calculation, we also have to specify the spacing of the integral grid where orbitals and integrals are evaluated for this code [28]. Our initial investigations into this issue involved structural optimization of clean bulk Si and Cu systems with the $SN_{5.5}$ and SN_6 basis sets, with one atom in the smallest cubic unit cells for these systems moved slightly away from its preferred position at the onset of calculations. These studies revealed that optimization produced the desired structure only for sufficiently fine grids (we shall postpone a detailed discussion until considering a Cu/Si system below), with a scatter of a few hundredths of an Å introduced in nearest neighbour distances for both systems for more coarse grids.

Calculations on Cu_i in a rigid 8 Si atom cell, performed using the basis set SN_6 and a (4, 4, 4) MP k mesh, provided further knowledge on the importance of using a very narrow spacing for the integral grid for reliable results to be obtained in the present studies. Fig. 8.6 shows the convergence of the energy with respect to this grid spacing

[7] As mentioned in Sec. 5.2.3, the same cell was used for the studies of bulk Si Cu_i^+ by Estreicher in Ref. [56].

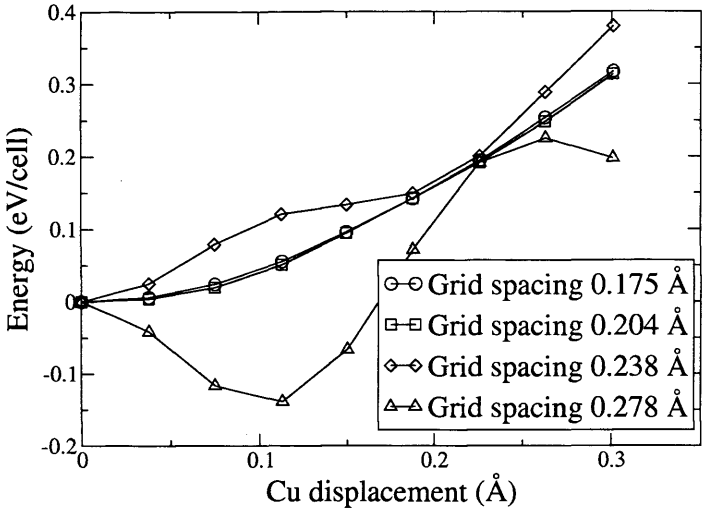

Figure 8.7: Energy as a function of Cu atom displacement from the tetrahedral (T) site towards a nearest neighbour Si atom in an unrelaxed 8 Si atom cell according to the Plato studies (see text for details) for a series of different integral grid spacings. Each set of energies are relative to the energy of the configuration with Cu at the T site. Note that the curves obtained with the two finest grids basically fall on top of each other.

for the configuration with Cu at the T site. Fig. 8.7 shows how the energy varies as the Cu atom is moved away from the T site directly towards a nearest neighbour Si atom for a series of different grid spacings.

It is evident from these results that the energy will have to be converged to better than 3 meV/atom (estimated energy error obtained with a grid mesh spacing of 0.238 Å). When this criterion is fulfilled, the minimum energy for the set of configurations in Fig. 8.7 is located at the T site with no signs of other local minima. [8] When the energy is not converged because the chosen mesh is too coarse, ripples will develop in the energy contour landscape. The T site configuration will become unstable, with the preferred off-center movement of the Cu atom as well as the gain in energy with respect to the T site configuration increasing with the mesh spacing. As shown in Fig. 8.7, there is a series of local minima as Cu is moved away from the T site, but it appears that the depth of these minima (calculated with respect to the smooth converged curve) is constant for a given grid mesh spacing. [9] As a consequence, it is always the minimum with the

[8] In particular, a movement of the Cu atom away from the T site along the chosen direction was found to increase the energy of the configuration monotonically even for Cu movements beyond 0.38 Å, i.e., the Plato calculations for Cu_i in the Si 8 atom supercell did not support the presence of the structural instablity for this system discussed in Sec. 5.2.1.1 (see Fig. 5.1). Similar calculations for Cu_i in a Si 64 atom supercell performed using the SN_6 and DN/DNP basis sets did not produce any signs of a structural instability either, with the DN/DNP energy contours around the T site being clearly ($\sim$ 50%) weaker, however. For further comments on this issue, see Sec. 5.2.4.3

[9] On the basis of this result, we suggest that the ripples should be explained essentially by the precision

Cu atom closest to the T site which corresponds to the most favourable configuration. Very similar results were observed when the Si 64 atom cell was substituted for the Si 8 atom cell in the above calculations. On the basis of these studies, we have chosen grid spacings of 0.150 (0.175) Å for the basis sets with cutoff-radius 5.5 (6.0) a_0 in the structural optimizations described in Sec. 5.2.4.

8.2.4 Cu OUTDIFFUSION TO THE CLEAN Si(001) SURFACE: SUPERCELL CONVERGENCE

For the initial studies of the complete set of configurations with Cu_i near the Si(001) surface investigated in the present work (Sec. 5.3.2), we used a slab geometry conceptually equivalent (i.e., same choice of lattice constant, vacuum gap width, and number of Si layers with fixed ionic coordinates) to the one described for the clean Si(001) surface studies in Sec. 8.1, with a single Cu atom in each supercell describing an isolated Cu atom near this surface. In order to be able to model a sufficiently large number of configurations in this approach, the chosen slab geometry contained 10 Si layers. The chosen Si(001) surface unit cell was a $p(2\times2)$ unit cell, with surface dimensions of 7.68×7.68 Å^2 (see Sec. 8.1). For simplicity in the discussion below, we shall use the nomenclature 'SC', as defined in Sec. 8.1 for this choice of surface unit cell, referring to the above system as the 10 layer SC slab. In the following, we shall present initially the various Cu_i near surface configurations investigated in the present work and the choice of precision in the studies performed. Subsequently, we shall discuss our investigations into the convergence of the formation energies for these configurations with respect to cell dimension, showing that the results for the Cu outdiffusion to clean Si(001) presented in Sec. 5.3.2 hold true also for the situation where the Cu atom is truly isolated.

The complete set of configurations with Cu_i near the Si(001) surface studied in the present work is schematically presented in Fig. 8.8. The position of the Cu atom as described in this figure refers to the choice at the onset of structural optimization of the configuration in question: our studies of bulk Si Cu_i(see Sec. 5.2.3), as well as other theoretical studies of this system [60], have suggested that Cu is located exactly at the tetrahedral site in the diamond structure. On the basis of this conclusion, we introduced a Cu atom for a given near surface configuration approximately at the center of the corresponding Si 'cage' near the Si(001) surface, expecting this choice to describe fairly well the completely optimized configuration. As will be clarified below, this was found to be the case for all but one of the configurations.

The cages near the surface are generally slightly distorted versions of the bulk Si cage, due to oscillating strain introduced by the surface reconstruction. The only exception is the last cage before the surface, right below the Si dimer bond, which is significantly smaller, being comprised of 9 rather than 10 atoms. The configuration with Cu in this cage is labelled distorted T site (DT). Those of the remaining configurations

in calculations being so low that the total energy can be determined only within a range of the correct value, the errors being largest at the extremal values of the oscillation curve. For further comments on this issue, we refer to Sec. 5.2.4.2.

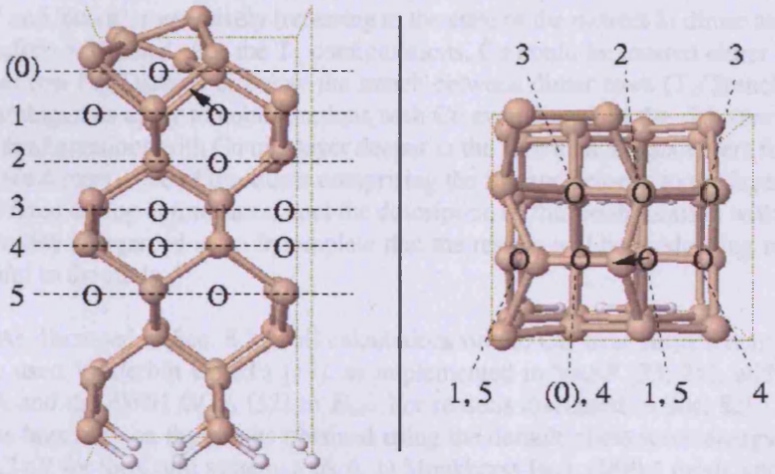

Figure 8.8: Schematic presentation of the configurations with Cu_i near the Si(001) surface investigated in the present work. The figure on the left shows a side view of the Si slab geometry used in calculations (vacuum gap excluded in the presentation), with the Si(001) surface being the uppermost layer for this cell. The figure on the right shows the same cell in top view. The Si atoms are represented by light brown spheres in the figure while the H atoms are represented by white spheres. The initial Cu atom positions for the various configurations investigated have been emphasized with circles in both figures. For simplicity, the full nomenclature for these configurations has not been described here (see text for details). Rather, only the approximate distance between the Cu atoms for these configurations and the surface, as determined by specifying the number of Si layers between the layer approximately at level with Cu and the uppermost layer of the slab (used for the configuration nomenclature), has been specified by the horizontal dashed lines and the numbers in the left figure. For the position of Cu to be fully specified, the same labelling has been used in the right figure. The arrow in both figures emphasizes the large movement of the Cu atom in question away from its initial position (discussed in further detail in the text), with remaining configurations being considerably less affected.

where Cu stayed close to the T site upon optimization would all be labelled T, with two additions: *(i)* a subscript specifying the number of the T site (DT excluded) containing the Cu atom as counted from the Si(001) surface (see Fig. 8.8) and *(ii)* an additional description in parentheses in situations where further ambiguities were present. Two such cases were encountered: for the T_1 configurations, the buckling of the nearest Si dimer were found not to be suppressed by the presence of the Cu atom. Two inequivalent configurations T_1(U) and T_1(D) , where 'U' and 'D' is shorthand notation for 'up' and 'down', respectively (referring to the state of the nearest Si dimer atom) could therefore be defined. For the T_3 configurations, Cu could be located either below the dimer row (T_3(Dimer)) or below the trench between dimer rows (T_3(Trench)). Similar ambiguities apply to configurations with Cu even deeper in the slab (see Fig. 8.8). For configurations with Cu one layer deeper in the slab than T_5 (six layers from the Si surface dimers), one of the atoms comprising the Si cage belongs to the layer which is kept fixed during optimization, and the description of this configuration with the Si 10 layer slab is regarded as so incomplete that the results will be misleading rather than helpful to the study. [10]

As discussed in Sec. 8.2.1, all calculations on the Cu_i near surface configurations have used Vanderbilt US PPs [17], as implemented in VASP [23, 24], with both the LDA and the PW91 GGA [12] to E_{xc}. For reasons discussed in Sec. 8.2.1, we shall focus here only on the results obtained using the default plane wave energy cutoff of 233.7 eV for the Cu/Si system, a (6, 6, 1) Monkhorst-Pack (MP) k mesh, and a setting in VASP which does not include the entire set of relevant plane wave components in the evaluation of the electronic charge density (see Sec. 8.2.1 for details). We do not believe that the effects of the change of precision discussed in Sec. 5.3.2.3 are of any significant importance to the considerations described below.

Optimization of the T_1(U) configuration defined as described previously in the text revealed that Cu remains near the T_1(U) site only for calculations using a (2, 2, 1) k mesh, while for studies using a (6, 6, 1) k mesh, this atom was found to move to a position approximately at the hexagonal face connecting the Si cages containing the T_1(U) and DT sites. We therefore renamed this configuration HF(Dimer).

The rest of this appendix concerns our investigations into the convergence in the calculated formation energies with respect to cell dimension, with calculations performed solely within the GGA: in order to explore theoretically a sufficiently wide range of configurations with Cu_i near the Si(001) surface for the properties of this surface as a sink for diffusing Cu to be fully revealed, we have made the choice, as described previously in this discussion, to perform studies using a 10 layer SC slab. As discussed in Sec. 5.3.2.1, these studies have revealed both *(i)* the long range nature of the mechanism attracting Cu to the surface and *(ii)* the short range of the actual trapping mechanism. However, in order to show that the well defined separation of these two regions suggested on the basis of these calculations is justifiable, we must consider the effect of the choice of surface dimensions, i.e., the separation between

[10] We shall discuss in Sec. 5.3.2.3 that already for the T_5 configurations, the formation energy of the configuration is affected significantly by the nearby presence of the fixed Si layer.

adjacent Cu atoms in the supercell approach, on the formation energies for configurations from both regions. Evidently, this supercell is generally too small for the impurity to be regarded as isolated, but our primary concern is not whether increasing the cell dimensions along the surface directions will significantly change the configuration formation energies. Rather, in order to truly verify that Si(001) is a highly efficient sink for an isolated interstitially diffusing Cu atom, we must require knowledge on whether the formation energies in the attraction and trapping regions defined in Sec. 5.3.2 are affected in significantly different ways by these changes.

The desired strategy for the study of the convergence of the formation energy with respect to cell size for the Cu_i near surface configurations can be separated into two steps: initially *(i)*, we shall investigate the variation of the formation energy for a given configuration with the number of Si layers in the SC slab. Subsequently *(ii)*, choosing a number of layers for the slab sufficiently large for the energy of this configuration to be almost converged with respect to this parameter, we want to study the change of the energy upon increasing the cell dimensions in the directions parallel to the surface, studying a LC slab (surface dimensions 15.36×15.36 Å^2, see Sec. 8.1) with the same number of layers. As will be discussed below, while this study can be carried out for all configurations in the trapping region, it is also feasible for the T_2 configuration, while furthermore, reasonable estimates for the fully converged energies of the T_3 configurations can also be obtained. As will be discussed below and in Sec. 5.3.2.3, this level of information provides us with sufficient knowledge to establish very definite conclusions on the properties of the clean Si(001) surface as a sink for isolated diffusing Cu_i.

In order to investigate the convergence of the formation energy with respect to the number of layers in the SC slab for the Cu_i near surface configurations in the attraction region, we have optimized the T_2 and T_3 configurations as described with the Si 8 and 10 layer SC slabs. The formation energies of the T_2, T_3(Trench), and T_3(Dimer) configurations upon increase of the number of Si layers from 8 to 10 decrease by 0.01, 0.05, and 0.07 eV, respectively. It seems evident that part of the reason for the variation in these energy changes can be explained by differences in the importance of remaining structural relaxations for these configurations at the 8 layer slab level: firstly, for the T_2 configuration, local structural parameters are very well converged at this level already: upon addition of two more layers to the slab, the change in the rms value for the Si-Si bond lengths in the cage surrounding the Cu atom ('size of the cage') is only 0.001 Å, the cage expanding slightly as expected upon addition of new layers to the slab. For the T_3(Trench) and T_3(Dimer) configurations, the corresponding values are 0.007 and 0.003 Å. Secondly, the movement of the uppermost Si atom in the cage relative to (away from) the bottom of the slab upon Cu insertion as obtained for the T_2 configuration described with the 10 layer slab has decreased by only 0.006 Å compared to the 8 layer slab result. For the T_3(Trench) and T_3(Dimer) configurations, the corresponding values (decrease) are 0.012 and 0.023 Å. The larger changes for the T_3 configurations are the expected consequence of Cu being located deeper in the slab, closer to the region where the Si environment is more affected by the addition of new layers. [11]

[11] If the Si cage surrounding the Cu atom is considered rigid (structural parameters well converged), the

Turning to an investigation of the electronic structure for the above set of configurations, we recall the conclusion obtained in Sec. 5.3.2.2 that the Cu_i near surface configurations in the attraction region have a highly delocalized Cu 4*s* state, all bearing a fairly close similarity to bulk Si Cu_i. Our studies of the electronic state of bulk Si Cu_i described in Sec. 5.2.4.2 suggest that the dispersion of the 4*s* level is still significant for a single Cu atom in a Si 64 atom supercell (a distance of 10.86 Å between adjacent Cu atoms) but almost eliminated at the 216 atom cell level (Cu separation 16.29 Å). For the T_2 configuration described with the Si 8 and 10 layer slabs, the distances between the Cu atom and the bottom of the slab are 6.5 and 9.2 Å, respectively. This suggests that slab geometry confinement of the Cu 4*s* level, leading to a decrease in the formation energy upon increase of the number of layers in the slab, would only have a weak effect on the formation energy for the T_2 configuration if the number of layers in the slab were increased beyond 10. Actually, as the decrease in the formation energy obtained for the T_2 configuration upon increase in the number of layers from 8 to 10 is already very small, 0.01 eV, it seems evident that slab geometry confinement of the Cu 4*s* level is unimportant for this configuration when described with an 8 layer slab.

Summarizing the investigations into the ionic and electronic structure for the T_2 and T_3 configurations, we conclude that the formation energy of the T_2 configuration is essentially converged with respect to the number of layers in the slab at the 8 layer slab level. Furthermore, considering *(i)* the similarity between the electronic state of Cu for these configurations and the fact that *(ii)* Cu is moved only one layer down in the slab for the T_3 configurations relative to the T_2 configuration, we suggest that the T_3 configuration formation energy is basically converged with respect to the number of layers in the slab at the 10 layer slab level.

In comparison with the configurations in the attraction region, we would expect the formation energies for the Cu_i near surface configurations in the trapping region to be more rapidly converging with respect to the number of layers in the slab: these configurations are characterized by Cu-Si bond formation involving the Cu 4*s* electron (see Sec. 5.3.2.2), leading to a higher degree of localization of the charge introduced with the insertion of Cu in the Si slab compared to the configurations in the attraction region. For all configurations in the trapping region, Cu moves away from the T site by a significant distance, reflecting the importance of the Cu-Si bond formation. This leads to larger distortions of the Si environment compared to the configurations in the attraction region. However, the changes obtained for the formation energies and structural parameters for these configurations upon increasing the number of layers in the slab from 6 to 10 suggest that structural relaxations converge quite fast in the direction away from the surface: the changes in the Si cage size obtained for the T_1(D) and DT configurations are 0.006 and 0.009 Å respectively, while for the HF(Dimer) configuration, the value obtained for the cage surrounding the T_1(U) (DT) site is 0.007 Å

change of the movement of the uppermost Si atom in the cage upon increase of the number of layers in the slab gives information solely on the importance of remaining structural relaxations deeper in the slab. This assumption breaks down for the T_3(Trench) configuration where the change in the size of the cage and movement of the uppermost Si atom for the cage are comparable. It does not, however, affect the conclusion that remaining relaxation effects for this configuration are clearly larger than obtained for the T_2 configuration.

(0.009 Å). In addition, the most important changes involve atoms closer to the surface than Cu. [12] The formation energies for the T_1(D), HF(Dimer), and DT configurations decrease by 0.04, 0.04, and 0.02 eV respectively. We conclude from these studies that the formation energies for the Cu_i near surface configurations in the trapping region are almost converged with respect to the number of layers in the slab at the 6 layer slab level.

On the basis of the above conclusions regarding the convergence of the formation energy with respect to the number of layers in the Si slab for Cu_i near surface configurations in the trapping and attraction regions, we have chosen a 6 layer (8 layer) SC and LC slab for our studies of convergence of the formation energy of the T_1(D), HF(Dimer), and DT configurations (T_2 configuration). [13] The distance between adjacent Cu atoms in the SC is 7.68 Å whereas for the LC, the separation has been increased to 15.36 Å. On the basis of our studies of bulk Si Cu_i in Sec. 5.2.4 and the previously mentioned similarity of the electronic state of Cu for the T_2 and bulk Si Cu_i configurations we would expect the dispersion of the Cu 4*s* level for the T_2 configuration to be almost eliminated at the LC level. As structural relaxations should be well converged before this point (although clearly not at the SC level, see Sec. 5.2.3), the formation energy for the T_2 configuration obtained with the 8 layer LC slab should be practically converged with respect to cell dimensions. In comparison with the 8 layer SC result, this energy has decreased by 0.22 eV. The energy changes (in all cases involving a reduction of the formation energy as well) obtained for the T_1(D), HF(Dimer), and DT configurations are somewhat smaller, 0.13, 0.13, and 0.20 eV, respectively. Studies of the changes in the structural parameters (for further comments, see Sec. 5.4.2.2) in the directions along and perpendicular to the dimer row for the T_1(D) and HF(Dimer) configurations suggest that the formation energies are practically converged with respect to cell dimensions as well in these situations, whereas for the DT configuration, this study did not provide us with sufficient information to draw conclusions about the level of convergence of the formation energy with respect to the separation of Cu impurities along the Si dimer row.

On the basis of the above studies of the convergence of the formation energies for the T_2, T_1(D), HF(Dimer), and DT configurations with respect to cell dimension, we have estimated the values for the fully converged (with respect to cell dimension) energies, relative to the practically converged energy for bulk Si Cu_i as obtained with the 216 Si atom cell (see Sec. 5.2.5), as obtained with the choice of precision in calculations described previously for the general Cu outdiffusion studies. At the chosen level of precision, the comparable (with regards to *k*-point grids, a (3, 3, 3) *k* mesh and a (2, 2, 2) *k* mesh being used for the 64 and 216 Si atom cell studies, respectively) bulk Si Cu_i energies for different choices of cell dimension suggest an increase in the formation energy of the impurity by 0.06 eV. These results have been included in Table 8.1.

[12] A study of the importance of remaining relaxations for the Si layers deeper in the slab than the Si cage containing the Cu atom has been avoided here as the Si-Si distances for the clean system are not sufficiently well converged at the 6 layer slab level.

[13] For all LC slab calculations, a (3, 3, 1) *k* mesh, producing the same *k*-point density as obtained using a (6, 6, 1) *k* mesh for the SC slab studies, was used, the choice of precision otherwise being the same as described above in the text for the general Cu outdiffusion studies.

Table 8.1: Energies for interstitial Cu (Cu_i) configurations near the Si(001) surface relative to bulk Si Cu_i as obtained in calculations for various slab geometries using VASP. The first column contains the energies obtained with a Si 10 layer SC slab (tabulated previously in Table 5.5). The second column contains the energies obtained with a Si LC slab containing either 6 (T_1(D), HF(Dimer), and DT configurations) or 8 layers (T_2 configuration). See text for details.

Configuration	E (10 layer SC) / eV/atom	E (cell converged) / eV/atom
DT	-0.99	-1.25
HF(Dimer)	-0.92	-1.11
T_1(D)	-0.71	-0.90
T_2	-0.42	-0.70

As will be discussed in Sec. 5.3.2.3, where the Cu outdiffusion results are summarized and evaluated, the energies in this table are not to be regarded as fully converged in all respects. From the present studies, we can only draw the conclusion that the separation of the trapping and attraction region is justifiable at the chosen precision in the above studies also when considering truly isolated Cu_i at the Si(001) surface.

8.3 COMPUTATIONAL DETAILS FOR CALCULATIONS INVOLVING Y/Si SYSTEMS

8.3.1 GENERAL COMMENTS

All our theoretical studies of Y/Si systems have employed DFT [5, 6, 7] as implemented in the plane wave code VASP [23, 24]. The calculations for bulk vacancy free Y disilicide in the AlB_2 structure, discussed in Sec. 8.3.2, have involved Vanderbilt US PPs [17], with the Y $4p$ semi-core states included either *(i)* explicitly in the calculations or *(ii)* in the PP (i.e., with only the Y valence electrons $5s^1\ 4d^2$ included explicitly), with extensive studies performed for both of these theoretical descriptions of this Y/Si system. The Si US PP included only the Si valence electrons $3s^2\ 3p^2$ explicitly. All studies have employed the PW91 GGA [12] to the exchange-correlation functional E_{xc}.

As discussed in Sec. 6.2.2.11 and in Sec. 8.3.2, the results obtained for bulk vacancy free Y disilicide in the AlB_2 structure show only little variation with the particular choice of theoretical description of a system containing Y and Si. In the remaining work performed on Y/Si systems, we have focussed our attention, therefore, on calculations employing the Vanderbilt US PP with the Y $4p$ electrons in the core, occasionally comparing with optimization results obtained upon including the Y $4p$ electrons explicitly in the calculation (we shall describe any such test calculations performed in more detail in the relevant parts of Sec. 8.3).

For the structural optimizations considered in Sec. 8.3.2, where the cell dimensions are varied, initial studies used the recommended plane wave energy cutoff values, defined as 1.25 $\times$ the VASP default value for the energy cutoff for a system containing Y and Si: unless otherwise noted in Sec. 8.3, the studies have been performed using the plane wave energy cutoff values obtained with this setting. For US PP based calculations, the energy cutoff value thus obtained is 188.3 eV, this value being determined in both cases by the presence of Si in the system (the Y plane wave energy cutoff being comparatively lower). In the calculations of Sec. 8.3.2, the recommended grid for the given value of the energy cutoff was chosen, as required in order to obtain reliable forces in a structural optimization where cell dimensions and cell volume are changed. The default choice of smearing scheme in the theoretical studies has been Gaussian smearing with a smearing width of 0.1 eV. Both the energy cutoff and the smearing width were varied for the two theoretical descriptions of Y disilicide considered in Sec. 8.3.2, in order to verify convergence of these parameters for each situation. We shall not summarize the results of these studies here, but refer to Sec. 8.3.2 for a brief description of the conclusions obtained, including remarks on the k mesh convergence. [14]

[14] As the studies described in Sec. 8.3 involve a series of different cells, with correspondingly different details for the k grids used and very few general remarks to make, we have made the choice not to summarize this topic at the outset of the discussion. We note that typically, Monkhorst-Pack k meshes have been used, the only exception being the structural optimization of the 3 atom cell unit cell for bulk vacancy free Y disilicide in the AlB_2 structure (and slightly distorted versions of this structure), where Γ centered k meshes are the recommended choice.

For the structural optimization of bulk Y disilicide with the $ThSi_2$ and $GdSi_2$ structures described in Sec. 8.3.3 and in Sec. 6.2.2.2, unless otherwise noted, the structural optimizations have employed the same choice of values for the plane wave energy cutoff and the smearing width as described above for the initial studies of bulk vacancy free Y disilicide in the AlB_2 structure. We refer to these parts of the thesis for information on the fully converged values for these parameters and results of k mesh convergence studies.

For the studies involving Y on Si(001) described in Sec. 8.3.4, 8.3.5, where *(i)* the structural optimization did not involve variation of the cell dimensions or shape and *(ii)* the system included H (the termination layer for the slab geometry), the initial studies were performed with the VASP default value for the plane wave energy cutoff, 200.0 eV, for the US PP based studies of a system containing Y, Si, and H. Furthermore, for the grid, the 'medium precision' setting, mentioned initially in Sec. 8.2.1, was used. The variation in the total energy and structural parameters with respect to changes in these choices was investigated for configurations with Y atoms on the Si(001) surface, with the results of these studies expected to be transferable to the other situations involving Y on Si(001): we refer to the discussions in Sec. 8.3.4 for details and to Sec. 6.2.4.2 for a brief presentation of the conclusions obtained in the convergence studies. For a full discussion of the k mesh convergence in these calculations, see Sec. 8.3.4, 8.3.5.

With the exception of the discussion in Sec. 8.3.5 of the calculations performed on the Y atomic string candidate structures, spin polarized calculations will not be mentioned below. Such calculations were performed in all of the studies described above but never found to have a significant effect on either structural parameters or the total energy of the system under investigation. For the bulk Y disilicide structures (including the Y disilicide nanowires), these results appear to be in agreement with the conclusion by Szwacki and Yakobson, [141] that the magnetic moment of the Y $4d$ electrons is quenched by the Y $4d$ - Si $3p$ hybridization obtained for the Y disilicide.

8.3.2 OPTIMIZATION OF BULK VACANCY FREE Y DISILICIDE ADOPTING THE AlB_2 STRUCTURE AND CLOSELY RELATED STRUCTURES

As discussed in Sec. 6.1, 6.2.2.3, bulk vacancy free Y disilicide in the AlB_2 structure and closely related atomic arrangements has been studied in this work using both the hexagonal primitive unit cell for the structure, shown in Fig. 6.1, and an orthorhombic unit cell, shown in Fig. 6.2 (a). The reasons for these choices of unit cells have been clarified in Sec. 6.2.2.3. The optimized structural parameters and energies for the system under investigation, as obtained using the two different theoretical descriptions of Y disilicide presented in Sec. 8.3.1, have been presented in Table 6.2 of Sec. 6.2.2.11, along with a full specification of the converged values for the variable parameters in the code required to obtain these results. The present part of the thesis discusses how we arrived at these conclusions.

Optimization of both of these systems in general allowed for variation in the an-

gles between basis vectors for the unit cells: for this reason, the above nomenclature 'hexagonal' and 'orthorhombic' is, strictly speaking, misleading, as it gives the impression that certain symmetry restrictions were always imposed in calculations. We shall clarify below whenever it is justifiable to e.g. describe the structure obtained in the optimization studies as the AlB_2 structure and otherwise refer to the two unit cells considered in the present study as the 3 and 6 atom unit cell, respectively, below.

The discussion below is organized as follows: at first, we shall describe the general optimization strategy which was followed in both studies considered. Subsequently, we shall present the structural optimization results obtained using Vanderbilt US PPs with the Y $4p$ electrons in the core, to which we have devoted the most attention: we shall compare the converged results obtained with the 3 and 6 atom unit cells and discuss any differences between the optimized structures. Finally, we shall compare the results obtained upon structural optimization using the Vanderbilt US PPs with the Y $4p$ electrons explicitly included in calculations with the results obtained in the first set of studies.

In general, for both theoretical descriptions of the bulk Y disilicide systems considered, two different types of structural optimization were performed for both the 3 and 6 atom unit cell systems. For the first choice of optimization, the ionic coordinates in the unit cell were held fixed, while all other structural parameters were varied. For the second choice, the ionic coordinates were optimized as well. There is no option in VASP for locking the symmetry of the structure under investigation and performing an optimization of the lattice parameters only. Strictly speaking, therefore, the first choice of optimization scheme mentioned above, when applied to the 3 atom unit cell, does not correspond to a complete optimization of the AlB_2 structure (which requires only lattice parameter optimization) but goes beyond this stage. However, as the optimized structure obtained in the actual studies was found to retain the AlB_2 structure symmetry with only insignificant deviations (see below), [15] in practice, for Y disilicide, this first optimization corresponded to a complete optimization of the AlB_2 structure. [16] The second choice of optimization scheme, on the other hand, is a truly complete optimization of both the 3 and 6 atom unit cell system, with Sec. 6.2.2.3 discussing the details of the full set of possible structures to be described in this study. We emphasize, in continuation of this discussion, that our present studies are not necessarily this complete: we have focussed only on atomic arrangements with structural parameters close to the values for the AlB_2 structure as we expect the Y disilicide nanowires to adopt a structure closely related to the AlB_2 structure. More specific details on our choice of strategy has been described below along with the presentation of the optimization results.

[15] This statement was found to hold true for the situations considered in this work where the optimization was started from a structure satisfying AlB_2 symmetry. The complete optimization of the 3 atom cell revealed a structural instability which was found to be partly retained if the positions of the ions in cell were kept fixed at AlB_2 structure values but with remaining structural parameters being those of the fully optimized configuration. This instability was found to be related to an insufficiently high number of k points in the IBZ, however, this additional remark therefore being of no practical importance.

[16] This comment justifies our remarks in Sec. 6.2.2.3 on the structural optimization of vacancy free Y disilicide with structures closely related to the AlB_2 structure, where the initial optimization results presented in Sec. 6.1 were described, for simplicity, as simply referring to the completely optimized AlB_2 structure.

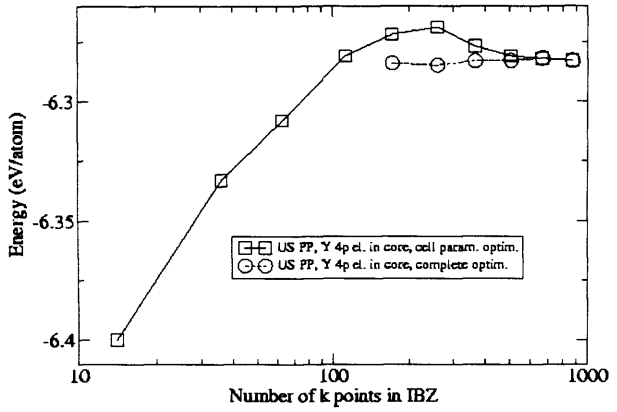

Figure 8.9: Total energies for bulk vacancy free Y disilicide in the AlB_2 and the OD AlB_2 structure (see text for details), as obtained upon structural optimization using Vanderbilt US PPs with the Y 4*p* electrons in the core, as a function of the number of *k* points in the IBZ (note logarithmic scale). For general comments on computational details, see Sec. 8.3.1. On the basis of these results and the optimized structural parameters in Fig. 8.10 we conclude that convergence in the total energy, with almost simultaneous disappearance of the structural instability, has been obtained for an (11, 11, 11) Γ centered *k* mesh (666 *k* points in the IBZ).

Fig. 8.9 shows the variation in the total energy of the Y disilicide 3 atom unit cell structure with the number of *k* points in the IBZ (squares in the figure) as obtained on optimization of the lattice parameters and basis vector angles in the US PP based calculations with the Y 4*p* electrons in the core. Fig. 8.10 shows the optimized lattice parameters for the unit cell as functions of the same parameter. The optimization was started from experimental lattice parameters [97] $a = 3.842$ Å, $c = 4.143$ Å for vacancy defected Y disilicide in the AlB_2 structure. As an AlB_2 structure was obtained for all *k* grids considered for this situation, [17] it suffices to include only the *a* and *c* lattice parameters for this structure in Fig. 8.10.

The 3 atom unit cell studies employed Γ centered (*N*, *N*, *N*) *k* meshes. As both the initial experimental and entire set of optimized theoretical *c*/*a* ratios are fairly close to 1, this choice leads to a reasonably homogeneously distributed set of *k* points in the IBZ. For the 6 atom unit cell calculations to be discussed below, MP (3*N*, 2*N*, 3*N*) *k* meshes were used. Once again, this choice generates a reasonably homogeneously

[17] In all cases considered, the difference in the length of the *a* and *b* lattice parameters for the monoclinic unit cell is within 0.001 Å while the angle between the basis vectors are well within 0.1° of their respective AlB_2 structure counterparts.

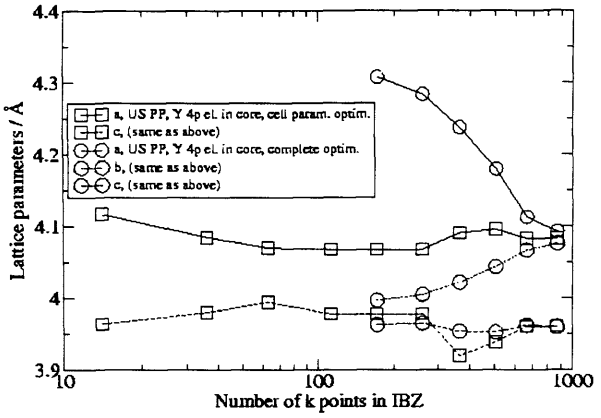

Figure 8.10: Optimized lattice parameters for bulk vacancy free Y disilicide in the AlB_2 and the OD AlB_2 structure (see text for details), as obtained upon structural optimization using Vanderbilt US PPs with the Y $4p$ electrons in the core, as a function of the number of k points in the IBZ (note logarithmic scale). The energies for these structures have been shown in Fig. 8.9. In addition to the parameters shown in the figure for the OD AlB_2 structure, the angle between the a and b basis vectors for this structure was found to change monotonically from 57.4° to 59.9° upon increasing the number of k points in the IBZ.

distributed set of k points in the IBZ: for the AlB_2 structure, the ratio between the a and b lattice parameters is $\sqrt{3} \sim 1.732$, which explains the chosen ratio of 3/2 for the number of k points along k_a and k_b direction in reciprocal space. [18]

We note, from comparison of Fig. 8.9 and Fig. 8.10, that relatively large variations in the lattice parameters are obtained even at the point where the variation of the total energy with the number of k points is quite weak, with only an apparent convergence of these parameters at the (8, 8, 8) k mesh level. [19] For this reason, we took great care to ensure that convergence had actually been reached at the (11, 11, 11) k mesh level, where both lattice parameters and total energies appeared to stabilize. As optimizations performed at more dense k grids did not lead to any changes in the lattice parameters,

[18]For simplicity, this discussion does not consider the distortions of the AlB_2 structure to be discussed below. These distortions, included in Fig. 8.10, are never so severe that the above conclusions break down, however.

[19]The relative difference between the maximum and minimum value for each lattice parameter obtained with the number of k points in the IBZ increased beyond 260 (as obtained with an (8, 8, 8) k mesh) is still as large as 0.6% (1.5%) for the a (c) lattice parameter. These variations are so considerable that they can not justifiably be neglected in a substrate/overlayer lattice mismatch discussion. Therefore, if we want to make predictions regarding the growth of vacancy free Y disilicide nanowires with the AlB_2 structure on the Si(001) surface, a necessary requirement is a significantly improved convergence in the lattice parameters compared to that obtained at the (8, 8, 8) k mesh level.

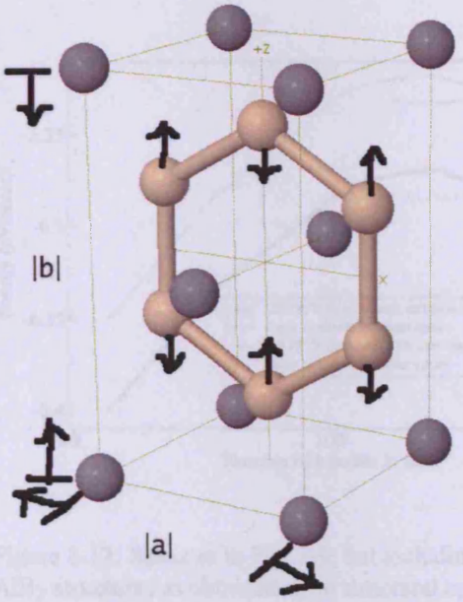

Figure 8.11: Schematic presentation of the main features of the orthorhombic structural distortion taking the AlB_2 structure into the OD AlB_2 structure: for the 6 atom unit cell in this figure to describe the AlB_2 structure, in particular, the identity $b/a = \sqrt{3}$ for the a and b lattice parameters of the cell must hold true. For the OD AlB_2 structure, the unit cell remains orthorhombic, but the a lattice parameter increases while the b lattice parameter decreases, as shown with the arrows at the edges of the unit cell in the figure. The Si atoms connected by a bond along the b axis direction are found to move along the b axis such as to stretch this Si-Si bond.

with the total energy changes being within a few meV/atom, we conclude that acceptable convergence has been reached at the (11, 11, 11) k mesh level. For this situation, the lattice parameters $a = 4.082$ Å and $c = 3.960$ Å are obtained.

When the ionic positions in the 3 atom unit cell are allowed to vary (second optimization scheme), all structural parameters are found to be unchanged if optimization is started from the above mentioned results. A transformation into an orthorhombically distorted (OD) AlB_2 structure is revealed, however, in the 6 atom unit cell studies: this structure can be fully described with the 3 atom unit cell (which will now be monoclinic rather than hexagonal) and we therefore performed complete optimizations using both the 6 atom unit cell and the 3 atom unit cell, starting in the latter case from 6 atom unit cell results, in order to clarify the stability of the OD AlB_2 structure. For clarity in the discussion below, we refer to Fig. 8.11 for a presentation of the features of the AlB_2 - OD AlB_2 structure transformation. [20]

[20]We find that the presentation of this structural instability is more transparent if the 6 atom unit cell is

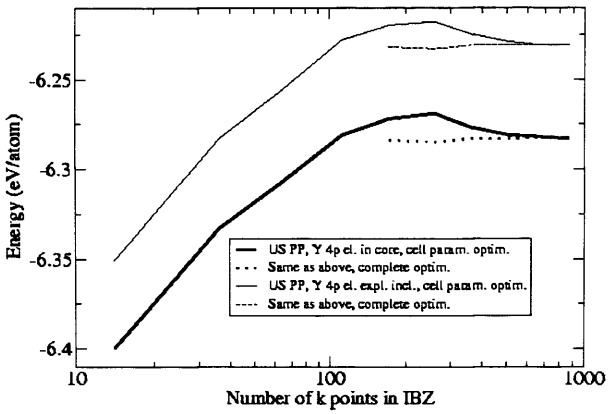

Figure 8.12: Same as in Fig. 8.9, but including the total energies for the AlB_2 and OD AlB_2 structures as obtained upon structural optimization using Vanderbilt US PPs with the Y 4*p* electrons explicitly in the calculations (upper set of curves). Apart from a translation in the energies of $\sim$ 0.05 eV/atom the explicit inclusion of these electrons is found to have little effect on the optimization results (see Fig. 8.13 for further details).

In both sets of OD AlB_2 structure optimization studies performed, a monotonic change in the values of the structural parameters for the unit cell towards the hexagonal AlB_2 structure unit cell values is obtained. For the 3 atom unit cell studies, the convergence to the AlB_2 structure is evident on the basis of the calculations performed (see Fig. 8.9, 8.10), whereas the change in the parameters is slower for the 6 atom unit cell studies, [21] with convergence not being immediately clear from these results. The reason for this difference is not clear to us, but we note that the optimized *a* and *b* lattice parameters for the 6 atom unit cell obtained when keeping the ionic positions in the cell fixed (also an OD AlB_2, rather than an AlB_2 structure) differ numerically from the fully optimized values by $\sim$ 0.07 and $\sim$ 0.13 Å, respectively, for the finest *k* meshes used, even though the structural energy difference is minute, $\sim$ 1 meV/atom,

used. It is emphasized, however, that the primitive unit cell for both the AlB_2 and the OD AlB_2structure is a cell containing only three atoms.

[21] When comparing the rate of the change in the lattice parameters in these two studies, we make reference to the *k* meshes used in the calculations. For the present situation, the difference in the rate of change is evident: at the (12, 12, 12) *k* mesh level in the 3 atom unit cell studies (868 *k* points in the IBZ), the length of the unit cell basis vectors and the angles they make with each other are within 0.01 Å and 0.1°, respectively, of the AlB_2 structure values (see Fig. 8.10), with the movements of the atoms in the cell away from the AlB_2 symmetry being negligible. For the 6 atom unit cell studies, at the (15, 15, 10) *k* mesh level (1125 *k* points in the IBZ, i.e., a comparatively denser *k* mesh), the *a* and *b* lattice parameters still have values 0.13 and 0.21 Å from the AlB_2 structure values and the Si atom movements away from AlB_2 symmetry in the cell have a magnitude of 0.02 Å, none of these parameters showing evident signs of convergence towards AlB_2 structure values.

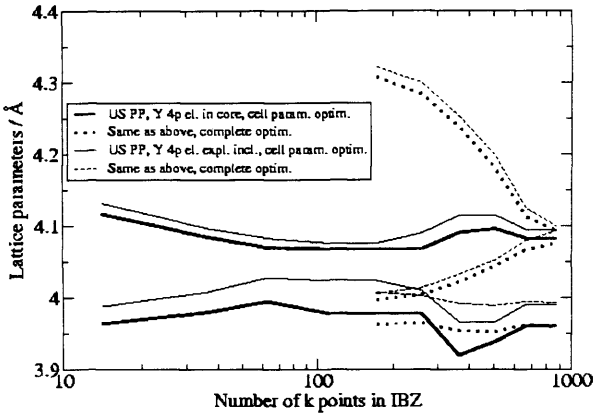

Figure 8.13: Same as in Fig. 8.10, but including the optimized lattice parameters for the AlB_2 and OD AlB_2 structures as obtained upon structural optimization using Vanderbilt US PPs with the Y 4p electrons explicitly in the calculations (thin set of curves). In comparison with the results obtained with the Y 4p electrons in the core, a translation of both the a, b, and c lattice parameters, in all cases only weakly dependent on the number of k points in the IBZ, is noted. In both of the studies, the angle between the a and b basis vectors for the OD AlB_2 structure was found to change monotonically towards the AlB_2 structure value of 60°, i.e., the OD AlB_2 structure changed into the AlB_2 structure in both cases considered as the number of k points was increased sufficiently.

at this point. Considering the results of the 3 atom unit cell studies, we interpret this result as the energy contours being very shallow in this region and therefore do not regard it as worrying that a definite statement regarding the convergence of the structural parameters for the OD AlB_2 structure as described with the 6 atom unit cell can not be made on the basis of our studies.

Following the conclusion that bulk vacancy free Y disilicide in the AlB_2 structure is stable according to our studies, we increased the plane wave energy cutoff beyond 188.3 eV and decreased the smearing width in the chosen Gaussian smearing scheme below 0.1 eV. These changes were found to have no influence on the structural parameters and the full variation in the total energy was within 0.01 eV/atom (energy cutoffs of up to 250.0 eV were tested). We therefore conclude that convergence in both structural parameters and total energy has been obtained with this choice of parameters and a (11, 11, 11) Γ centered k mesh.

The structural optimizations of bulk vacancy Y disilicide in the AlB_2 structure employing Vanderbilt US PPs with the Y 4p electrons included explicitly in the calculations have focussed on the 3 atom unit cells only: for this situation, the full range of

structural optimizations described previously in this part of the appendix for the calculations employing Vanderbilt US PPs with the Y 4*p* electrons in the core have been repeated, with an optimization result for the 6 atom unit cell obtained in these previous studies being used as the starting point for the complete optimization of the 3 atom unit cell (the second optimization scheme). In our comparison of the results of these structural optimizations with the results described in Fig. 8.9, 8.10, we have focussed on both the total energies and structural parameters as the two studies used the same value for the plane wave energy cutoff.

Fig. 8.12 shows the total energies as obtained for the AlB_2 and OD AlB_2 structures for these two theoretical description of bulk vacancy free Y disilicide, while Fig. 8.13 includes the optimized lattice parameters for the 3 atom unit cells obtained in these studies. The results obtained with the Y 4*p* electrons included explicitly in the calculations support the conclusion that the apparent instability of the AlB_2 structure disappears when a sufficiently dense *k* mesh is used. This comment does not fully reveal the close similarity of these results, however: when comparing the complete set of results in Fig. 8.12, 8.13, it is evident that the variation of these parameters with the number of *k* points in the IBZ is also practically equivalent. [22] In other words, the inclusion of the Y 4*p* electrons to a good approximation has the effect only of changing both the lattice parameters and the total energy by values practically independent of the *k* mesh used. The difference in the lattice parameters is not negligible, the converged (see below for further comments) values for the *a* (*c*) lattice parameter of 4.094 Å (3.990 Å) as obtained with the Y 4*p* electrons included being larger by 0.3% (0.8%) compared to the values obtained with the Y 4*p* electrons in the core, but the results nevertheless suggest that the Y 4*p* electron states are hardly affected by structural changes in the crystal environment, i.e., that these electrons can safely be regarded as core electrons for bulk vacancy free Y disilicide according to our studies. It is beyond the scope of this discussion to go into further details with this issue, and we refer to Sec. 6.2.2.11 for a more detailed comparison (including the electronic structure) of the similarity of the two theoretical descriptions of bulk vacancy free Y disilicide.

Following the calculations leading to the results described in Fig. 8.12, 8.13 for the theoretical studies of bulk vacancy free Y disilicide in the AlB_2 structure as obtained using Vanderbilt US PPs with the Y 4*p* electrons included explicitly, convergence of these results with respect to changes in the values for the plane wave energy cutoff (values of up to 250.0 eV) and smearing width was investigated. Both lattice parameters and total energies were found to be practically unaffected by these changes, the remaining variation in the total energy being highly similar to the situation described previously for the Y 4*p* electrons in the core. We therefore conclude that acceptable convergence in both structural parameters and total energy has been reached for this theoretical description of the system for a plane wave energy cutoff of 188.3 eV, a Gaussian smearing scheme with smearing width 0.1 eV, and a (11, 11, 11) Γ centered *k* mesh.

[22] This conclusion is not changed when e.g. the plane wave energy cutoff is increased in the theoretical studies with the Y 4*p* electrons in the core (see below in the text).

8.3.3 BULK Y DISILICIDE IN THE $ThSi_2$ AND $GdSi_2$ STRUCTURE

As discussed in Sec. 6.2.2.2, the main aim of the structural optimization of bulk Y disilicide in the $ThSi_2$ and $GdSi_2$ structures is to compare the lattice parameters obtained in this study with the experimental lattice parameters for these systems, subsequently using the adjustment of the theoretical lattice parameters thus obtained as a correction of the theoretical lattice parameters in Table 6.1 for bulk vacancy free Y disilicide in the AlB_2 structure, where no comparison with an experimental system can be made. In other words, as the studies discussed below are not aimed at obtaining very precise convergence in either the lattice parameters or the total energies (with this statement to be clarified below), we aimed at keeping calculations as simple as possible: we assumed from the outset of the structural optimization of bulk Y disilicide in the $ThSi_2$ and $GdSi_2$ structures that the convergence considerations described in Sec. 8.3.2 and Sec. 6.2.2.11 for the studies of bulk vacancy free Y disilicide in the AlB_2 structure would apply to the current situation as well. More specifically, the calculations below employed only Vanderbilt US PPs with the Y $4p$ electrons in the core, using a value of 188.3 eV for the plane wave energy cutoff and a smearing width of 0.1 eV for the chosen Gaussian smearing scheme for partial occupancies. We shall not comment on the justifiability of these choices in the discussion below. Only, we note that no clear warning signs (such as a comparatively large entropy term in the formally finite temperature optimization scheme) were obtained on optimization for these systems.

All structural optimization studies employed the primitive unit cell for the $ThSi_2$ and $GdSi_2$ structures (see Sec. 4.2.3). The same two optimization procedures as described in Sec. 8.3.2 for the studies of bulk vacancy free Y disilicide in the AlB_2 structure were employed in the present studies: initially, all structural parameters but the ionic positions in the cell were optimized, and subsequently, also these parameters were relaxed in a truly complete optimization. The initial choice of lattice parameters for the systems under investigation in both cases were the experimental lattice parameters as reported in Ref. [148]: for bulk Y disilicide in the tetragonal $ThSi_2$ structure, these parameters attained the values $a = b = 4.04$ Å, $c = 13.42$ Å, while for bulk Y disilicide in the $GdSi_2$ structure, these values had all changed slightly, yielding $a = 4.05$ Å, $b = 3.954$ Å, and $c = 13.36$ Å. All calculations were performed using Monkhorst-Pack (MP) ($3N$, $3N$, N) k meshes. This choice of mesh yielded a fairly homogeneous distribution of k points in the IBZ, with the ratio c/a for these systems being reasonably close to 3.5 according to both experiment and theory (see below).

The total energies and lattice parameters obtained in the studies of these two systems are shown in Fig. 8.14 - 8.16. It is evident from these results that the $GdSi_2$ structure is not stable according to our studies, the lattice parameters and total energy differing from the $ThSi_2$values by an insignificant amount for all k meshes considered. [23] Below, therefore, we shall concentrate only on the $ThSi_2$ structure. For this system, both the lattice parameters and the total energy appear to be reasonably well converged beyond the (9, 9, 3) k mesh level ($\sim$ 125 k points in the IBZ). The strength

[23] We note that complete optimizations starting from the experimental lattice parameters for the $GdSi_2$ structure did not change this conclusion. We shall return to this issue at the end of this discussion.

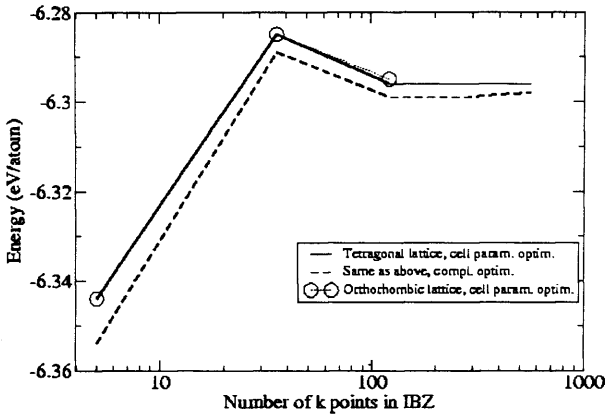

Figure 8.14: Total energies for bulk Y disilicide in the tetragonal $ThSi_2$ and orthorhombic $GdSi_2$ structures, as obtained upon structural optimization using Vanderbilt US PPs with the Y $4p$ electrons in the core, as a function of the number of k points in the IBZ (note logarithmic scale). For general comments on computational details, see Sec. 8.3.1. On the basis of these results and the optimized structural parameters in Fig. 8.15 , 8.16 we conclude that the $GdSi_2$ structure is never stable. There are also indications (see text for details) that the $ThSi_2$ structure would be stabilized upon further increase in the number of k points in the IBZ.

of this statement is somewhat limited by the fact that only two calculations have been performed for finer k grids. Furthermore, we noted in Sec. 8.3.2, in our studies of bulk vacancy free Y disilicide in the AlB_2 structure, that k mesh convergence appears to be very slow for this system, in particular when using an orthorhombic cell for the structural optimization.

In the present studies of Y disilicide in the $ThSi_2$ structure, these comments are of interest especially when evaluating the apparent structural instability, conceptually similar to the one described for bulk vacancy free Y disilicide in the AlB_2 structure in Sec. 8.3.2, obtained upon complete optimization of the structure. In Sec. 8.3.2 we argued, primarily on the basis of calculations for the 3 atom unit cell for the system under investigation, that this structural distortion was explained by *(i)* an insufficient number of k points in the IBZ and *(ii)* very shallow energy contours for the system, whereas a definite conclusion on this issue could not have been obtained on the basis of the 6 atom unit cell calculations only in Sec. 8.3.2. There are indications in Fig. 8.14 - 8.16 that the structural distortion observed in the present studies would have the same explanation, and we therefore speculate that theory would actually predict stability of bulk Y disilicide in the $ThSi_2$ structure upon further increase in the number of k points in

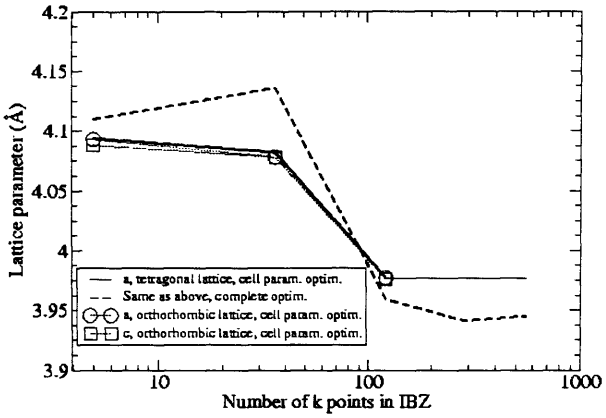

Figure 8.15: Optimized a and c lattice parameters for bulk Y disilicide in the tetragonal $ThSi_2$ and orthorhombic $GdSi_2$ structures, as obtained upon structural optimization using Vanderbilt US PPs with the Y $4p$ electrons in the core, as a function of the number of k points in the IBZ (note logarithmic scale). The energies for these structures have been shown in Fig. 8.14. In addition to the parameters shown in the figure for the completely optimized $ThSi_2$ structure, the movement of the Si atoms away from their positions for the arrangement obeying $ThSi_2$ structure symmetries vary between 0.019 Å and 0.032 Å over the range of k points considered.

the IBZ. [24] For this reason, we shall not go into detail with the results of the complete optimization of the $ThSi_2$ structure below but focus only on the cell parameter optimization results.

In comparison with the experimental values (see Ref. [148]) for the Y disilicide $ThSi_2$ structure lattice parameters, the optimized values obtained in the present work are markedly different. Focussing on the apparently well converged values obtained using a (9, 9, 3) k mesh, we find that the a and b lattice parameters, attaining values of 3.977 and 14.541 Å, respectively, differ from their experimental counterparts by 0.063 Åand 1.12 Å, the theoretical a (b) lattice parameter being smaller (larger) than the experimental value. In other words, the unit cell for this system is significantly stretched along the b axis, with the relative changes in the above mentioned lattice parameters, compared to the experimental values, being -1.6% and 8.3%, respectively: for experimentally reported Y disilicide in the $ThSi_2$ structure, the Si-Si bond lengths

[24] Most importantly, both the difference in the lattice parameters and total energies between the true $ThSi_2$ structure and the slightly distorted version of this structure are relatively small for the finest k meshes considered: the a (b) lattice parameters are within 0.032 Å (0.225 Å) of each other (relative difference 0.8% [1.5%]) while the total energies differ by 0.003 eV/atom. These remarks act as further justification for the concluding remark above in the text.

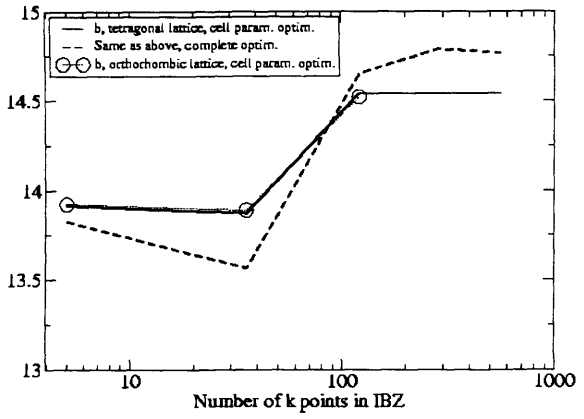

Figure 8.16: Optimized b lattice parameters for bulk Y disilicide in the tetragonal $ThSi_2$ and orthorhombic $GdSi_2$ structures, as obtained upon structural optimization using Vanderbilt US PPs with the Y $4p$ electrons in the core, as a function of the number of k points in the IBZ (note logarithmic scale). The energies for these structures have been shown in Fig. 8.14.

attain values of 2.27 - 2.31 Å, somewhat closer to the value for bulk Si in the diamond structure, 2.351 Å, than what is obtained (2.21 Å) for bulk vacancy defected Y disilicide in the AlB_2 structure [97]. For the optimized structure obtained in our studies, the Si-Si bond lengths are somewhat larger, 2.33 - 2.42 Å, but they are not farther away from the value for bulk Si, [25] and thus not clearly at variance with the expectation that Si-Si bond lengths fairly close to the bulk Si values are obtained for bulk Y disilicide in the $ThSi_2$ structure. [26] The reason for the large difference between the theoretical and experimental lattice parameters for this structure must be more subtle.

Given the relatively limited studies of Y disilicide in the $ThSi_2$ structure performed in this work, we can not properly address the above issue. We would regard it as unlikely, considering the results of our theoretical studies of bulk vacancy free Y disilicide in the AlB_2 structure in Sec. 8.3.2, that explicit inclusion of the Y $4p$ electrons will change the conclusions dramatically. Rather, we speculate that rigorous k mesh convergence has not been obtained in the present studies: we note from Fig. 8.15 , 8.16

[25] As noted in Sec. 8.2.2, the theoretical lattice parameter for this system as obtained with VASP differs only slightly from the experimental value. For simplicity, we shall make no distinction between these values in the present discussion.

[26] As discussed briefly in Sec. 6.2.2.11, the presence of Si vacancies bulk Y disilicide in the AlB_2 structure is believed to be connected with the fact that this criterion can not be fulfilled for this system in the absence of vacancies (as clarified above), i.e., the graphite-like Si planes experiencing a considerable amount of strain in the absence of Si vacancies. For Y disilicide in the $ThSi_2$ structure, reversing the argument, the absence of Si vacancies would be expected to be associated with the Si-Si bond lengths being considerably closer to 2.35 Å.

that a drastic change in the theoretical lattice parameters occurs upon a relatively small increase in the number of k points in the IBZ. This, and the suggestions discussed in the above that the energy contours for this system are quite shallow, i.e., that an appreciable change in the lattice parameters is not necessarily associated with a large change in the total energy of the system, makes us speculate that an atomic arrangement with the lattice parameters considerable closer to the experimental values for this system, above the cell parameter optimized results in energy by a relatively small amount, might exist. If this were the case, the theoretical result might be explained by the number of k points in the IBZ being insufficient for the true theoretical structure to be stabilized. [27] This argument gains some support from the observation in Fig. 8.14 - 8.16 that bulk Y disilicide in the $GdSi_2$ structure is unstable, in contrast with experimental results [148], even for a k mesh sufficiently dense for the above mentioned change in the $ThSi_2$ structure lattice parameters to have occured. A study of the energy contours for Y disilicide in the $ThSi_2$ structure, involving optimization of the cell volume but locking the b/a ratio for the system at various values between the theoretical and the experimental values would yield more information on this issue. We have not performed such studies in the present work, though. As discussed in Sec. 6.2.2.2, given the high level of uncertainty in the present conclusions, we have not used the optimization results for Y disilicide in the $ThSi_2$ structure for their intended purpose presented at the beginning of the present part of the appendix.

8.3.4 Y AND Y DISILICIDE NANOWIRES ON THE Si(001) SURFACE

As discussed briefly in Sec. 8.3.1, the bulk of our theoretical studies involving Y on the Si(001) surface have employed Vanderbilt US PPs with the Y $4p$ electrons in the core, using, in initial considerations, a 200.0 eV energy cutoff for the plane waves (as determined by the presence of H for the model system) and a Gaussian smearing scheme with smearing width 0.1 eV. These choices have been made on the basis of the studies described in Sec. 8.3.2 for bulk vacancy free Y disilicide in the AlB_2 structure. For a more complete description of computational details for the initial studies we refer to Sec. 8.3.1. We will discuss convergence of the structural parameters and total energies with respect to the variable parameters for the code later in this discussion.

For the studies involving Y on the Si(001) surface, we have used a slab geometry which has been described in general detail in Sec. 8.1. We refer to this part of the thesis for a discussion of the calculations performed on clean Si(001) of relevance to the present studies, i.e., we shall comment below only calculations performed on systems with Y on the Si(001) surface. We shall focus mainly on Y atoms on Si(001), describing initially the optimizations of the complete set of wetting layer unit candidate structures presented in Sec. 6.2.3.5 and clarifying why only a few of these configurations were

[27] The same argument could be used, on the face of it, to justify explicit inclusion of the Y $4p$ electrons in the calculations on Y disilicide in the $ThSi_2$ structure as a way of obtaining more reliable lattice parameters for this system, the lattice parameters for bulk vacancy free Y disilicide in the AlB_2 structure showing nonnegligible changes upon this change of theoretical description of the Y/Si system. For a more detailed explanation of our lack of confidence in the explicit inclusion of the Y $4p$ electrons being a way of solving the present issues, we refer to the discussion in Sec. 6.2.2.11.

Table 8.2: Optimized total energies for the configurations with Y atoms and dimers on the Si(001) surface investigated in the present work (see Fig. 6.14), as obtained using Vanderbilt US PPs with the Y 4*p* electrons in the core and a $p(2\times2)$ surface unit cell with surface dimensions 7.68 × 7.68 Å^2. The configurations have been ordered according to increasing binding energy. See text for details.

Configuration	Energy / eV/atom
Dimer Bridge	-5.38
Y Dimer$_S$	-5.75
Interdimer Bridge	-5.88
Pedestal Y Dimer, $\parallel$	-5.96
Pedestal Y Dimer, $\perp$	-6.47
Hollow Y Dimer, $\perp$	-6.47
Pedestal	-7.13
Cave	-7.26
Hollow	-7.32
Y Atom$_S$	-7.37
Hollow Y Dimer, $\parallel$	-7.43

selected for the actual studies of the Y/Si(001) 2×4 wetting layer in Sec. 6.2.4.3. Following these considerations, we shall comment on the convergence tests performed for selected configurations with Y atoms on Si(001) (with the results expected to apply to the Y/Si(001) wetting layer and Y disilicide nanowire configurations unless otherwise noted). Finally, we shall present results of structural optimizations for the energetically most favourable wetting layer unit, wetting layer, and nanowire configurations with the Y 4*p* electrons included explicitly in calculations, in order to clarify whether these semi-core states have an effect on the relative energies of these systems.

The total energies as obtained on structural optimization of the complete set of Y/Si(001) wetting layer unit candidate structures presented in Sec. 6.2.3.5, using the theoretical approach described at the beginning of this discussion and a $p(2\times2)$ surface unit cell with surface dimensions 7.68 × 7.68 Å^2 (see Sec. 8.1 for further comments), have been included in Table 8.2. These energies were obtained using a (6, 6, 1) Monkhorst-Pack (MP) *k* mesh (see Sec. 8.1 for general remarks): we shall discuss below that convergence in the energies and structural parameters has been obtained with this choice. For comments on the calculated energy gain obtained upon binding the removed Si atoms for the substitutional configurations elsewhere on the substrate, we refer to Sec. 6.2.3.6. It is evident from these results that only a few of the configurations are to be regarded as stable configurations for the adsorption of Y on the Si(001) surface. We shall clarify below why only the Pedestal, Cave, Hollow, and Y Atom$_S$ configurations should be included as wetting layer candidate units, i.e, possible explanations for a single protrusion for the Y/Si(001) 2×4 wetting layer, in our further studies.

On the face of it, from the results in Table 8.2, the Hollow Y Dimer, $\parallel$ configuration is the most favourable wetting layer unit candidate from the set of configurations

studied. On investigating the optimized structural parameters for this configuration, however, it becomes clear, that it resembles two adjacent Cave configurations rather than an Y dimer configuration, i.e., the Y atoms are paired, but with no evident signs of dimerization: [28] the Hollow Y Dimer, $\parallel$ configuration thus describes effects of agglomeration of Y atoms in the Cave configuration and is not to be regarded as a wetting layer unit, regardless of the suggestion that this agglomeration is energetically favourable. [29] For the other dimer configurations investigated, we have not gone into details with distinguishing between pairing and dimerization as all of these configurations are clearly energetically unfavourable: *(i)* the Hollow Y Dimer, $\perp$ configuration, the energetically most favourable dimer configuration in Table 8.2 with the Hollow Y Dimer, $\parallel$ configuration excluded, is higher in energy by 0.66 eV/atom compared to the least favourable configuration from the previously mentioned interesting quadruple, the Pedestal configuration. In addition, *(ii)* while the surface dimensions for the cell used for the present studies are evidently too small for any of the configurations to be regarded as reasonably isolated, the energy difference of 0.90 eV/atom between the Hollow Y Dimer, $\perp$ and Y Atom_S configurations must be regarded as sufficiently large for the Hollow Y Dimer, $\perp$ configuration, and energetically less favourable configurations in Table 8.2 to be excluded as potential candidates for wetting layer units. We do emphasize, however, the importance of the conclusion that the Y Dimer_S configuration is energetically highly unfavourable according to our studies. Considering that this configuration is the only dimer configuration satisfying the requirements from experiment for the registry of the wetting layer protrusion with respect to the surrounding Si dimers on the terrace (see Sec. 6.2.3.4), this result in particular makes us rule out an Y dimer as an explanation for a single protrusion for the Y/Si(001) 2×4 wetting layer reported in Ref. [128].

Following the studies described above, we investigated the dependence of the formation energy for selected configurations from Table 8.2 on changes in the slab geometry, within the restriction of fixed surface unit cell dimensions: [30] we changed the vacuum gap width for the slab geometry away from its initial value ($\sim$ 11.8 Å, see Sec. 8.1) and increased the number of layers in the slab beyond the initial choice of 6 Si layers for the slab, keeping the vacuum gap width fixed. In both studies, these changes were found to have only weak influence on the structural parameters and total energies for the configurations investigated, and we shall not go into further into detail with these studies here. Decreasing the smearing width from the initial choice of 0.1 eV to 0.05 eV in calculations did not affect the structural parameters for the configurations investigated, with the formation energy changes being $\sim$ 0.01 eV. These changes, which were not a general displacement, are not negligible, but clearly smaller than the energy differences between the configurations in Table 8.2 and we therefore made did

[28] For each Y atom for the Hollow Y Dimer, $\parallel$ configuration, the Y-Si distances involving Si atoms in the uppermost two layers for the surface are changed by 0.02 Å or less compared to the single Y atom for the Cave configuration. The distance to the Si atom in the third layer is larger by $\sim$ 0.1 Å, presumably connected to the agglomeration of the Y atoms, the Si atoms for this layer, on either side of the single Y atom for the Cave configuration, being pulled apart by 0.06 Å.

[29] Ultimately, this conclusion would be reached anyway during the construction of a Y/Si(001) wetting layer with Y atoms in the Cave configuration as the wetting layer unit.

[30] For considerations on the effects of increasing the unit cell dimensions along the surface directions, see Sec. 6.2.4.2.

not change the smearing width in remaining studies. Finally, increasing the energy cutoff value to 250 eV and using the recommended grid in calculations was not found to have a significant influence on structural parameters or energies for the configurations tested, further calculations at this precision there abandoned in order to reduce the amount of time spent on these studies. For comments on results obtained upon including the Y 4*p* electrons as semi-core states in calculations, we refer to Sec. 6.2.4.2.

8.3.5 Y ATOMIC STRINGS ON THE Si(001) SURFACE

The strategy for the theoretical modelling of the Y atomic string candidate structures investigated in the present work (Sec. 6.3) has been presented in Sec. 6.3.2.2: we are aiming at obtaining the formation energies of isolated Y strings and pairs of strings on the A Type and Haiku structure, respectively, on the otherwise clean Si(001) surface. For the convergence of the formation energy with respect to separation of the adjacent strings (as obtained within the supercell approximation) to be investigated, we have performed calculations on slab geometries always containing a single Si dimer row, but with 4, 6, and 8 Si dimers contained within each cell, i.e., with surface dimensions 7.68 × 15.36, 7.68 × 23.04, and 7.68 × 30.72 Å^2. [31] In order to fully accommodate the local surface reconstructions of the Si(001) surface, i.e., with an acceptable level of convergence for the structural parameters with respect to the number of layers in the slab, all the Si slabs considered in the studies contained 10 Si layers as opposed to the standard choice of 6 layers throughout this work for the calculations involving adatoms and nanostructures on the Si(001) surface. Previous investigations for the Haiku structure by Owen *et al.*, [85] the more extended of the two surface reconstructions, have reported that reliable results should be obtained using a 10 layer slab. In order to reduce computational effort slightly for 10 layer slab studies, the cell dimension along the direction of the surface normal for the system was kept at 21.72 Å, the typical value for the 6 layer slab, or, in other words, the vacuum gap width was reduced, from 13.82 to 8.36 Å. A test calculation for the clean Si(001) surface showed that increasing the vacuum gap width beyond the smaller of the above values had no significant effect on the structural parameters and total energy of the system.

The calculations performed on these systems have employed the Vanderbilt US PP [17] with the Y 4*p* electrons in the core only, as implemented in VASP [23, 24], with the PW91 GGA [12] to E_{xc}. On the basis of the convergence tests described for Y on Si(001) in Sec. 8.3.4, we have chosen a plane wave energy cutoff value of 200.0 eV and a smearing width of 0.1 eV for the Gaussian smearing scheme in the studies to be presented below (see Sec. 8.3.4 for further details). The convergence discussion below, therefore, will only address *k* mesh convergence. In addition, we shall comment on the results of *(i)* a spin polarized calculation for the energetically two most favourable Y atomic string candidate structures and *(ii)* explicit inclusion of the Y 4*p* electrons in calculations for the same two configurations.

[31] As shown in Fig. 6.25 of Sec. 6.3.2.2, the Y atomic string candidate structures run perpendicular to the Si dimer row on the surrounding terrace, so the separation of adjacent nanostructures is increased by increasing the number of Si dimers in the dimer row running in the intermediate region between these structures.

The generally recommended procedure with respect to the choice of k mesh when comparing results of structural optimizations for a single adatom or nanostructure on surfaces with changing surface cell dimensions is to use cells, if possible, where the various chosen k meshes corresponds to the same spacing of k points in the IBZ. Convergence in this case is tested for one cell only, with the equivalent (in the above sense) k grid used for the other cells. This approach, however, is not easy to implement for the set of cells investigated in the present studies, where the variation of the cell dimension along one direction is changed with respect to the smallest cell by both a factor 1.5 and 2: in addition, it is potentially unnecessary, as a set of equivalent k meshes for the different systems will probably correspond to a situation where k mesh convergence has already been reached for a considerably lower number of k points in the IBZ for each cell. Rather, we have at the outset tested k mesh convergence independently for every cell considered, although we shall make some comments below on how to draw conclusions on this issue from comparison of results obtained for different cells.

With the unit cell a lattice parameter defined as being parallel to the Si dimer row direction for all cells considered, the chosen k meshes for the studies of the 4, 6, and 8 dimer cell were Monkhorst-Pack (MP) k meshes, with the number of k points along the three basis vectors for the unit cell in reciprocal space being ($2N$, N, 1), ($3N$, N, 1), and ($4N$, N, 1), respectively. In all cases, these choices produced a homogeneous distribution of k points in the IBZ. Values of N up to 6, 3, and 2 were investigated for the different cells (the maximum value considered decreasing with increasing surface cell dimensions).

For the discussion of the convergence of the structural parameters with respect to k mesh below, we have focussed, for simplicity, only on a few parameters of key importance for the configurations: *(i)* the distance between adjacent Si atoms on either side of the Y chain, *(ii)* the Y-Si distances involving Si atoms from the uppermost layer of the substrate (i.e., the Si atoms with dangling bonds), and *(iii)* the distance between Y atoms for the chain. All optimizations were started with the same choice of values for these parameters: in particular, adjacent Y atoms were moved together (the shorter initial distance being 3.11 Å) in order to investigate pairing of these atoms.

The structural optimizations did not reveal any tendencies for the Y atoms in the chain to dimerize. For the 4, 6, and 8 dimer cells, k meshes with $N = 4$, 3, and 2, referring to the introduction above of the sets of k meshes used in calculations, were found to be sufficiently dense for the above mentioned structural parameters to be converged within 0.01 Å and the relative energies to be converged within a few meV/Y atom. We regarded these results as satisfactory and furthermore noted that they agreed with expectations on the basis of the calculations for Y atoms on the Si(001) surface described in Sec. 8.3.4.

Both the spin polarized calculations and the inclusion of Y $4p$ electrons as semicore states (separate studies, i.e., the latter study referring to non-spin polarized calculations) introduced significant dimerization effects for the H_H configuration (see Table 6.11 for an explanation of the nomenclature), with a lowering of the formation energy of this configuration by 0.04 eV/Y atom obtained in the spin-polarized studies. Considering that the studies of Y atomic strings on Si(001) are at a preliminary stage, even with respect to the modelling of the candidate configurations investigated in the

present work (see Sec. 6.3.3), we did not investigate these effects further.

Bibliography

[1] N. W. Ashcroft and N. D. Mermin, *Solid State Physics*, Saunders College Publishing (1976).

[2] J. C. Slater, *Phys. Rev.* **81**, 385 (1951).

[3] B. Paulus, *Phys. Rep.* **428**, 1 (2006).

[4] F. R. Manby, D. Alfe, and M. J. Gillan, *Phys. Chem. Chem. Phys.* **8**, 5178 (2006).

[5] P. Hohenberg and W. Kohn, *Phys. Rev.* **136**, B864 (1964).

[6] M. Levy, *Proc. Natl. Acad. Sci. U.S.A.* **76**, 6062 (1979).

[7] W. Kohn and L. J. Sham, *Phys. Rev.* **140**, A1133 (1965).

[8] A. E. Mattsson, P. A. Schulz, M. P. Desjarlais, T. R. Mattsson, and K. Leung, *Modelling Simul. Mater. Sci. Eng.* **13** R1 (2005).

[9] D. M. Ceperley and B. J. Alder, *Phys. Rev. Lett.* **45**, 566 (1980).

[10] J. P. Perdew, *Phys. Rev. Lett.* **55**, 1665 (1985).

[11] J. P. Perdew and Y. Wang, *Phys. Rev. B* **33**, 8800 (1986).

[12] J. P. Perdew, J. A. Chevary, S. H. Vosko, K. A. Jackson, M. R. Pederson, D. J. Singh, and C. Fiolhais, *Phys. Rev. B* **46**, 6671 (1992).

[13] J. P. Perdew, K. Burke, and M. Ernzerhof, *Phys. Rev. Lett.* **77**, 3865 (1996).

[14] R. M. Martin, *Electronic Structure*, Cambridge University Press (2004).

[15] B. J. Austin, V. Heine, and L. J. Sham, *Phys. Rev.* **127**, 276 (1962).

[16] D. R. Hamann, M. Schluter, and C. Chiang, *Phys. Rev. Lett.* **43**, 1494 (1979).

[17] D. Vanderbilt, *Phys. Rev. B* **41**, 7892 (1990).

[18] J. C. Philips and L. Kleinman, *Phys. Rev.* **116**, 287 (1959).

[19] E. Antoncik, *J. Phys. Chem. Solids* **10**, 314 (1959).

[20] S. Goedecker, M. Teter, and J. Hutter, *Phys. Rev. B* **54**, 1703 (1996).

[21] P. E. Bloechl, *Phys. Rev. B* **50**, 17953 (1994).

[22] G. Kresse and J. Joubert, *Phys. Rev. B* **59**, 1758 (1999).

[23] G. Kresse and J. Hafner, *Phys. Rev. B* **47**, 558 (1993).

[24] G. Kresse and J. Furthmuller, *Comput. Mater. Sci.* **6**, 15 (1996).

[25] D. Sanchez-Portal, E. Artacho, and J. M. Soler, *Sol. State Commun.* **95**, 685 (1995).

[26] P. Ordejon, E. Artacho, and J. M. Soler, *Phys. Rev. B* **53**, R10441 (1995).

[27] E. Artacho, D. Sanchez-Portal, P. Ordejon, A. Garcia, and J. M. Soler, *Phys. Stat. Solidi B* **215**, 809 (1999).

[28] S. D. Kenny, A. P. Horsfield, and H. Fujitani, *Phys. Rev. B* **62**, 4899 (2000).

[29] F. J. H. Ehlers, A. P. Horsfield, and D. R. Bowler, *Phys. Rev. B* **73**, 165207 (2006).

[30] D. R. Bowler, T. Miyazaki, and M. J. Gillan, *J. Phys.:Condens. Matter* **14**, 2781 (2002).

[31] D. J. Chadi and M. L. Cohen, *Phys. Rev. B* **8**, 5747 (1973).

[32] H. J. Monkhorst and J. D. Pack, *Phys. Rev. B* **13**, 5188 (1976).

[33] P. E. Bloechl, O. Jepsen, and O. K. Andersen, *Phys. Rev. B* **49**, 16223 (1994).

[34] M. J. Gillan, *J. Phys.: Condens. Matter* **1**, 689 (1989).

[35] M. Methfessel and A. T. Paxton, *Phys. Rev. B* **40**, 3616 (1989).

[36] C. W. M. Castleton and S. Mirbt, *Physica B* **340-342**, 407 (2003).

[37] C. W. M. Castleton and S. Mirbt, *Phys. Rev. B* **70**, 195202 (2004).

[38] G. Makov and M. C. Payne, *Phys. Rev. B* **51**, 4014 (1995).

[39] C. W. M. Castleton, A. Hoglund, and S. Mirbt, *Phys. Rev. B* **73**, 035215 (2006).

[40] W. A. Hofer, A. S. Foster, and A. L. Shluger, *Rev. Mod. Phys.* **75**, 1287 (2003).

[41] J. Tersoff and D. R. Hamann, *Phys. Rev. B* **31**, 805 (1985).

[42] J. Tersoff and D. R. Hamann, *Phys. Rev. Lett.* **50**, 1998 (1985).

[43] J. Bardeen, *Phys. Rev. Lett.* **6**, 57 (1961).

[44] W. Hofer, *Progs. Surf. Sci.* **71**, 147 (2003).

[45] W. Hofer and J. Redinger, *Surf. Sci.* **447**, 51 (2000).

[46] D. Edelstein, J. Heidenreich, R. Goldblatt, W. Cote, C. Uzoh, N. Lustig, P. Roper, T. McDevitt, W. Motsiff, A. Simon, J. Dukovic, R. Wachnik, H. Rathore, R. Schulz, L. Su, S. Luce, and J. Slattery, *Technical Digest, IEEE International Electron Devices Meeting*, 773 (1997).

[47] A. A. Istratov, H. Hedemann, M. Seibt, O. F. Vyvenko, W. Schroeter, T. Heiser, C. Flink, H. Hieslmair, and E. R. Weber, *J. Electrochem. Soc.* **145**, 3889 (1998).

[48] A. A. Istratov and E. R. Weber, *J. Electrochem. Soc.* **149**, G21 (2002).

[49] W. Kern, *J. Electrochem. Soc.* **137**, 1887 (1990).

[50] A. A. Istratov, C. Flink, H. Hieslmair, E. R. Weber, and T. Heiser, *Phys. Rev. Lett.* **81**, 1243 (1998).

[51] E. R. Weber, *Physica B* **340-342**, 1 (2003).

[52] R. N. Hall and J. H. Racette, *J. Appl. Phys.* **35**, 379 (1964).

[53] R. L. Meek and T. E. Seidel, *J. Phys. Chem. Solids* **36**, 731 (1975).

[54] A. A. Istratov, C. Flink, H. Hieslmair, S. A. McHugo, and E. R. Weber, *Mat. Sci. Eng. B* **72**, 99 (2000).

[55] S. K. Estreicher, *Phys. Rev. B* **60**, 5375 (1999).

[56] S. K. Estreicher, *Mater. Sci. Semicond. Process.* **7**, 101 (2004).

[57] D. E. Woon, D. S. Marynick, and S. K. Estreicher, *Phys. Rev. B* **45**, 13383 (1992).

[58] Y. Kamon, H. Harima, A. Yanase, and H. Katayama-Yoshida, *Physica B***308-310**, 391 (2001).

[59] K. Shirai, T. Michikita, and H. Katayama-Yoshida, *Jap. Soc. Appl. Phys.* **44**, 7760 (2005).

[60] C. D. Latham, M. Alatalo, R. M. Nieminen, R. Jones, S. Oberg, and P. R. Briddon. *Phys. Rev. B* **72**, 235205 (2005).

[61] A. A. Istratov, H. Hieslmair, T. Heiser, C. Flink, and E. R. Weber, *Appl. Phys. Lett.* **72**, 474 (1998).

[62] M. O. Aboelfotoh and B. G. Svenson, *Phys. Rev. B* **44**, 12742 (1991).

[63] T. Prescha and J. Weber, *Mater. Sci. Forum* **83-87**, 167 (1992).

[64] A. Mesli and T. Heiser, *Phys. Rev. B* **45**, 11632 (1992).

[65] S. M. Myers and D. M. Follstaedt, *J. Appl. Phys.* **79**, 1337 (1996).

[66] S. K. Estreicher, *Phys. Rev. B* **41**, 5447 (1990).

[67] D. West, S. K. Estreicher, S. Knack, and J. Weber, *Phys. Rev. B* **68**, 35210 (2003).

[68] T. Michikita, K. Shirai, and H. Katayama-Yoshida, *Jpn. Journ. Appl. Phys.* **44**, 7904 (2005).

[69] K. Matsukawa, N. Hattori, S. Maegawa, K. Shirai, and H. Katayama-Yoshida, *Physica B* **376-377**, 224 (2006).

[70] E. R. Weber, *Appl. Phys. A* **30**, 1 (1983).

[71] M. B. Shabani, T. Yoshimi, and H. Abe, *J. Electrochem. Soc.* **143**, 2025 (1996).

[72] C. Flink, H. Feick, S. A. McHugo, W. Seifert, H. Hieslmair, T. Heiser, A. A. Istratov, and E. R. Weber, *Phys. Rev. Lett.* **85**, 4900 (2000).

[73] A. A. Istratov and E. R. Weber, *Appl. Phys. A: Mater. Sci. Process.* **66**, 123 (1998).

[74] K. Hara and I. Ohdomari, *Jpn. J. Appl. Phys.* **37**, L1333 (1998).

[75] Y. Suda, H. Tanaka, and M. Sekiguchi, *Jpn. J. Appl. Phys.* **42**, 4887 (2003).

[76] H. Alouach and G. J. Mankey, *J. Mat. Research* **19**, 3620 (2004).

[77] H. Alouach and G. J. Mankey, *Appl. Phys. Lett.* **86**, 123114 (2005).

[78] M. Stepanova and S. K. Dew, *J. Vac. Sci. Technol. B* **24**, 592 (2006).

[79] N. Tokuda, D. Hojo, S. Yamasaki, K. Miki, and K. Yamabe, *Jpn. J. Appl. Phys.* **42**, L1210 (2003).

[80] N. Tokuda, H. Watanabe, D. Hojo, S. Yamasaki, K. Miki, and K. Yamabe, *Appl. Surf. Sci.* **237**, 529 (2004).

[81] N. Tokuda, M. Nishizawa, K. Miki, S. Yamasaki, R. Hasunuma, and K. Yamabe, *Jpn. J. Appl. Phys.* **44**, L613 (2005).

[82] K. Tatsumura, T. Watanabe, K. Hara, T. Hoshino, and I. Ohdimari, *Phys. Rev. B* **64**, 115406 (2001).

[83] R. Hasunuma, T. Yada, J. Okamoto, D. Hojo, N. Tokuda, and K. Yamabe, *Sci. Techn. Adv. Mat.* **6**, 667 (2005).

[84] D. R. Bowler, *J. Phys.: Condens. Matter* **16**, R721 (2004).

[85] J. H. G. Owen, K. Miki, H. Koh, H. W. Yeom, and D. R. Bowler, *Phys. Rev. Lett.* **88**, 226104 (2002).

[86] C. Bonet and S. P. Tear, *Appl. Phys. Lett.* **89**, 203119 (2006).

[87] J. H. G. Owen, K. Miki, and D. R. Bowler, *J. Mat. Sci.* **41**, 4568 (2006).

[88] J. W. Lyding, T. C. Shen, J. S. Hubacek, J. R. Tucker, and G. C. Abeln, *Appl. Phys. Lett.* **64**, 2010 (1994).

[89] T. Hitosugi, T. Hashizume, S. Heike, S. Watanabe, Y. Wada, T. Hasegawa, and K. Kitazawa, *Jpn. Journ. Appl. Phys.* **36**, L361 (1997).

[90] M. J. Haye, P. M. L. O. Scholte, A. F. Bakker, S. W. de Leeuw, F. Tuinstra, and G. Brocks, *Phys. Rev. B* **56** R1708 (1997).

[91] K. Miki, D. R. Bowler, J. H. G. Owen, G. A. D. Briggs, and K. Sakamoto, *Phys. Rev. B* **59**, 14868 (1999).

[92] J. H. G. Owen, K. Miki, and D. R. Bowler, *Surf. Sci.* **527**, L177 (2003).

[93] W. E. McMahon, I. G. Batyrev, T. Hannappel, J. M. Olson, and S. B. Zhang, *Phys. Rev. B* **74**, 033304 (2006).

[94] C. Preinesberger, S. Vandre, T. Kalka, and M. Dahne-Prietsch, *J. Phys. D: Appl. Phys.* **31**, L43 (1998).

[95] J. A. Knapp and S. T. Picraux, *Appl. Phys. Lett.* **48**, 466 (1986).

[96] J.-Y. Duboz, P.-A. Badoz, A. Perio, J.-C. Oberlin, F. A. D.'Avitaya, Y. Campidelli, and J. A. Chroboczek, *Appl. Surf. Sci.* **38**, 171 (1989).

[97] C.-X. Ji, M. Huang, J.-H. Yang, Y. A. Chang, R. Ragan, Y. Chen, D. A. A. Ohlberg, and R. S. Williams, *Appl. Phys. A* **78**, 287 (2004).

[98] J. Nogami, B. Z. Liu, M. V. Katkov, C. Ohbuchi, and N. O. Birge, *Phys. Rev. B* **63**, 233305 (2001).

[99] S. Harako, K. Kouno, S. Komuro, A. Ohata, and X. Zhao, *J. Cryst. Growth* **275**, e2263 (2005).

[100] S. K. Estreicher and J. L. Hastings, *Mat. Sci. Eng. B* **58**, 155 (1999).

[101] N. Troullier and J. L. Martins, *Phys. Rev. B* **43**, 1993 (1991).

[102] J. P. Perdew and A. Zunger, *Phys. Rev. B* **23**, 5048 (1981).

[103] C. Hartwigsen, S. Goedecker, and J. Hutter, *Phys. Rev. B* **58**, 3641 (1998).

[104] P. R. Briddon and R. Jones, *Phys. Status Solidi B* **217**, 131 (2000).

[105] J. Coutinho, R. Jones, P. R. Briddon, and S. Oberg, *Phys. Rev. B* **62**, 10824 (2000).

[106] A. A. Istratov, H. Hieslmair, C. Flink, T. Heiser, and E. R. Weber, *Appl. Phys. Lett.* **71**, 2349 (1997).

[107] L. Kleinman and D. M. Bylander, *Phys. Rev. Lett.* **48**, 1425 (1982).

[108] D. Sanchez-Portal, P. Ordejon, E. Artacho, and J. M. Soler, *Int. J. Quant. Chem.* **65**, 453 (1997).

[109] R. S. Mulliken, *J. Chem. Phys.* **23**, 1833 (1955).

[110] J. M. Soler, E. Artacho, J. D. Gale, A. Garcia, J. Junquera, P. Ordejon, and D. Sanchez-Portal, *J. Phys.: Condens. Matter* **14**, 2745 (2002).

[111] M. Seibt, M. Griess, A. A. Istratov, H. Hedemann, A. Sattler, and W. Schroeter, *Phys. Stat. Solidi A* **166**, 171 (1998).

[112] M. Seibt, H. Hedemann, A. A. Istratov, F. Riedel, A. Sattler, and W. Schroeter, *Phys. Stat. Solidi A* **171**, 301 (1999).

[113] K. Hozawa, S. Isomae, and J. Yugami, *Jpn. J. Appl. Phys.* **41**, 5887 (2002).

[114] K. Hozawa and J. Yugami, *Jpn. J. Appl. Phys.* **43**, 1 (2004).

[115] A. Bongiorno, A. Pasquarello, M. S. Hybertsen, and L. C. Feldman, *Phys. Rev. B* **74**, 075316 (2006).

[116] L. Barbier and J. Lapujoulade, *J. Vac. Sci. Technol. A* **8**, 2662 (1990).

[117] P. W. Murray, R. Lindsay, F. M. Leibsle, P. L. Wincott, and G. Thornton, *Phys. Rev. B* **54**, 13468 (1996).

[118] X. Hu and Z. Lin, *Appl. Surf. Sci.* **90**, 111 (1995).

[119] T. Kubo, T. Aruga, N. Takagi, and M. Nishijama, *Jpn. J. Appl. Phys.* **36**, L975 (1997).

[120] T. Ikeda, Y. Kawashima, H. Itoh, and T. Ichinokawa, *Surf. Sci.* **336**, 76 (1995).

[121] T. Ikeda, T. Watanabe, H. Itoh, and T. Ichinokawa, *Surf. Rev. Lett.* **3**, 1377 (1996).

[122] H. Itoh, T. Ann, T. Kawasaki, and T. Ichinokawa, *Surf. Rev. Lett.* **5**, 747 (1998).

[123] B. Z. Liu, M. V. Katkov, and J. Nogami, *Surf. Sci.* **453**, 137 (2000).

[124] L. A. Baker, A. R. Laracuente, and L. J. Whitman, *Phys. Rev. B* **71**, 153302 (2005).

[125] S. K. Estreicher, *Physica B* **273-274**, 424 (1999).

[126] A. E. Dolbak, R. A. Zhachuk, and B. Z. Olshanetsky, *Centr. Europ. Journ. Phys.* **1**, 463 (2003).

[127] A. Ramstad, G. Brocks, and P. J. Kelly, *Phys. Rev. B* **51**, 14504 (1995).

[128] M. Katkov and J. Nogami, *Bull. Am. Phys. Soc.* **47**, 283 (2002).

[129] Y. Chen, D. A. A. Ohlberg, and R. S. Williams, *J. Appl. Phys.* **91**, 3213 (2002).

[130] J. Nogami, *priv. comm.*

[131] C. Ohbuchi and J. Nogami, *Phys. Rev. B* **66**, 165323 (2002).

[132] B. Z. Liu and J. Nogami, *Nanotech.* **14**, 873 (2003).

[133] C. Polop, C. Rogero, J. L. Sacedón, and J. A. Martín-Gago, *Surf. Sci.* **482-485**, 1337 (2001).

[134] C. Rogero, C. Polop, L. Magaud, J. L. Sacedón, P. L. de Andrés, and J. A. Martín-Gago, *Phys. Rev. B* **66**, 235421 (2002).

[135] C. Rogero, C. Koitzsch, M. E. González, P. Aebi, J. Cerdá, and J. A. Martín-Gago, *Phys. Rev. B* **69**, 045312 (2004).

[136] T. J. Wood, C. Bonet, T. C. Q. Noakes, P. Bailey, and S. P. Tear, *Surf. Sci.* **598**, 120 (2005).

[137] I. Mayer and I. Felner, *J. Less-Common Met.* **29**, 25 (1972).

[138] L. Magaud, A. Pasturel, G. Kresse, and J. Hafner, *Phys. Rev. B* **55**, 13479 (1997).

[139] M. Methfessel, *Phys. Rev. B* **38**, 1537 (1988).

[140] C. Rogero, J. A. Martín-Gago, and J. I. Cerdá, *Phys. Rev. B* **74**, 121404 (2006).

[141] N. Gonzalez Szwacki and B. I. Yakobson, *Phys. Rev. B* **75**, 035406 (2006).

[142] S. Baroni, A. dal Corso, S. de Gironcoli, P. Giannozzi, C. Cavazzoni, G. Ballabio, S. Scandalo, G. Chiarotti, P. Focher, A. Pasquarello, K. Laasonen, A. Trave, R. Car, N. Marzari, and A. Kokalj, *hhtp://www.pwscf.org/* (2006).

[143] L. Magaud, J. P. Julien, and F. Cyrot-Lackmann, *J. Phys: Condens. Matter* **4**, 5399 (1992).

[144] L. Magaud, J. Y. Veuillen, D. Lollman, T. A. Nguyen Tan, D. A. Papaconstantopoulos, and M. J. Mehl, *Phys. Rev. B* **46**, 1299 (1992).

[145] L. Braicovich, E. Puppin, I. Lindau, A, Iandelli, G. L. Olcese, and A. Palenzona, *Phys. Rev. B* **41**, 3123 (1990).

[146] Y. Chen, D. A. A. Ohlberg, G. Medeiros-Ribeiro, Y. A. Chang, and R. S. Williams, *Appl. Phys. Lett.* **76**, 4004 (2000).

[147] E. Duverger, F. Palmino, E. Ehret, and J.-C. Labrune, *Surf. Sci.* **595**, 40 (2005).

[148] M.-A. Nicolet and S. S. Lau, *Formation and characterization of transition-metal silicides, VLSI Electronics-microstructure science, Vol. 6*, Eds N. G. Einspruch and G. B. Larrabee (1983).

[149] M. F. Wu, S. D. Yao, A. Vantomme, S. Hogg, H. Pattyn, G. Langouche, Q. Q. Yang, and Q. M. Wang, *J. Vac. Sci. Technol. B* **16**, 1901 (1998).

[150] J. J. Yang, C. J. Rawn, C.-X. Ji, Y. A. Chang, Y. Chen, R. Ragan, D. A. A. Ohlberg, and R. S. Williams, *Appl. Phys. A* **82**, 39 (2006).

[151] Y. Zhu, W. Zhou, S. Wang, T. Ji, X. Hou, and Q. Cai, *J. Appl. Phys.* **100**, 114312 (2006).

[152] S. Fujii, Y. Michishita, N. Miyamae, H. Suto, S. Honda, H. Okado, K. Oura, and M. Katayama, *Thin Sol. Films* **508**, 82 (2006).

[153] C. Preinesberger, S. K. Becker, S. Vandré, T. Kalka, and M. Dähne, *J. Appl. Phys.* **91**, 1695 (2002).

[154] Z. He, D. J. Smith, and P. A. Bennett, *Phys. Rev. B* **70**, 241402 (2004).

[155] G. Ye, M. A. Crimp, and J. Nogami, *Phys. Rev. B* **74**, 033104 (2006).

[156] T. Kobayashi, *Phys. Rev. B* **75**, 125401 (2007).

[157] B. Z. Liu and J. Nogami, *J. Appl. Phys.* **93**, 593 (2003).

[158] Y. Chen, D. A. A. Ohlberg, and R. S. Williams, *Mat. Sci. Eng. B* **87**, 222 (2001).

[159] V. B. Shenoy, *Appl. Phys. Lett.* **85**, 2376 (2004).

[160] A. Pradhan, N.-Y. Ma, and F. Liu, *Phys. Rev. B* **70**, 193405 (2004).

[161] J. A. Venables, J. DeGraffenreid, D. Kay, and P. Yang, *Phys. Rev. B* **74**, 075412 (2006).

[162] Y. Chen, D. A. A. Ohlberg, G. Medeiros-Ribeiro, Y. A. Chang, and R. S. Williams, *Appl. Phys. A* **75**, 353 (2002).

[163] W. Zhou, Y. Zhu, T. Ji, Z. Hou, and Q. Cai, *Nanotechn.* **17**, 852 (2006).

[164] G. Chen, J. Wan, J. Yang, X. Ding, L. Ye, and X. Wang, *Surf. Sci.* **513**, 203 (2002).

[165] J. Yang, Q. Cai, X. D. Wang, and R. Koch, *Surf. Int. Anal.* **36**, 104 (2004).

[166] B. Z. Liu and J. Nogami, *Surf. Sci.* **540**, 136 (2003).

[167] B. C. Harrison, P. Ryan, and J. J. Boland, *Surf. Sci.* **582**, 79 (2005).

[168] B. J. Min and K. M. Ho, *Phys. Rev. B* **40**, 7532 (1989).

[169] B. Z. Liu and J. Nogami, *Surf. Sci.* **488**, 399 (2001).

[170] M.-H. Tuilier, C. Pirri, D. Berling, D. Bolmont, G. Gewinner, and P. Wetzel, *Surf. Sci.* **555**, 94 (2004).

[171] J. Yang, Q. Cai, X.-D. Wang, and R. Koch, *Surf. Sci.* **526**, 291 (2003).

[172] J. H. G. Owen, D. R. Bowler, and K. Miki, *Surf. Sci.* **596**, 163 (2005).

[173] J. H. G. Owen, *priv. comm.*

[174] J. E. E. Baglin, F. M. d'Heurle, and C. S. Petersson, *J. Appl. Phys.* **52**, 2841 (1981).

[175] S. L. Liew, B. Balaikrisnan, S. Y. Chow, M. Y. Lai, W. D. Wang, K. Y. Lee, C. S. Ho, T. Osipowicz, and D. Z. Chi, *Thin Solid Films* **504**, 81 (2006).

[176] D. J. Chadi, *J. Vac. Sci. Technol.* **16**, 1290 (1979).

[177] R. A. Wolkow, *Phys. Rev. Lett.* **68**, 2636 (1992).

[178] C. Elsasser, J. Zhu, S. G. Louie, M. Fahnle, and C. T. Chan, *J. Phys.: Condens. Matter* **10**, 5081 (1998).